Drone-Borne SAR Imaging and Change Detection

By

Ali Bekar

A thesis submitted to

the University of Birmingham

for the degree of

DOCTOR OF PHILOSOPHY

School of Engineering

College of Engineering and Physical Sciences

University of Birmingham

January 2023

ABSTRACT

This thesis aims to carry out fundamental and systematic research on the formation of high-frequency, high-resolution drone-borne Synthetic Aperture Radar (SAR) imagery of an extended target area and the detection of both sizeable object displacements and subtle changes in it. Drone-borne systems are affordable, rapidly deployable, and capable of accessing difficult areas where human access is dangerous or unsafe. However, they are better suited to relatively short-range applications due to their limited payload capacities which restrict transmit powers and sensor sizes. At high operating frequencies, the radar form factor is reduced and the potential for obtaining very fine-resolution imagery and the sensitivity to temporal changes in the scene are improved. On the other hand, short-range operation at high frequencies leads to significant space-variant/invariant errors induced by motion errors resulting from wind turbulence and drone vibration. Further, for temporal change detection that relies on comparison of “before/after” radar imagery, motion errors are unique for each drone pass. Even if two focused images are formed, residual co-registration errors and residual spatially invariant/variant phase errors can degrade the resulting change map.

The research presented in this thesis sets out to develop image formation and change detection algorithms capable of handling the mentioned difficulties above based on theoretical analyses, validate the algorithms using simulations and evaluate the experimental performance in real-world conditions using a drone-borne SAR demonstrator built within this thesis' scope. In the experiments, low-cost vehicular radars operating at 24 and 77 GHz are used, and novel short-range, fine-resolution imagery (up to 1.7 cm in cross-range) of an extended target area is formed without employing a dedicated positional system. Also, it is shown, for the first time, that a high-frequency, high-resolution drone-borne SAR system operating at short ranges is capable of discerning both sizeable object displacements such as human replacement, and subtle changes such as the human footprint or car tyre marks.

To the memory of my grandfather, Ali Bekar

1939-2009

Acknowledgments

I would like to express my sincere gratitude to my thesis supervisors, Dr. Mike Antoniou and Prof. Chris Baker for their continued support, guidance, and encouragement to push the boundaries of the cutting edge.

I would like to thank Muge Bekar who is my wife, friend, and colleague for supporting and believing in me. I also would like to thank all the members of the MISL group for creating an active and stimulating research environment.

I would like to thank my parents, Filiz and Vedat Bekar, my aunt, Pembe Bekar, my mother-in-low, Emine Ozturk, my sisters, Esra and Seda, and my brother, Ahmet Berk for their unending love and support throughout the time of my PhD.

I would also like to express my love and gratitude to my precious son, Göktuğ who has been a source of joy and inspiration throughout this journey.

Last but not the least, I would like to thank Republic of Türkiye Ministry of National Education for funding and sponsoring my PhD project.

.

Table of Contents

List of Figures

List of Tables

Abbreviation List

2D: Two-dimensional

3D: Three-dimensional

ADC: Analog-to-digital Converter

BP: Back-projection

CCD: Coherent Change Detection

CNR: Clutter to Noise Ratio

COTS: Commercial-off-the-shelf

CSA: Chirp Scaling Algorithm

DInSAR: Differential Interferometric SAR

ICD: Incoherent Change Detection

IF: Intermediate Frequency

IMU: Inertial Measurement Unit

INS: Inertial Navigation System

InSAR: Interferometric SAR

FMCW: Frequency Modulated Continuous Wave

GA: Genetic Algortihm

GNSS: Global Navigation Satellite System

GPR: Ground Penetrating Radars (GPR)

GPS: Global Positioning System

GPU: Graphics Processing Unit

LOS: Line of Sight

LQMD: Local Quadratic Map-Drift

MD: Map-Drift

MEA: Minimum Entropy Algorithm

MoCo: Motion Compensation

NESZ: Noise Equivalent Sigma Zero

PGA: Phase Gradient Algorithm

PolInSAR: Polarimetric Interferometric SAR

POSP: Principle of Stationary Phase

PRF: Pulse Repetition Frequency

PRI: Pulse Repetition Interval

PSLR: Peak Sidelobe Ratio

PSP: Principle of Stationary Phase

Radar: Radio Detection and Ranging

RCM: Range Cell Migration

RCMC: Range Cell Migration Correction

RCS: Radar Cross Section

RDA: Range-Doppler Algorithm

RMA: Range Migration Algorithm

RMS: Root Mean Square

RTK: Real Time Kinematic

RVP: Residual Video Phase

SAR: Synthetic Aperture Radar

SNR: Signal to Noise Ratio

SW: Swath Width

sUAV: Small Unmanned Aerial Vehicle

Chapter 1

Introduction

1.1 Background

Small unmanned aerial vehicles (sUAV), drones, have started to become a part of modern life. Their use is drastically increasing, and their intended uses include security, monitoring, search & rescue operations, mapping, delivery, and agricultural spraying, to name but a few. According to the projection in [1], the global drone market capacity will triple by 2025, in comparison to 2018.

This popularity has been aided by the advantages of drones in comparison to other aerial vehicles, and the progress in drone technology. The attractive features of drones can be summarized as follows:

- Capable of accessing difficult areas where human access is dangerous or unsafe
- Simple to operate
- Rapidly deployable

- Lightweight
- Inexpensive

In parallel, drone technology has been progressing and drone technical specifications have been improving. That includes:

- Increasing flight time
- Better positioning accuracy
- Higher resistance to changing weather conditions
- Advanced algorithms to achieve multi-drone tasks

Depending on the application, drones can be equipped with different kinds of sensors such as cameras, ultrasonic range finders, lidars, and infrared detectors. The physical principles of operation of these sensors, and their limitations determine the remote sensing capability of the system. Hence, what these sensors cannot do is just as significant as what they can.

1.2 Motivations

Unlike other sensors, radar operation is independent of weather or lighting conditions. Moreover, radar can provide different types of information about the nature of the target such as relative position, radial velocity, size, shape, and dielectric properties. Therefore, in a drone-based system, radar can be used on its own or as part of a multi-sensor solution to further extend the ever-increasing suite of drone applications now and in the future.

Synthetic aperture radar (SAR) technology that allows high-resolution imaging of target areas may exploit the unique characteristics of drones to make SAR an affordable, rapidly deployable, and easily accessible remote sensing technique. In this way, SAR images that would otherwise necessitate advanced, space-borne, or airborne SAR, can be formed using drone-

borne SAR which is orders of magnitude less expensive for certain applications over specific periods of time. However, in contrast to air or space-borne systems, the size of the target area that a drone-borne system can cover is small since the payload capacity restricts the radar's sensor size and transmit power. This means that drone-borne SAR imaging is more suitable for operating at relatively shorter ranges, in many instances, consistent with areas of air-space which conventional manned aircraft cannot access. Nevertheless, as revisiting time is not a limitation for drones, the covered target area size can be increased by using multi-passes, either with or without multi-drone configurations.

A single-pass SAR system that uses one transmit and one receive antenna can form high-resolution two-dimensional (2D) images whereas SAR systems with multi-antenna or multi-pass configurations can form multiple images and provide more information about the target area. For example, coherent 2D SAR images formed by different apertures can be used to generate interferograms, volumetric images, and change-maps. Additionally, at high operating frequencies, the radar form factor is reduced and the potential for obtaining very fine-resolution imagery and the sensitivity to subtle changes in the scene are improved. Thereby, a drone-borne SAR system able to use these SAR techniques is capable of precisely measuring the distances and dimensions of an object in addition to quantifying the degree of change a surface has undergone. Moreover, the progress in drone technology is highly promising to expand the boundaries of drone-borne SAR imaging and techniques.

In view of the mentioned capabilities above, a drone-borne SAR system can be employed in many applications such as infrastructure monitoring to detect defects and changes that occur over time, security applications for situational awareness and intelligence gathering, agricultural crop growth monitoring, and post-disaster scene assessment.

As a result, research on enabling drone-borne SAR techniques for the imaging of terrain and the detection of subtle changes in it is highly attractive.

1.3 An Overview on State-of-the-Art Drone-Borne SAR

Up to now, many drone-based radar projects have been conducted and more than 150 papers have been published since 2015 [2]. Most of the works are summarized in [2] and [3] which are review papers. In this section, the main drone-based radar imaging works are considered and presented. Table 1.1 summarises the literature whereas an overview of the radar frequency ranges for NATO and IEEE band designations is demonstrated as a guide in Figure 1.1.

The initial experiments on drone-based radar remote sensing have started in 2005. Chenchen J. Li and Hao Ling built a drone-based radar imaging system by using a small consumer drone and a 4.3 GHz pulsed radar that is controlled by a laptop remotely via an onboard computer [4]. In the first experiment, corner reflectors were detected by using the range migration algorithm. In the second experiment [5], the range profiles of trees, humans and vehicles were compared with each other. However, the resulting images were not focused well due to the drone's undesired deviations from the nominal trajectory. On the other hand, these works showed that drones can be used for radar imaging. In 2017, another feasibility report was published by Giancarmine Fasano et al. [6]. A drone-based radar system operating at 4 GHz was built similar to the previous work. By using a 1.2 GHz bandwidth, corner reflectors were imaged with some geometric errors. The authors noted that more advanced navigation techniques are needed to form well focused and accurate images.

Drone-based radar research continued in applications requiring low signal frequencies such as buried object detection with ground penetrating radars (GPR). The first experiment

conducted in 2017 by J. Colorado and M. Perez et al. from the Pontifical Xavierian University [7]. They used a 2 GHz radar with 56 MHz bandwidth mounted onboard a drone. They achieved the detection of buried landmines up to 20 cm in depth with the aid of the developed navigation flight control system based on optical lasers. M. Garcia Fernandez et al. developed a drone-borne SAR system to generate a high-resolution underground image in 2018 [8]. They used a down-looking S-band radar, and the impact of the undesired deviations were minimized by using a Real Time Kinematic (RTK) system with a cm-level accuracy and a lidar altimeter. The SAR processing was completed by using the backprojection (BP) method that considers the drone's recorded positional data. In the experiment, the synthetic aperture length was adjusted to 70 cm, and the drone flew at an altitude of 0.75 m and at a speed of 0.3 m/s. As a result, they detected both plastic and metallic buried objects with 7.5 cm range and 2.6 cm cross-range resolution. It was reported that when the aperture length is increased, the cross-range resolution does not improve due to motion errors. In 2019, they extended the work from 2D imaging to three-dimensional (3D) imaging by using an m-sequence Ultra-Wide-Band radar [9]. Later on, they improved the system by employing a multi-channel radar to increase the scanning area size [10]. Another research on buried object detection was conducted by a group from the Institute German Aerospace Center [11]. The developed S-band multi-channel drone-borne SAR system has two main operational modes; one for detection and other is for identification. In detection mode, the drone moves forward and applies digital beamforming. In identification mode, the drone follows a helical or circular trajectory to provide high resolution and tomographic imaging. In the experiment, a GPS-RTK system and a 4K camera are used to enhance the positional information of the drone. In addition to these works, Markus Schartel, Ralf Burry, and their colleagues have conducted research on drone based GPR systems. They built a side-looking SAR system by using a Frequency Modulated Continuous Wave (FMCW)

radar, an altimeter and a GPS-RTK system [12]-[14]. The SAR system obtained around 10 cm spatial resolution by using the BP algorithm in stripmap mode as shown in [12]. The data collection geometry was changed to circular in [13] to extract height information. In [14], another antenna pair that use a different frequency band was mounted to the drone. In this way, interferometric capability was added to the system to generate digital elevation model of the surface.

Researchers from the University of Politecnica de Catalunya developed the first fully polarimetric SAR system for a drone in 2018 [15]. An X-band FMCW radar which has a 100 MHz bandwidth was used. Their aim was to evaluate the drone usage for different SAR applications such as interferometry, polymetric measurement and tomography. The use of repeat-pass interferometry and trajectories in the horizontal, vertical, and circular planes was examined. However, the main challenge was unwanted deviations of the drone. The phase history of point-like scatterers and polarimetric active radar calibrators were used to correct phase errors. However, there were no apparent space-variant phase errors. In the experiment, they flew the drone at a height of 150 m with 9 m/s velocity. The single look images were formed by BP algorithm, and the resolution achieved was approximately 30 cm.

Then, polarimetry and interferometry have started to be attractive topics. Laila Moreira et al. published a paper on a drone-based multiband differential interferometric SAR (DInSAR) system in 2019 [16]. They presented possible applications of the system with some experimental results. The first application is the subsurface tomography According to the paper, it can be achieved by employing holographic SAR or a bistatic drone-based radar system. The second application is forming a subsidence map. For measurements with high accuracy and within a short period of time, C and X bands were suggested whereas P and L bands were suggested for long-term measurements and in the presence of vegetation. The third application

is agriculture. It was stated that measuring soil moisture can be done in C band whereas crop classification can be achieved in C and L bands. In the drone-borne SAR system, three different radars operating at C, L and P bands were employed in order to test the system for different applications. Also, a differential Global Navigation Satellite System (GNSS) was used to improve the positional error estimation. In the experiment, the drone's height was 120 m and the swath range was 260 m. The C band image was generated with 1 m resolution whereas P band image had a 6 m resolution. Also, a C band Interferometric SAR (InSAR) image was presented. They noted that some areas appeared blurred because of atmospheric turbulence that results in undesired deviations. Later on, by using the same drone-borne SAR system, crop growth deficit maps with a 1 m spatial resolution and 5 cm accuracy were generated as shown in [17]. However, only the L-band was used to generate deficit maps. Another work that uses L band is [18]. In this work, differential SAR interferometry capability of the drone-borne SAR system in [16] was investigated. As a result, corner reflector displacements were detected with a better than 1 cm accuracy. The same SAR system operating in the P, L, and C-bands used in [19] to predict the sugarcane harvesting date and productivity. Data was collected in 7 survey flights over 6 months, and the saturation problem was avoided by combining L, P, and C band signals. Another research on drone-borne SAR interferometry is [20]. In this work, a drone-borne polarimetric interferometric SAR (PolInSAR) method was proposed. They used a Ku-band radar with a 1.2 GHz bandwidth. The baseline between the antennas was 0.62 cm. In the experiments, the incidence angle was adjusted as 70 degrees whereas the altitude of the drone was 206 m. The SAR images were formed by using $w - k$ algorithm with a one-step Motion Compensation (MoCo). The residual phase errors were compensated by Phase Gradient Algorithm (PGA). As a result, a 0.3 m spatial resolution was achieved. After implementing the interferometric SAR processing steps, the heights of the buildings were obtained with a 2.83 m

Root Mean Square (RMS) error. It is worth noting that authors investigated the effects of residual error and polarization distortion on drone borne PolInSAR in [21].

The Radar Research Laboratory at the Beijing Institute of Technology conducted a few projects that exploit P-band. In [22], an autofocus approach for drone-based ultrawideband ultra-wide beam SAR has been proposed to remove frequency-dependent and 2D space-variant motion errors. Then, tomographic SAR processing with 30 data acquisitions at an altitude of 170 ~ 260 meters was completed by using a deep learning method [23]. Later on, a single pass distributed SAR tomographic imaging was presented [24]. The experiment was conducted by employing four drone-borne SAR systems distributed along the height direction. As a result, a 3D SAR image was formed with a 2.7 m range resolution, 1.1 m azimuth resolution, and 2.5 m elevation resolution.

Apart from P, L and C bands, many drone-borne SAR imaging papers have been published that considers higher frequency bands. In 2017, a method for indoor drone-based SAR was proposed [25]. In the work, a range-direction-movement technique based on the wavenumber domain algorithm was presented to have a full coverage image. An experiment was carried out by using two corner reflectors and a 24 GHz FMCW radar. Also, they used an indoor Global Positioning System (GPS) system in order to compensate undesired deviations by recording the position of the drone.

In 2017, using a Ku-band radar, a high-resolution SAR image was created. [26]. High-accuracy positional data was provided by a differential GPS. Later, to correct the remaining phase errors, motion compensation using GPS data, PGA, and the Minimum Entropy Algorithm (MEA) were implemented. By making the phase errors spatially invariant, [27] formed SAR imagery without relying on navigational information (using the same SAR system as [26]). A

quasipolar-based fast factorized BP algorithm was proposed that also terminates the dependence on navigational data. Fast-factorized BP is computationally less expensive than BP, but it is slower than frequency-domain algorithms. A resolution of roughly 4 cm across the cross-range was attained.

A group of researchers from the Nanjing University of Aeronautics and Astronautics have conducted a few research on drone-borne SAR imaging. In 2018, a drone-borne SAR system that uses a 9.7-GHz FMCW radar with 1.8 GHz bandwidth was presented in [28], and the Graphics Processing Unit (GPU) architecture was reported in [29]. After applying a polar format algorithm, a 2D autofocus technique was used to achieve a 10-cm resolution. The slant range to the scene centre in the experiment was about 2.5 km. In [30], a 360-degree video SAR system development and signal processing was presented. According to experimental findings, a cost-effective system can acquire focused video sequences through the use of a Field Programmable Gate Array (FPGA) processor, which offers a quick response and perception of the scene. Later on, a repeat-pass circular stripmap VideoSAR was proposed to improve the wide-area surveillance capability of the drone-borne SAR system [31].

Another interesting work came in 2018. Jiaming Yan et al. developed a drone-based SAR system for security and rescue operations named as Vital-SAR-Imaging [32]. The proposed method had two different modes: one for detecting people by exploiting micro-Doppler phenomena and other for SAR imaging and target extraction. Firstly, an image of the environment was generated by implementing the Wavenumber Domain Algorithm (WDA). Then, possible targets were extracted by setting a threshold on the image. The last step was distinguishing human targets from others. This was achieved by sensing the chest vibrations of people by using micro-Doppler processing. As a result, it was shown that human targets can be

identified with a small error. In the experiment, a quadrotor drone with an optical flow sensor and a 5.8 GHz FMCW radar used with 320 MHz bandwidth.

A group form National University of Singapore proposed a signal processing approach for drone-borne SAR in 2018 [33]. When radar beam steering is away from zero Doppler direction, squint angle-dependent scattering information can be captured. Nevertheless, undesired deviations from the nominal trajectory and range azimuth coupling are main difficulties for this. They used the squint minimisation method to decrease range-azimuth coupling. For undesired deviation compensation, it was assumed that the drone's position cannot be determined by the onboard positioning systems. Therefore, they employed autofocus methods. A Doppler tracker, PGA, and minimum entropy-based autofocusing algorithm were used for raw data-based motion compensation. Doppler tracker fixes large perturbations of the drone by a large extend. Then, PGA is applied to sub-apertures refined by MEA. Finally, azimuth compression was completed via azimuth nonlinear chirp scaling. In the experiment, 35 GHz FMCW radar with 300 MHz bandwidth was used. The drone flew at 65 m with 3 m/s velocity for 60 seconds. The results showed that the Doppler tracker provided some improvements on the focusing. Then, applied PGA and MEA based motion compensation removed most of the phase errors, and a focused image with 20 cm cross-range resolution was obtained.

Researchers from the National Key Laboratory of Microwave Imaging Technology, Aerospace Information Research Institute in Beijing have undertaken important works on drone-borne SAR. In 2018, Manlai Ding et al. developed a lightweight and miniaturized K-band FMCW radar for drone-borne SAR applications [34]. Initial results obtained by using Range-Doppler Algorithm (RDA) showed that the system was able to form SAR images. Later on, they developed a W-band radar to exploit its unique reflective and broadband

characteristics. The architecture and sensitivity of the system were shown in [35]. Also, an initial experimental result was presented. Then, the detailed W-band mini-SAR system was shown in [36]. In this work, the focused SAR image was formed by using a MoCo technique that relies on combining information from the inertial measurement unit (IMU) and SAR. The maximum imaging range in experiments was set at 600 m. An imagery with 4.5-cm range and 3.5-cm cross-range resolution was produced. In [37], the imaged swath range was increased by employing a W-Band active phased array miniaturized scan-SAR. In this way, beam scanning feature for the SAR system was enabled. Experiments showed that the new system has a resolution of 4.5 cm, the imaging swath is 1000 m, and the operating range is 800 m. The SAR system presented in [38] was used with a symmetric triangular FMCW signal in [39]. In this work, a motion compensation approach was proposed for symmetric triangular FMCW signals. The method was based on splitting the up-chirp and down-chirp signals into sub-bands and measuring the range cell migration error by using signal interferometry and range envelope tracking. It was shown that the method can form better images compared with the two-step MoCo and the cross-correlation methods. In [40], a motion error estimation technique was proposed for the presented waveform based on the signal interferometry. The proposed technique was compared with the previous work and shown that finer images can be generated as the original motion errors was obtained.

Yixiang Luomei et al. built a Ku-band drone-borne SAR system that has three modes as full polarization, polarization interference and interference. In [41], a time-domain segmentation-based imaging algorithm was proposed. As a result, a 10 cm cross-range and 15 cm range resolution were obtained. Then, a polarimetric calibration method was given in [42]. Also, the segmentation-based algorithm was implemented to the real-time SAR imaging [43]. Later, they improved the algorithm that was based on an accurate phase error model of the

drone's translational and rotational motion to estimate and reconstruct the drone's three-dimensional trajectory using parameters derived from motion compensation [44]. Thus, it was reported that simultaneous location and imaging using drone-borne radar were achieved.

Also, bistatic and multi-static configurations have been examined. In [45], a MoCo algorithm suitable for drone-borne bistatic SAR was proposed. In the experiment, 15 GHz radars were used. The transmitter's altitude was 674 m whereas the receiver's altitude was 711 m. As a result, about 1.8 m range and 0.7 m cross-range resolution were obtained. In [46], the swarm drone SAR to form 3D images was considered. The compressed sensing algorithm was used to process the sparse data. The system analysis and sensing matrix design were presented in detail. The high-resolution 3D imaging in a single flight was achieved with the swarm drone 3D linear array SAR. The proposed method was validated through simulations.

Table 1.1: State-of-the-Art Drone-Borne SAR

Papers	**Operating frequency**	**Autofocus Algorithm**	**Altitude of the drone**	**Obtained range/azimuth resolution**	**Used for**
[4], [5]	4.3 GHz	No autofocus	2 m	Not well focused	2D imaging
[6]	4 GHz	No autofocus	N/A	Not well focused	2D imaging
[7]	2 GHz	No autofocus	0.5 m	N/A	Buried object detection
[8]	S-band	No autofocus	0.75 m	7.5 cm / 2.6 cm	Underground imaging
[9], [10]	0.6 to 3 GHz	No autofocus	2.3 m	N/A	3D underground imaging / increasing the area size scanned
[11]	S-band	No autofocus	2.5 m – 4.5 m	N/A	Detection and identification
[12], [13]	S-band	No autofocus	1.5 m - 2.5 m	10 cm / 10 cm	Underground imaging, height extraction.
[14]	S, X band	No autofocus	4 m	1 cm / 1 cm	Underground imaging & interferometry

[15]	X-band	No autofocus	150 m	1.5 m / 30 cm	Interferometry, polymetric & tomography
[16]	P, C bands	No autofocus	120 m	C-band: 1 m P-band: 6 m	Differential interferometric SAR
[17]	L- band	No autofocus	N/A	1 m / 1 m	Crop-growth monitoring
[18]	L-band	No autofocus	120 m	1 m / 0.1 m	Differential interferometric SAR
[19]	P, L, C bands	No autofocus	120 m	N/A	Sugarcane harvesting date prediction
[20]	Ku-band	PGA	206 m	0.3 m / 0.3 m	Polarimetric interferometric SAR
[22]-[24]	P-band	Frequency-dependent and 2D space-variant motion errors are removed using a proposed method.	170 m - 260 m	2.7 m / 1.1 m / 2.5 m	Multi-pass tomographic SAR & single pass distributed tomographic SAR
[26]	Ku-band	PGA and MEA	120 m	30 cm / 3 cm	2D imaging
[27]	Ku-band	Quasipolar-based fast factorized BP algorithm is proposed.	120 m	32 cm / 4 cm	2D imaging
[28] – [31]	9.7 GHz	2D autofocus method is proposed	2.5 km - SR	10 cm / 10 cm	2D imaging, 360-degree video SAR
[32]	5.8 GHz	No autofocus	NA	47 cm / NA	Vital-SAR-imaging
[33]	35 GHz	Doppler tracker, PGA, and MEA	65 m	0.5 m / 0.2 m	2D imaging
[35], [36]	W-band	MoCo by combining information from IMU and SAR	600 m	4.5 cm / 3.5 cm	2D imaging
[37]	W-band	MoCo based on the symmetrical triangle LFMCW signal [39], [40].	800 m - SR	4.5 cm /4.5 cm	2D imaging with beam scanning
[38] – [40]	W-band	MoCo approach for a symmetric triangular FMCW signal is proposed	100 m	8~8.6 cm / 2.2~7.5 cm	2D imaging

[41] – [43]	Ku-band	Time-domain segmentation-based imaging algorithm is proposed.	300~400 m	12.5~15 cm / 9.4~10 cm	2D imaging, real-time SAR imaging
[44]	Ku-band	A phase error model is proposed to estimate and reconstruct the drone's three-dimensional trajectory	450 m	10 cm / 10 cm	Simultaneous location and imaging
[45]	15 GHz	MoCo algorithm suitable for drone-borne bistatic SAR is proposed.	674 m - 711 m	1.8 m / 0.7 m	Bistatic SAR

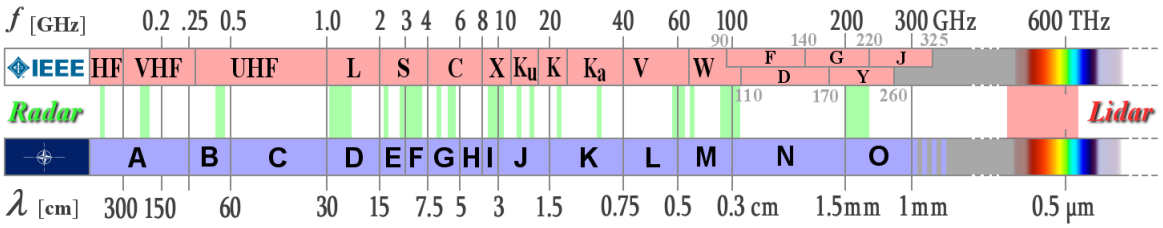

Figure 1.1: Waves and frequency ranges used by radar [47].

1.4 Problem Statement and Scope

The existing knowledge and methods given in the previous section are the state-of-the-art. In the beginning of this project, there were some completed works on low frequency systems and at X-band, with custom-built radar systems. However, high-resolution drone-borne SAR imaging with commercial-off-the-shelf (COTS) high frequency radars and change detection were less explored.

On the other hand, the use of high-frequency radars onboard drones is not straightforward due to drones' limited payload capacities, low accuracy of the positioning systems, as well as

their motion instabilities caused mainly by gusts of wind. The fundamental challenge originates from unknown deviations from the nominal flight trajectory resulting in phase errors that degrade SAR image focus, sharpness, and coherence. In the case of finer resolutions at high frequencies and shorter ranges, flight irregularities of drones lead to high degrees of spatially variant phase and geometric errors. The integrated positioning systems in drones are not accurate or fast enough to compensate for these errors. Hence, new remote sensing algorithms and techniques should be developed for drone-borne SAR imaging and change detection.

The goal of the thesis is to conduct fundamental and systematic research on the topics mentioned above. That includes theoretical analyses, validation using simulations, and experimental performance assessments in real conditions with a drone-borne SAR demonstrator I built and tested that operates at 24 and 77 GHz.

The thesis investigates whether it is possible to form high-resolution SAR imagery of a target area and detect subtle changes in it, by enabling remote sensing techniques for drone-borne SAR systems operating at high frequencies and short ranges. Precision SAR focusing and high coherence between repeat-pass images are preconditions for subtle change detection that relies on comparing “before/after” radar imagery. Hence, the first objective of this research is to develop algorithms for drone-borne SAR image formation whereas developing subtle change detection algorithms and methods is the second objective of the thesis. As evident from the literature review carried out, this kind of research has not been considered before.

1.5 Contributions

To address the fundamental challenges of this research, the thesis includes a proof-of-concept theoretical and experimental research study. The work done and my contribution to the drone-borne SAR include:

- Planning, designing, and building a drone-borne SAR system that uses a high-frequency off-the-shelf compact radar.
- Evaluating drone motion errors and possible difficulties in image formation.
- Developing an algorithm suitable to produce high-resolution SAR imagery in the presence of space-variant phase errors and range-walk errors and validating it through simulations.
- Deriving SAR change detection characteristics and examining the motion error impact on the change map formed by a high-frequency, high-resolution drone-borne SAR system.
- Developing an algorithm able to produce change maps by maximizing the coherency of temporally separated image pairs.
- Validating the performance of both proposed algorithms - the image formation algorithm and the change detection algorithm - through experiments. In the experiments, less than 2 cm cross-range resolution was achieved, and the ability of the drone-borne SAR system to detect both sizeable and subtle changes was proven by detecting human footprint and car tyre marks on a grass floor.

Based on the summarised works above, two journal papers and two conference papers have been published/submitted as listed below. Publications contain the work outlined in the thesis.

1- A. Bekar, M. Antoniou and C. J. Baker, "Low-Cost, High-Resolution, Drone-Borne SAR Imaging," in IEEE Transactions on Geoscience and Remote Sensing, vol. 60, pp. 1-11, 2022, Art no. 5208811, doi: 10.1109/TGRS.2021.3085235.

2- A. Bekar, M. Antoniou and C. J. Baker, "High-Resolution Drone-Borne SAR using Off-the-Shelf High-Frequency Radars," 2021 IEEE Radar Conference (RadarConf21), 2021, pp. 1-6, doi: 10.1109/RadarConf2147009.2021.9455342.

3- A. Bekar, M. Antoniou and C. J. Baker, "Change Detection for High-Resolution Drone-Borne SAR at High Frequencies - First Results," 2023 IEEE Radar Conference (RadarConf23), San Antonio, TX, USA, 2023, pp. 1-5, doi: 10.1109/RadarConf2351548.2023.10149798.

4- A. Bekar, M. Bekar, M. Antoniou and C. J. Baker, "Coherent Change Detection for High-Resolution Drone-Borne SAR at 24 GHz", submitted to IEEE Journal of Selected Topics in Applied Earth Observations and Remote Sensing.

1.6 Thesis Outline

- Chapter 2 provides a foundation for the topics covered in subsequent chapters. It explains the radar basics, SAR basics, and range-Doppler algorithm for dechirp-on-receive systems.
- Chapter 3 examines commonly used motion compensation methods. Specifically, the algorithms capable of compensating for phase errors and correcting range-walk errors for positional data-based MoCo, Local Quadratic MD (LQMD), and PGA are presented and validated through simulations.
- Chapter 4 details the built two drone-borne SAR systems built at the University of Birmingham. Also, based on the employed COTS devices and the SAR geometry, the major SAR system characteristics such as the data collection limits, spatial resolution, sensitivity, and swath limits are derived. Finally, the motion errors are evaluated and possible difficulties in image formation are discussed.
- Chapter 5 develops and examines methods for the production of real-world, very high-resolution imagery using a high-frequency drone-borne SAR operating at short-ranges. At first, an imaging algorithm capable of handling the motion errors discussed in

Chapter 3 is proposed and presented. The performance of this algorithm is validated through both simulation and experiments. As a result, a novel short-range, fine-resolution imagery of an extended target area is generated using a low-cost drone-borne FMCW radar operating at 24 and 77 GHz, without employing dedicated positioning systems.

- Chapter 6 develops and examines techniques to enable incoherent and coherent change detection for short-range, high-resolution drone-borne SAR systems operating at high frequencies. The potential of using high frequencies at short ranges for fine-resolution imagery and sensitivity to temporal change detection is highlighted, as are the challenges in terms of sensitivity to SAR motion errors. After evaluating change detection parameters, decorrelation sources, and limitations of the SAR system, a change detection algorithm is proposed. The validity of the approach is tested through various experimental scenarios. As a result, both subtle changes such as the human footprint or car tyre marks, and sizeable object displacement such as human replacements are possible to discern with a drone-borne SAR demonstrator operating at 24 GHz.
- Chapter 7 draws the conclusions of this thesis along with future work.

1.7 References

[1] Larisa Kapustina, Natalia Izakova, Elizaveta Makovkina, Michail Khmelkov, “The global drone market: main development trends” *in SHS Web Conf*. 2021, DOI: 10.1051/shsconf/202112911004.

[2] Miccinesi L, Beni A, Pieraccini M. UAS-Borne Radar for Remote Sensing: A Review. *Electronics*. 2022; 11(20):3324. https://doi.org/10.3390/electronics11203324

[3] Y. Á. López, M. García-Fernández, G. Álvarez-Narciandi and F. L. -H. Andrés, "Unmanned Aerial Vehicle-Based Ground-Penetrating Radar Systems: A review," in *IEEE Geoscience and Remote Sensing Magazine*, vol. 10, no. 2, pp. 66-86, June 2022, doi: 10.1109/MGRS.2022.3160664.

[4] Li, Chenchen J. and Hao Ling. “Synthetic aperture radar imaging using a small consumer drone.” *2015 IEEE International Symposium on Antennas and Propagation & USNC/URSI National Radio Science Meeting* (2015): 685-686.

[5] Li, Chenchen J. and Hao Ling. “High-resolution, downward-looking radar imaging using a small consumer drone.” *2016 IEEE International Symposium on Antennas and Propagation (APSURSI)* (2016): 2037-2038.

[6] G. Fasano, A. Renga, A. R. Vetrella, G. Ludeno, I. Catapano and F. Soldovieri, "Proof of concept of micro-UAV-based radar imaging," *2017 International Conference on Unmanned Aircraft Systems (ICUAS)*, 2017, pp. 1316-1323, doi: 10.1109/ICUAS.2017.7991432.

[7] J. Colorado, M. Perez, I. Mondragon, D. Mendez, C. Parra, C. Devia, J. Martinez-Moritz & L. Neira (2017) An integrated aerial system for landmine detection: SDR-based Ground Penetrating Radar onboard an autonomous drone, Advanced Robotics, 31:15, 791-808, DOI: 10.1080/01691864.2017.1351393

[8] M. García Fernández et al., "Synthetic Aperture Radar Imaging System for Landmine Detection Using a Ground Penetrating Radar on Board a Unmanned Aerial Vehicle," in IEEE Access, vol. 6, pp. 45100-45112, 2018, doi: 10.1109/ACCESS.2018.2863572.

[9] Garcia-Fernandez M, Alvarez-Lopez Y, Las Heras F. Autonomous Airborne 3D SAR Imaging System for Subsurface Sensing: UWB-GPR on Board a UAV for Landmine and IED Detection. *Remote Sensing*. 2019; 11(20):2357. https://doi.org/10.3390/rs11202357

[10] M. García-Fernández, Y. Á. López and F. L. -H. Andrés, "Airborne Multi-Channel Ground Penetrating Radar for Improvised Explosive Devices and Landmine Detection," in IEEE Access, vol. 8, pp. 165927-165943, 2020, doi: 10.1109/ACCESS.2020.3022624.

[11] E. Schreiber, A. Heinzel, M. Peichl, M. Engel and W. Wiesbeck, "Advanced Buried Object Detection by Multichannel, UAV/Drone Carried Synthetic Aperture Radar," 2019 13th European Conference on Antennas and Propagation (EuCAP), 2019, pp. 1-5.

[12] M. Schartel, R. Burr, W. Mayer, N. Docci and C. Waldschmidt, "UAV-Based Ground Penetrating Synthetic Aperture Radar," 2018 IEEE MTT-S International Conference on Microwaves for Intelligent Mobility (ICMIM), 2018, pp. 1-4, doi: 10.1109/ICMIM.2018.8443503.

[13] M. Schartel, R. Burr, R. Bähnemann, W. Mayer, and C. Waldschmidt, ``An experimental study on airborne landmine detection using a circular synthetic aperture radar," 2020, arXiv:2005.02600. [Online]. Available: http://arxiv.org/abs/2005.02600

[14] R. Burr, M. Schartel, A. Grathwohl, W. Mayer, T. Walter and C. Waldschmidt, "UAV-Borne FMCW InSAR for Focusing Buried Objects," in IEEE Geoscience and Remote

Sensing Letters, vol. 19, pp. 1-5, 2022, Art no. 4014505, doi: 10.1109/LGRS.2021.3094165.

[15] M. Lort, A. Aguasca, C. López-Martínez and T. M. Marín, "Initial Evaluation of SAR Capabilities in UAV Multicopter Platforms," in IEEE Journal of Selected Topics in Applied Earth Observations and Remote Sensing, vol. 11, no. 1, pp. 127-140, Jan. 2018, doi: 10.1109/JSTARS.2017.2752418.

[16] L. Moreira et al., "A Drone-borne Multiband DInSAR: Results and Applications," 2019 IEEE Radar Conference (RadarConf), 2019, pp. 1-6, doi: 10.1109/RADAR.2019.8835653.

[17] G. Oré *et al.*, "Crop Growth Monitoring with Drone-Borne DInSAR," *Remote Sensing*, vol. 12, no. 4, p. 615, Feb. 2020, doi: 10.3390/rs12040615

[18] D. Luebeck *et al.*, "Drone-borne Differential SAR Interferometry," *Remote Sensing*, vol. 12, no. 5, p. 778, Feb. 2020, doi: 10.3390/rs12050778.

[19] G. Oré et al., "Predicting Sugarcane Harvest Date and Productivity with a Drone-Borne Tri-Band SAR," Remote Sensing, vol. 14, no. 7, p. 1734, Apr. 2022, doi: 10.3390/rs14071734

[20] Lv Z, Qiu X, Cheng Y, Shangguan S, Li F, Ding C. Multi-Rotor UAV-Borne PolInSAR Data Processing and Preliminary Analysis of Height Inversion in Urban Area. *Remote Sensing*. 2022; 14(9):2161. https://doi.org/10.3390/rs14092161

[21] Lv Z, Li F, Qiu X, Ding C. Effects of Motion Compensation Residual Error and Polarization Distortion on UAV-Borne PolInSAR. *Remote Sensing*. 2021; 13(4):618. https://doi.org/10.3390/rs13040618

[22] Z. Ding et al., "An Autofocus Approach for UAV-Based Ultrawideband Ultrawidebeam SAR Data With Frequency-Dependent and 2-D Space-Variant Motion Errors," in IEEE

Transactions on Geoscience and Remote Sensing, vol. 60, pp. 1-18, 2022, Art no. 5203518, doi: 10.1109/TGRS.2021.3062183.

[23] C. Liu, Y. Wang, Z. Ding, Y. Wei, J. Huang and Y. Cai, "Analysis of Deep Learning 3-D Imaging Methods Based on UAV SAR," *IGARSS 2022 - 2022 IEEE International Geoscience and Remote Sensing Symposium*, 2022, pp. 2951-2954, doi: 10.1109/IGARSS46834.2022.9883292.

[24] Y. Wang *et al.*, "First Demonstration of Single-Pass Distributed SAR Tomographic Imaging With a P-Band UAV SAR Prototype," in *IEEE Transactions on Geoscience and Remote Sensing*, vol. 60, pp. 1-18, 2022, Art no. 5238618, doi: 10.1109/TGRS.2022.3221859.

[25] J. Yan et al., "Indoor range-direction-movement SAR for drone-based radar systems," 2017 IEEE Asia Pacific Microwave Conference (APMC), 2017, pp. 1290-1293, doi: 10.1109/APMC.2017.8251698.

[26] Y. A. Su, W. Liu, H. Feng and B. P. Ng, "Study of multi-rotor UAV SAR processing," 2017 IEEE Radar Conference (RadarConf), Seattle, WA, 2017, pp. 0226-0232, doi: 10.1109/RADAR.2017.7944202.

[27] S. Zhou, L. Yang, L. Zhao and G. Bi, "Quasi-Polar-Based FFBP Algorithm for Miniature UAV SAR Imaging Without Navigational Data," in IEEE Transactions on Geoscience and Remote Sensing, vol. 55, no. 12, pp. 7053-7065, Dec. 2017, doi: 10.1109/TGRS.2017.2739133.

[28] X. Mao, D. Li, L. Ding, and D. Zhu, “Signal processing for multi-rotors UAV SAR,” in Proceedings of IET International Radar Conference, Nanjing, China, Oct. 2018.

[29] Z. Xu and D. Zhu, “High-resolution miniature UAV SAR imaging based on GPU Architecture,” J. Phys. Conf. Ser., vol. 1074, no. 1, p. 012122, Sep. 2018.

[30] Y. Zhang, D. Zhu, X. Mao, X. Yu, J. Zhang and Y. Li, "Multirotors Video Synthetic Aperture Radar: System Development and Signal Processing," in *IEEE Aerospace and Electronic Systems Magazine*, vol. 35, no. 12, pp. 32-43, 1 Dec. 2020, doi: 10.1109/MAES.2020.3000318.

[31] Y. Zhang, D. Zhu, X. Mao, G. Zhang and H. Leung, "Multirotor UAV-Borne Repeat-Pass CSM-VideoSAR," in *IEEE Transactions on Aerospace and Electronic Systems*, vol. 58, no. 3, pp. 2601-2605, June 2022, doi: 10.1109/TAES.2021.3117895.

[32] J. Yan, Z. Peng, H. Hong, H. Chu, X. Zhu and C. Li, "Vital-SAR-Imaging With a Drone-Based Hybrid Radar System," in IEEE Transactions on Microwave Theory and Techniques, vol. 66, no. 12, pp. 5852-5862, Dec. 2018, doi: 10.1109/TMTT.2018.2874268.

[33] Hu X, Ma C, Hu R, Yeo TS. Imaging for Small UAV-Borne FMCW SAR. *Sensors*. 2019; 19(1):87. https://doi.org/10.3390/s19010087

[34] M. Ding, X. Liang, L. Tang, Z. Wen, X. Wang and Y. Wang, "Micro FMCW SAR with High Resolution for Mini UAV," *2018 International Conference on Microwave and Millimeter Wave Technology (ICMMT)*, 2018, pp. 1-3, doi: 10.1109/ICMMT.2018.8563465.

[35] M. Ding, L. Tang, L. Zhou, X. Wang, Z. Weng and J. Qu, "W Band Mini-SAR on Multi Rotor UAV Platform," *2019 IEEE 2nd International Conference on Electronic Information and Communication Technology (ICEICT)*, 2019, pp. 416-418, doi: 10.1109/ICEICT.2019.8846356.

[36] M. Ding, C. Ding, L. Tang, X. Wang, J. Qu and R. Wu, "A W-Band 3-D Integrated Mini-SAR System With High Imaging Resolution on UAV Platform," in IEEE Access, vol. 8, pp. 113601-113609, 2020, doi: 10.1109/ACCESS.2020.3003273.

[37] Ding M, Wang X, Tang L, Qu J, Wang Y, Zhou L, Wang B. A W-Band Active Phased Array Miniaturized Scan-SAR with High Resolution on Multi-Rotor UAVs. *Remote Sensing*. 2022; 14(22):5840. https://doi.org/10.3390/rs14225840

[38] M. Ding, L. Tang, L. Zhou, X. Wang, Z. Weng and J. Qu, "W Band Mini-SAR on Multi Rotor UAV Platform," *2019 IEEE 2nd International Conference on Electronic Information and Communication Technology (ICEICT)*, 2019, pp. 416-418, doi: 10.1109/ICEICT.2019.8846356.

[39] W. Xu, B. Wang, M. Xiang, S. Wang and Y. Jianfeng, "A Novel Motion Compensation Approach Based on Symmetric Triangle Wave Interferometry for UAV SAR Imagery," in IEEE Access, vol. 8, pp. 104996-105007, 2020, doi: 10.1109/ACCESS.2020.2999908.

[40] W. Xu, B. Wang, M. Xiang, C. Song and Z. Wang, "A Novel Autofocus Framework for UAV SAR Imagery: Motion Error Extraction From Symmetric Triangular FMCW Differential Signal," in *IEEE Transactions on Geoscience and Remote Sensing*, vol. 60, pp. 1-15, 2022, Art no. 5218915, doi: 10.1109/TGRS.2021.3133331.

[41] Y. Luomei and F. Xu, "Motion Compensation for Multirotors Minisar System," *2021 IEEE International Geoscience and Remote Sensing Symposium IGARSS*, 2021, pp. 5143-5146, doi: 10.1109/IGARSS47720.2021.9553707.

[42] J. Liu, Y. Luomei, X. Yuan and F. Xu, "Polarimetric Calibration of Mini SAR based on UAV Platform," *2021 Signal Processing Symposium (SPSympo)*, 2021, pp. 165-170, doi: 10.1109/SPSympo51155.2020.9593511.

[43] Y. Luomei and F. Xu, "Real-Time Implementation of Segmental Aperture Imaging Algorithm for Multirotor-Borne Minisar," *IGARSS 2022 - 2022 IEEE International*

Geoscience and Remote Sensing Symposium, 2022, pp. 4529-4532, doi: 10.1109/IGARSS46834.2022.9883374.

[44] Y. Luomei, F. Xu, F. Wang and Y. Dong, "Demonstration of Simultaneous Localization and Imaging With Multirotor-Borne MiniSAR," in *IEEE Journal of Selected Topics in Applied Earth Observations and Remote Sensing*, vol. 15, pp. 6548-6558, 2022, doi: 10.1109/JSTARS.2022.3190940.

[45] Z. Wang, F. Liu, T. Zeng and S. He, "A High-Frequency Motion Error Compensation Algorithm Based on Multiple Errors Separation in BiSAR Onboard Mini-UAVs," in *IEEE Transactions on Geoscience and Remote Sensing*, vol. 60, pp. 1-13, 2022, Art no. 5223013, doi: 10.1109/TGRS.2022.3150081.

[46] H. Ren *et al*., "Swarm UAV SAR for 3-D Imaging: System Analysis and Sensing Matrix Design," in *IEEE Transactions on Geoscience and Remote Sensing*, vol. 60, pp. 1-16, 2022, Art no. 5238316, doi: 10.1109/TGRS.2022.3221775.

[47] Waves and frequency ranges used by radar https://www.radartutorial.eu/07.waves/Waves%20and%20Frequency%20Ranges.en.html Accessed 03 Oct. 2023.

Chapter 2

Fundamentals of Radar Imaging

2.1 Radar Basics

Radio Detection and Ranging (RADAR) is a system that uses electromagnetic waves to measure the radar cross-section (RCS), dielectrics, range, relative velocity, and angle of a target regardless of weather or lighting conditions [1], [2]. A radar system includes at least one transmitter, one target, and one receiver. Figure 2.1 shows the basic principles of operation and components used in radar transmission and reception. The formed and amplified electromagnetic wave in the transmitter is named the transmitted signal. The signal radiates from the transmit antenna, propagates in space, and illuminates an area depending on the antenna beam pattern. An object called a target within this area scatters the incoming signal's energy. A small amount of scattered energy reaches the receive antenna. The collected electromagnetic waves by the receiver are named the received signal. The information about the target is extracted by using the received signal's properties such as the signal delay, Doppler

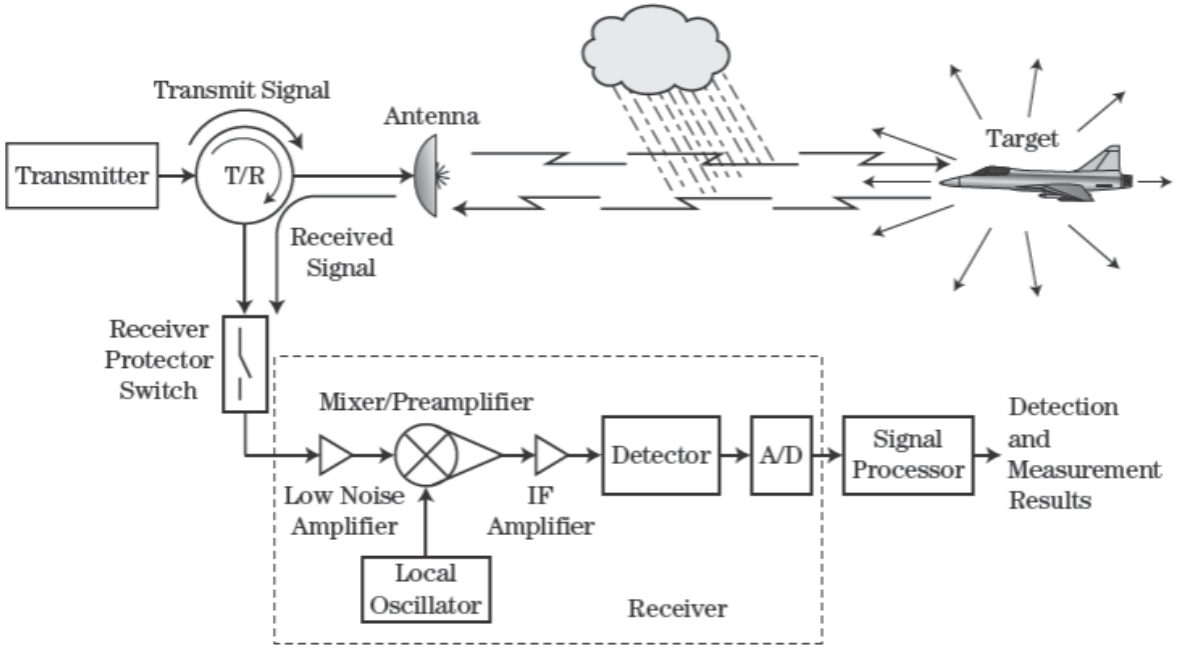

Figure 2.1 Radar transmission and reception process [4].

frequency and phase. How much detail can be extracted about the target is determined by the resolution which is defined as the minimum separation between two targets in order to be discriminated by the radar. The distance between the radar and the target is obtained from the signal delay. If the initial phases of the transmitted signals are known or the same with each other, this kind of radar is a coherent radar that enables relative velocity and angle estimation by using the phase difference of the incoming signals. When two consecutive coherent signals are transmitted towards a moving target, a phase difference occurs between two received signals due to the Doppler effect. By exploiting this phase difference, the radial velocity can be estimated. This feature is used in tracking radars to determine the trajectory of a moving target. Regarding the angle, the echo signal should be collected from different locations to estimate it. If the scattered signal is received by multiple receiver antennas separated by a small distance, a phase difference depending on the target's angle occurs between the received signals. By using this phase difference, relative angle estimation can be done. This kind of radars are known

as single-input-multiple-output (SIMO) radars. If the system includes multiple transmitters, the system is named the multiple-input-multiple-output (MIMO) radar. Also, the angle can be measured by moving the radar from one point to another. When a signal is transmitted and received at each point, a phase shift occurs in each received signal depending on the target's relative angle. Similar to the previous method, the angle is estimated by extracting the phase shift. This method is known as the synthetic-aperture-radar (SAR) and used in radar imagery. It will be examined in this and later chapters.

The radar operating frequency is another factor that makes the radar system more suitable for particular applications than for others [2]. The operating frequency can be as low as a few megahertz or high enough to be in the ultraviolet region of the spectrum. As an example, L and S band radars are commonly used by the land-based air surveillance radars whereas X band is used for many applications such as weapon tracking, airborne radar, or shipboard navigation [2]. At high frequencies, the radar form factor is reduced and the potential for obtaining wider bandwidths and narrower beams are improved. Today's automotive radars use millimetre wavelengths for their applications [3].

2.1.1 Radar Equation

The radar equation shows the basic relationship between the fundamental radar parameters, and it can be used to calculate the maximum detectable range, sensitivity, and signal to noise ratio (SNR) ([2], [4], [5]). The power of the received signal at the receive antenna output is given by:

$$P_r = \frac{P_t G_t}{4\pi R^2} \cdot \frac{\sigma}{4\pi R^2} \cdot A_e \tag{2.1}$$

where P_r is the received signal's power, P_t is the transmitted signal's power, G_t is the transmit antenna gain, R is the range between the radar and the target, σ is the radar cross section (RCS) of the target, A_e is the effective aperture of the receive antenna.

The first factor in (2.1) is the power loss of the transmitted signal during propagation in free space. The second part is responsible for the power loss of the back-scattered signal towards the radar receiver in free space. The last term of the equation is related to the size of the receive antenna. The effective aperture of the antenna assuming 100% antenna efficiency is expressed by:

$$A_e = \frac{\lambda^2 G_r}{4\pi} \tag{2.2}$$

where λ is the wavelength of the signal, and G_r is the receive antenna gain.

The maximum detectable range can be calculated by using (2.1) and (2.2). When the received signal power, P_r, is equal to the minimum required received power, $P_{r_{min}}$, to detect a target, the range, R, can be expressed as the maximum detectable range, R_{max}, and written as: [5]

$$R_{max} = \sqrt[4]{\frac{P_t G_t G_r \sigma \lambda^2}{(4\pi)^3 P_{r_{min}}}} \tag{2.3}$$

This equation states that when the transmit power or antenna gains are increased by a given factor, R_{max} increases by the fourth root of that factor. In (2.3), $P_{r_{min}}$ also represents the sensitivity of the radar receiver, which is limited by the thermal noise. Lower noise power provides better sensitivity as will be shown later. The noise power in a receiver is expressed by:

$$P_n = kTBF \tag{2.4}$$

where P_n is the noise power, k is the Boltzmann constant, T is the noise temperature, B is the 3-dB bandwidth of the signal, and F is the noise figure.

In (2.4), k is a constant, and T is not an adjustable parameter. Hence, there are only two parameters that can be altered to adjust the noise power. However, reducing the bandwidth is not a preferred method to reduce the noise power since higher bandwidths provide better resolutions as will be indicated in Section 2.1.3. On the other hand, the noise figure can be reduced as much as possible to keep the noise power at a certain level. The noise figure is a measure of the receiver's sensitivity in processing low-power signals. Each component in the receiver chain contributes to the noise figure. Nonetheless, the first component in the chain dominates the system's noise figure when it has a high gain [6]. Therefore, a low noise amplifier is always used after the antenna as the first component in the receiver chain. In this way, the noise power level of the receiver can be controlled.

Defining the noise power enables us to derive one of the most important radar parameters, the signal-to-noise ratio (SNR). It always must be higher than a specific value depending on the sensitivity of the receiver. SNR can be calculated by the ratio of (2.1) to (2.4). However, until that point, the radar equation has been presented without considering losses. As mentioned in [4], there are five different losses named as the system loss, the transmit loss, the atmospheric loss, the receiver loss, and the processing loss. If the sum of all the losses is represented by L_s, SNR can be expressed by:

$$SNR = \frac{P_r}{P_n} = \frac{P_t G_t G_r \sigma \lambda^2}{(4\pi)^3 R^4 k T B F L_s} \tag{2.5}$$

2.1.2 Radar Waveform

The most common radar waveform is the linear frequency modulated (LFM) signal. There are a few reasons for this such as compatibility to pulse compression, robustness to Doppler shift, suitability for stretch processing, and easiness of implementation on transmit [5]. The generated LFM signal in the transmitter is given by: [1]

$$s_t(t) = p(t) \cdot \cos(2\pi f_c t + \pi\gamma t^2), \qquad t \in [-\frac{T_m}{2}, \frac{T_m}{2}] \tag{2.6}$$

where s_t is the transmitted signal, $p(t)$ is the envelope of the signal, t is time, f_c is the radar operating frequency, γ is the chirp rate, and T_m is the sweep time.

The real valued LFM signal in the time domain is shown in Figure 2.2 (a). This real signal can be expressed in the complex exponential form as:

$$s_t(t) = \boldsymbol{RE}\{p(t) \cdot e^{j2\pi f_c t} \cdot e^{j\pi\gamma t^2}\} \tag{2.7}$$

where $\boldsymbol{RE}\{\cdot\}$ denotes the real part of the complex term.

$$p(t) = rect\left(\frac{t}{T_m}\right) \tag{2.8}$$

The carrier wave is represented by the first exponential term in (2.7) whereas the second exponential term that includes the quadratic phase is the modulation of the signal. The quadratic phase of the signal with the peak value of $\pi\gamma\left(\frac{T_m}{2}\right)^2$ is shown in Figure 2.2 (b).

The instantaneous frequency of the signal, $f(t)$, is determined by the derivative of the LFM signal's phase with respect to time as follows:

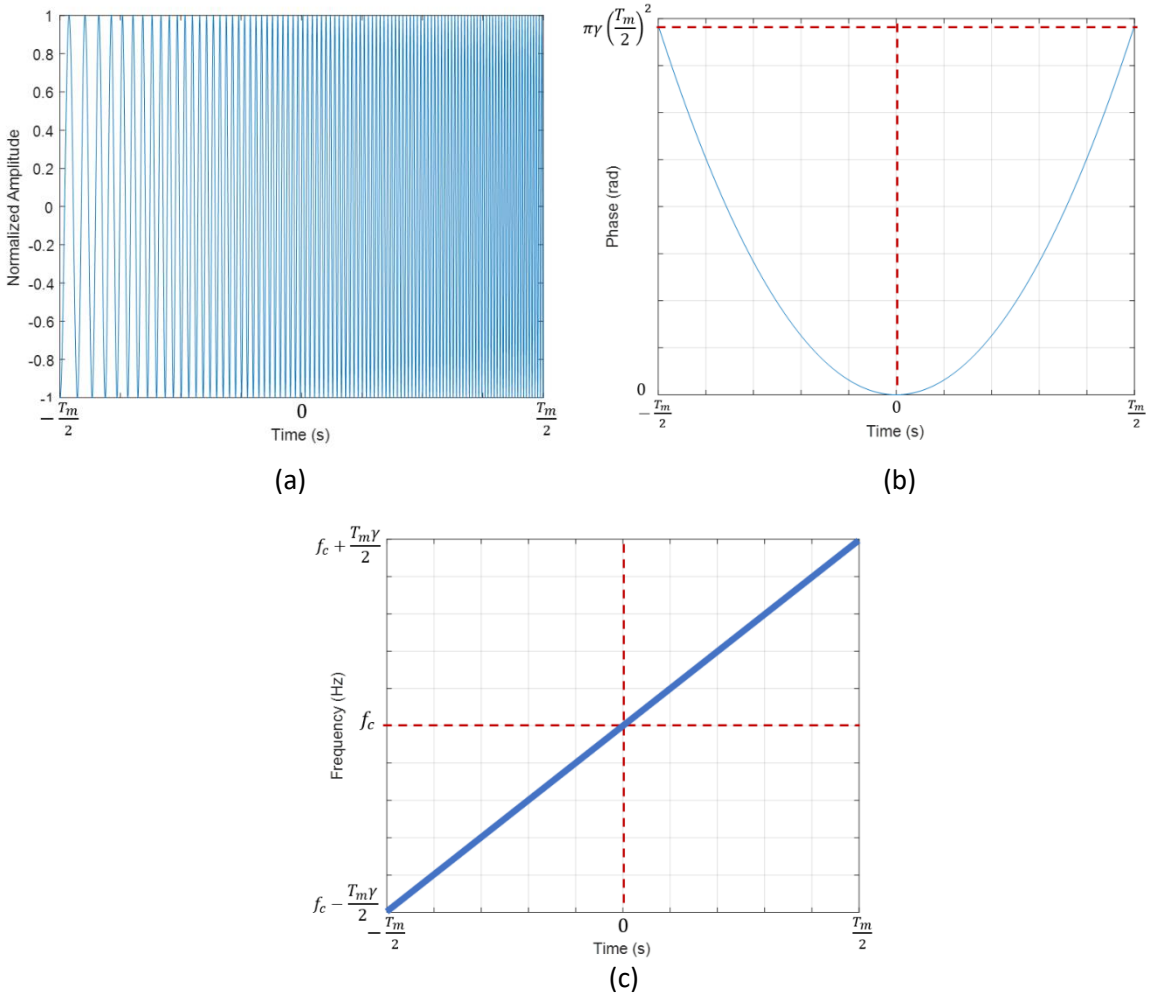

Figure 2.2 (a) The real valued LFM signal in the fast time domain, (b) The quadratic phase of the LFM signal, (c) LFM signal spectrogram.

$$f(t) = \frac{1}{2\pi}\frac{d}{dt}(2\pi f_c t + \pi\gamma t^2) = f_c + \gamma t \tag{2.9}$$

As seen, the frequency changes linearly over time. This phenomenon is shown in Figure 2.2 (c). The maximum frequency, f_{max}, and the minimum frequency, f_{min}, can be calculated by replacing t with its minimum and maximum values given in (2.6).

$$f_{max} = f_c + \frac{\gamma T_m}{2} \tag{2.10}$$

$$f_{min} = f_c - \frac{\gamma T_m}{2} \tag{2.11}$$

As a result, the bandwidth of the signal can be expressed as:

$$B = f_{max} - f_{min} = \ \gamma T_m \tag{2.12}$$

Also, the chirp rate becomes:

$$\gamma = \frac{B}{T_m} \tag{2.13}$$

2.1.3 Range Compression

The echo signal from a target located at (x_t, y_t, z_t) is received with some delay, τ, by the radar receiver located at the origin of the coordinate system. If the target's radar cross-section properties do not vary depending on the frequency and aspect angle, and the radar system is stationary, the received signal can be written as:

$$s_r(t) = \boldsymbol{RE}\{Q \cdot p(t-\tau) \cdot e^{j2\pi f_c(t-\tau)} \cdot e^{j\pi\gamma(t-\tau)^2}\} \tag{2.14}$$

where Q is the amplitude of the signal, and it is proportional to the square root of the received power given in (2.1).

The time delay is induced by the two-way propagation of the signal, and is given as:

$$\tau = \frac{2R}{c} \tag{2.15}$$

where R is the range between the radar and the target, and c is the speed of light.

Pulse compression maximizes SNR to extract information about the target from the received signal. There are two basic approaches to pulse compression, matched filtering and

stretch processing. Throughout the dissertation, stretch processing is used as the range compression method. Therefore, the stretch processing method is explained in detail in this section, whereas the matched filtering method is briefly summarized.

In matched filtering, the received signal is demodulated to the baseband, and the whole bandwidth is sampled by an analog-to-digital converter (ADC). Then, the digitized baseband signal is convolved with the reference signal which is the complex conjugate of the quadratic term of (2.7). The processing steps are detailed in [6]. Also, convolution in the time domain is equivalent to multiplication in the frequency domain. Hence, the range compression can be done in the frequency domain [6]. At first, the received signal and the reference signal are multiplied by each other in the frequency domain. Followed by an inverse Fourier transform, the compressed signal can be obtained.

However, today's systems have much wider bandwidths to have a better resolution. Therefore, much faster ADCs are needed. To reduce this requirement, the stretch processing technique is employed as in [5], [7]-[9]. The systems that use this technique are known as dechirp-on-receive systems. The procedure is shown in Figure 2.3 (a) and (b). This technique uses a time-delayed or a non-delayed replica of the transmitted signal as the reference signal at the demodulation stage as shown in Figure 2.3 (b). The reference signal in the complex exponential form is given by:

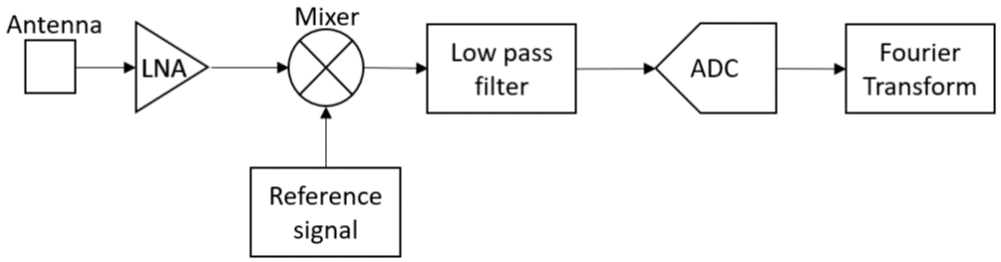

(a)

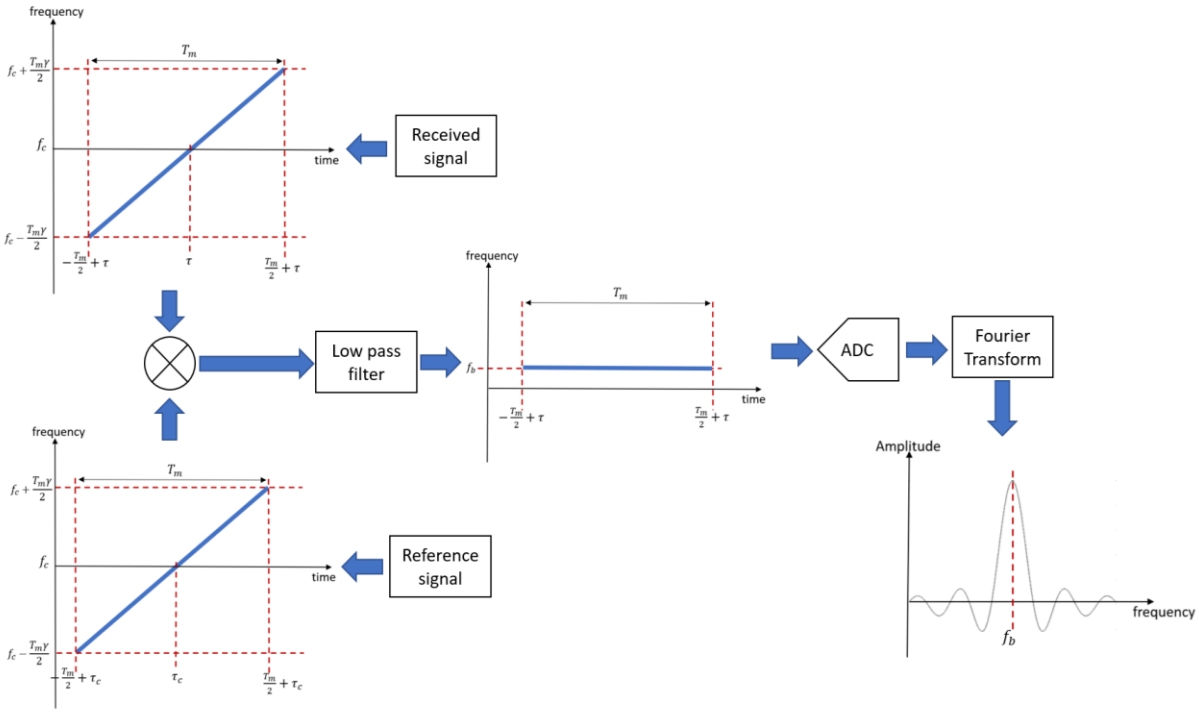

(b)

Figure 2.3 (a) Dechirp-on-receive system, (b) Echo signal from a target at different points in the receiver chain.

$$s_{ref}(t) = e^{-j2\pi f_c(t-\tau_c)} \cdot e^{-j\pi\gamma(t-\tau_c)^2} \tag{2.16}$$

where τ_c is the reference two-way time delay.

When the echo signal is mixed with this reference signal by using in-phase and quadrature channels, the mixer output gives the dechirped signal [9]. However, this signal includes high (upconversion) and low-frequency (downconversion) components due to the nature of the mixing operation. The high-frequency component should be removed by using a low pass filter since higher frequencies require faster ADCs. After this operation, a dechirped baseband signal is obtained, and each target at different ranges has a unique frequency (beat frequency, f_b) in the signal as Figure 2.3 (b) illustrates. Whereas the frequency of the target at the reference point is zero, the magnitude of the frequency increases as one moves away from the reference point. It is worth mentioning that the signal is still in the analogue domain. Hence, by windowing the bandwidth based on the desired minimum and maximum detection range, the ADC's speed requirement can be decreased. The ADC's sampling frequency must be sufficient to satisfy the Nyquist's criterion. [7]. This criterion states that the sampling frequency must be at least twice the maximum input frequency, otherwise, aliasing would be inevitable.

In this dissertation, the reference delay, τ_c, is assumed as zero, which makes the reference signal a nondelayed version of the transmitted signal. The resulting intermediate frequency (IF) signal after dechirping and filtering the LFM signal can be expressed by:

$$s_{IF}(t) = \frac{Q}{2} \cdot p(t-\tau) \cdot e^{-j2\pi f_c\tau} \cdot e^{j\pi\gamma\tau^2} \cdot e^{-j2\pi(\gamma\tau)t} \tag{2.17}$$

The first and second exponential terms are constant, and only the third exponential term is time dependent. The derivative of the IF signal's phase with respect to time gives the beat frequency, f_b, as:

$$f_b = \frac{1}{2\pi}\frac{d}{dt}(2\pi\gamma\tau t) = \gamma\tau \tag{2.18}$$

By substituting (2.15) into (2.18), we obtain:

$$f_b = \gamma\frac{2R}{c} \tag{2.19}$$

The beat frequency depends on the time delay of the received signal. This result confirms that each target at different ranges has a different beat frequency. As a result, computing the Fourier transform of the IF signal yields the range-compressed signal as demonstrated in Figure 2.3 (b) and Figure 2.4. The spectrum of the IF signal can be obtained as below by using the Principle of Stationary Phase (PSP) approximation that assumes the envelope of the signal changes very slowly with respect to time [7].

$$S_{IF}(f_r) = \int_{-\infty}^{\infty} s_{IF}(t)\cdot e^{-j2\pi f_r t}dt \approx W\cdot sinc[T_m(f_r-\gamma\tau)]\cdot e^{j\emptyset_r} \tag{2.20}$$

where f_r is the range frequency and limited by the sampling frequency, f_s, as $f_r \in [-\frac{f_s}{2}, \frac{f_s}{2}]$,

$$W = \frac{T_m Q}{2} \tag{2.21}$$

$$\emptyset_r = \ e^{-j2\pi f_c\tau}\cdot e^{j\pi\gamma\tau^2} \tag{2.22}$$

The range compressed signal is in the frequency domain, and the result is shown in Figure 2.4(a). As seen, the $sinc$ function reaches its peak value at the beat frequency. The frequency

axis is on the interval $[0, \frac{f_s}{2}]$. When this axis is converted into the range axis, Figure 2.4(b) is obtained. As expected, the peak is at R which is the target's range. Also, the first sidelobe has -13 dB less power compared with the main lobe. This ratio is named the peak sidelobe ratio (PSLR).

The range resolution, ρ_r, is proportional to the bandwidth of the LFM signal and is stated as:

$$\rho_r = \frac{c}{2B} \tag{2.23}$$

The half-to-null distance or the distance between the -3 dB power points can be used to determine the range resolution as illustrated in Figure 2.4(b).

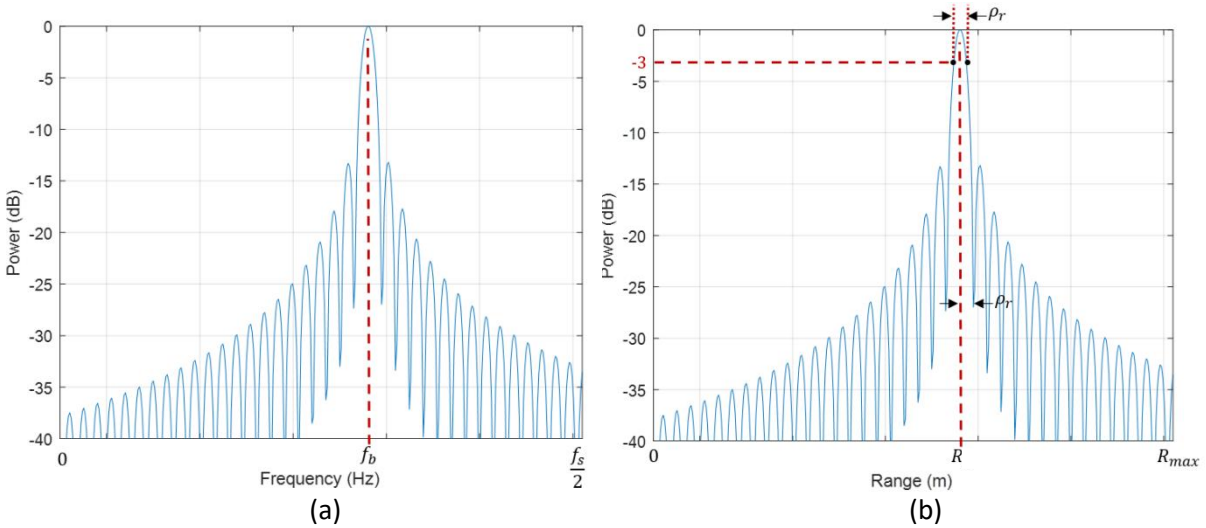

Figure 2.4 The range compressed signal (a) with the frequency axis, (b) with the range axis.

2.2 Synthetic Aperture Radar

Radar resolution is obtained in range by employing the range compression techniques as shown in section 2.1.3. Regarding the azimuth direction, it is perpendicular to the range direction, and azimuth resolution is obtained based on the antenna beam pattern and range of the target. The relationship is given as:

$$\rho_a = \Theta_{3dB} R \approx \frac{\lambda}{D} R \tag{2.24}$$

where ρ_a is the azimuth or cross-range resolution, D is the horizontal dimension of the antenna, and Θ_{3dB} is half power azimuth beamwidth of the antenna and approximately equal to λ/D.

As the length of the antenna or the operating frequency of the radar increase, the azimuth resolution of the target at a specific range improves. However, when a high-resolution is desired at a long range, a very long antenna or very high operating frequency are required, which are impractical.

In the middle of the 20th century, the synthetic aperture idea was proposed for the first time to improve the azimuth resolution by Carl Wiley [10]. Rather than using a long physical antenna, a synthetic aperture is created by moving the radar from one point to another in a line. The received signal at each point on the line is recorded. As a result of combining the recorded data via signal processing techniques, much finer azimuth resolutions are obtained than those provided by the physical antenna.

This concept allows for two-dimensional (2D) image formation. From this point of view, synthetic aperture radar (SAR) can be defined as a coherent imaging method able to form high-

resolution images regardless of weather or lighting conditions. SAR has been extensively developed to maturity and subsequently, widely used as a remote sensing tool [7]-[9].

2.2.1 SAR Geometry and Data Collection

According to the data collection method, there are three main SAR modes known as stripmap, spotlight and scanSAR. The stripmap SAR geometry is illustrated in Figure 2.5(a) and (b). A platform (generally an aircraft or spacecraft) equipped with an onboard radar moves in a straight line at a constant speed. The platform's flight direction is usually perpendicular to the antenna line-of-sight as shown in Figure 2.5(a). This setup is known as broadside SAR. If there is a squint angle between the two directions, it is referred as squint SAR.

As seen in Figure 2.5(a), the radar antenna illuminates an elliptically shaped area on the ground and sweeps along a strip of ground depending on the platform's speed and flight duration. In this way, SAR data is collected, and imaging of the swept area becomes possible. This SAR mode is called stripmap SAR.

In spotlight SAR mode, the antenna is steered continuously, mechanically or electronically, to illuminate a particular area on the ground. This operation makes obtaining higher azimuth resolutions possible compared with stripmap SAR. However, the size of the imaged area is limited by the footprint of the antenna beam on the ground.

In scanSAR mode, the imaged area along the ground range direction is increased by scanning the antenna. However, the obtained azimuth resolution is less than stripmap SAR due to the illumination time reduction of the target.

Throughout this dissertation, the broadside stripmap mode SAR will be used as the data collection method.

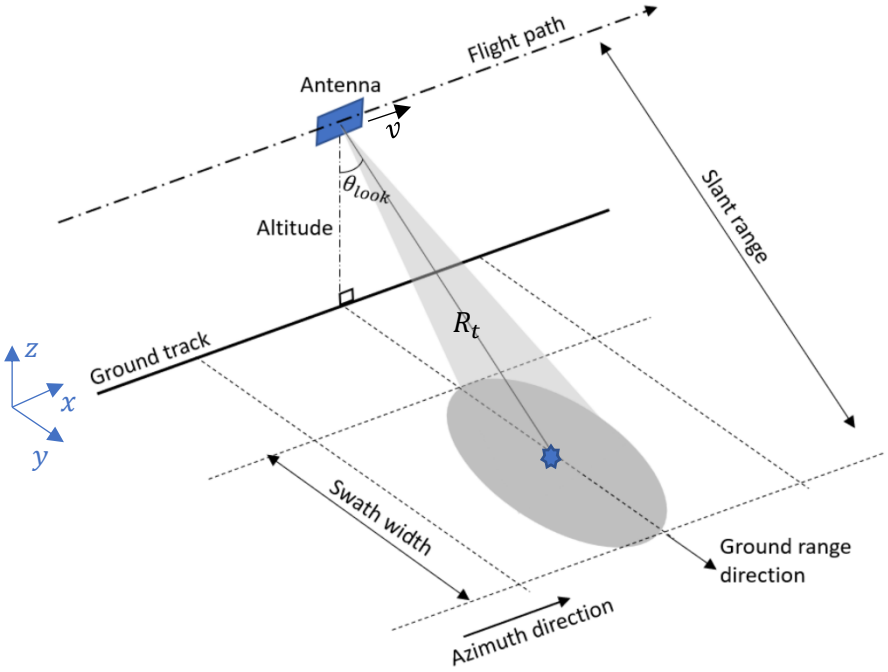

(a)

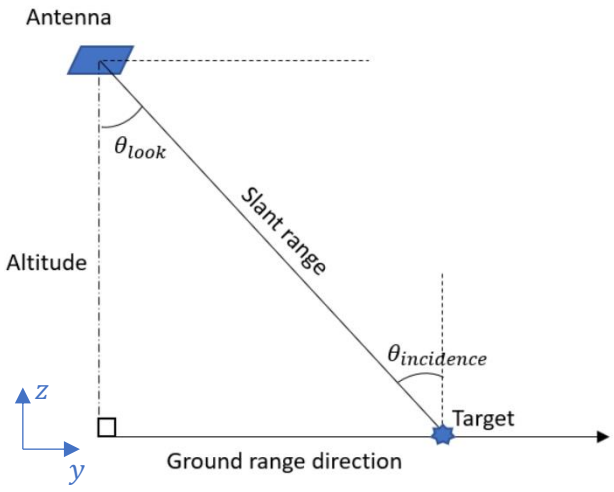

(b)

Figure 2.5 SAR geometry; (a) three-dimensional view, (b) yz plane.

Before a detailed explanation of SAR, we should define some important terms used to explain SAR geometry and imagery. The ground track is the line that is exactly underneath the flight path, and it is parallel to the azimuth direction. The term, slant range, represents the range between the radar antenna phase centre and the target. The illuminated area along the ground range direction is known as the swath width. As seen in Figure 2.5(b), the look angle is the angle between the vertical axis and the antenna beam centre and is equal to the incidence angle. It is worth noting that XYZ-axes represent the azimuth (cross-range), ground range, and vertical directions, respectively.

The stripmap mode data collection geometry is shown in Figure 2.6(a). The term, u, represents the slow-time or azimuth-time, which is related to the radar's position whereas the term, u_t, is the slow-time component related to the target's azimuth position. $R(u)$ is the instantaneous slant range of the target. The slant range between the radar and the target changes with the forward movement of the platform in the slow-time domain. Without considering motion errors, the slant range, $R(u)$, for a target at (x_t, y_t, z_t), is given as:

$$R(u) = \sqrt{v^2(u-u_t)^2 + {R_t}^2}, \qquad u \in [u_t - \frac{T_a}{2}, u_t + \frac{T_a}{2}] \tag{2.25}$$

where $u_t = x_t/v,\ v$ is the SAR platform's velocity, T_a is the total time the target is illuminated by the radar, and R_t is the closest approach to the target and given as:

$$R_t = R(u_t) = \sqrt{y_t^2 + (h - z_t)^2} \tag{2.26}$$

where h is the altitude of the platform.

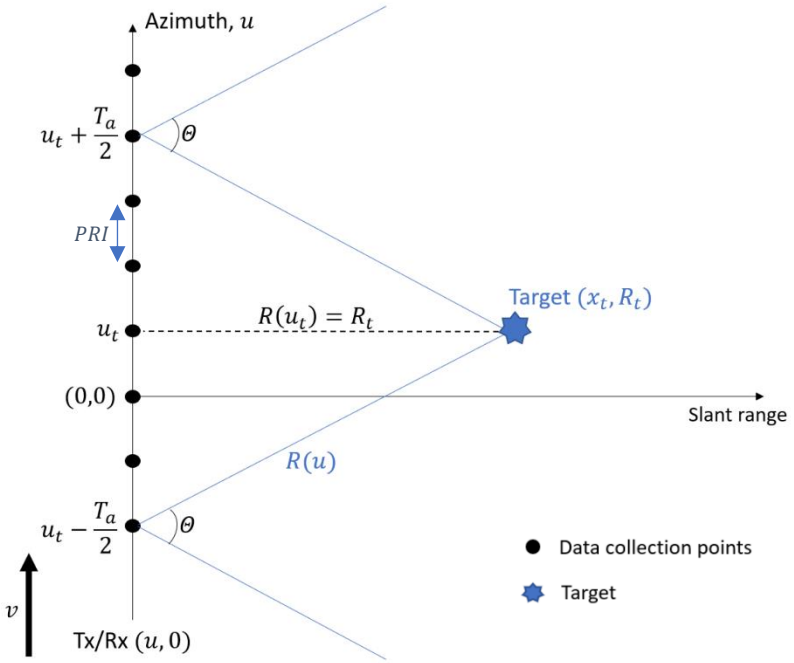

(a)

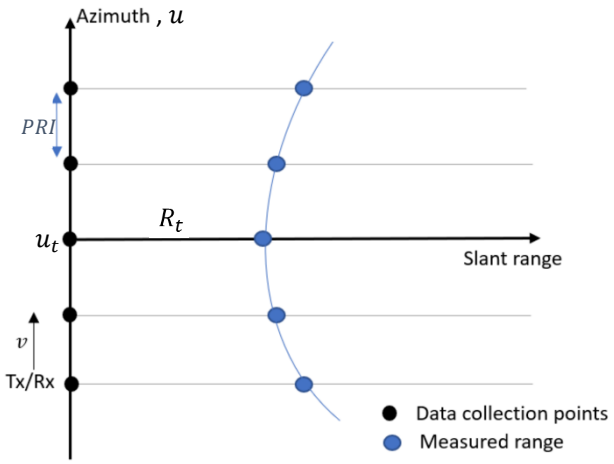

(b)

Figure 2.6 (a) SAR data collection, (b) Measured slant range of the target at each azimuth position.

The target is illuminated during the dwell time, T_a, as shown in Figure 2.6(a). The dwell time is determined by the -3 dB azimuth beamwidth of the physical antenna, Θ_{3dB}, the closest range to the target, and the velocity of the SAR platform.

$$T_a = \Theta_{3dB} \frac{R_t}{v} = \frac{\lambda R_t}{Dv} \tag{2.27}$$

The measured range by the radar at each slow-time position is shown in Figure 2.6(b). As expected, the slant range reduces as the radar approaches the target and it reaches the minimum value at slow-time u_t. This effect makes the shape of the range history of the target a curve, which is named range cell migration (RCM). The effect can be observed in Figure 2.6(b). If the RCM exceeds the range resolution, a fully focused image cannot be formed without correcting the RCM. The RCM will be explained in detail in Section 2.2.3.1.

The platform velocity is constant, so the data collection points are uniformly distributed along the flight path as in Figure 2.6. The distance between two sampling points is:

$$d = v \cdot PRI = \frac{v}{PRF} \tag{2.28}$$

where d is the distance between the two data collection points, PRI represents the pulse repetition interval, and PRF is the pulse repetition frequency.

The data collection points can be described as the sampling points of the azimuth signal. In order to satisfy the Nyquist criterion, the distance, d should be smaller than half of the desired azimuth resolution [4].

$$d \leq \frac{\rho_a}{2} \tag{2.29}$$

The received radar echo at each sampling point is demodulated by the receiver and recorded for the digital signal processing. In this way, data collection process is completed.

2.2.2 2D SAR Signal

The demodulated and recorded SAR data has two dimensions fast-time and slow-time, t represents fast-time, and u denotes slow-time. Based on (2.17), the normalized 2D SAR signal after demodulation can be written as:

$$s(t,u) = A_z(u) \cdot p\left(t - \frac{2R(u)}{c}\right) \cdot e^{-j2\pi f_c \frac{2R(u)}{c}} \cdot e^{-j2\pi\left(\gamma \frac{2R(u)}{c}\right)t} \cdot e^{j\pi\gamma\left(\frac{2R(u)}{c}\right)^2} \tag{2.30}$$

where A_z includes the azimuth envelope.

The first exponential term in (2.30) preserves the target's azimuth information, whereas the second exponential term contains the target's range information. After expressing the signal in the range-frequency domain, the second term becomes a $sinc$ function, the peak point of which represents the target's beat frequency, as shown in section 2.1.3. The last exponential term is known as the residual video phase (RVP). By introducing phase errors and geometric distortion, RVP can degrade the image quality when the imaged swath is long. As shown in [1], the allowable scene radius size, r_0, can be calculated as below by assuming the allowable quadratic phase error is $\frac{\pi}{2}$.

$$r_0 \leq \frac{\rho c}{\lambda G_b \sqrt{\gamma}} \tag{2.31}$$

where ρ is the resolution (the range and azimuth resolutions are assumed equal), and G_b is the main lobe broadening factor for both range and azimuth resolutions.

Also, based on the scene radius size, the size of the distortion due to RVP is given in [1] as:

$$\delta_{rvp} \approx \frac{2\gamma\lambda \sin(\theta_{inc})\, r_0^2}{c^2} \tag{2.32}$$

where δ_{rvp} is the geometric distortion size, and θ_{inc} is the incidence angle.

If allowable scene size is less than the actual scene size or the geometric distortion size is higher than the resolution cell, RVP should be removed. In [1], a method named the range deskew to remove the RVP term from the SAR signal is presented. However, this is out of the scope of this thesis since its impact can be ignored in our SAR applications that have short sweep time, short range, short swath, and high frequency.

Hence, equation (2.30) can be approximated to:

$$s(t,u) \approx p\left(t - \frac{2R(u)}{c}\right) \cdot A_z(u) \cdot e^{-j2\pi f_c \frac{2R(u)}{c}} \cdot e^{-j2\pi\left(\gamma \frac{2R(u)}{c}\right)t} \tag{2.33}$$

The second and third terms in (2.33) represent the azimuth signal. Here, $\frac{4\pi}{\lambda} R(u)$ is the phase of the azimuth signal, and its derivative with respect to slow time gives the instantaneous azimuth frequency.

At this point, an example may lead to a better understanding of the SAR signal. If the target's range, R_0, is 100 m and the target is located at the azimuth centre, the range history of the target, $R(u)$, is shown in Figure 2.7 (assuming $v = 5$ m/s and $T_a = 4$ s). The mentioned RCM in section 2.2.1 can be seen in Figure 2.7. There is almost a half-meter RCM, and the azimuth signal's energy is distributed along the shown curve. When the amount of the RCM is larger than the range resolution, the RCM should be corrected. That is because all the azimuth signal's energy should be concentrated in a single range bin for the proper azimuth compression.

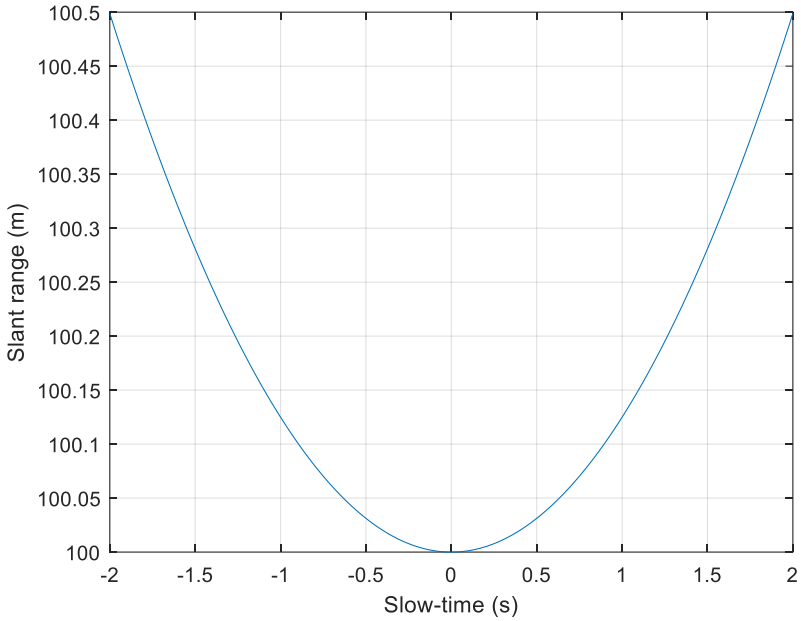

Figure 2.7 Range history of a target located at (0,100) on the azimuth-slant range plane when $v = 5$ m/s and $T_a = 4$ s.

When the radar operating frequency is assumed as 24 GHz, the azimuth signal (real part) shown in Figure 2.8(a) is generated. Also, the phase and the instantaneous azimuth frequency of the signal can be seen in Figure 2.8(b) and (c), respectively. These results indicate that the azimuth signal has an LFM-like waveform. On the other hand, it is not the same as the LFM signal. The waveform difference is obvious when (2.7) and (2.33) are compared with each other. The difference can be examined by removing the linear term from the instantaneous azimuth frequency. As shown in Figure 2.8(d), the azimuth signal has non-linear frequency components that separate it from the LFM signal. The impact of these components on the signal becomes less as the range to the target becomes greater than the formed azimuth aperture length. Hence, it can be said that the azimuth signal has a similar waveform to an LFM signal when $R_0 \gg vT_a$.

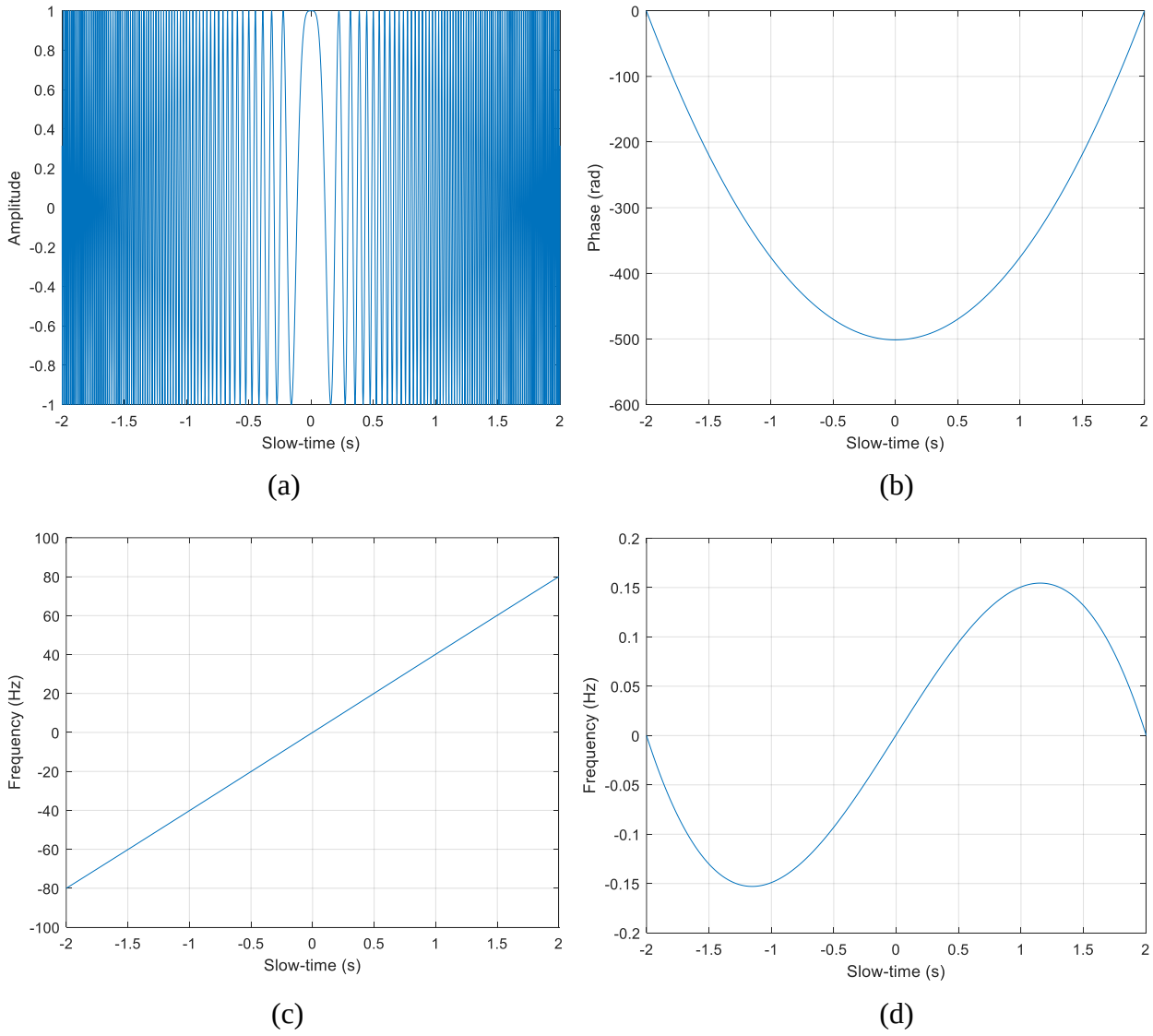

Figure 2.8 (a) The azimuth signal in time domain (real part), (b) the phase of the azimuth signal, (c) instantaneous azimuth frequency, (d) non-linear part of the instantaneous azimuth frequency.

2.2.3 Image Formation

The range compressed SAR signal turns into an image after azimuth compression. Numerous image formation algorithms that use different approximations and models have been proposed for specific scenarios and applications. However, there are a few fundamental algorithms that are widely used by the SAR community. For instance, the range migration algorithm (RMA) does not use the planar wavefront assumption and considers the coupling between the range and azimuth signals. Therefore, a two-dimensional filter is applied to form an image [1], [7]. This gives a highly accurate result. However, the Stolt interpolation that is required to focus on all targets makes the RMA a computationally expensive algorithm. The chirp scaling algorithm (CSA) contains two-phase multiplication functions implemented in the frequency domain to correct the RCM [1], [7]. This method is effective since does not employ an interpolator, but it is still an approximation compared with the RMA. Also, it works if only the demodulated received signal is an LFM signal. Unlike CSA, the frequency scaling algorithm can be used for non-LFM received signals [11]. Moreover, it does not need an interpolator and uses only Fourier transforms and phase multiplications to form focused images. The subaperture approach is used for an efficient azimuth processing. Another method is the back-projection (BP) algorithm. In contrast to the other algorithms, BP is a time-domain algorithm. It uses an integration to generate the image, and it corrects all the RCMs automatically. However, it also needs an interpolator, and the processing takes long time compared with others [8]. The range-Doppler algorithm (RDA) is a frequency-domain algorithm, and its steps are used throughout the thesis as a part of the proof-of-concept research study. Hence, in the next section, the RDA processing is explained in detail.

2.2.3.1 Range-Doppler Algorithm for Dechirp-on-Receive Systems

The range-Doppler algorithm has been commonly used for spaceborne and airborne SAR. It assumes that range and azimuth signals are independent [7]. Hence, two independent filters can be used to form an image. The main difference between the conventional RDA and the method presented in this section is the range compression implementation. In conventional RDA, range compression is done by using a matched filter, and the range-compressed signal is in the time domain. For dechirp-on-receive systems, the range-compressed signal is obtained by applying a Fourier transform. Hence, the obtained signal is in the frequency domain. Apart from this difference, other steps are identical to the conventional RDA. The block diagram of the algorithm is shown in Figure 2.9.

Let us first examine the SAR azimuth signal in terms of RDA. The parabolic approximation of the target range history which is valid only if $R_t \gg vT_a$ is the precondition in RDA. Under this assumption, the range history, $R(u)$, can be rewritten as below by using the Taylor series expansion up to the quadratic term [7] (higher order terms of the expansion are ignored).

$$R(u) \cong R_t + \frac{v^2(u-u_t)^2}{2R_t} \tag{2.34}$$

In (2.34), the first term is the range to the target whereas the second term corresponds to the range cell migration (RCM). The azimuth signal's phase and frequency can be analysed based on this equation. The exponent of the first exponential term in (2.33) indicates the azimuth phase of the SAR signal (RVP is ignored), and given by:

$$\varphi(u) \approx -\frac{4\pi}{\lambda} R(u) \tag{2.35}$$

The derivative of the azimuth phase with respect to slow-time gives instantaneous azimuth frequency or Doppler frequency as follows [7].

$$f_u(u) = \frac{1}{2\pi}\frac{d}{du}\left(-\frac{4\pi}{\lambda}R(u)\right) = -\frac{2v^2}{\lambda R_t}(u - u_t) \tag{2.36}$$

The dwell time is between $(u_t - \frac{T_a}{2})$ and $(u_t + \frac{T_a}{2})$. Hence, the target's maximum Doppler frequency, $f_{u_{max}}$, and the minimum Doppler frequency, $f_{u_{min}}$, can be obtained by replacing u with its minimum and maximum values.

$$f_{u_{max}} = \frac{v^2}{\lambda R_t}T_a \tag{2.37}$$

$$f_{u_{min}} = -\frac{v^2}{\lambda R_t}T_a \tag{2.38}$$

As a result, the Doppler bandwidth of the target, B_a, can be expressed as

$$B_a = f_{u_{max}} - f_{u_{min}} = \frac{2v^2 T_a}{\lambda R_t} \tag{2.39}$$

The azimuth or Doppler frequency change rate can be obtained by taking the second derivative of the azimuth phase with respect to slow-time.

$$K_a = \frac{1}{2\pi}\frac{d^2\varphi(u)}{du^2} = \frac{2v^2}{\lambda R_t} \tag{2.40}$$

When equations from (2.35) to (2.40) are examined, it is noticed that targets at the same range have the same Doppler frequency, Doppler rate, and bandwidth. This is an important SAR characteristic that RDA exploits in the Range Cell Migration Correction (RCMC) stage.

Next, each RDA step shown in Figure 2.9 is explained, and theoretical results are validated through simulations. In the simulation, a drone-borne SAR configuration at a short

range is considered without motion errors and with no squint angle. Simulation parameters are demonstrated in Table 2.1 whereas the aperture and the target area are shown in Figure 2.10.

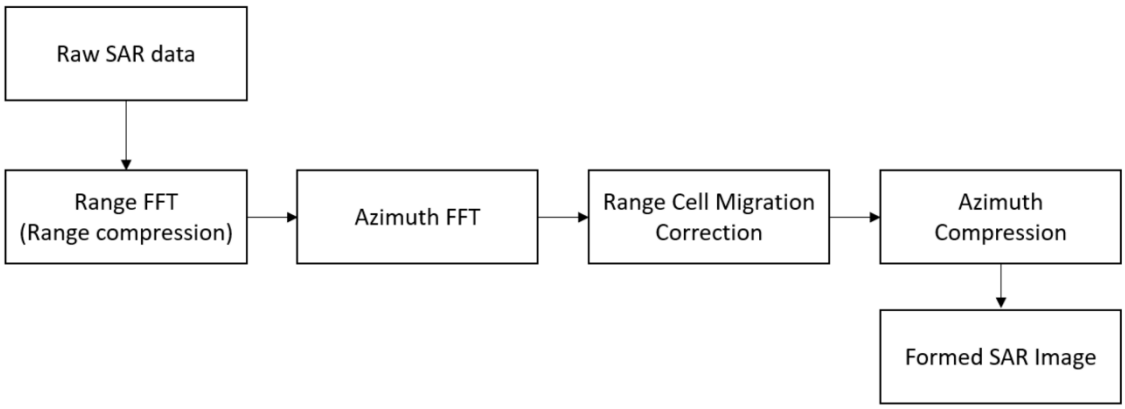

Figure 2.9 Range-Doppler Algorithm block diagram

Table 2.1: Simulation Parameters

Parameter	**Value**
Operating frequency	24 GHz
Bandwidth	1 GHz
Number of targets	4
1st target location	$(-4,73,0)$ m
2nd target location	$(2,73,0)$ m
3rd target location	$(5,73,0)$ m
4th target location	$(0,91,0)$ m
SAR platform velocity	5 m/s
Flight duration	4 s
Altitude	50 m
Scene center point	$(0,86,0)$ m
Antenna horizontal dimension	0.2 m

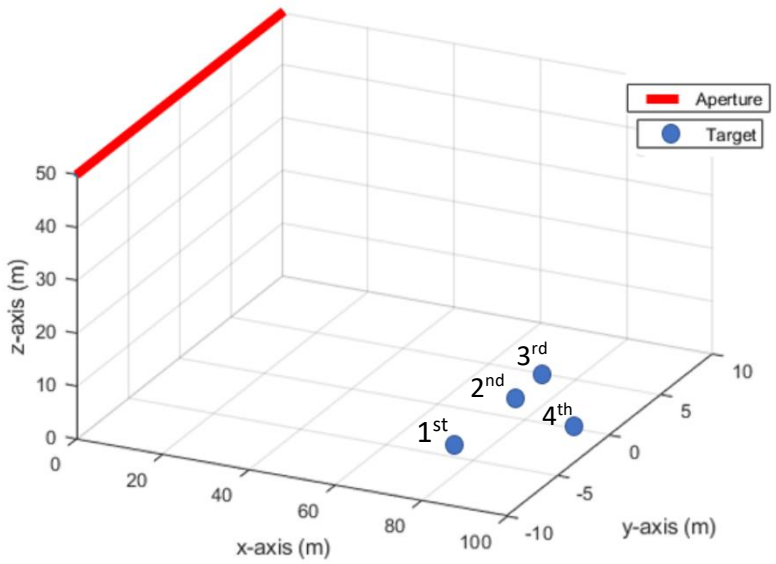

Figure 2.10 Simulation Scenario.

2.2.3.1.1 Range Compression

Range-compressed data is obtained as below by applying a Fourier transform to the de-chirped SAR data in the fast-time domain given in (2.30).

$$s(f_r, u) = \int_{-\frac{T_m}{2}}^{\frac{T_m}{2}} s(t, u) \cdot e^{-j2\pi f_r t} dt \tag{2.41}$$

As RVP is ignored/removed, and the azimuth and range signals are assumed as independent from each other, the 2D range-compressed signal can be approximated to the equation below by using the principle of stationary phase.

$$s(f_r, u) \approx W \cdot sinc\left[T_m\left(f_r - \gamma\frac{2R(u)}{c}\right)\right] \cdot A_z(u - u_t) \cdot e^{-j2\pi f_c\frac{2R(u)}{c}} \tag{2.42}$$

where W is the signal amplitude, f_r is the range frequency, and A_z is the azimuth envelope of the signal which is approximately rectangular since the dwell time is determined by the -3 dB azimuth beamwidth of the physical antenna as explained before.

After the range compression, the range resolution, ρ_r, is determined by depending on the transmitted signal's bandwidth as explained in Section 2.1.3.

In the simulation, $s(t,u)$ is generated for four targets by using the given parameters in Table 2.1. Also, the real antenna azimuth beam pattern is shown in Figure 2.11(a). Figure 2.11(b) indicates $s(f_r,u)$ which is the range compressed data. Here, the SAR data is up-sampled

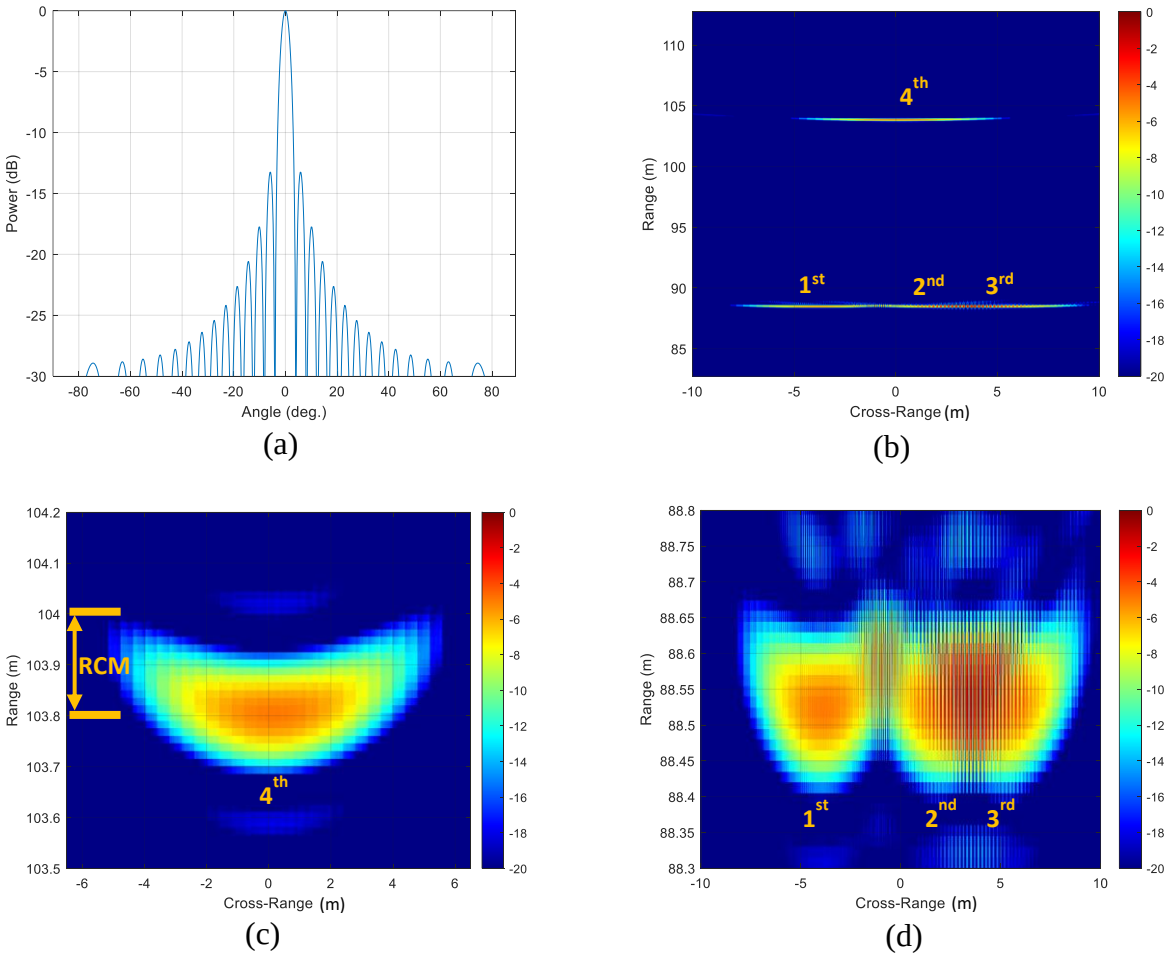

Figure 2.11 (a) Antenna azimuth beam pattern, (b) Range compressed data, (c) 4th target's closeup image, (d) Closeup image for the 1st, 2nd and 3rd targets.

for better visualization. Closeups for the targets' range histories are given in Figure 2.11(c) and (d). Range cell migration can be easily observed in the images. In order to form high-resolution images, RCM should be corrected. The amount of RCM for each target is known from (2.34). When RCM is desired to be corrected in the azimuth-time domain, a different filter for each target is required due to different range and azimuth locations of the targets. Instead of this method, correcting the RCM in the range-Doppler domain is a more effective technique. This will be explained in the next section.

2.2.3.1.2 Azimuth Fourier Transform

In order to express the signal into the Doppler domain, an azimuth Fourier transform is implemented as

$$s(f_r, f_a) = \int_{-\infty}^{\infty} s(f_r, u) \cdot e^{-j2\pi f_a u} du\,, \qquad f_a \in [-\frac{f_{PRF}}{2}, \frac{f_{PRF}}{2}] \tag{2.43}$$

where f_{PRF} is the pulse repetition frequency, and f_a is the azimuth frequency.

This integral can be solved by applying PSP,

$$s(f_r, f_a) \approx W \cdot sinc\left[T_m\left(f_r - \gamma\frac{2R(f_a)}{c}\right)\right] \cdot A_z(f_a) \cdot e^{j(\Theta(f_a))} \tag{2.44}$$

where

$$R(f_a) = R_t + \frac{\lambda^2 R_t}{8v^2} f_a^2 \tag{2.45}$$

$$A_z(f_a) = rect\left(\frac{f_a}{T_a K_a}\right) \tag{2.46}$$

$$\Theta(f_a) = -\frac{4\pi f_c R_t}{c} + \frac{\pi f_a^2}{K_a} - 2\pi f_a u_t \tag{2.47}$$

The second term in (2.45) is the RCM in the range-Doppler domain. By removing this term for each range bin, RCM can be corrected for all targets regardless of their azimuth positions. That is because all targets in the same range bin have the same Doppler frequency as (2.37) and (2.38) suggest.

This phenomenon can be demonstrated visually by the simulation. When an azimuth Fourier transform is implemented to the range compressed data shown in Figure 2.11, the 2D SAR data is obtained in the range-Doppler domain as shown in Figure 2.12(a) and (b). As seen, centre point of the targets' range histories appears at the zero Doppler point. As a result, the first three targets' range histories appear at the same position as shown in Figure 2.12(b), and in this configuration, RCM can be corrected for three targets at the same time by using a single filter.

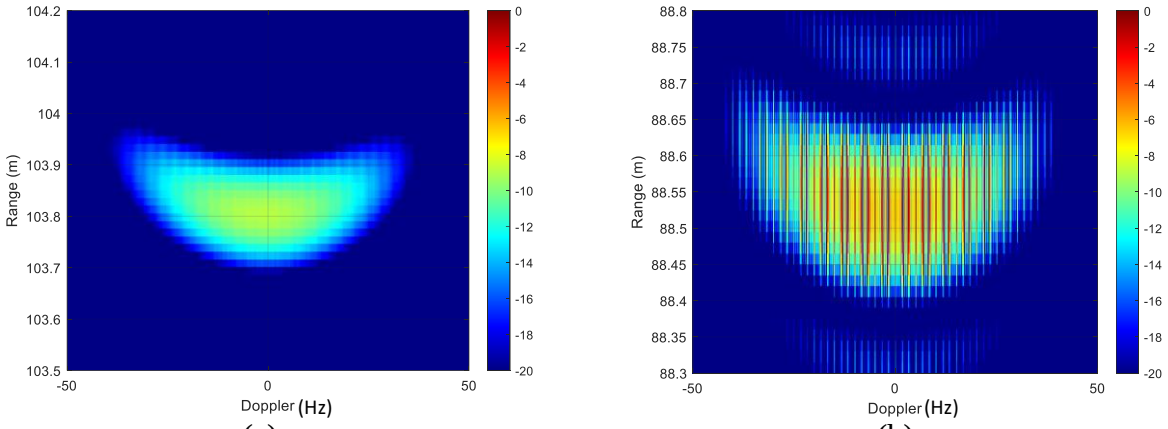

(a) (b)

Figure 2.12 SAR data in the range-Doppler domain, (a) 4th target's closeup image, (b) closeup image for the 1st, 2nd, and 3rd targets.

2.2.3.1.3 Range Cell Migration Correction

Two methods are recommended in [7] to correct the RCM. In the first one, RCM is corrected by using linear phase multiplication. This method considers only a small range interval, and assumes RCM is range-invariant. The phase multiplier for dechirp-on-receive systems can be given as,

$$e^{j\pi t\gamma\frac{\lambda^2 R_c f_a^2}{2v^2 c}} \tag{2.48}$$

where R_c is the range to the scene centre.

The phase multiplier is implemented in the range-time, azimuth-frequency domain since the phase multiplication in the range-time domain results in a shift in the range-frequency domain. In this way, RCM is corrected. However, this method does not give a high accuracy result due to the assumption of the range-invariant RCM. In some cases, residual RCM may exist for the targets that are far away from the scene centre.

When more precision is needed, the nearest neighbour method is recommended. Throughout this work, the nearest neighbour method is used for RCMC in simulations and experiments.

As a first step, the SAR signal should be up-sampled to recover the true range history of the targets. Up-sampling can be done by zero-padding the data in the range-time, azimuth-time domain. That is because zero-padding in the time domain equates to interpolation in the frequency domain.

The next step is to convert the SAR data into the range-Doppler domain. Then, the RCM is calculated as below in the discrete form for each azimuth-frequency sampling point, f_{a_j}, by considering a single range bin, r_i.

$$RCM_{i,j} = \frac{\lambda^2 r_i}{8v^2} f_{a_j}^2 \tag{2.49}$$

where i represents range bins ($i = 1, 2, \cdots, N$), and j represents azimuth bins ($j = 1, 2, \cdots, M$) in a $N \times M$ data matrix.

If the instantaneous range is $(r_i + RCM_{i,j})$, the range sampling point of this instantaneous range can be found as follows;

$$g = round\left[\frac{(r_i + RCM_{i,j})}{dr}\right] \tag{2.50}$$

where dr is the range sample spacing.

The last step is replacing the value of the sampling point (i, j) with the value of the sampling point (g, j). Then, the RCM corrected signal is obtained. After the RCM correction, the signal becomes,

$$S_c(f_r, f_a) \approx W \cdot sinc\left[T_m\left(f_r - \gamma\frac{2R_t}{c}\right)\right] \cdot A_z(f_a) \cdot e^{j(\Theta(f_a))} \tag{2.51}$$

In the simulation, RCM correction is done by using the nearest neighbour method. The up-sampling ratio is used as 16. The result is shown in Figure 2.13(a) and (b). Compared with Figure 2.12, it is apparent that RCM is corrected for all targets. The next step is the azimuth compression.

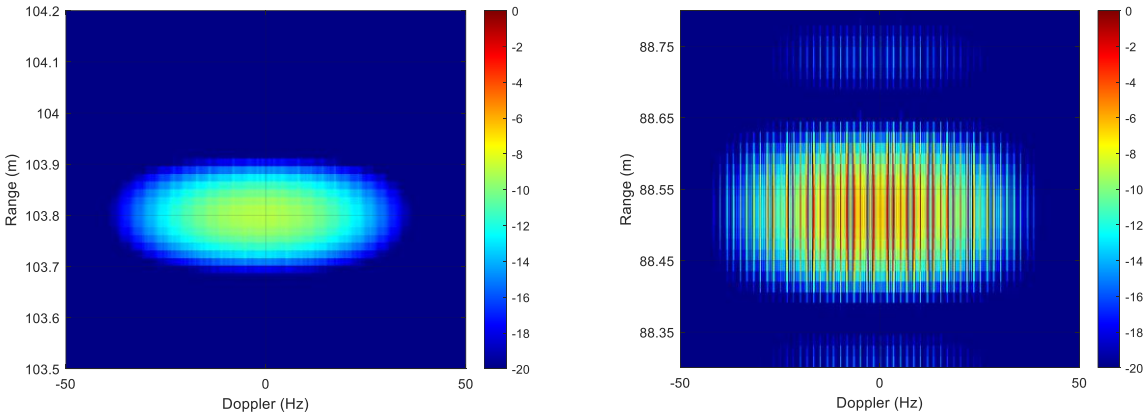

(a) (b)

Figure 2.13 RCM corrected data, (a) 4th target's closeup image, (b) closeup image for the 1st, 2nd, and 3rd targets.

2.2.3.1.4 Azimuth Compression

The azimuth position information is kept by the linear term in (2.47). The constant term does not have an impact on the final image. However, the quadratic term in (2.47) which is the azimuth signal modulation degrades the image. Therefore, the azimuth compression is done by implementing an azimuth matched filter in order to remove the quadratic term in (2.47).

The filter in the slow-time domain is given as

$$h(u) = A_z(u) \cdot e^{-j2\pi \frac{v^2 u^2}{\lambda R_t}} \tag{2.52}$$

If it is converted into the frequency domain, the filter becomes;

$$H(f_a) = \int_{-\frac{T_a}{2}}^{\frac{T_a}{2}} h(u) \cdot e^{-j2\pi f_a u} du \;\; = A_z(f_a) \cdot e^{-j\frac{\pi f_a^2}{K_a}} \tag{2.53}$$

The filter in (2.53) is range-dependent, so each range bin has a different filter depending on the value of R_t. The filter is applied to the RCM corrected data in the range-Doppler domain as

$$S_I(f_r, f_a) = S_c(f_r, f_a) \cdot H(f_a)$$

$$= W \cdot sinc\left[T_m\left(f_r - \gamma \frac{2R_t}{c}\right)\right] \cdot |A_z(f_a)|^2 \cdot e^{-j2\pi f_a u_t} \cdot e^{-j\frac{4\pi f_c R_t}{c}} \tag{2.54}$$

Then, by implementing an inverse Fourier transform to the azimuth signal, the azimuth compressed signal is obtained as

$$S_I(f_r, u) = W \cdot sinc\left[T_m\left(f_r - \gamma \frac{2R_t}{c}\right)\right] \cdot sinc[T_a K_a (u - u_t)] \cdot e^{-j\frac{4\pi f_c R_t}{c}} \tag{2.55}$$

Here, the obtained cross-range resolution, ρ_a, depends on the Doppler bandwidth, and given as

$$\rho_a = \frac{v}{B_a} \tag{2.56}$$

Substituting (2.39) into (2.56), the cross-range resolution becomes

$$\rho_a = \frac{\lambda R_t}{2vT_a} \tag{2.57}$$

Also, substituting (2.27) into (2.57),

$$\rho_a = \frac{D}{2} \tag{2.58}$$

Equation (2.58) shows that the maximum obtainable cross-range resolution is half of the antenna length, and the smaller antenna provides the higher resolution. Also, the cross-range resolution can be altered by modifying the azimuth matched filter's envelope if a different resolution is desired rather than the maximum resolution.

Regarding the simulation, the first step is to form the matched filter, $H(f_a)$. The envelope of the filter is generated based on the desired resolution. When the integration time is equal to the dwell time, the maximum resolution is obtained. The envelope that provides the maximum resolution can be seen in Figure 2.14(a). For better precision, the envelope considers the half-power curve of the antenna azimuth pattern shown in Figure 2.11(a). By using this envelope, the matched filter can be created according to (2.52) in the slow-time domain, and (2.53) in the frequency domain. The simulation result obtained after implementing the matched filter as in (2.54) is shown in Figure 2.14(b). The closeup images of the targets can be seen in Figure 2.14(c) and (d). As observed, all targets are well-focused and appeared at the correct range and cross-range positions. The range and cross-range profiles of the fourth target are given in Figure 2.14(e) and (f), respectively. As expected, both profiles are approximately $sinc$ functions. The obtained range resolution is about 0.15 m and confirms the theoretical calculation in Section 2.1.3. Also, the -3dB cross-range resolution is found as 0.1 m from Figure 2.14(f). This result validates (2.58) since the obtained resolution is the half of the real antenna's horizontal dimension.

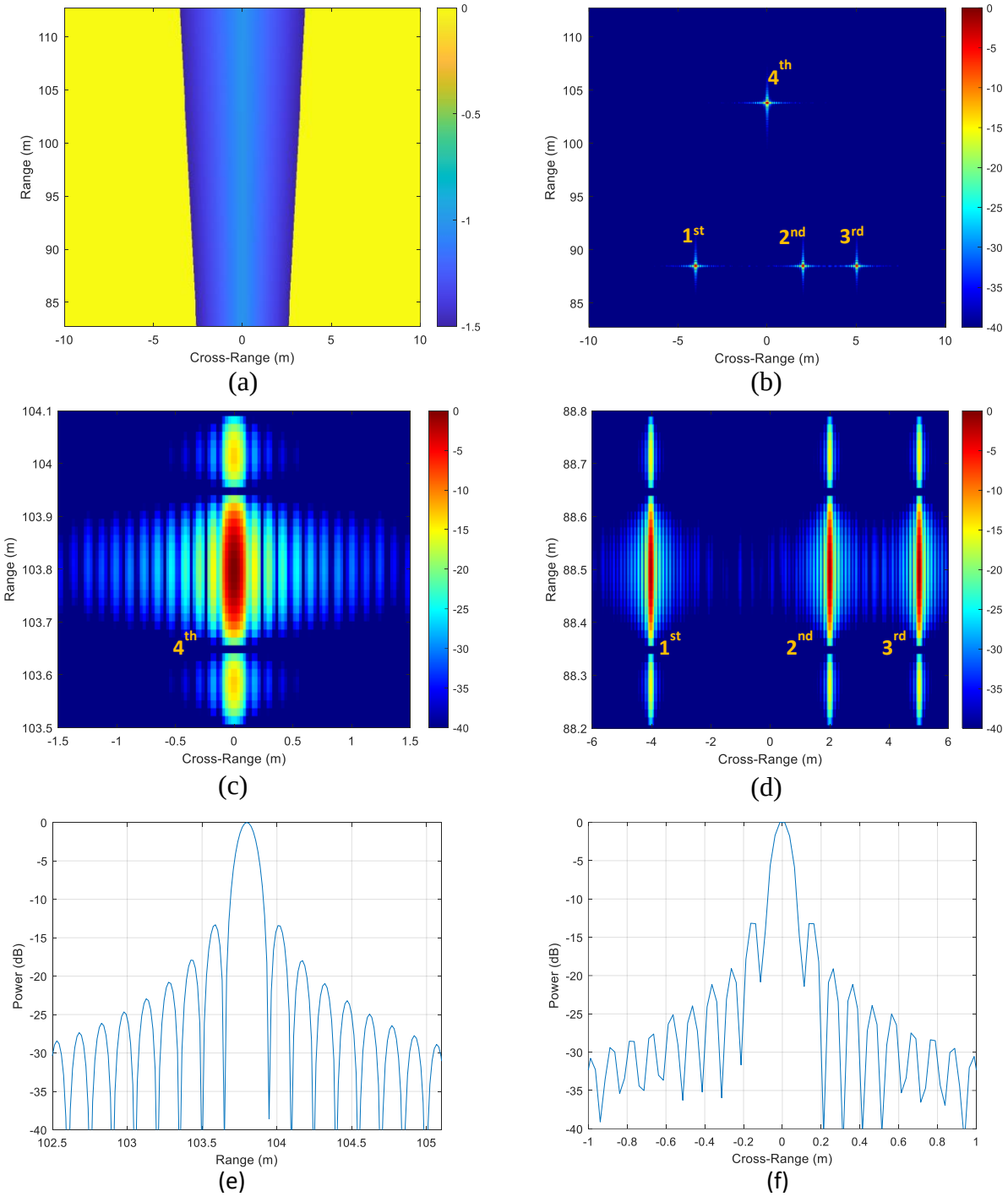

Figure 2.14 (a) Antenna azimuth beam pattern, (b) Focused image, (c) 4th target's closeup image, (d) Closeup image for the 1st, 2nd and 3rd targets, (e) Range profile of the 4th target, (f) cross-range profile of the 4th target.

2.2.4 SAR with Motion Errors

SAR platforms, especially airborne, are prone to velocity errors and deviations from the nominal trajectory due to the instability of the platform and wind turbulence as shown in Figure 2.15. These motion errors lead to phase errors and range-walk errors in the image. As a result, motion compensation (MoCo) has become a fundamental process for SAR systems.

When motion errors exist, the range history of the target includes the range errors in Line of Sight (LOS) direction.

$$R(u) = R_i(u) + R_{er}(u) \tag{2.59}$$

where $R_i(u)$ is the ideal range history of the target, and $R_{er}(u)$ represents the range error history of the target.

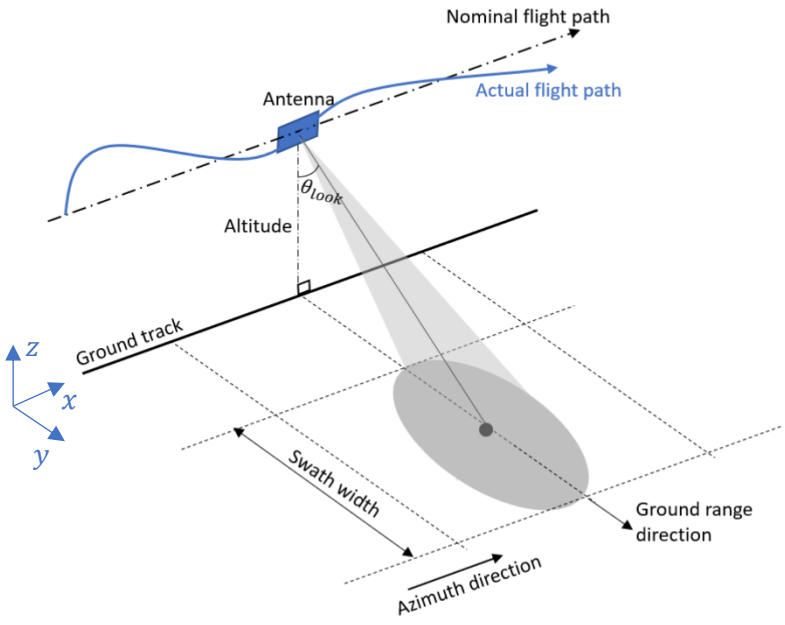

Figure 2.15 SAR geometry with motion errors.

Then, the demodulated received signal in (2.30) can be rewritten as:

$$s(t,u) = A_z(u) \cdot p\left(t - \frac{2R(u)}{c}\right) \cdot e^{-j2\pi f_c \frac{2(R_i(u)+R_{er}(u))}{c}} \cdot e^{-j2\pi\left(\gamma \frac{2(R_i(u)+R_{er}(u))}{c}\right)t} \cdot e^{j\pi\gamma\left(\frac{2(R_i(u)+R_{er}(u))}{c}\right)^2} \tag{2.60}$$

As a result, the signal which represents the two-dimensional error function, $s_e(t,u)$, can be written as

$$s_e = e^{-j2\pi f_c \frac{2R_{er}(u)}{c}} \cdot e^{-j2\pi\left(\gamma \frac{2R_{er}(u)}{c}\right)t} \cdot e^{j\pi\gamma\left(\frac{4R_{er}(u)\left(2R_i(u)+R_{er}(u)\right)}{c^2}\right)} \tag{2.61}$$

In (2.61), the first term and the third term are not fast-time dependent whereas the second term is a fast-time dependent component in the error function. The contribution of the last term is generally low enough to neglect it when γ/c^2 is very small. The main phase error is caused by the first term, whereas the second term results in range walk error in the image.

As categorized in [1], low frequency errors cause geometric distortions and loss of resolution whereas high frequency errors cause loss of contrast and spurious targets. Low frequency errors include linear, quadratic, a single cycle sinusoidal, and cubic variation in phase over the processing aperture. Here, the single cycle sinusoidal and cubic variations are defined as higher order errors. Also, high frequency errors include more rapid variations such as quartic or multicycle sinusoids [1].

In the MoCo stage of the SAR algorithms, range-walk errors should be corrected, and phase errors should be compensated. There are several methods to remove motion errors from the image. If the platform has a GPS and IMU, motion errors can be compensated by using the positional data. However, the accuracy and the update rate of the positional system must be

sufficiently high to fulfil the requirements for image formation. On the other hand, the positional system is not generally accurate enough to remove all the errors. Therefore, additional data-driven autofocus techniques are implemented to remove residual motion errors.

There are two different approaches as parametric and non-parametric. Parametric approaches assume that the error can be represented by a polynomial model, and the error function can be constructed by estimating the parameters of the model. For instance, the model parameters are estimated according to maximum contrast criterion in [12], maximum sharpness criterion in [13] and minimum entropy criterion in [14]. On the other hand, non-parametric approaches do not use a model, and estimate the error function by using the phase or phase gradient of the data.

Two of the most popular methods are map-drift (MD) and phase gradient algorithm (PGA). As a parametric model, MD estimates quadratic phase errors by cross correlating the sub-intensity images, iteratively [1]. Local quadratic map-drift (LQMD) algorithm can estimate higher-order phase errors by dividing the whole aperture into multiple sub-apertures [15] and [16]. In this approach, double integration of the vector which includes estimated local quadratic phase error coefficients for each sub-aperture gives the actual phase error function. The other method, PGA, is a non-parametric model and proposed to compensate high-frequency phase errors over a wide variety of scenes for spotlight mode SAR [1], [17]. In this approach, the gradient of the phase error is estimated iteratively by the linear unbiased minimum variance [17] or maximum likelihood estimators [18]. PGA is extended for a broadside stripmap SAR in [19]. The LQMD and PGA autofocus techniques will be explained in detail in Chapter 3.

2.2.5 Repeat-Pass SAR

By employing one of the three data collection modes given in section 2.2.1, different SAR techniques that use multiple 2D images to extract more information about the target area can be enabled. For instance, interferometric SAR (InSAR) forms at least two SAR apertures for the interested area, and depending on the baseline distance between the apertures, it can extract the height or displacement information of the target by using interferograms [9]. Data from the multiple apertures can be collected either by using multiple antennas at the same time or by using a single antenna with the repeat-pass method. Figure 2.16 shows the repeat-pass SAR geometry where B_n is the baseline between the apertures and B_y and B_z represent the horizontal and vertical baselines between the apertures. When the number of the repeat-passes is increased by keeping the baseline constant, the target's height can be resolved by tomographic SAR

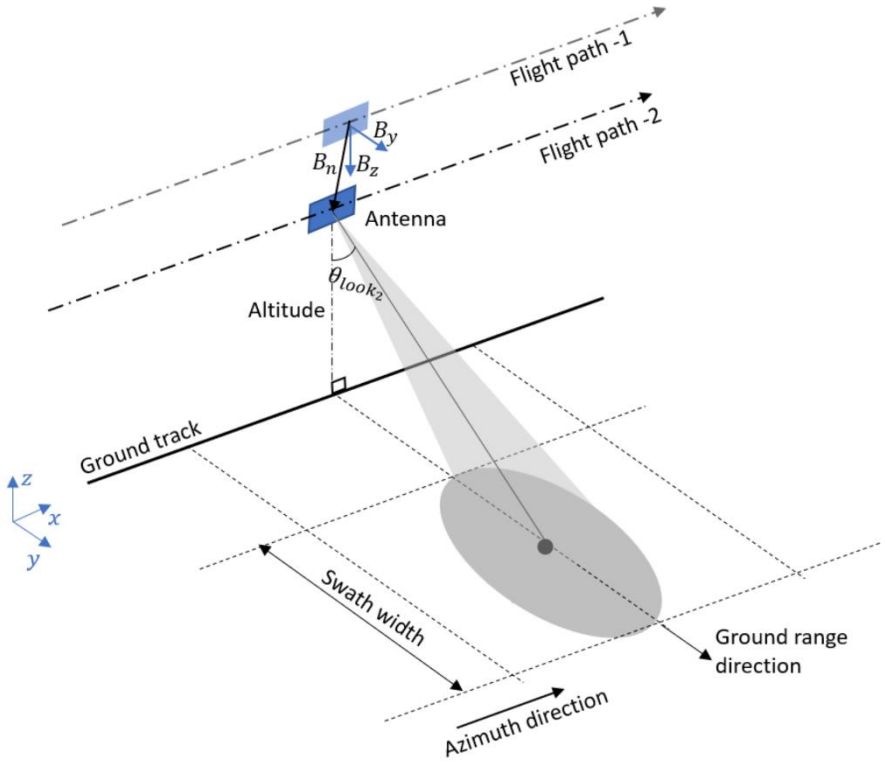

Figure 2.16 Repeat-pass SAR geometry.

techniques [20]. However, height estimation or 3D SAR imaging is out of the scope of this thesis. Detailed information is available in [9] and [20].

On the other hand, the change detection technique that relies on the comparison of temporally separated SAR images is investigated in depth in Chapter 6. In this technique, the secondary track repeats the first flights geometry. In other words, the baseline between the apertures, B_n, are zero. SAR change detection have been thoroughly developed and widely used by the SAR community [9], [20]-[24]. Fundamentally, there are two different approaches as the incoherent change detection (ICD) and coherent change detection (CCD).

Incoherent methods are sensitive to large-scale changes, such as the displacement of a sizeable object. In ICD, the change map is generated by considering the ratio of the mean intensities of the images [24],

$$CD_N = 10\ log\left(\frac{\sum_{k=1}^{N}|f_k|^2}{\sum_{k=1}^{N}|g_k|^2}\right) \tag{2.62}$$

where CD_N is the measure of the change, f_k is the first SAR image, g_k is the repeat-pass image, and N is the number of resolution cell samples.

In CCD, the classical coherence estimator [9] is given as:

$$CD_C = \frac{|\sum_{k=1}^{N} f_k g_k^*|}{\sqrt{\sum_{k=1}^{N}|f_k|^2 \sum_{k=1}^{N}|g_k|^2}} \tag{2.63}$$

where CD_C is the correlation, and the symbol $[\cdot]^*$ denotes the complex conjugate.

As seen, the coherent method uses the phase of the images. Therefore, it is more sensitive to subtle changes, such as tire marks and footprints.

2.3 Summary

In this chapter, at first, radar basics including the radar equation, used waveform, and range compression are presented so that providing a better understanding of the SAR concept. Then, SAR geometry and data collection are examined, and the 2D SAR signal is presented. In image formation, RDA is explained in detail, and its capability is validated through simulations. Later on, SAR imaging under a realistic scenario is discussed, and the two-dimensional error function is presented. Finally, some advanced SAR modes that use repeat-pass geometry are briefly explained.

2.4 References

[1] W.G. Carrara, R.S. Goodman, R.M. Majewski, *Spotlight Synthetic Aperture Radar*, Artech House, 1995.

[2] M. Skolnik et al., *RADAR Handbook*. New York: McGraw-Hill, 2008.

[3] J. Hasch, E. Topak, R. Schnabel, T. Zwick, R. Weigel and C. Waldschmidt, "Millimeter-Wave Technology for Automotive Radar Sensors in the 77 GHz Frequency Band," in IEEE Transactions on Microwave Theory and Techniques, vol. 60, no. 3, pp. 845-860, March 2012, doi: 10.1109/TMTT.2011.2178427.

[4] M. Richards, M. A. Richards, J. A. Scheer, and W. A. Holm, *Principles of Modern Radar: Basic Principles*. Institution of Engineering and Technology, 2010.

[5] G. W. Stimson, H. Griffiths, C. Baker, and D. Adamy, *Stimson's Introduction to Airborne Radar*, 3rd ed. Edison, NJ: SciTech Publishing, 2014.

[6] R. E. Collin, *Foundations for Microwave Engineering.* New York: McGraw-Hill, 1992.

[7] I.G. Cumming, F.H. Wong, Digital processing of Synthetic Aperture Radar data, Artech House, 2005.

[8] M. Soumekh, *Synthetic Aperture Radar Signal Processing With MATLAB Algorithms*. New York: J. Wiley, 1999.

[9] C. V. Jakowatz et al., *Spotlight-Mode Synthetic Aperture Radar: A Signal Processsing Approach*. New York: Springer, 1996

[10] C. A. Wiley, "Synthetic Aperture Radars," in *IEEE Transactions on Aerospace and Electronic Systems*, vol. AES-21, no. 3, pp. 440-443, May 1985, doi: 10.1109/TAES.1985.310578.

[11] J. Mittermayer, A. Moreira and O. Loffeld, "Spotlight SAR data processing using the frequency scaling algorithm," in *IEEE Transactions on Geoscience and Remote Sensing*, vol. 37, no. 5, pp. 2198-2214, Sept. 1999, doi: 10.1109/36.789617.

[12] Gao, Y.; Yu, W.; Liu, Y.; Wang, R.; Shi, C. Sharpness-Based Autofocusing for Stripmap SAR Using an Adaptive-Order Polynomial Model. IEEE Geosci. Remote Sens. Lett. 2014, 11, 1086–1090.

[13] Berizzi, F.; Martorella, M.; Cacciamano, A.; Capria, A. A Contrast-Based Algorithm For Synthetic Range-Profile Motion Compensation. IEEE Trans. Geosci. Remote Sens. 2008, 46, 3053–3062.

[14] Xiong, T.; Xing, M.;Wang, Y.;Wang, S.; Sheng, J.; Guo, L. Minimum-Entropy-Based Autofocus Algorithm for SAR Data Using Chebyshev Approximation and Method of Series Reversion, and Its Implementation in a Data Processor. IEEE Trans. Geosci. Remote Sens. 2014, 52, 1719–1728.

[15] O. O. Bezvesilniy, I. M. Gorovyi and D. M. Vavriv, "Estimation of phase errors in SAR data by Local-Quadratic map-drift autofocus," 2012 13th International Radar Symposium, Warsaw, 2012, pp. 376-381, doi: 10.1109/IRS.2012.6233350.

[16] Bezvesilniy, O., Gorovyi, I., & Vavriv, D. (2016). Autofocusing SAR images via local estimates of flight trajectory. *International Journal of Microwave and Wireless Technologies, 8*(6), 881-889. doi:10.1017/S1759078716000180.

[17] D. E. Wahl, P. H. Eichel, D. C. Ghiglia and C. V. Jakowatz, "Phase gradient autofocus - a robust tool for high resolution SAR phase correction," in IEEE Transactions on Aerospace and Electronic Systems, vol. 30, no. 3, pp. 827-835, July 1994, doi: 10.1109/7.303752.

[18] Charles V. Jakowatz Jr. and Daniel E. Wahl. Eigenvector method for maximum-likelihood estimation of phase errors in synthetic-aperture-radar imagery. Journal of the Optical Society of America A, 10(12):2539-2546, December 1993.

[19] D. G. Thompson, J. S. Bates and D. V. Arnold, "Extending the phase gradient autofocus algorithm for low-altitude stripmap mode SAR," Proceedings of the 1999 IEEE Radar Conference. Radar into the Next Millennium (Cat. No.99CH36249), 1999, pp. 36-40, doi: 10.1109/NRC.1999.767199.

[20] A. Reigber and A. Moreira, "First demonstration of airborne SAR tomography using multibaseline L-band data," in *IEEE Transactions on Geoscience and Remote Sensing*, vol. 38, no. 5, pp. 2142-2152, Sept. 2000, doi: 10.1109/36.868873.

[21] M. L. Williams and M. Preiss, “Physics-based predictions for coherent change detection using X-band synthetic aperture radar,” EURASIP J. Adv. Signal Process., vol. 2005, no. 20, pp. 3243–3258, Dec. 2005.

[22] M. Preiss, D. A. Gray and N. J. S. Stacy, "Detecting scene changes using synthetic aperture Radar interferometry," in IEEE Transactions on Geoscience and Remote Sensing, vol. 44, no. 8, pp. 2041-2054, Aug. 2006, doi: 10.1109/TGRS.2006.872910.

[23] E. J. M. Rignot and J. J. van Zyl, "Change detection techniques for ERS-1 SAR data," in *IEEE Transactions on Geoscience and Remote Sensing*, vol. 31, no. 4, pp. 896-906, July 1993, doi: 10.1109/36.239913.

[24] Preiss, M. and N. Stacy, "Coherent Change Detection: Theoretical Description and Experimental Results," Intelligence, Surveillance and Reconnaissance Division, Defense Science and Technology Organisation, DSTO–TR–1851.

Chapter 3

Motion Compensation Methods

3.1 Introduction

The explained image formation algorithm in Section 2.2.3 assumes there is no motion errors. However, in fact, SAR platforms are prone to deviations from the nominal trajectory as shown in Figure 3.1, which may lead to phase errors and range-walk errors in the formed image. Hence, motion compensation (MoCo) is required to form a focused image. There are several methods to compensate motion errors. For instance, in [1], motion compensation methods are presented for BP algorithm and Fourier domain algorithms. The method given in [2] can be implemented on RDA. Also, different approaches can be seen in [3]-[5]. If the platform has a GPS and IMU, motion errors can be compensated by using the positional data provided by these systems. Nevertheless, the accuracy and the update rate of the positional system must be sufficiently high to fulfil the requirements for image formation. On the other hand, the positional system is not generally accurate and fast enough to remove motion errors. Therefore, additional data-driven autofocus techniques are implemented to remove residual motion errors.

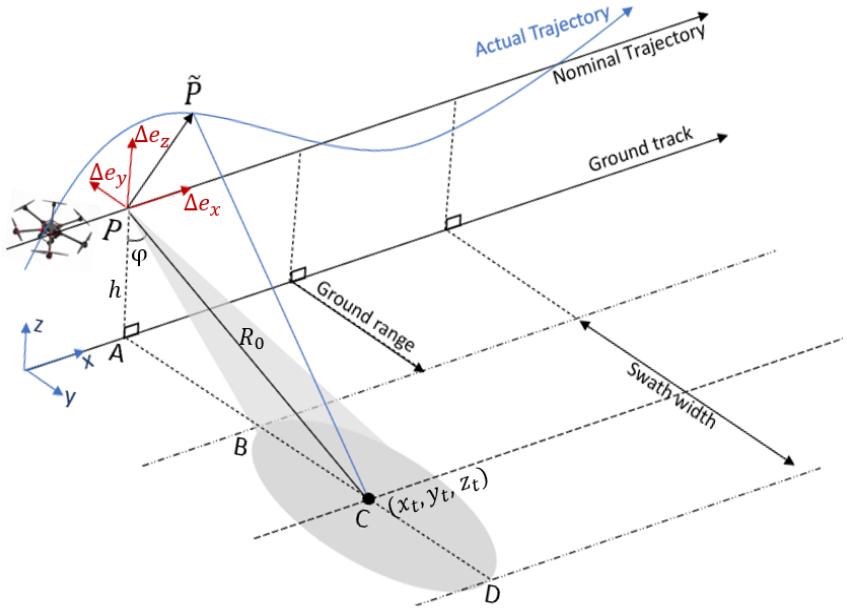

Figure 3.1 SAR with motion deviations.

Two of the most popular methods are map-drift (MD) and phase gradient algorithm (PGA). MD estimates quadratic (second order) phase errors. However, high-frequency phase errors can degrade MD's performance [6] and [7]. Local-quadratic-map-drift (LQMD) which is the modified version of MD can estimate higher-order phase errors, but its high-frequency phase error estimation performance is poor. The other method, PGA, is proposed to compensate high-frequency phase errors over a wide variety of scenes, but its precision can be degraded by noise and clutter. Both LQMD and PGA are space-invariant algorithms. Although there are extended versions of both algorithms for estimating range-dependent phase errors as shown in [8] and [9], these approaches are out of this study's scope. As will be shown in subsequent chapters, a range and azimuth blocks-based strategy is followed in this work to compensate for the spatially variant errors. In this section, at first the 2D error function is given, and then, positional data-based MoCo, LQMD, and PGA methods are examined to compensate space-invariant errors. Also, simulation results are provided to confirm the validity of each approach and discuss their performances.

3.2 2D Error Function

Section 2.2.4 derives the 2D error function. For the sake of completeness of the content, it will be briefly repeated in this section. As equation (2.59) indicates, the actual range history, $R(u)$, includes the ideal range history of the target located at (x_t, y_t, z_t), and the range errors in the LOS direction. If $R_{er}(u)$ represents the range error history in the LOS direction, and $R_i(u)$ represents the ideal range history, equation (2.60) can be rewritten as follows:

$$\tilde{s}(t,u) = A_z \cdot p\left(t - \frac{2R(u)}{c}\right) \cdot e^{-j2\pi f_c \frac{2(R_i(u)+R_{er}(u))}{c}} \cdot e^{-j2\pi\left(\gamma\frac{2(R_i(u)+R_{er}(u))}{c}\right)t} \cdot e^{j\pi\gamma\left(\frac{2(R_i(u)+R_{er}(u))}{c}\right)^2} \tag{3.1}$$

As a result, the signal which represents the two-dimensional error function, $s_e(t,u)$, can be written as:

$$s_e = \Phi_1(u) \cdot \Phi_2(t,u) \cdot \Phi_3(u)$$

$$= e^{-j2\pi f_c \frac{2R_{er}(u)}{c}} \cdot e^{-j2\pi\left(\gamma\frac{2R_{er}(u)}{c}\right)t} \cdot e^{j\pi\gamma\left(\frac{4R_{er}(u)(2R_i(u)+R_{er}(u))}{c^2}\right)} \tag{3.2}$$

In equation (3.2), the first term and the third term are not fast-time dependent whereas the second term is a fast-time dependent component in the error function. These three terms are represented by $\Phi_1(u)$, $\Phi_2(t,u)$, $\Phi_3(u)$, respectively. The contribution of $\Phi_3(u)$ is generally low enough to neglect it when γ/c^2 is very small. The main phase error is caused by $\Phi_1(u)$, whereas $\Phi_2(t,u)$ results in range walk error in the image. In the MoCo stage, the range-walk error should be compensated before range compression, and the phase error should be compensated after range compression.

3.3 Positional Data-Based MoCo

Most of the SAR platforms carry an IMU, GPS or INS (and often a combination of these) for recording the radar's motional and positional data for each transmitted signal. Positional data can be used to remove the motion error impact partially or completely from the image depending on the accuracy of the positional data, operating frequency, cross-range resolution, and the range to the target area. For example, when the operating frequency and desired cross-range resolution are high, the accuracy of the current positional systems is generally not good enough to form a focused image. Also, the MoCo algorithm gets more complicated to compensate for the space-variant errors which arise due to high-frequency, high-resolution, and short-range operations. On the other hand, if the desired spatial resolution and operating frequency are not high and space-variant errors are negligible, phase and range-walk errors can be compensated simply in two steps [1], [10].

In order to compensate for space-invariant errors, our processing begins by calculating the range error history based on the scene centre as shown in Figure 3.2. As mentioned before, $R_{er}(u)$ is the difference between the actual range history and the ideal range history, and it can be given as follows:

$$\begin{aligned} R_{er}(u) &= R(u) - R_i(u) \\ &= \sqrt{(vu + \Delta e_x(u) - x_t)^2 + \left(\Delta e_y(u) - y_t\right)^2 + (h + \Delta e_z(u) - z_t)^2} \\ &\quad - \sqrt{(vu - x_t)^2 + {y_t}^2 + (h - z_t)^2} \end{aligned} \tag{3.3}$$

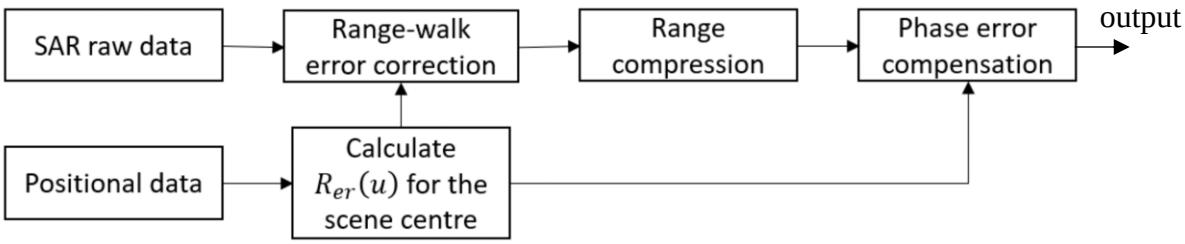

Figure 3.2 Positional Data-Based MoCo.

Calculating $R_{er}(u)$ is straightforward as the 3D motion error, $[\Delta e_x(u), \Delta e_y(u), \Delta e_z(u)]$, included in (3.3) and shown in Figure 3.1 is assumed as known with the help of the positional data. After obtaining $R_{er}(u)$, space-invariant phase errors and range walk errors are compensated in two steps as illustrated in (3.4) and Figure 3.2. First, the term, $\Phi_2(t,u)$ is compensated before range compression. Then, range compression is performed, and phase errors are compensated by using $\Phi_1(u)$. The motion compensated range-compressed signal can be written as:

$$s_{PD}(f_r,u) = \left(\int_{-\frac{T_m}{2}}^{\frac{T_m}{2}} \tilde{s}(t,u)\, e^{\left(j4\pi\gamma\frac{R_{er}(u)}{c}t\right)} e^{-j2\pi f_r t} dt \right) e^{j4\pi f_c \frac{R_{er}(u)}{c}} \tag{3.4}$$

If the SAR data contains space-variant errors, two extra MoCo stages, one for range-dependent errors, and one for cross-range dependent errors should be added to the algorithm. To compensate range-dependent errors, the range error function is calculated for all range-bins after space-invariant MoCo and RCMC correction. Then, errors are compensated in a similar way shown in (3.4). To compensate for cross-range dependent errors, the data should be resampled according to cross-range displacement.

3.4 Local Quadratic Map Drift

LQMD is an improved version of the conventional MD which can estimate quadratic phase errors. MD divides the aperture into 2 sub-apertures and estimates the error by using the cross-correlation of the 2 sub-images. The main steps of MD are shown in Figure 3.3. On the other hand, LQMD uses multiple sub-apertures and estimates local Doppler rates as its coefficients. Then, double integration of the stored coefficients gives the phase error function [11],[12]. In this way, higher order errors can be estimated. The algorithm flow-chart is shown in Figure 3.4.

In MD, as the first step, SAR data is de-chirped. Then the whole aperture is divided into 2 sub-apertures and transformed into the azimuth-frequency domain. Then, the cross-correlation of the two intensity images is generated. If there is a phase error, the peak of the cross-correlation function shifts by depending on the error as shown in Figure 3.3. The relationship between the shift, Δf, the Doppler rate, K_e, and the dwell time, u_a, is given as

$$K_e = \frac{\Delta f}{u_a} \tag{3.5}$$

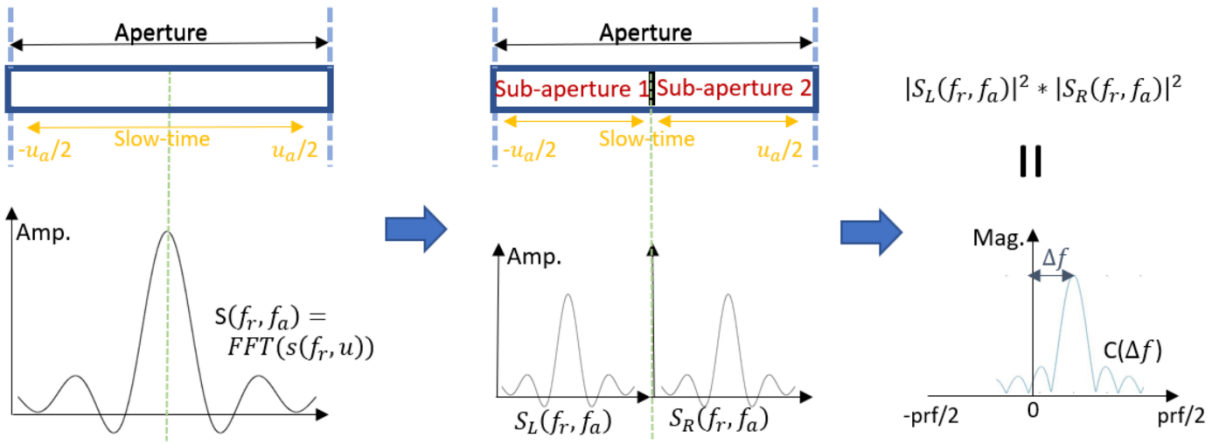

Figure 3.3 Map-Drift.

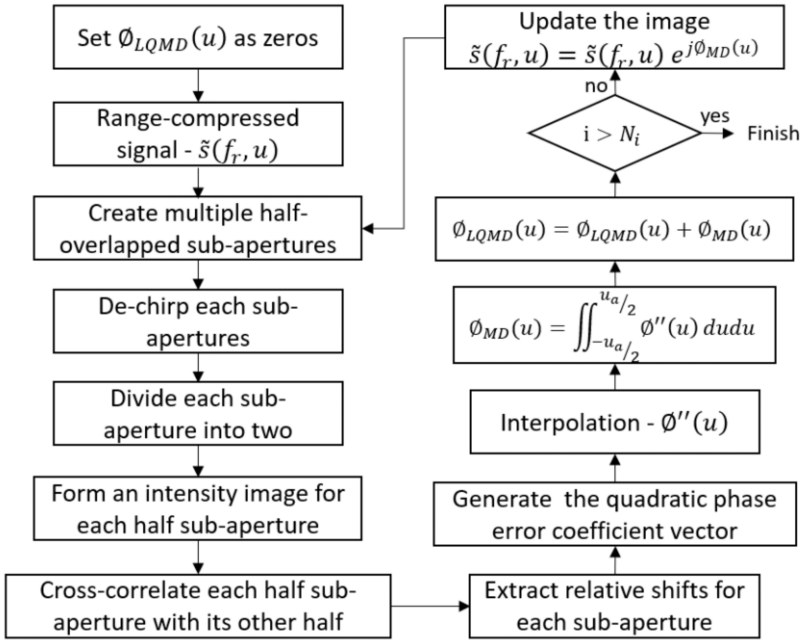

Figure 3.4 LQMD steps.

In LQMD, the same processing steps with MD are used. However, instead of generating 2 sub-apertures, multiple sub-apertures are generated as in Figure 3.4. Also, an example is shown in Figure 3.5. The aperture is divided into 10 sub-apertures. Then, by using each sub-aperture pair, the Doppler rate is estimated for each pair. At this point, if the local quadratic error functions are plotted, the first graph in Figure 3.5 is obtained. As indicated, there is one quadratic error estimation for each sub-aperture pair, and discontinuities exist between the estimated error functions. If each estimated Doppler rate is stored in a vector, double integration of this vector over slow time gives the phase error function without discontinuities as shown in the second graph in Figure 3.5.

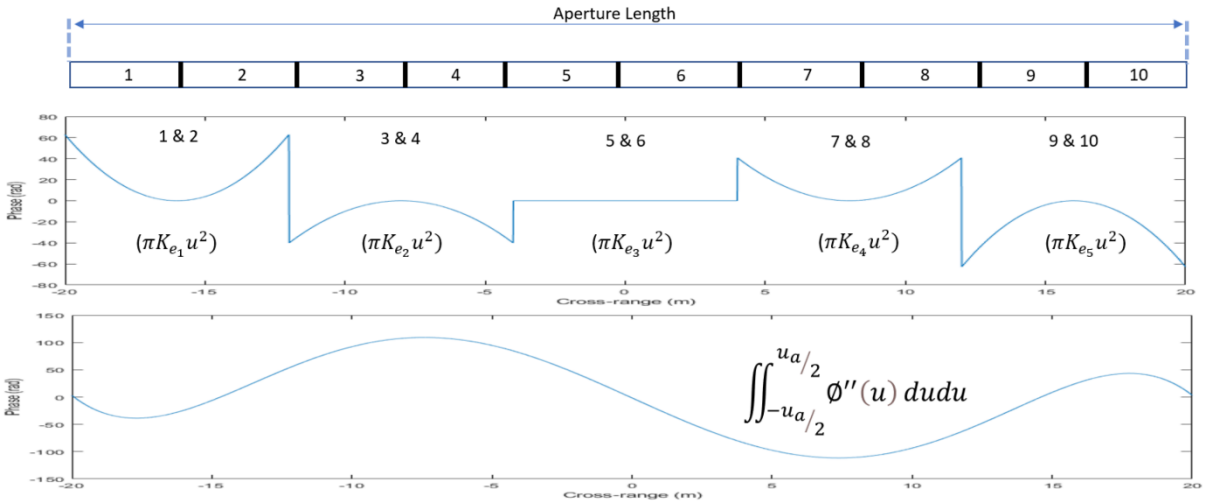

Figure 3.5 Phase error estimation in LQMD.

Using half-overlapped apertures increases the estimated accuracy because of the higher number of sampling points. In the analytical explanation given in this section, it is assumed that half-overlapped apertures are used. The main steps of LQMD are shown in Figure 3.4. If the whole aperture is divided into half overlapped azimuth blocks, N_b sub-apertures are created.

$$N_b = \frac{2u_a}{u_{s_l}} - 1 \tag{3.6}$$

where u_{s_l} is the azimuth block time.

Then, each block is de-chirped (3.7) and divided into two parts. After converting the data into frequency domain, two local intensity images are generated as in (3.8) and (3.9).

$$s_{ab}(f_r, u) = \tilde{s}(f_r, u) \cdot e^{j\pi \frac{2v^2\left(u - \frac{(nu_{s_l} - u_a)}{2}\right)^2}{\lambda R_0}} \tag{3.7}$$

where $\frac{(n-1)u_{s_l} - u_a}{2} \leq u < \frac{(n+1)u_{s_l} - u_a}{2}$, s_{ab} is the de-chirped signal for each azimuth block and n is nth $(\mathrm{n} = 1, 2, \cdots, N_b)$ azimuth block.

$$S_L(f_r, f_a) = \left| \int_{\frac{-u_{s_l}}{2}}^{0} s_{ab}(f_r, u) \cdot e^{-j2\pi f_a u} du \right|^2 \tag{3.8}$$

$$S_R(f_r, f_a) = \left| \int_{0}^{\frac{u_{s_l}}{2}} s_{ab}(f_r, u) \cdot e^{-j2\pi f_a u}\, du \right|^2 \tag{3.9}$$

where f_a is the azimuth frequency, $S_L(f_r, f_a)$ and $S_R(f_r, f_a)$ represent the left and right part intensity image of each azimuth block, respectively.

In the presence of phase errors, the peak position of the cross-correlation of the two images is shifted. Cross-correlation functions of each range-bin are incoherently summed for a more accurate estimation as

$$c_n(\Delta f) = \sum_{r_b=1}^{N_r} \int S_L(r_b, f_a) \cdot S_R(r_b, f_a + \Delta f) df_a \tag{3.10}$$

where $\frac{-f_{PRF}}{2} \leq \Delta f < \frac{f_{PRF}}{2}$, f_{PRF} is pulse repetition frequency, $c_n(\Delta f)$ is the cross-correlation response of the nth azimuth block, r_b indicates a particular range-bin and N_r is the number of range-bins.

The local quadratic phase error coefficient is given as $2\pi \frac{\Delta f_m}{u_{s_l}}$ where Δf_m is the relative shift extracted from $c_n(\Delta f)$. Local quadratic phase error coefficients for each azimuth block are stored in a vector as $\frac{2\pi}{u_{s_l}}[\Delta f_{m_1}, \Delta f_{m_2}, \cdots, \Delta f_{m_{N_b}}]$. After interpolating this vector, the second derivative of the phase error function, $\emptyset''(u)$, is obtained as explained in [11] and [12]. Next, double integration is applied to this function to produce the phase error function, $\emptyset_{MD}(u)$.

$$\emptyset_{MD}(u) = \iint_{-u_a/2}^{u_a/2} \emptyset''(u)\, du du \tag{3.11}$$

However, the estimated phase error function includes constant and linear components. Autofocus algorithms are not able to estimates these terms. Therefore, the constant and the linear error should be removed from the estimation. Then, the error function is applied to the original data in order to compensate the estimated phase error.

$$s(f_r, u) = \tilde{s}(f_r, u)\, e^{j\emptyset_{MD}(u)} \tag{3.12}$$

Here, $s(f_r, u)$ may still have high phase errors. Therefore, LQMD steps are repeated by assuming the input SAR data is $s(f_r, u)$. In each iteration, $\emptyset_{MD}(u)$ is updated and added to the total estimated phase error function, $\emptyset_{LQMD}(u)$.

As shown in (3.13), the estimated phase error is used first to correct range walk error in the range-time domain, then to compensate the phase error in the range-frequency domain. The correction functions are formed using $\Phi_1(u)$ and $\Phi_2(t, u)$ in (3.2).

$$s_{MD}(f_r, u) = \left(\int_{-\frac{T_m}{2}}^{\frac{T_m}{2}} x_s(t, u)\, e^{-j2\pi f_r t} dt \right) e^{j\emptyset_{LQMD}(u)} \tag{3.13}$$

where $x_s(t, u) = \left(\int_a^b \tilde{s}(f_r, u)\, e^{j2\pi f_r t} df_r \right) e^{\left(j\frac{\emptyset_{LQMD}(u)\gamma}{f_c} t \right)}$, a and b are minimum and maximum range frequencies, respectively.

These steps are repeated several times to increase the accuracy of the estimation.

3.5 Phase Gradient Algorithm

As described in [13], PGA has four main steps which are circular shifting, windowing, phase gradient estimation and iterative phase correction as shown in Figure 3.6. The basic idea behind PGA is computing the gradient of the azimuth signal's phase. The other three steps apart from the phase gradient estimation are used to improve the accuracy and robustness of the estimation. The error free range compressed SAR signal can be written as below by using (2.34) and (2.42) for a target located at (x_t, R_0).

$$s(f_r, u) = A_z(u - u_t)\, M(f_r) \exp\left(-j\, {4\pi R_0}/{\lambda}\right) exp\left(-j4\pi \frac{{x_t}^2 + (vu)^2}{2R_0\lambda}\right) exp\left(j4\pi \frac{x_t vu}{R_0\lambda}\right) \quad (3.14)$$

where $M(f_r)$ includes the range profile of the target.

When (3.14) is de-chirped, the quadratic term is compensated, and the equation below is obtained.

$$s_d(f_r, u) = A_z(u - u_t)\, M(f_r) \exp\left(-j\, {4\pi R_0}/{\lambda}\right) exp\left(-j4\pi \frac{{x_t}^2}{2R_0\lambda}\right) exp\left(j4\pi \frac{x_t vu}{R_0\lambda}\right) \quad (3.15)$$

In equation (3.15), only the last term is slow-time dependent. The phase gradient of this equation is found as a constant when it is calculated by the linear unbiased minimum variance (3.16) or maximum likelihood estimators (3.17) as there are no phase errors. The integral of this constant term over slow time gives a linear function. As known, only non-linear errors are considered in autofocus algorithms. Hence, the non-linear phase error is found as zero as expected. On the other hand, if the signal in (3.14) includes some non-linear phase errors, the

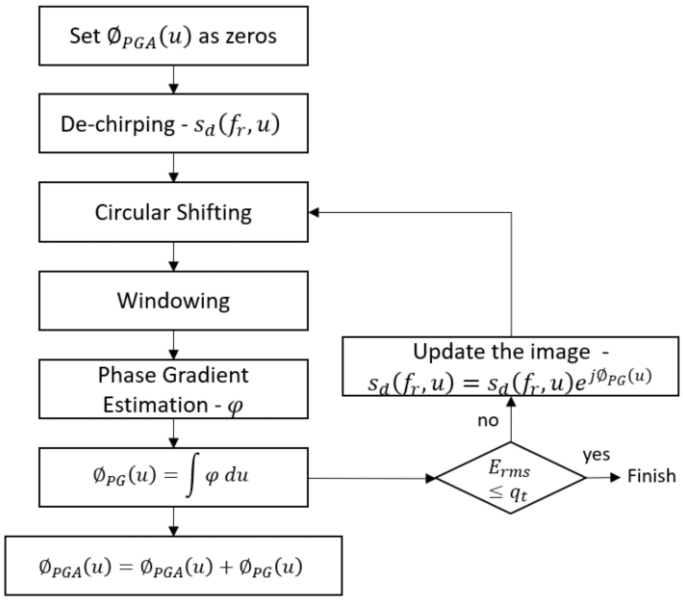

Figure 3.6 PGA steps.

phase gradient of the de-chirped signal is found as a varying function depending on slow time. The integral of the phase gradient function over slow time gives the non-linear phase error.

$$\frac{\sum_{r_b=1}^{N_r} Im\{\dot{s_d}(r_b, 1{:}\,n_a)\; {s_d}^*(r_b, 1{:}\,n_a)\}}{\sum_{r_b=1}^{N_r} |s_d(r_b, 1{:}\,n_a)|^2} \tag{3.16}$$

where r_b is the range-bin number, N_r is the total number of range bins used to calculate the phase gradient, n_a is the total number of azimuth-bins.

$$ang\left\{\sum_{r_b=1}^{N_r} s_d(r_b, 2{:}\,n_a){s_d}^*(r_b, 1{:}\,n_a - 1)\right\} \tag{3.17}$$

In order to enhance the phase error estimation of the algorithm, circular shifting and windowing are implemented. In circular shifting, at first, the azimuth dechirped SAR data (3.14) is converted into the azimuth-frequency (Doppler) domain. Then, range bins with the largest amount of energy are selected and moved to the Doppler centre. That is because it is

assumed that the best estimation for the phase errors is generated when the phase of strongly reflecting objects is measured. Also, it is worth noting that the frequency offset caused by the scatterer's azimuth position in the corresponding Fourier domain is eliminated by circular shifting. Finally, the process is ended by converting the circularly shifted SAR data into the slow time domain.

After shifting the strongest bins to the Doppler centre, the rest of the data appear as noise. To improve the estimation accuracy by reducing the noise, the data is windowed. The major problem with windowing is the selection of the window size. When the window is chosen large, spurious targets can appear. On the other hand, when a small window is used, the azimuth signal's energy spreading to high Doppler frequencies due to phase errors may be outside the window and not considered by the algorithm.

The phase gradient algorithm's flow chart is shown in Figure 3.6. In PGA, the algorithm gets the de-chirped SAR data (3.15) as its input. Then, circular shifting and windowing steps are implemented as described above. At this point, the data is ready for the phase gradient estimation. To do this, one of the estimators, (3.16) or (3.17) is chosen, and the gradient of the data is estimated. By integrating the phase gradient, the phase error function, $\emptyset_{PG}(u)$ is obtained. However, the constant and the linear error should be removed from the estimation because autofocus algorithms are not able to estimates these terms. Then, the error function is applied to the original selected data in order to compensate the phase error.

$$\tilde{s}_d(f_r, u) = s_d(f_r, u)\, e^{j\emptyset_{PG}(u)} \tag{3.18}$$

Iterating the PGA process improves phase error compensation accuracy. Therefore, PGA steps are repeated by assuming the input dechirped SAR data is $\tilde{s}_d(f_r, u)$. In each iteration,

$\emptyset_{PG}(u)$ is updated and added to the total estimated phase error function, $\emptyset_{PGA}(u)$. As a rule of thumb, the window size is chosen to be large at the beginning, and its size is reduced in each iteration. The iteration continues until the RMS value of the estimated phase error, E_{rms} drops to a few tenths of a radian specified by a threshold, q_t.

As shown in (3.19), the estimated phase error is used first to correct range walk error in the range-time domain, then to compensate the phase error in the range-frequency domain. The correction functions are formed using $\Phi_1(u)$ and $\Phi_2(t,u)$ in (3.2).

$$\tilde{s}_{PGA}(f_r,u) = \left(\int_{-\frac{T_m}{2}}^{\frac{T_m}{2}} x(t,u)\, e^{-j2\pi f_r t} dt \right) e^{j\emptyset_{PGA}(u)} \tag{3.19}$$

where $x(t,u) = \left(\int_a^b \tilde{s}(f_r,u)\, e^{j2\pi f_r t} df_r \right) e^{\left(j\frac{\emptyset_{PGA}(u)\gamma}{f_c} t\right)}$, a and b are minimum and maximum range frequencies, respectively.

On the other hand, PGA was originally developed for spotlight mode SAR. In stripmap mode, the data must be divided into N_p azimuth blocks to avoid aliasing [14]. For PGA, the sub-aperture time, u_s, can be specified by (3.20). Here, u_s must be given the maximum value it can get to improve space-invariant phase error estimation.

$$u_s \leq \frac{R_0 \lambda\, f_{PRF}}{2v^2} \tag{3.20}$$

where λ is the wavelength.

After determining the subaperture time, the signal is dechirped, and conventional PGA steps are implemented for each subaperture. Then, the error function, $\emptyset_i(u)$, is generated for each subaperture. In this function, values of samples that are outside of the relevant subaperture

time are set to zero. By using overlapped apertures, the phase information among subapertures is obtained without discontinuity as shown in [15]. After extracting the linear phase difference between apertures, estimated phase errors are combined with each other based on their azimuth positions. For example, in the case of half-overlapped sub-apertures, $\emptyset_{PGA}(u)$ is obtained as

$$\emptyset_{PGA}(u) = \begin{cases} \emptyset_1(u), & \frac{-u_a}{2} \leq u < \frac{2u_s - u_a}{2} \\ \emptyset_i(u) + \alpha_i, & \frac{2(i-1)\,u_s - u_a}{2} \leq u < \frac{(i+1)u_s - u_a}{2} \end{cases} \tag{3.21}$$

where i is ith $(\mathrm{i} = 2, \cdots, N_b)$ sub-aperture and α_i is the extracted linear phase difference between ith and $(i-1)th$ sub-aperture.

The phase error function is applied to data in the same way as shown in (3.19).

3.6 Simulations

In order to validate the introduced MoCo approaches, simulation results are provided in this section. The simulation aims to obtain the maximum azimuth resolution by using the RDA and MoCo algorithms. In the simulation, stripmap drone-borne SAR geometry and parameters are considered. The given motion errors include both low and high-frequency components. However, low-frequency components have a higher magnitude than high-frequency components as in real-world measurements. At first, the magnitude of the motion error is kept low, and the MoCo capability of each method is illustrated by repeating the simulation. Later on, the phase error estimation performance of LQMD and PGA is evaluated against a motion error that includes high-magnitude and high-frequency errors. Finally, it is shown that the autofocus performance improves when PGA and LQMD are used together.

In the simulation, a 25 m synthetic aperture is formed by using a 24 GHz radar with a 0.5 GHz bandwidth at a 100 m altitude. The simulation parameters and the geometry are chosen based on a drone-borne SAR configuration as shown in Table 3.1 and Figure 3.7, respectively. The scene includes 14-point targets as shown in Figure 3.8(a). All presented MoCo approaches

Table 3.1: Simulation Parameters

Parameter	Value
Operating frequency	24 GHz
Bandwidth	0.5 GHz
Number of targets	14
Drone velocity	5 m/s
Altitude	100 m
Scene center point	(0,175,0) m
Aperture length	25 m
Cross-range resolution	5 cm
Range-resolution	30 cm
Swath width	50 m

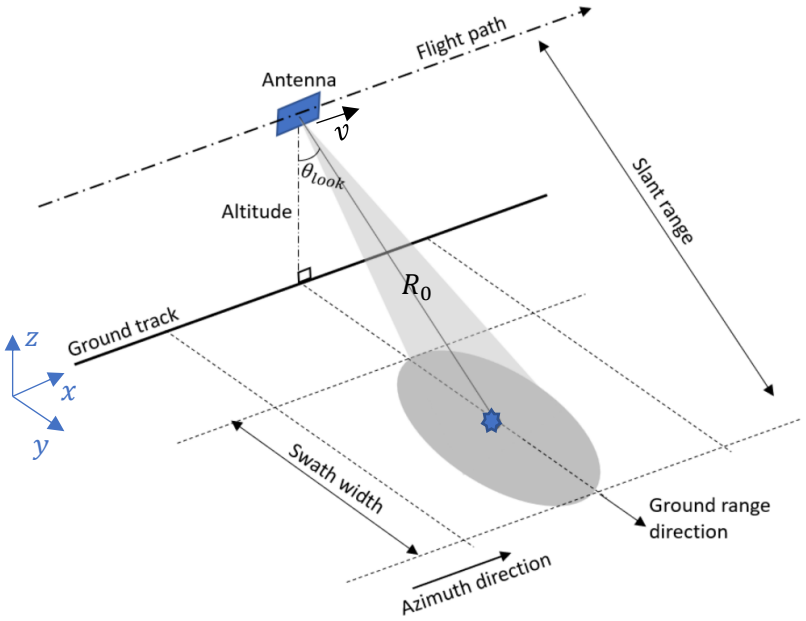

Figure 3.7 SAR geometry in the simulation.

are tested with the motion error shown in Figure 3.8(b). The corresponding phase error at the scene centre is shown in Figure 3.8(c). The peak phase error is around 20 radians. The image without MoCo is given in Figure 3.8(d). As seen, all targets are unfocused when the 25 m synthetic aperture is processed by RDA.

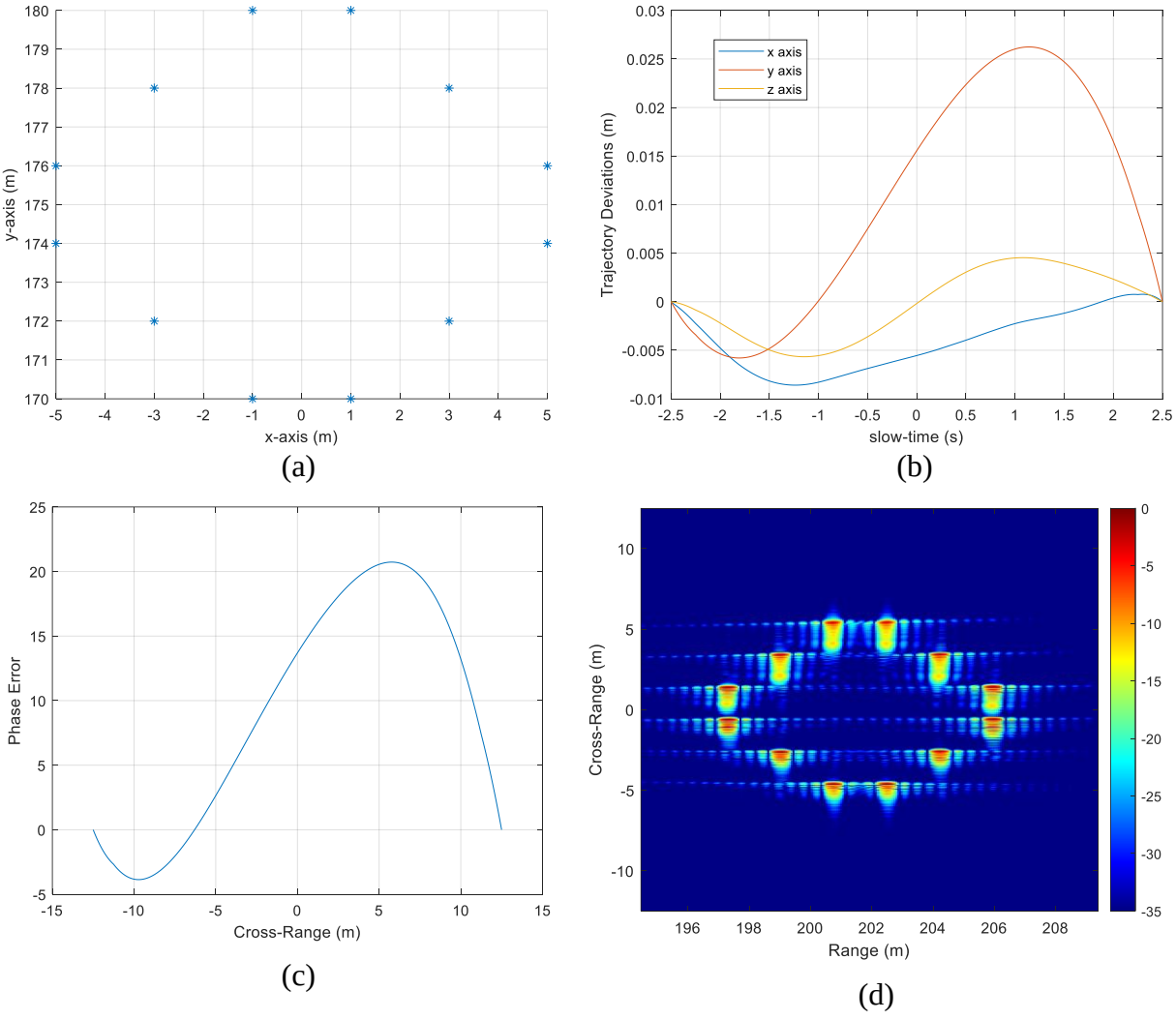

Figure 3.8 (a)14-point targets, (b) The given motion error, (c) The corresponding phase error at the scene centre, (d) The obtained image without MoCo.

In the positional data based MoCo simulation, the motion error is assumed as known. Therefore, the range error history and the resulting phase error can be calculated precisely. As observed in Figure 3.9(a), the calculated phase error, $\Phi_1(u)$, and the actual phase error are the same at the scene centre. As shown in Section 3.3, $\Phi_1(u)$ and $\Phi_2(t,u)$ are computed to compensate the error. In this scenario, space-variant errors are low, so the space-invariant MoCo approach is enough to fix the focusing problem. The resulting image is shown in Figure

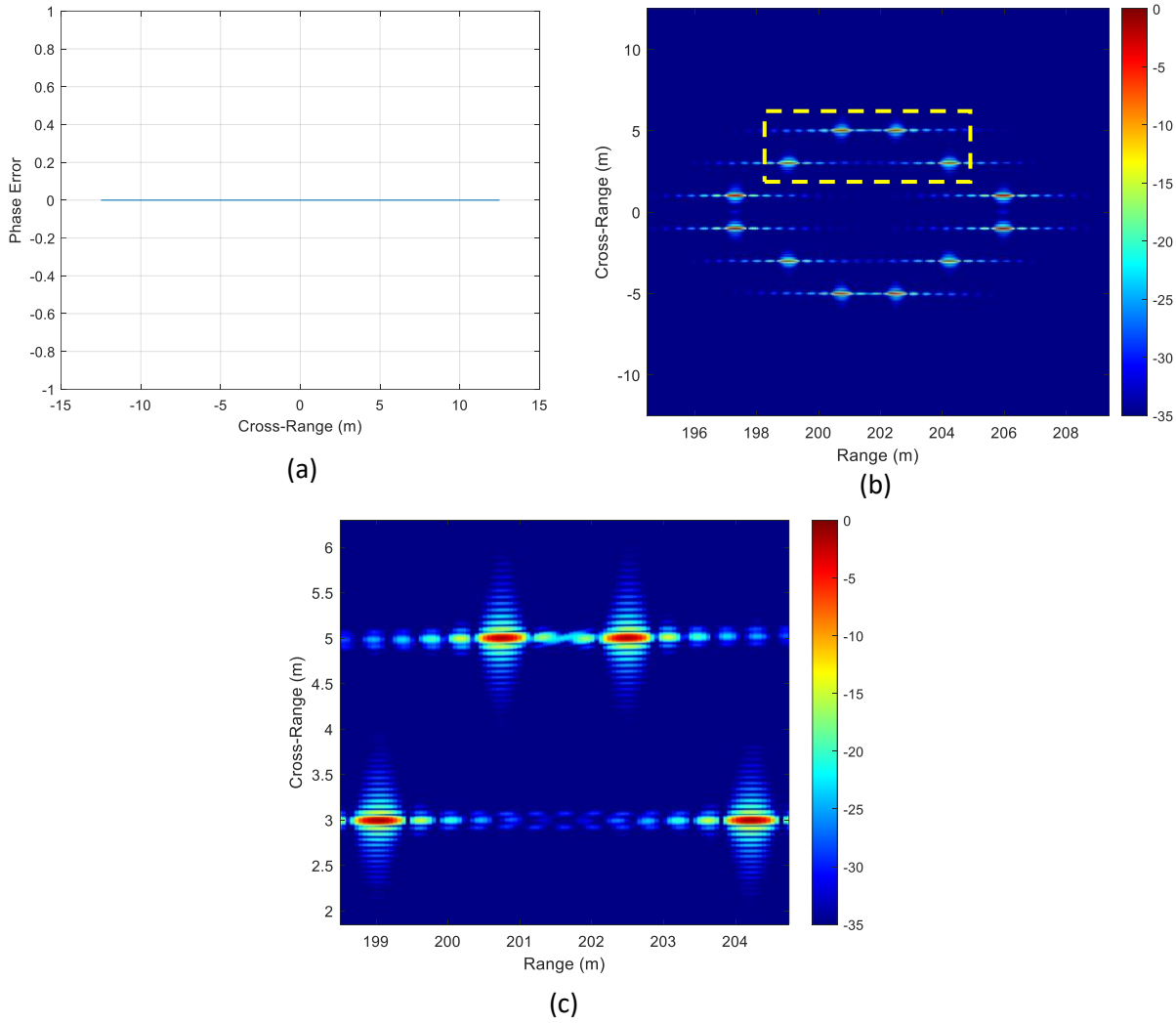

Figure 3.9 Positional data based MoCo results, (a) The residual phase error, (b) The obtained image after MoCo, (c) The local image shown in yellow rectangle in (b).

3.9(b). Also, the four targets in the yellow rectangle in Figure 3.9(b) is shown in Figure 3.9(c). As expected, all targets are well focused, and a 5 cm cross-range resolution is obtained.

In LQMD, the aperture is divided into multiple sub-apertures, and the error estimation is done by cross correlating the sub-images. Hence, choosing an appropriate sub-aperture length is crucial to have an accurate estimation. In this simulation, the whole aperture is divided into 10 half-overlapped sub-apertures, and a phase error is estimated in 6 iterations as described in 3.1.3. The residual phase error is less than 1.5 radian as shown in Figure 3.10(a). The resulting image is shown in Figure 3.10(b). Also, the four targets in the yellow rectangle in Figure 3.10(b) are shown in Figure 3.11(a). As expected, majority of the phase error is removed, and a better focused image is obtained. The cross-range profile of the target in the yellow box (in Figure 3.10(b)) is shown in Figure 3.11(b), and around 6 cm resolution is obtained. This is worse than the theoretical resolution, and the loss occurs due to residual errors. If the subaperture length is optimized or the length is changed in each iteration repeatedly, a better result may be obtained. However, the result shown here validates the method presented in Section 3.4.

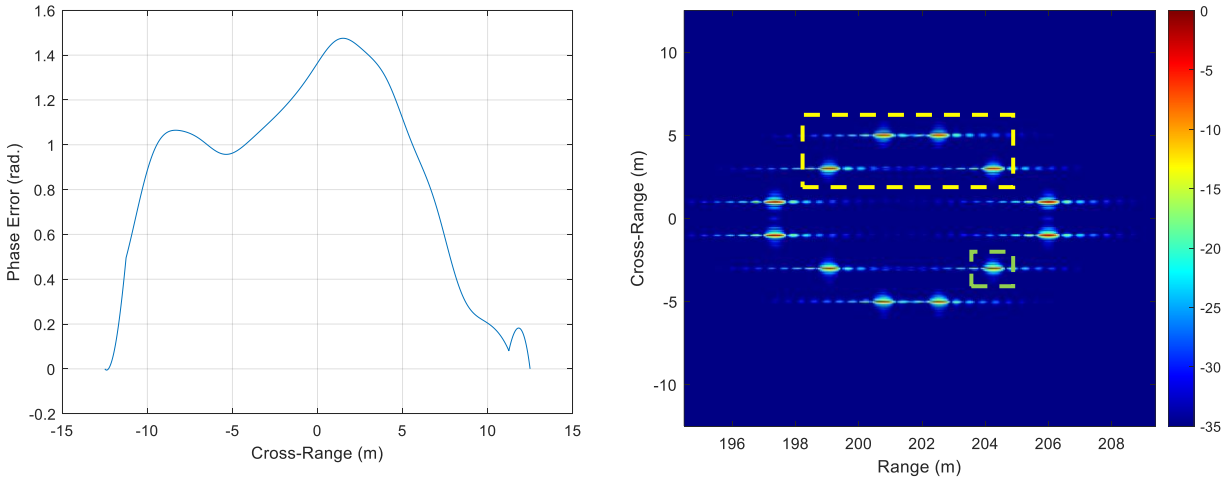

(a) (b)

Figure 3.10 LQMD results, (a) The residual phase error, (b) The obtained image after MoCo.

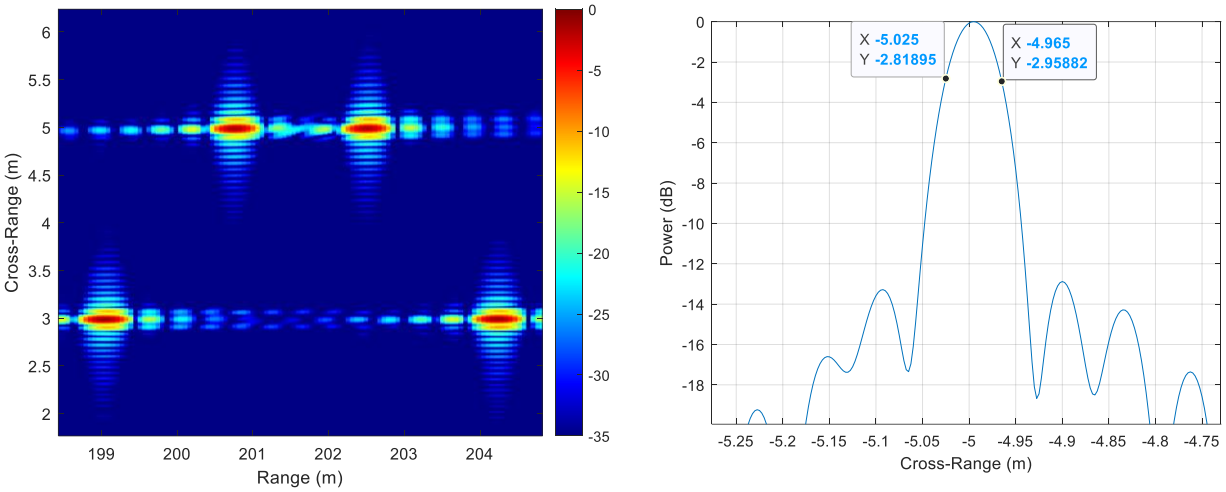

(a) (b)

Figure 3.11 (a) The local image shown in yellow rectangle in Figure 3.10(b), (b) The cross-range profile of the target in the green rectangle in Figure 3.10(b).

In PGA, the crucial point is to choose the right window length. The performance of the algorithm changes according to the initial window length. Here, the possible smallest window which includes all the errors is chosen. After 5 iterations, the phase error estimation process is done. The residual phase error is shown in Figure 3.12(a). The peak value of the residual error is 1.5 radians. The resulting image is shown in Figure 3.12(b). Also, the four targets in the yellow rectangle in Figure 3.12(b) is shown in Figure 3.12(c). As illustrated, a focused image is obtained by removing most of the errors. Similar to the LQMD case, a 6 cm resolution is obtained as shown in Figure 3.12(d). The phase error estimation accuracy may be enhanced by optimizing the window length. However, the obtained result is sufficient to show the validity of PGA.

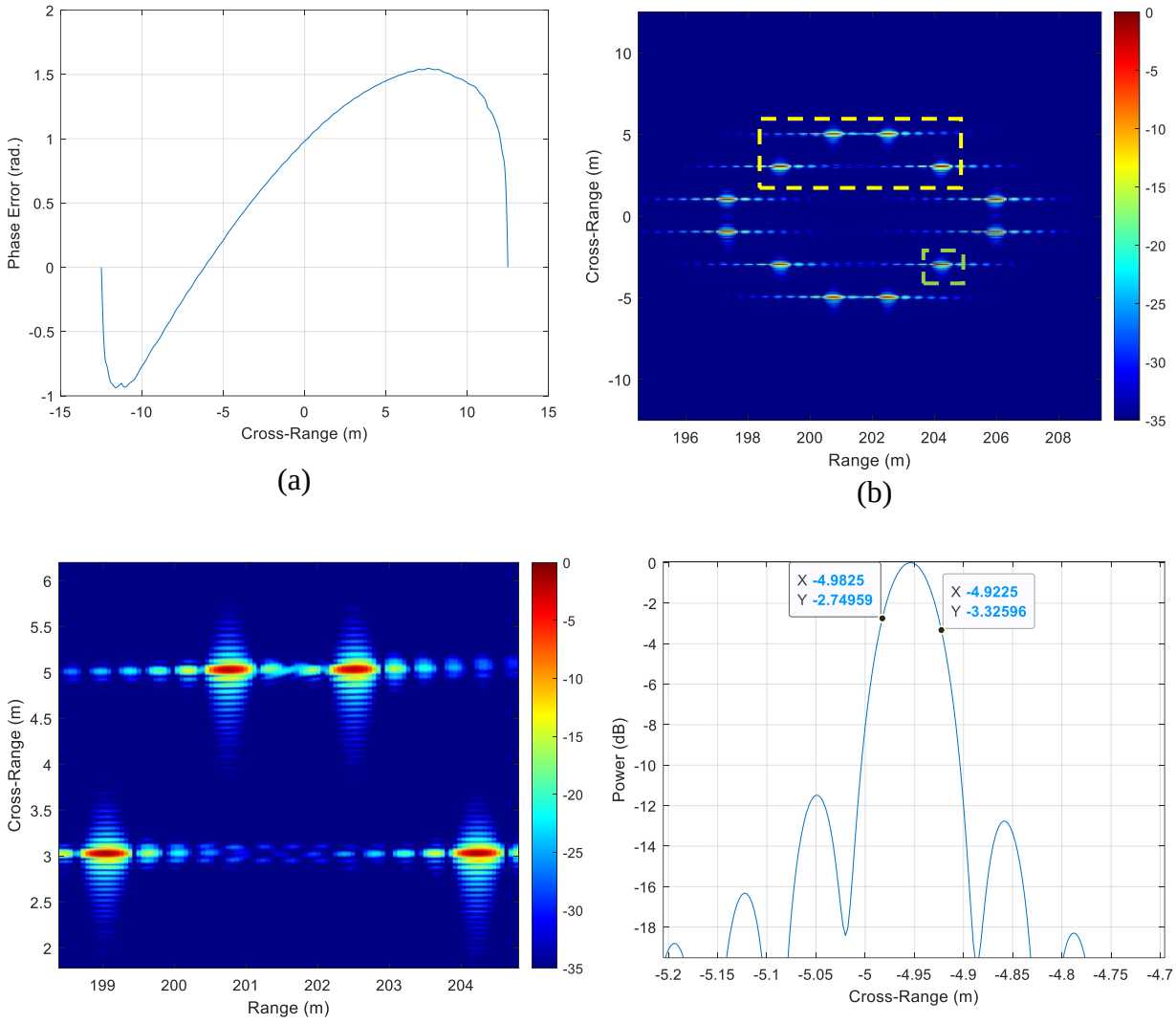

Figure 3.12 PGA results, (a) The residual phase error, (b) The obtained image after MoCo, (c) The local image shown in yellow rectangle in (b), (d) The cross-range profile of the target in the green rectangle in (b).

As seen, the autofocus algorithms performance depends on some parameters, and they are not robust methods. Also, increasing magnitude and frequency in the motion error may degrade the estimation accuracy. Figure 3.13(b) shows that the LQMD result becomes worse compared with the result in Figure 3.10 when the motion error's magnitude and frequency are increased as given in Figure 3.13(a). Similarly, the PGA result has some blurry targets and high sidelobes as shown in Figure 3.13(c). In order to make the phase estimation accuracy better and the

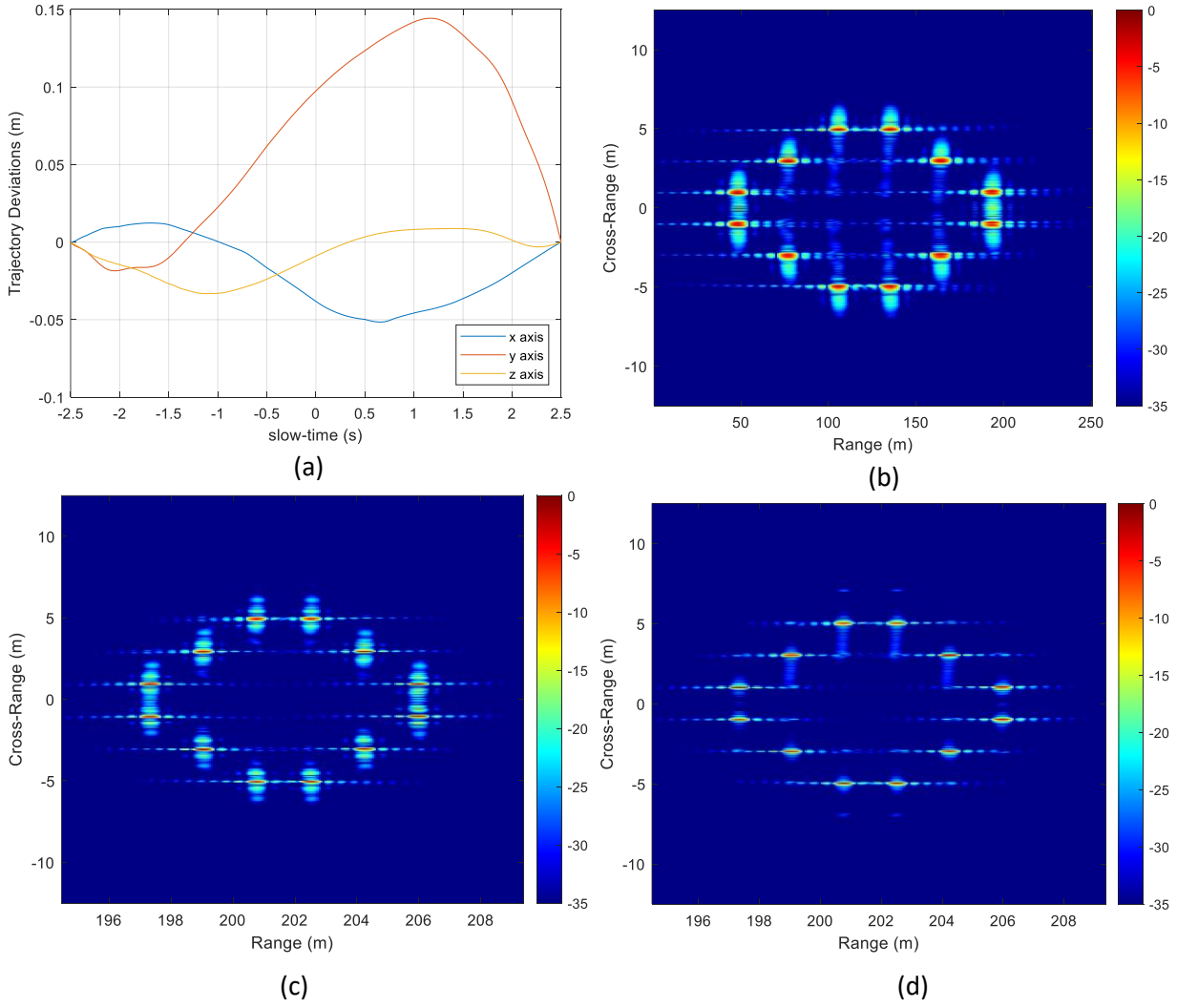

Figure 3.13 Comparison of LQMD and PGA, (a) The given motion error, (b) The obtained image with LQMD, (c) The obtained image with PGA (d) The obtained image after implementing LQMD and PGA, respectively.

autofocus algorithm more robust, LQMD and PGA can be used together. The image shown in Figure 3.13(d) is obtained by implementing PGA after LQMD implementation. As a result, a well-focused image is formed. That is because LQMD is better to estimate high-magnitude errors whereas PGA is better to estimate high-frequency errors. When they are used together, high-magnitude and high-frequency phase errors can be estimated correctly.

3.7 Summary

In this chapter, commonly used motion compensation methods are investigated in terms of their space-invariant error estimation capability. The algorithms capable of compensating for spatially invariant phase errors and correct range-walk errors for positional data-based MoCo, LQMD, and PGA are presented. Also, the algorithms are validated through simulations. Finally, it is shown that using LQMD and PGA together may improve the accuracy and robustness of the phase error estimation.

3.8 References

[1] M. Soumekh, Synthetic aperture radar signal processing: with MATLAB algorithms / Mehrdad Soumekh. New York, Chichester: Wiley, 1999.

[2] A. Moudgalya, P. J. Morris and C. V. Giriraja, "Motion Compensation on Range Doppler Algorithm for Airborne SAR," 2018 International Conference on Advances in Computing, Communications and Informatics (ICACCI), 2018, pp. 1303-1306, doi: 10.1109/ICACCI.2018.8554378.

[3] S. Buckreuss, \Motion compensation for airborne sar based on inertial data, rdm and gps," in Proceedings of IGARSS '94 - 1994 IEEE International Geoscience and Remote Sensing Symposium, vol. 4, Aug 1994, pp. 1971{1973 vol.4.

[4] Y. Li, M. Xing and Z. Bao, "A new method of motion error extraction from radar raw data for SAR motion compensation," 2006 CIE International Conference on Radar, 2006, pp. 1-4, doi: 10.1109/ICR.2006.343498.

[5] J. Li, P. Wang, J. Chen, J. Wang and W. Yang, "An improved two-step motion compensation method based on raw data," 2015 IEEE International Geoscience and Remote Sensing Symposium (IGARSS), 2015, pp. 4484-4486, doi: 10.1109/IGARSS.2015.7326823.

[6] M. Xing, X. Jiang, R. Wu, F. Zhou and Z. Bao, "Motion Compensation for UAV SAR Based on Raw Radar Data," in *IEEE Transactions on Geoscience and Remote Sensing*, vol. 47, no. 8, pp. 2870-2883, Aug. 2009, doi: 10.1109/TGRS.2009.2015657.

[7] W.G. Carrara, R.S. Goodman, R.M. Majewski, *Spotlight Synthetic Aperture Radar*, Artech House, 1995.

[8] D. G. Thompson, J. S. Bates and D. V. Arnold, "Extending the phase gradient autofocus algorithm for low-altitude stripmap mode SAR," Proceedings of the 1999 IEEE Radar

Conference. Radar into the Next Millennium (Cat. No.99CH36249), 1999, pp. 36-40, doi: 10.1109/NRC.1999.767199.

[9] Zhang, M. Hu, G. Wang and H. Wang, "Range-Dependent Map-Drift Algorithm for Focusing UAV SAR Imagery," in *IEEE Geoscience and Remote Sensing Letters*, vol. 13, no. 8, pp. 1158-1162, Aug. 2016, doi: 10.1109/LGRS.2016.2574752.

[10] A. Moreira, J. Mittermayer and R. Scheiber, "Extended chirp scaling algorithm for air- and spaceborne SAR data processing in stripmap and ScanSAR imaging modes," in IEEE Transactions on Geoscience and Remote Sensing, vol. 34, no. 5, pp. 1123-1136, Sept. 1996, doi: 10.1109/36.536528.

[11] O. O. Bezvesilniy, I. M. Gorovyi and D. M. Vavriv, "Estimation of phase errors in SAR data by Local-Quadratic map-drift autofocus," 2012 13th International Radar Symposium, Warsaw, 2012, pp. 376-381, doi: 10.1109/IRS.2012.6233350.

[12] Bezvesilniy, O., Gorovyi, I., & Vavriv, D. (2016). Autofocusing SAR images via local estimates of flight trajectory. *International Journal of Microwave and Wireless Technologies, 8*(6), 881-889. doi:10.1017/S1759078716000180.

[13] D. E. Wahl, P. H. Eichel, D. C. Ghiglia and C. V. Jakowatz, "Phase gradient autofocus - a robust tool for high resolution SAR phase correction," in IEEE Transactions on Aerospace and Electronic Systems, vol. 30, no. 3, pp. 827-835, July 1994, doi: 10.1109/7.303752.

[14] D. G. Thompson, J. S. Bates, D. V. Arnold and D. G. Long, "Extending the phase gradient autofocus algorithm for low-altitude stripmap mode SAR," IEEE 1999 International Geoscience and Remote Sensing Symposium. IGARSS'99 (Cat. No.99CH36293), Hamburg, Germany, 1999, pp. 564-566 vol.1, doi: 10.1109/IGARSS.1999.773566.

[15] L. Zhang, J. Sheng, M. Xing, Z. Qiao, T. Xiong and Z. Bao, "Wavenumber-Domain Autofocusing for Highly Squinted UAV SAR Imagery," in *IEEE Sensors Journal*, vol. 12, no. 5, pp. 1574-1588, May 2012, doi: 10.1109/JSEN.2011.2175216.

Chapter 4

Drone-Borne SAR System Overview

4.1 Introduction

A drone-borne SAR system includes at least a microcontroller, a radar, a drone, and a base station. The base station which is generally a laptop operates the radar remotely via the onboard microcontroller. The transmit powers and sensor sizes of the employed radars, in general, are restricted due to the limited payload capacities of drone platforms. Moreover, wind turbulence and drone's vibration may cause fluctuations in the drone's trajectory due to its light weight. The negligible motion error is proportional to the wavelength of the transmitted signal. According to [1] and [2], deviations higher that $\lambda/16$ can degrade the formed image. Although the potential for obtaining very fine-resolution imagery is improved at high frequencies due to the low radar form factor, the sensitivity to motion errors is also higher.

In this chapter, the built drone-borne SAR systems using the DJI S900 drone, DJI M300 drone, and INRAS Radarbook with its 24 GHz and 77 GHz frontends are presented. Then, the

main system characteristics such as the data collection limitations, spatial resolution, sensitivity, and swath limits are derived. Finally, motion errors resulting from the drone's instability are discussed for short-range SAR applications at high frequencies.

It is important to note that a part of this chapter has been published in [3] and [4].

4.2 Drone-Borne SAR System

The drone-borne SAR systems for short-range applications are designed and built in the Microwave Integrated Systems Laboratory (MISL), the University of Birmingham. Fundamentally, the systems include two sub-systems. One is the drone itself which includes a flight controller, a remote controller, and a battery pack. The other one is the radar sensing system which includes an onboard microcontroller, a radar, a battery, and a laptop as a base station.

Two different drone-borne SAR systems have been built using DJI S900 and DJI M300 drones. The built systems are demonstrated in Figure 4.1 and Figure 4.2, respectively. In short, the radar is controlled by a laptop remotely via a Raspberry-Pi (Pi). Also, the Pi stores the radar raw data and optionally the GPS/IMU data. The drone and the radar are powered by the drone's battery whereas the Pi is powered by a 5V power bank. The maximum data transfer speed between the radar and the Pi is about 100 Mbps with the ethernet connection and 300 Mbps with the USB connection.

The maximum payload is 4.5 kg for DJI S900 and 2.7 kg for DJI M300. The radar is approximately 0.5 kg, including its connecting apparatus. The Raspberry-Pi and its battery is around 0.1 kg. Also, the radar mounting apparatus is almost 0.2 kg. As a result, the total payload is less than 1 kg, well within the maximum payload capacity in both systems. This also means

that the payload could also be installed on drones with a much-reduced payload capacity. By keeping the payload as low as possible, the flight time is also maximized. The drones' maximum speed is around 16 m/s. The IMU refresh rate is 40 Hz whereas the GPS update rate

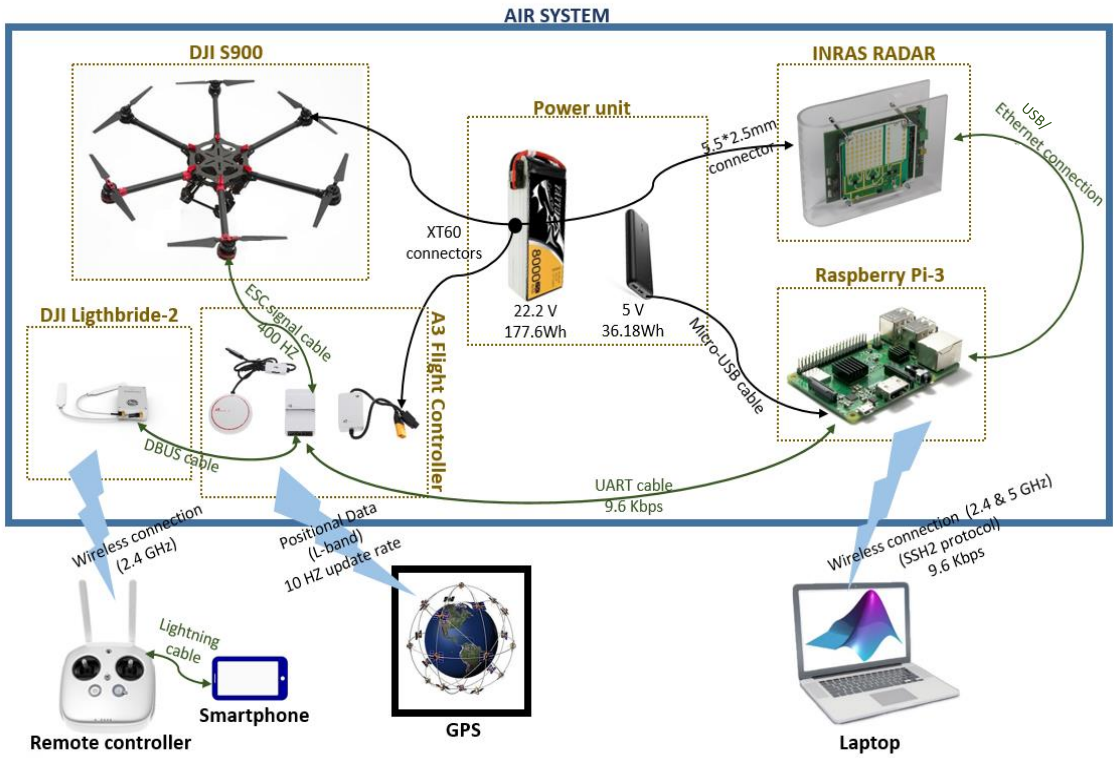

(a)

(b)

Figure 4.1 (a) SAR system diagram with DJI S900 drone, (b) The picture of the built drone-borne SAR system with DJI S900.

is just 10 Hz. Additionally, DJI M300 has an RTK system to enhance the flight stability. Later in this section, each component of the drone-borne SAR system is explained in detail.

(a)

(b)

Figure 4.2 (a) SAR system diagram with DJI M300 drone, (b) The picture of the built drone-borne SAR system with DJI M300.

4.2.1 Drone System

4.2.1.1 DJI S900

The DJI Spreading Wings S900 in Figure 4.3(a) has been designed for professional aerial photographers and cinematographers in 2014. We use the DJI S900 with the DJI A3 flight controller, Lightbridge 2 and Tattu LiPo battery as shown in Figure 4.1. This system offers high payload capacity and stable flight. The basic parameters are given in Table 4.1. The user guide

(a)

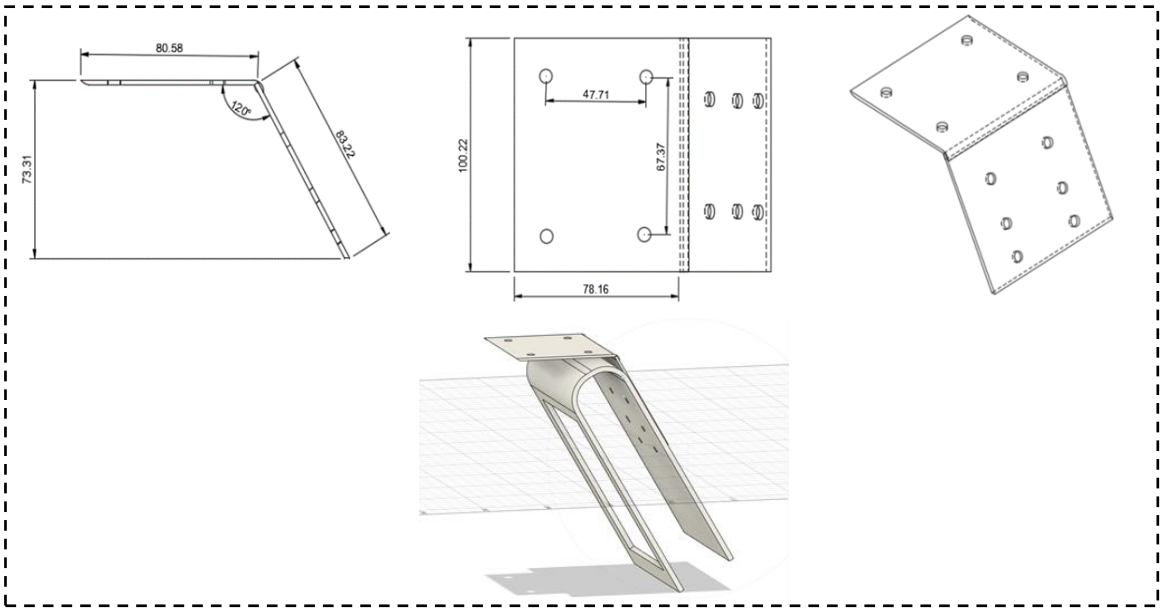

(b)

Figure 4.3 (a) The DJI Spreading Wings S900, (b) The designed mounting apparatus.

Table 4.1: DJI S900 Parameters

Parameters	DJI S900 with A3 flight controller
Weight	3.3 kg
Maximum takeoff weight	8.2 kg
Maximum speed	16 m/s
Average flight duration	15 mins
Maximum wind resistance	10 m/s
Diagonal wheelbase	900 mm
Vertical hovering accuracy	0.5 m
Horizontal hovering accuracy	1.5 m

is available in [5] and [6]. Also, it is needed to design a mounting apparatus to mount the radar to the drone. This was developed in-house and its CAD drawing is shown in Figure 4.3(b).

The GPS and IMU data are recorded on the flight controller's storage space. The data can be taken from the flight controller as a post-processing option. For real-time applications, the GPS/IMU data can be directly taken by an onboard computer (like a Raspberry Pi). All the needed information is available in [7].

4.2.1.2 DJI M300

DJI M300 in Figure 4.4 is a commercial drone platform with a 55-minute maximum flight time, advanced capabilities, and six directional sensing and positioning. Also, it offers improved relative positioning accuracy when it is used with the RTK system (D-RTK 2). The basic parameters are given in Table 4.2. Also, it is needed to design a mounting apparatus to mount the radar to the drone. The sketch can be seen in Figure 4.4(b).

(a)

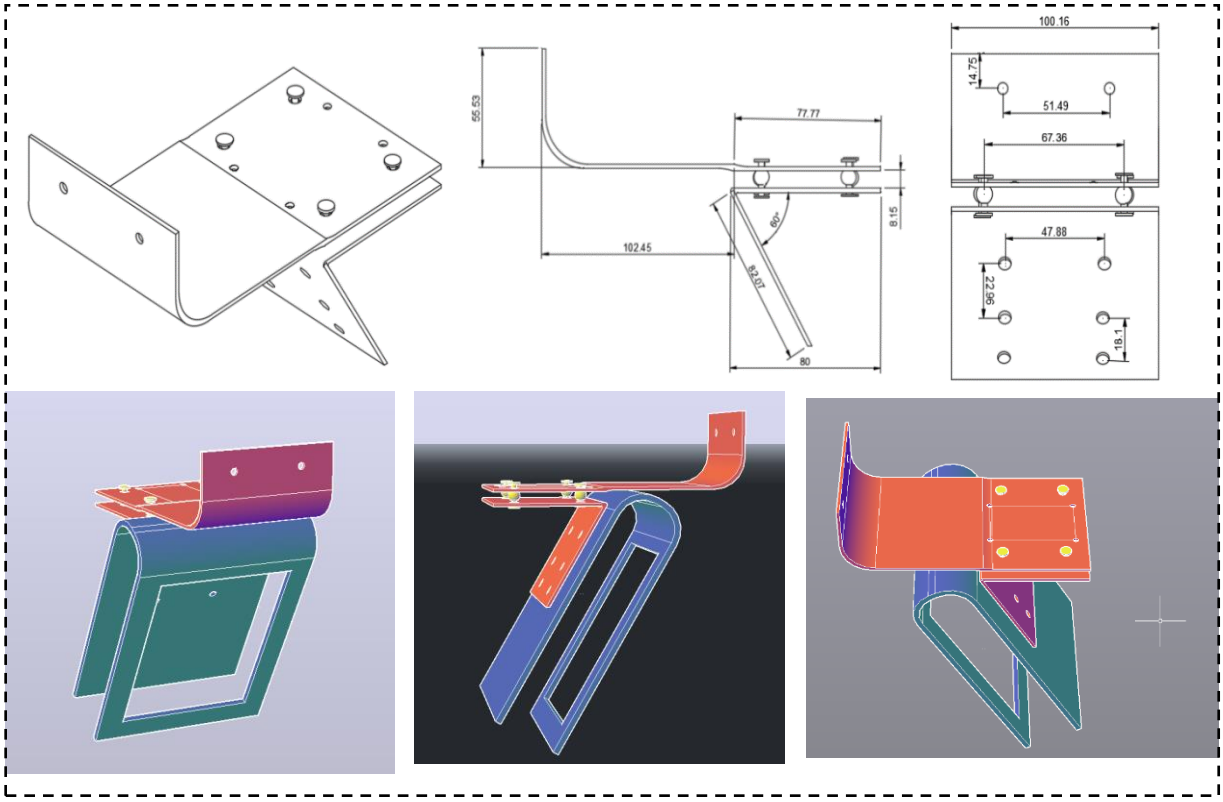

(b)

Figure 4.4 (a) DJI M300, (b) The designed mounting apparatus.

Table 4.2: DJI M300 Parameters

Parameters	DJI M300
Weight with batteries	6.3 kg
Maximum takeoff weight	9 kg
Maximum speed	17 m/s
Maximum flight duration	55 mins
Maximum wind resistance	15 m/s
Diagonal wheelbase	895 mm
Vertical hovering accuracy	0.5 m (GPS) 0.1 m (visual system) 0.1 m (RTK)
Horizontal hovering accuracy	1.5 m (GPS) 0.3 m (visual system) 0.1 m (RTK)

As a post-processing solution, the positional data can be extracted from the remote controller. A similar way as in Section 4.2.1.1 was followed to record the GPS/IMU data on an onboard computer.

4.2.2 Radar Sensing System

The radar sensing system includes the INRAS Radarbook, Raspberry Pi, a 5V power bank and a PC running Microsoft Windows. In this system, the radar is controlled by a PC remotely via the Raspberry Pi. The Pi runs the radar using a script written in Python. In the radar sensing system, this Python script was executed remotely using the Secure Shell protocol via a laptop. It is worth noting that the power bank was used only for powering up the Raspberry Pi whereas the radar was powered from the drone's battery. In the following subsections, the Raspberry Pi and the radar's specifications are explained.

4.2.2.1 Raspberry Pi

Raspberry Pi is a cheap and small single-board computer that runs Linux. It offers wireless LAN, Bluetooth, Ethernet, USB and a 40-pin GPIO header. For a drone-borne radar application, Raspberry Pi 3 Model B+ or Raspberry Pi 4 Model B can be used. Some parameters of both models are given in Table 4.3. The fourth-generation Pi offers up to 8GB RAM, USB 3.0 ports, dual HDMI slots, and high performance.

Table 4.3: Raspberry Pi Parameters

Parameters	**Pi 3 B+**	**Pi 4 B**
Operating System	Linux	Linux
Power	5V, 2.5 A	5V, 3 A
Ethernet	Gigabit Ethernet	Gigabit Ethernet
Wi-Fi	2.4 GHz & 5 GHz	2.4 GHz & 5 GHz
RAM	1 GB	Up to 8 GB
CPU	1.4 GHz 64-bit	1.5 GHz 64-bit

4.2.2.2 FMCW Radar

An INRAS-Radarbook MIMO radar was used [8], [9]. There are two separate front-end options: 24 and 77 GHz, and both were available to us. The 24 GHz front-end has 2 transmit and 8 receive channels whereas the 77 GHz front-end has 4 transmit and 8 receive channels. This off-the-shelf high-frequency radar was originally developed for automotive applications. However, it was also a good candidate for short-range drone-borne radar applications. That is because the overall cost, power consumption and weight are low as demonstrated in Table 4.4 and in [8] and [9]. The radar has three available frameworks as sampling, range-Doppler, and beamforming. The basic parameters are given in Table 4.4.

Table 4.4: INRAS Radarbook Parameters

Parameters	24 GHz	77 GHz
Bandwidth	0.5 GHz	0.5 - 2 GHz
Elevation Beamwidth*	76.5°	51°
Azimuth Beamwidth*	12.6°	13.2°
Transmit and Receive Channels	2-Tx, 8-Rx	4-Tx, 8-Rx
Tx/Rx Antenna gains	13.2 dBi	16 dBi
Transmit Power	8 dBm	10 dBm
Noise Figure	~10 dB	~12 dB
System Losses	~3 dB	~3 dB
Power Supply	10 – 36 V	10 – 36 V
Weight	0.41 kg	0.41 kg

* Radar was turned by 90° in the drone-borne SAR system**.**

4.3 SAR System's Operational Limits

The imaging geometry is very similar to stripmap mode airborne SAR (Figure 4.5). The differences arise due to the altitude, the platform velocity, and the motion characteristics of the platform. Drones have low altitude, low velocity, and generally, are less-stable platforms. Also, some of the assumptions made in airborne SAR such as narrow beam and constant target height may not be applicable for short-range operation.

At first, the SAR sensitivity is derived based on the built drone-borne SAR system parameters. Then, the maximum range to the target area is determined, and the maximum swath width depending on the drone's altitude is calculated. In addition, limitations on data collection are discussed. In Figure 4.5, the drone's ideal position is represented by P, altitude is represented by h, and the swath width is the distance between points B and D.

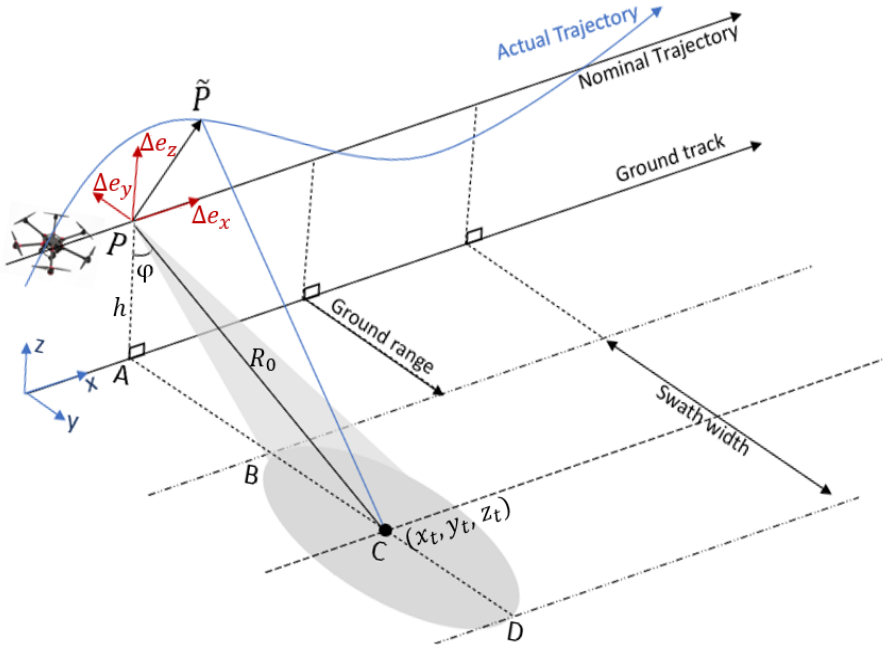

Figure 4.5 Drone-borne SAR image geometry.

4.3.1 SAR Sensitivity

Sensitivity is one of the most important parameters for a radar system. As mentioned in Chapter 2, SNR is given with equation (2.5). In [10], the bandwidth is replaced with coherent integration time which is equal to the $1/B$. Then, the following expression is obtained by expanding the coherent integration time.

$$SNR = \frac{P_{av} G_t G_r \sigma \lambda^3}{2v(4\pi)^3 R^3 k T F L_s \Delta C R} \tag{4.1}$$

where P_{av} is the average power and it is given as

$$P_{av} = P_t \times T_m \times PRF \tag{4.2}$$

After that, clutter to noise ratio (CNR) can be derived from SNR by changing the point target RCS with a real target which has three dimensions. CNR is given as follows in [10].

$$CNR = \frac{P_{av} G_t G_r \sigma^0 \lambda^3 \Delta R}{2v cos(\delta)(4\pi)^3 R^3 k T F L_s} \tag{4.3}$$

where σ^0 is the clutter backscatter coefficient, ΔR is the range resolution and δ is the grazing angle. Here, if CNR is assumed as 1 and the equation is solved for σ^0, this gives the noise-equivalent backscatter coefficient (NESZ) 'σ_n' as follows.

$$\sigma_n = \frac{2v\ cos(\delta)(4\pi)^3 R^3 k T F L_s}{P_{av} G_t G_r \lambda^3 \Delta R} \tag{4.4}$$

σ_n is a measure of the sensitivity of SAR. It gives the equivalent terrain reflectivity presented by thermal noise. NESZ is plotted against the range for both 24 and 77 GHz radars as shown in Figure 4.6. The radar parameters of the system are given in Table 4.4. As indicated, the transmit powers of the 24 and 77 GHz radars are 8 dBm and 10 dBm, respectively.

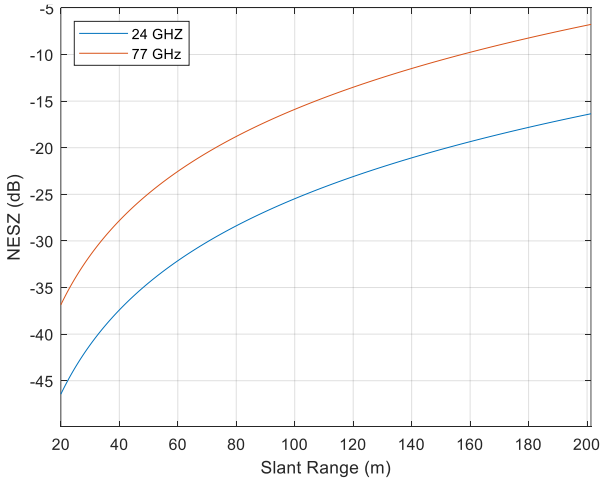

Figure 4.6 NESZ graph of the SAR system.

The bandwidth of both radars is assumed as 500 MHz to enable them to be directly compared. This bandwidth gives a 30 cm range resolution. When the velocity is 5 m/s and the duty cycle ($PRF \times T_m$) is 0.3, the result in Figure 4 .6 is obtained using the parameters in Table 4.4. As seen, the slant range between the antenna phase centre and the target must be small in order to achieve a high sensitivity and reasonable imaging range. If -24 dB NESZ is taken as giving a good quality image as shown in [11], the maximum slant range would be about 60 m for the 77 GHz radar and around 120 m for the 24 GHz radar. The maximum slant range can be increased by increasing the duty cycle, by decreasing the bandwidth or by decreasing the velocity of the platform. On the other hand, if the duty cycle is increased, the required data rate between the radar and the Pi increases. Decreasing the bandwidth makes the range resolution less fine. However, if the velocity of the drone decreases, the flight time increases. In turn, increasing flight time causes additional undesired motion deviations within the aperture.

The altitude of the drone can be set according to the desired swath width (SW). The imaged swath width can be calculated using (4.5). As mentioned before, the maximum slant range is limited by the sensitivity. The minimum slant range, $R_{0_{min}}$, is calculated using (4.6).

$$SW = \sqrt{{R_{0_{max}}}^2 - h^2} - \sqrt{{R_{0_{min}}}^2 - h^2} \tag{4.5}$$

where SW is the imaged swath width and $R_{0_{max}}$ is the maximum slant range. $R_{0_{min}}$ is the minimum slant range, and it represents the distance between the point-P and the point-B in Figure 4.5.

$$R_{0_{min}} = \frac{h}{cos(\varphi - {\emptyset}/{2})} \tag{4.6}$$

where φ is the look angle and $\emptyset$ is the elevation beamwidth.

If $R_{0_{max}}$ is assumed as 120 m for the 24 GHz radar and 60 m for the 77 GHz radar, the obtained swath widths for different altitudes are as shown in Figure 4.7. As expected, the imaged swath goes down whereas the altitude goes up. When the altitude is 20 m, the swath is approximately 40 m and 115 m for the 77 & 24 GHz radars, respectively.

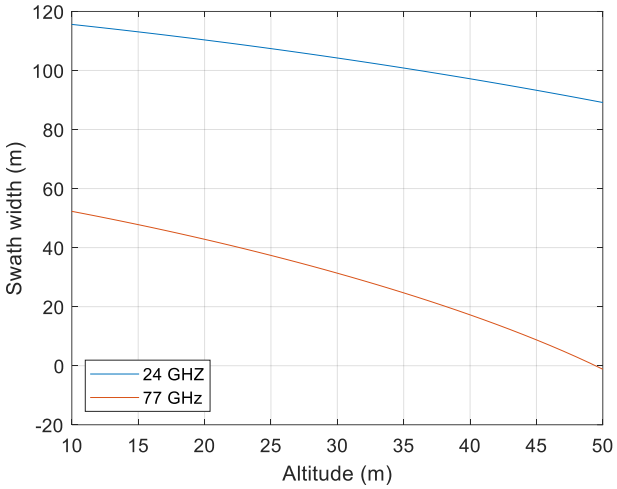

Figure 4.7 Swath width vs height.

4.3.2 Limitations on Data Collection

The number of range sampling points, N_{rs},, is related to the range resolution, ρ_r, and the maximum range between the target and the radar, $R_{0_{max}}$.

$$N_{rs} = \frac{2R_{0_{max}}}{\rho_r} \tag{4.7}$$

Additionally, in INRAS Radarbook there is a requirement that N_{rs} must be a multiple of eight to adjust a proper ADC sampling frequency that is equal to N_{rs}/T_m.

Regarding the azimuth sampling requirement, it is given in (2.29). If it is rearranged based on the obtainable maximum resolution, the distance between the data collection points, d, becomes:

$$d < \frac{D}{4} \tag{4.8}$$

where D is the antenna horizontal dimension.

If the total data collection time is T_u, and the velocity is v, the number of azimuth sampling points, N_{as}, can be written as:

$$N_{as} = \frac{vT_u}{d} \tag{4.9}$$

The required pulse repetition frequency, f_{PRF}, becomes:

$$f_{PRF} = \frac{N_{as}}{T_u} = \frac{v}{d} \tag{4.10}$$

By substituting (4.8) into (4.10), f_{PRF} can also be expressed as:

$$f_{PRF} > \frac{4v}{D} \tag{4.11}$$

Equation (4.11) indicates the minimum f_{PRF}. The maximum value for f_{PRF} is related to N_{rs}, and the maximum data transfer speed between the radar and the Raspberry Pi, given as:

$$f_{PRF} < \frac{\varsigma}{\Upsilon N_c N_{rs}} \tag{4.12}$$

where ς is the maximum data transfer speed, N_c is the number of receive channels, and Υ is the data size value for each range sample.

The maximum data collection time, $T_{u_{max}}$, that is another important parameter is written as:

$$T_{u_{max}} = \frac{M_m}{f_{PRF}\Upsilon N_c N_{rs}} \tag{4.13}$$

where M_m is the available memory of the Raspberry Pi.

At 24 GHz, the available bandwidth is 0.5 GHz as given in Table 4.4, and the resulting range resolution is found as 0.3 m by using (2.23). Also, the maximum slant range, $R_{0_{max}}$, was found as 120 m from the sensitivity calculation in Section 4.3.1. Hence, the number of range sampling points, N_{rs} is obtained as 800 from (4.7). It is known that the data samples are stored as 16-bit integer values with a signed fractional integer number format [12]. As mentioned before, the maximum data transfer speed is 100 Mbps with the ethernet connection and 300 Mbps with the USB connection. As a result, the upper limit for the pulse repetition frequency can be calculated from (4.12). To determine the lower limit of the pulse repetition frequency, equation (4.11) is used. The antenna's horizontal dimension is approximately 57 mm for the 24 GHz frontend, so the minimum required f_{PRF} can be obtained depending on the velocity of the platform. It is worth noting that we always need to choose a higher f_{PRF} than the minimum required one to sample the azimuth signal that contains motion errors. Finally, the maximum data collection time can be calculated by using (4.13). We have two types of Raspberry Pi as shown in Section 4.2.2.1. The Pi 3B+ has a 1 GB memory whereas the Pi 4B has 4 GB memory.

Regarding the 77 GHz frontend, the available bandwidth varies between 0.5 GHz and 2 GHz as given in Table 4.4. The resulting range resolution is between 0.3 m and 0.075 m depending on the used bandwidth whereas the maximum slant range, $R_{0_{max}}$, was found as 60 m from the sensitivity calculation in Section 4.3.1. Also, the antenna's horizontal dimension is 17 mm. The parameters such as the maximum data collection time and pulse repetition frequency can be calculated using equations from (4.7) to (4.13).

It is obvious that there is always a trade-off between the velocity of the platform, used number of channels, data transfer speed, and range resolution. For instance, if 77 GHz radar is

used with its eight receive channels and the data is transferred over an ethernet connection, the upper limit for the pulse repetition frequency is obtained as 1.8 kHz for 0.5 GHz bandwidth. If the bandwidth is increased to 2 GHz, the upper limit for f_{PRF} reduces to 450 Hz. Assuming this f_{PRF} is selected, and there is no motion error, the maximum velocity of the drone is calculated as 1.9 m/s from (4.11). Nonetheless, according to the empirical measurements, the velocity should be at least 50% less to decrease the distance between the data collection points when motion errors are considered. When the velocity of the drone is higher than this value, azimuth sampling would be sparse, and ambiguities would appear in the image. If higher velocities are desired to have a more stable flight, the number of channels or the bandwidth should be decreased.

4.3.3 Space-Variant Phase Error Induced by Motion Error

Investigation of phase errors induced by motion errors starts with deriving range errors in LOS direction. Ideally, the platform moves on a straight line with a constant velocity v and altitude h during the aperture time u_a. On the other hand, the actual trajectory has deviations due to turbulence as shown in Figure 4.5. In this figure, P indicates the ideal position of the platform whereas $\tilde{P}$ shows its actual position. The instantaneous motion error consists of cross-range motion errors, $\Delta e_x(u)$, and down-range motion errors, $\Delta e_y(u)$ and $\Delta e_z(u)$, where u is slow-time and between $\mp\frac{u_a}{2}$. As given in (3.3), the range error is the difference between the actual range history and the ideal range history, and it is given as follows for a target located at (x_t, y_t, z_t) by assuming the ideal sensor position is $(vu, 0, h)$:

$$R_{er}(u) = R(u) - R_i(u) \tag{4.14}$$

where

$$R(u) = \sqrt{(vu + \Delta e_x(u) - x_t)^2 + \left(\Delta e_y(u) - y_t\right)^2 + (h + \Delta e_z(u) - z_t)^2} \quad (4.15)$$

$$R_i(u) = \sqrt{(vu - x_t)^2 + {y_t}^2 + (h - z_t)^2} \quad (4.16)$$

If the actual range history is rearranged as follows and rewritten by using the Taylor series expansion up to the quadratic term, the actual range history is approximately equal to:

$$R(u) = \sqrt{\left(R_i(u)\right)^2 + \Lambda^2} \approx R_i(u) + \frac{\Lambda^2}{2R_i(u)} \quad (4.17)$$

where

$$\Lambda = \left(\Delta e_x(u)\right)^2 + \left(\Delta e_y(u)\right)^2 + \left(\Delta e_z(u)\right)^2 - 2x_t\Delta e_x(u) - 2y_t\Delta e_y(u) - 2z_t\Delta e_z(u) + 2vu\Delta e_x(u) + 2h\Delta e_z(u) \quad (4.18)$$

By substituting (4.17) into (4.14), the range error in LOS direction becomes:

$$R_{er}(u) = \frac{\Delta e_x(u)(\Delta e_x(u) + 2vu - 2x_t)}{2R_i(u)} + \frac{\Delta e_y(u)\left(\Delta e_y(u) - 2y_t\right)}{2R_i(u)} + \frac{\Delta e_z(u)(\Delta e_z(u) - 2z_t + 2h)}{2R_i(u)} \quad (4.19)$$

If $y_t >> \Delta e_y$ and $h >> \Delta e_z$:

$$R_{er}(u) \approx \frac{(vu - x_t)}{R_i(u)}\Delta e_x(u) - \frac{y_t}{R_i(u)}\Delta e_y(u) + \frac{-z_t + h}{R_i(u)}\Delta e_z(u) \quad (4.20)$$

This equation indicates that the error is dependent on both the target's range and cross-range position. Also, there is a coupling between the range-dependent and cross-range dependent errors. If $R_0 >> vu_a$, it can be assumed that down-range motion errors do not cause cross-range dependent errors, and (4.20) can be rewritten as:

$$R_{er}(u) = \frac{(vu - x_t)}{R_0}\Delta e_x(u) - \frac{y_t}{R_0}\Delta e_y(u) + \frac{-z_t + h}{R_0}\Delta e_z(u) \qquad (4.21)$$

where $R_0 = \sqrt{{y_t}^2 + (h - z_t)^2}$ and represents the closest approach to the target.

On the other hand, as shown in Section 4.3.1, our drone-borne systems are more suitable for short-range operations. Hence, coupling between the range and cross-range dependent errors may not be ignored, especially, when a fine-resolution is desired. For instance, if $\Delta e_x(u)$ and $\Delta e_z(u)$ are zero, and $\Delta e_y(u)$ is a single cycle $sine$ function with a 5 cm peak value as shown in Figure 4.8(a), the resulting range error, $R_{er}(u)$, can be plotted using (4.20) for targets that have different azimuth positions as in Figure 4.8(b) ($v = 5$ m/s, $u_a = 4$ s, $R_0 = 50$ m). The difference between these two range error functions varies in time and reaches to 2 mm peak value as shown in Figure 4.8(c). If this peak value is not much smaller than the wavelength, targets at different azimuth positions cannot be focused simultaneously using a single filter, and cross-range dependent errors appear in the image. Also, motion errors that have greater magnitude would increase the cross-range dependent errors induced by $\Delta e_y(u)$ and $\Delta e_z(u)$. Hence, the following drone-borne SAR phase error analysis uses (4.20) instead of (4.21).

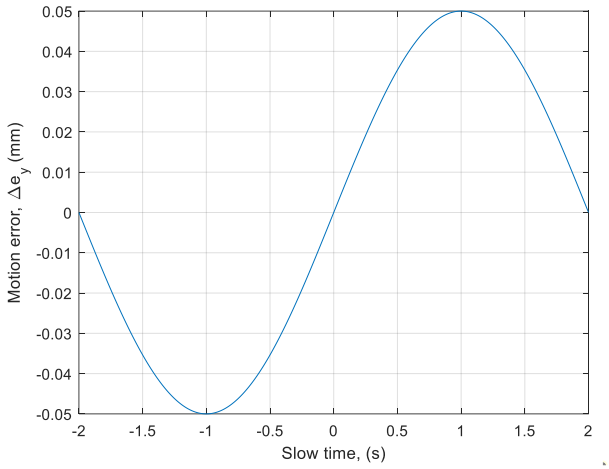

(a)

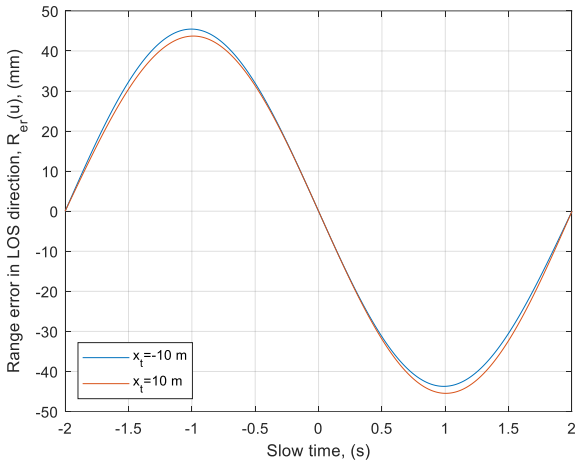

(b)

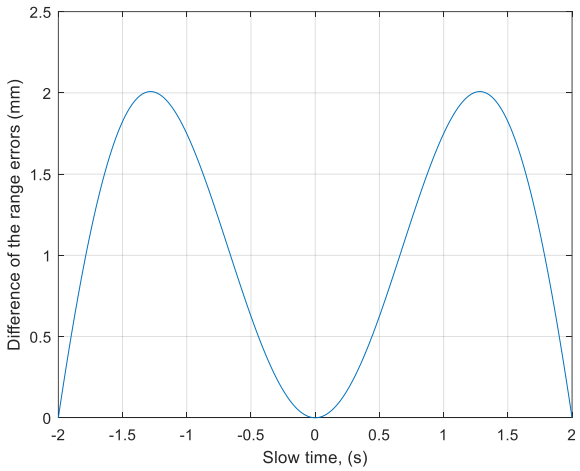

(c)

Figure 4.8 (a) Given motion error along the ground range direction, (b) calculated range error for targets that have different azimuth positions, (c) the difference between these two range error functions.

Under the conditions in Section 4.3.1, the phase error, $\frac{4\pi}{\lambda}R_{er}(u)$, can be examined through equation (4.20). In order to analyze the space-variant phase errors induced by motion errors, two examples are presented next. In the first one, the change in the phase error depending on the position of the target is calculated by assuming the motion error vector at $u = 0$ is $[\Delta e_x(0), \Delta e_y(0), \Delta e_z(0)]$ =[0.03, -0.05, 0.05]. The result is illustrated in Figure 4.9. The mean value is subtracted in each plot. In Figure 4.9 (a), the phase error versus the target's range is shown, assuming $(x, z) = (0, 0)$. In Figure 4.9 (b), $(y, z) = (34, 0)$ is assumed, and the variation of

the phase error depending on the azimuth position is plotted. In Figure 4.9 (c), the phase error change is shown against the target's height, assuming $(x, y) = (0, 34)$. Obviously, even if the motion error is low and the mean values are removed, the phase error is high, non-linear, and a function of target position.

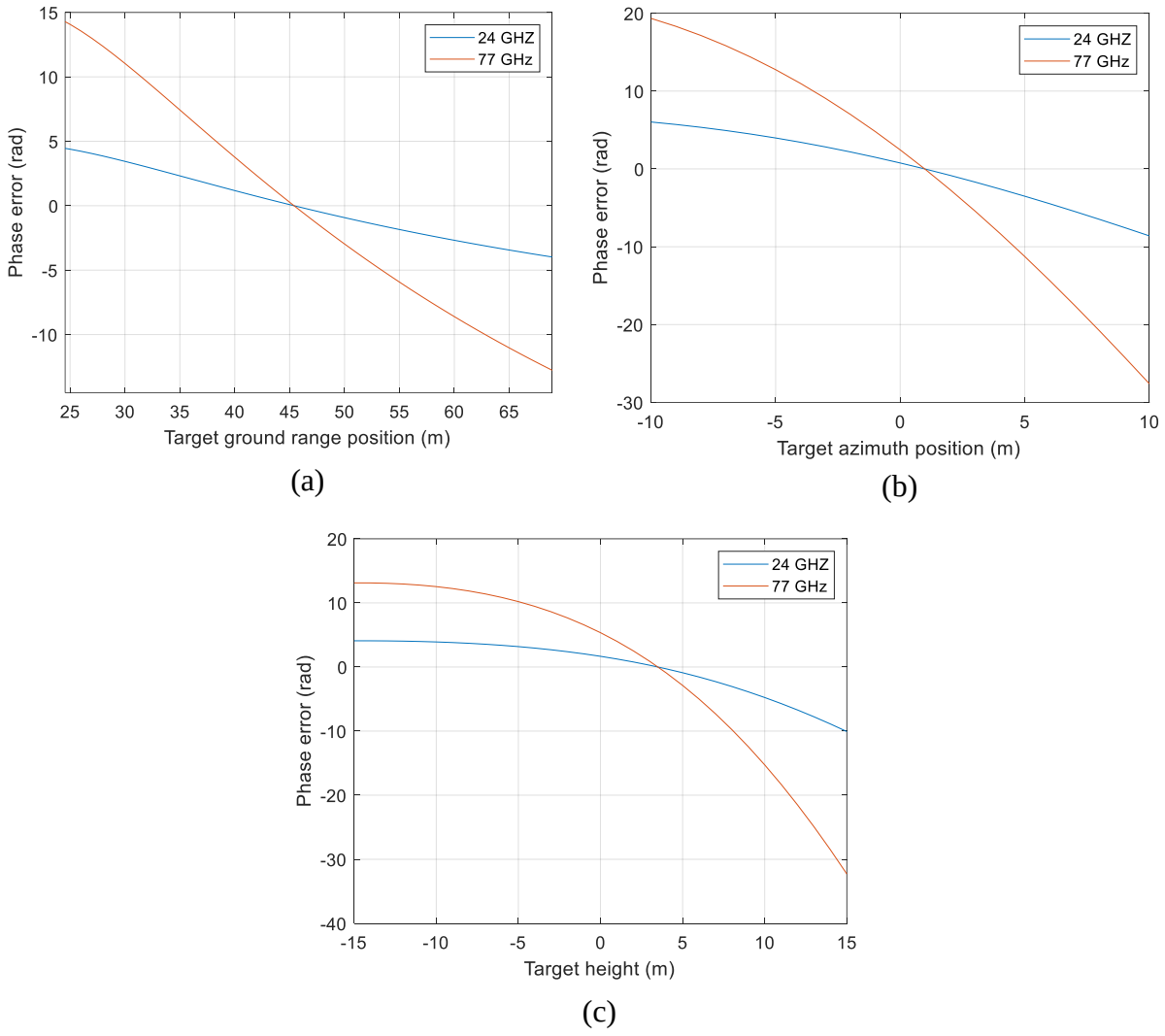

Figure 4.9 The residual phase error (a) depending on the target's ground range position, (b) depending on the target's azimuth position, (c) depending on the target's height.

In the second example, to get a more realistic sense of motion errors and their dynamics, positional information extracted from the flight controller of our drone (DJI S900) during flight is used. The trajectory itself is shown in Figure 4.10. The resulting phase error, $\frac{4\pi}{\lambda}R_{er}(u)$, was evaluated using (4.20), and the phase error difference to a reference target located at $(x_t, y_t, z_t) = (0, 40, 0)$ (without linear term) is presented in Figure 4.11. The figure shows how the phase errors (in radians) depend on the target's position (x_t, y_t, z_t) at a frequency of 77 GHz. Here, h is assumed as 20 m whereas v is 5 m/s. In Figure 4.11 (a), the phase error versus the target's ground range is plotted, assuming $(x_t, z_t) = (0, 0)$. The phase error is calculated for each slow-time position by changing the target's ground range. The linear term is removed, and the phase error is compensated based on the reference target. As expected, the error increases further away from the center and reaches up to 120 radians at the edge. In Figure 4.11 (b), after subtracting the linear phase error and the error of the reference target, the phase error change depending on the target's cross-range position is demonstrated, assuming $(y_t, z_t) = (40, 0)$. The resulting error is changing between +20 and −60 radians. Finally, in Figure 4.11 (c), by assuming $(x_t, y_t) = (0, 40)$, the phase error change is shown against the target's height after subtracting the linear phase error and the reference target's error. The

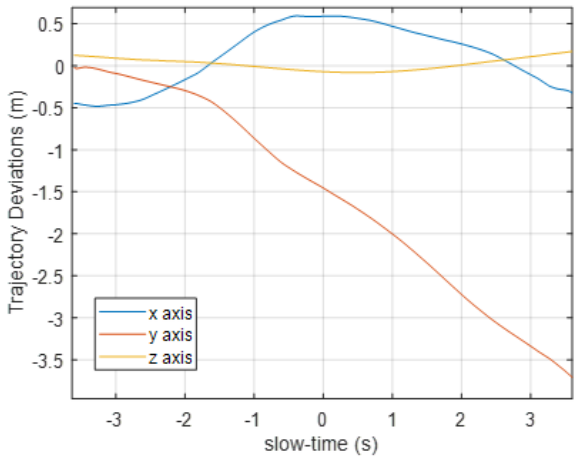

Figure 4.10 The given motion errors (deviation from the ideal trajectory).

resulting error can exceed 20 radians for a target which has 10 m height. As seen, the residual phase errors are high and changing non-linearly depending on the target position. Ultimately, this spatial variance limits the imaging capability even at short ranges. The space-variant errors can be minimized by creating azimuth and range blocks as will be shown in Chapter 5.

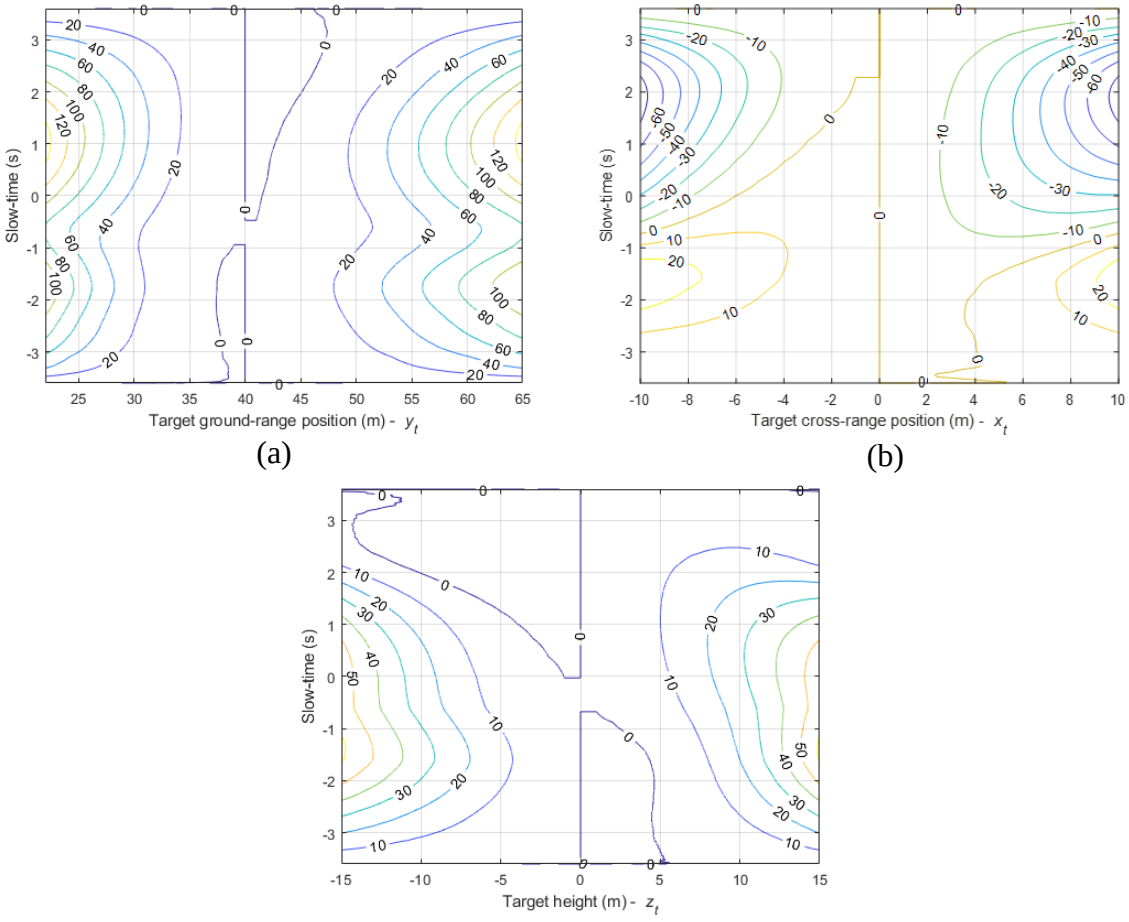

Figure 4.11 (a) Residual phase error depending on ground range, y_t, for target position (0, y_t, 0), compensated based on target at (0, 40, 0). (b) Residual phase error depending on cross-range, x_t, for target position (x_t, 40, 0), compensated based on target at (0, 40, 0). (c) Residual phase error depending on height, z_t, for target position (0, 40, z_t), compensated based on target at (0, 40, 0). Phase errors are shown in radians.

The range error causes a phase error, and the higher the frequency, the higher the phase error. Consequently, it might be thought that obtaining an image at higher frequencies is more problematic. However, if the resolution is limited, there can be balancing effects. For instance, if a 5 cm azimuth resolution is desired, apertures of 5 m (for 24 GHz) and 1.56 m (for 77 GHz) are needed at a range of 40 m. As the aperture needed is smaller for 77 GHz the opportunity for motion error is less and hence the resulting phase error is less.

4.4 Summary

This chapter begins by introducing the built two drone-borne SAR systems at the University of Birmingham in detail. Both systems use off-the-shelf high-frequency radars originally developed for automotive applications and commercial drones. Based on the employed COTS devices and the SAR geometry, the major SAR system characteristics such as the spatial resolution, sensitivity, swath limits, and pulse repetition frequency limitations are derived. Finally, the motion errors are evaluated and possible difficulties in image formation are discussed.

4.5 References

[1] W.G. Carrara, R.S. Goodman, R.M. Majewski, *Spotlight Synthetic Aperture Radar*, Artech House, 1995.

[2] C. V. Jakowatz et al., Spotlight-Mode Synthetic Aperture Radar: A Signal Processsing Approach. New York: Springer, 1996

[3] A. Bekar, M. Antoniou and C. J. Baker, "High-Resolution Drone-Borne SAR using Off-the-Shelf High-Frequency Radars," *2021 IEEE Radar Conference (RadarConf21)*, 2021, pp. 1-6, doi: 10.1109/RadarConf2147009.2021.9455342.

[4] A. Bekar, M. Antoniou and C. J. Baker, "Low-Cost, High-Resolution, Drone-Borne SAR Imaging," in *IEEE Transactions on Geoscience and Remote Sensing*, vol. 60, pp. 1-11, 2022, Art no. 5208811, doi: 10.1109/TGRS.2021.3085235.

[5] https://www.dji.com/uk/spreading-wings-s900/info#downloads.

[6] https://www.dji.com/uk/a3/info#downloads.

[7] https://developer.dji.com/onboard-sdk/documentation/development-workflow/hardware-setup.html.

[8] Haderer, A., ADF-24G-TX2RX8 Frontend (User Manual). 2015.

[9] Haderer, A., MIMO-77-TX4RX8 Frontend (User Manual). 2015.

[10] Mark A. Richards, James A. Scheer, William A. Holm., *Principles of modern radar. Vol. I, basic principles* ser. Radar, Sonar, Navigation and Avionics, 2010.

[11] A. Doerry, “Performance limits for synthetic aperture radar—Second edition,” Sandia Nat. Lab., Albuquerque, NM, USA, Tech. Rep. 02, 2006

[12] Haderer, A., Radarbook User Manual. 2014.

Chapter 5

Drone-borne SAR Imaging

5.1 Introduction

SAR has been extensively developed and, subsequently, widely used as a remote sensing tool [1], [2]. Previous research has, almost exclusively, used airborne and spaceborne platforms to carry the radar sensor. As mentioned in Chapter 1, drones have a number of unique characteristics, which are already opening up new applications for SAR imaging. For example, drones are cheap, easily accessible and rapidly deployable. Also, they can follow trajectories and fly into areas which are otherwise difficult for conventional air or space-craft, if possible at all. However, Chapter 4 indicates that the drone-borne SAR imaging that employs a high-frequency, low-power radar is more suitable for operating at relatively short ranges. Further, it is shown that drones are prone to flight irregularities due to wind and turbulence, which lead to space-invariant and variant phase errors, and range-walk errors. Combining these flight irregularities and inaccuracies of modern onboard INS/GPS, potentially, makes image formation more challenging. Typically, the accuracy of a GPS on a drone is between 0.5 m and

2 m. This can be increased to centimetre level by using dedicated positional systems. However, this would begin to make the SAR system expensive.

As shown in Chapter 1, there are systems that can rely on capable positional instrumentation, where the spatial variance of errors is low in both range and azimuth. For example, in [3] – [6], drone-borne SAR systems using ground penetrating radar were introduced with the aim of underground imaging for landmine detection. Undesired motion errors were compensated by using GPS-RTK systems. In these reports, due to the low operating frequencies, the GPS-RTK system provides sufficiently accurate positional data to compensate for motion errors. Some systems use dedicated GPS/INS to ease the implementation of the autofocus algorithms. As an example, in [7], a high-resolution SAR image was generated using a Ku-band radar. A differential-GPS was employed to give high accuracy positional data. After, MoCo with GPS data, PGA and MEA are implemented to compensate residual phase errors. The reported W-band mini-SAR system in [8] uses a motion compensation method based on fusing a combination of the IMU and SAR data. In experimentation, the maximum imaging range was set at 600 m. Imagery with 4.5 cm range and 3.5 cm cross-range resolution was produced. Systems that do not rely on dedicated positioning systems have also been reported. For example, in [9], horizontal, vertical, and circular trajectories and repeat-pass interferometry using a drone-based system were investigated. The experiments were carried out using a 10 GHz radar. Phase errors were compensated using the phase history of point-like scatterers and polarimetric active radar calibrators. The resolution achieved was approximately 30 cm. However, space-variant phase errors were not apparent. In [10], a method was proposed to deal with range-azimuth coupling using a squint minimization technique. Squinted Azimuth-dependent PGA and MEA were used as autofocus algorithms. As a result, imagery with a resolution of 20 cm in cross-range was obtained using a 35 GHz radar. Employing the same

SAR system as [7], [11] made the phase errors spatially invariant and formed imagery without using navigational data. A Quasi-Polar-Based fast factorized back-projection (FFBP) algorithm was proposed that also terminates the dependency on navigational data. Although FFBP is computationally less expensive than BP, it is not as fast as frequency domain algorithms. Approximately, a 4 cm cross-range resolution was achieved. In [12] and [13], a drone-borne SAR system was reported using a 9.7 GHz radar. A 10 cm resolution was reported using a 2D autofocus method after application of a polar format algorithm. In the experiment, the slant range to the scene center was around 2.5 km. In the case of finer resolutions at high-frequencies and shorter ranges, high degrees of spatial variance will exist, and methods will be needed to correct them without the use of a dedicated positional system.

The objective of the research presented here is to create an image formation algorithm that can push the spatial resolution limits for short-range, very high-resolution SAR imaging without the use of an onboard dedicated INS. To the knowledge of the author, the current work presents novel short-range, fine-resolution imagery of extended target areas generated using a low-cost drone-borne vehicular FMCW radars operating at 24 & 77 GHz, and a part of this work was presented in 2021 at the IEEE Radar Conference [21]. The paper was awarded "The Best Student Paper (2nd place)" award. Also, the work was published in the journal of IEEE Transactions on Geoscience and Remote Sensing in 2022 [22].

In the algorithm developed, some of the range walk and phase errors are compensated by the help of the positional information provided by the drone's flight controller. Subsequently, LQMD [14], [15] and PGA techniques are applied, respectively, to correct for residual range walk error and to compensate space-invariant phase errors. After RCMC, the image is divided into range and azimuth blocks and the residual phase errors are estimated and compensated

within each local scene using PGA. Next, by applying another LQMD to each range block, discontinuities between azimuth blocks are reduced. The final image is formed using RDA. The validity of the approach is tested through simulation and experiments. The experimental demonstrator built for this purpose comprised a hexacopter drone equipped with low-cost, high-frequency FMCW radar systems originally developed for advanced automotive applications. The details of the built system are presented in Chapter 4. In this way, images with resolution that would otherwise require advanced, multi-million airborne SAR, can now be formed with drone-borne SAR that costs orders of magnitude less (approximately £15k).

5.2 Imaging Algorithm

The flow-chart representing the algorithm is shown in Figure 5.1. Fundamentally, after positional data based MoCo, LQMD and PGA are implemented to compensate space-invariant errors. Then, based on azimuth and range blocking, space-variant errors are compensated locally. Although the accuracy of standard GPS/INS onboard drones is not as high as RTK measurements, it still has the potential to compensate at least some of the bulk motion errors. Nonetheless, significant phase and range-walk errors remain after positional data based MoCo. Therefore, autofocus algorithms must also be employed. PGA is widely used to form high resolution SAR imagery. However, its performance is degraded if the amount of range-walk is high. Therefore, an option is to apply LQMD before PGA. LQMD can make accurate phase error estimations despite range-walk error. Also, it can estimate higher order phase errors compared to the conventional MD. After LQMD phase error estimation, range walk error is corrected, and the phase error is compensated. Nevertheless, LQMD is not a perfect algorithm to estimate higher-order motion errors. Also, these types of error can degrade image quality. In most cases, the data is not still accurate enough for RCMC due to residual errors. Consequently,

PGA is applied to correct residual errors. At the short-ranges considered here, the footprint of the beam is small. This leads to less prominent targets within the beam. Also, target location may affect the phase error as indicated in Figure 4.9 and Figure 4.11 in Section 4.3.3. As a result, it is not always possible to compensate space-variant errors globally. Therefore, a strategy is followed that is based on range/azimuth blocks. The residual phase errors within the local scenes are estimated by PGA and then compensated. Also, by implementing another LQMD to each range-block, discontinuities between the azimuth blocks are reduced. This method does not promise a global solution, and the image quality may vary from one local image to another depending on spatially variant phase errors and user-defined parameters such as LQMD-PGA parameters, and the size of the range-azimuth blocks. Nevertheless, the method is easy to implement and has the potential to give satisfying results, as will be shown later.

As shown in Section 3.1.1, $R(u)$ can be written as a summation of the ideal range history and the range error history. As a result, the signal which represents the two-dimensional error function, $s_e(t,u)$, can be rewritten as in (3.2).

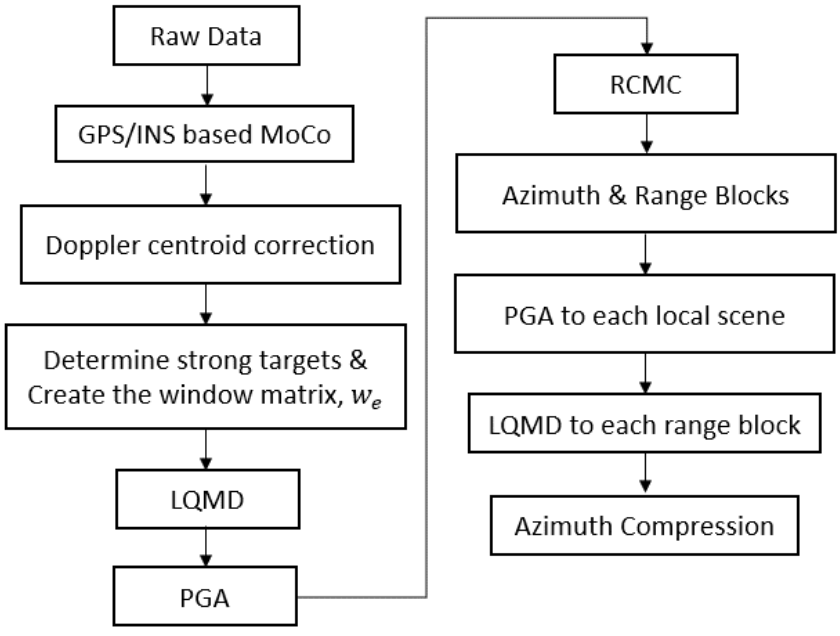

Figure 5.1 The flow chart of the algorithm.

$$s_e(t,u) = \Phi_1(u) \cdot \Phi_2(t,u) \cdot \Phi_3(u)$$

$$= e^{-j2\pi f_c \frac{2R_{er}(u)}{c}} \cdot e^{-j2\pi\left(\gamma \frac{2R_{er}(u)}{c}\right)t} \cdot e^{j\pi\gamma\left(\frac{4R_{er}(u)\left(2R_i(u)+R_{er}(u)\right)}{c^2}\right)} \quad (5.1)$$

Here, the second term is both a fast and slow-time dependent error whereas the first and third terms are only slow-time dependent. These three terms are represented by $\Phi_1(u)$, $\Phi_2(t,u)$, $\Phi_3(u)$, respectively. The contribution of $\Phi_3(u)$ is generally low enough to neglect it. The main phase error is caused by $\Phi_1(u)$, whereas $\Phi_2(t,u)$ results in range walk error in the image.

5.2.1 Positional Data Based MoCo

In the first step, GPS/INS data is used for coarse MoCo. At first, as explained in Chapter 3, most of the range walk error is corrected using $\Phi_2(t,u)$, referenced to the scene centre, by exploiting the shift theorem. Next, the phase error, $\Phi_1(u)$, is compensated on the range-compressed data as shown in Figure 5.2. The third term, $\Phi_3(u)$, is low and negligible because γ/c^2 is very small. Also, the Doppler centroid is estimated and then shifted to zero Doppler. It is worth noting that the phase error function generated using the GPS/INS data cannot be used to compensate the range dependent errors as in the two-step MoCo [16] due to the low accuracy

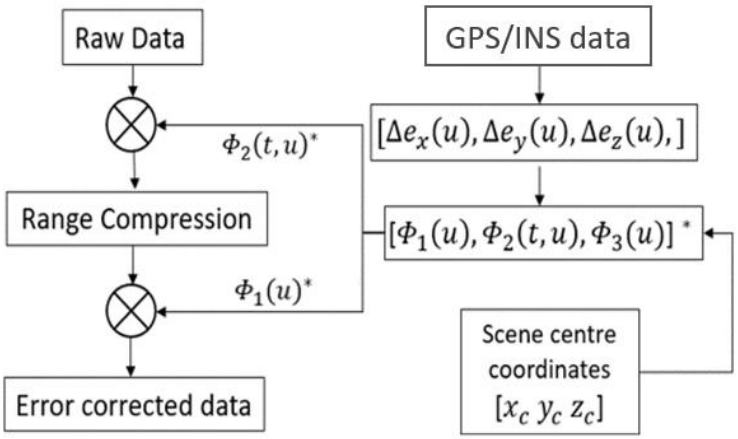

Figure 5.2 GPS/INS based MoCo.

of GPS/INS. At the end of this stage, although less than $s_e(t,u)$, the error function, $\tilde{s}_e(t,u)$, still includes both phase error and range walk error. The range compressed signal after positional data based MoCo can be written as:

$$\tilde{s}(f_r,u) = \int_{-\frac{T_m}{2}}^{\frac{T_m}{2}} \tilde{s}_i(t,u) \cdot \tilde{s}_e(t,u) \cdot e^{-j2\pi f_r t} dt \tag{5.2}$$

where $\tilde{s}_i(f_r,u)$ represents the ideal range compressed signal and f_r represents range frequency. The slant range, r, can be expressed as $cf_r/2\gamma$.

5.2.2 Space-Invariant Phase Error Estimation

In the second step, the residual space-invariant phase error is estimated in a similar way with LQMD as explained in Section 3.1.3. However, before autofocusing, more suitable parts of the data must be determined for the error estimation process. This is because the antenna footprint is small, and there are limited prominent targets within the beam. Firstly, the positions of prominent/strong targets are determined in the coarse image generated after positional data based MoCo. The range history of each target is limited by the target's location and the beamwidth of the antenna. The length of the target's range history in azimuth, L_t, is given as:

$$L_t = 2R_0 tan(\theta/2) \tag{5.3}$$

where θ is beamwidth of the antenna.

When targets are selected from a particular range, at least N_t targets, uniformly distributed along azimuth direction must exist. However, in most cases, strong targets are randomly distributed. To enhance the phase error estimation, targets' range histories are windowed, and other parts of the data are set to 0. This is achieved by multiplying the data, $\tilde{s}(f_r,u)$, by the

window matrix, w_e, which has the same size as $\tilde{s}(f_r, u)$ and consist of ones and zeros depending on the targets' positions and L_t. However, there must be at least one range sample which is different from zero for each azimuth bin.

$$N_t = \frac{vu_a}{L_t} \tag{5.4}$$

Subsequently, LQMD is implemented as explained in Section 3.1.3. As a summary, the data is divided into half overlapped, N_b, azimuth blocks (3.6) and, each block is dechirped as:

$$s_{ab}(f_r, u) = w_e \cdot \tilde{s}(f_r, u) \cdot e^{j\pi \frac{2v^2\left(u - \frac{(nu_{s_l} - u_a)}{2}\right)^2}{\lambda r}} \tag{5.5}$$

where $\frac{(n-1)u_{s_l} - u_a}{2} \leq u < \frac{(n+1)u_{s_l} - u_a}{2}$, s_{ab} is the de-chirped signal for each azimuth block and n is nth (n $= 1, 2, \cdots, N_b$) azimuth block.

The dechirped blocks are divided into two parts, and each part converted into the Doppler domain. In this way, two local intensity images are generated. In the presence of phase errors, the peak position of the cross-correlation of the two intensity images is shifted as given in (3.10). The resulting shift is a measure of the Doppler rate. Doppler rates of all azimuth blocks constitute a vector, which gives the second derivative of the phase error function. When a double integration is applied to this vector the phase error function, $\emptyset_{LQMD}(u)$ is obtained.

As shown in Section 3.1 and in (5.6), the estimated phase error is used first to correct range walk error in the range-time domain, then to compensate the phase error in the range-frequency domain. The correction functions are formed using $\Phi_1(u)$ and $\Phi_2(t, u)$ in (5.1).

$$\tilde{s}_{MD}(f_r,u)=\left(\int_{-\frac{T_m}{2}}^{\frac{T_m}{2}} x(t,u)\, e^{-j2\pi f_r t}dt\right)e^{j\emptyset_{LQMD}(u)} \tag{5.6}$$

where $x(t,u)=\left(\int_a^b \tilde{s}(f_r,u)\, e^{j2\pi f_r t}df_r\right)e^{\left(j\frac{\emptyset_{LQMD}(u)\gamma}{f_c}t\right)}$, a and b are minimum and maximum range frequencies, respectively.

The steps of LQMD are repeated several times to increase the accuracy of the estimation. However, in the case of the low SNR or contrast the performance of the algorithm may reduce. To overcome this issue, as reported in [17], the local images expressed by (3.8) and (3.9) in Section 3.1.3 are formed on a logarithmic scale, the dynamic range narrowed, and local centering performed.

On the other hand, $\tilde{s}_{MD}(f_r,u)$ still includes some range walk and higher order phase errors. Hence, PGA is implemented to correct the residual space-invariant errors. As shown in Section 3.1.4, PGA has four main steps which are circular shifting, windowing, phase gradient estimation and iterative phase correction. However, the aperture may need to be divided into multiple sub-apertures when it is used in stripmap mode SAR. For PGA, the process presented in Section 3.1.4 is implemented, but additionally, the window matrix, w_e, is multiplied by the range-compressed data to enhance the estimation result. As a result, the phase error estimation, $\emptyset_{PGA}(u)$, is obtained. The phase error function is applied to data in the same way as described by (5.6). The phase error corrected data is given by the following equation.

$$\tilde{s}_{PGA}(f_r,u)=\left(\int_{-\frac{T_m}{2}}^{\frac{T_m}{2}} \tilde{x}(t,u)e^{-j2\pi f_r t}dt\right)e^{j\emptyset_{PGA}(u)} \tag{5.7}$$

where $\tilde{x}(t,u)=\left(\int_a^b \tilde{s}_{MD}(f_r,u)\, e^{j2\pi f_r t}df_r\right)e^{\left(j\frac{\emptyset_{PGA}(u)\gamma}{f_c}t\right)}$.

5.2.3 Azimuth & Range Blocks Based Phase Error Estimation

After PGA autofocus, RCMC is done as described in 2.2.3.1.3. At this point, the generated image suffers from space-variant phase errors which are examined in Section 4.3.3. Therefore, the image is divided into the azimuth and range blocks, and N_{LS} local scenes are created. By implementing PGA to each local scene, the residual phase error, $\emptyset_{LS_g}(u)$, is estimated, and compensated within each local scene as

$$\tilde{s}_{LS_g}(f_r, u) = \tilde{s}_{PGA}(f_r, u) e^{j\emptyset_{LS_g}(u)} \tag{5.8}$$

where $\tilde{s}_{LS_g}$ is gth ($g = 1, 2, \cdots, N_{LS}$) phase error corrected local scene.

At this point, the data can be expressed as:

$$\tilde{s}_{LS} = \left[\tilde{s}_{LS_1},\ \tilde{s}_{LS_2}, \cdots, \tilde{s}_{LS_{N_{LS}}}\right] \tag{5.9}$$

Then, a further LQMD is applied to each range block, based on azimuth block sizes, to suppress phase discontinuities between azimuth blocks. In this way, the data, $\tilde{s}_{LSMD}(f_r, u)$, is obtained. The Fourier transform of this data, $\tilde{S}_{LSMD}(f_r, f_a)$, is multiplied by the Fourier transform of the reference function, $H(f_r, f_a)$. By taking the inverse Fourier transform of this multiplication, the focused image is produced as

$$\tilde{s}_F(f_r, u) = \int_{\frac{-f_{PRF}}{2}}^{\frac{f_{PRF}}{2}} \tilde{S}_{LSMD}(f_r, f_a) \cdot H(f_r, f_a) e^{-j2\pi f_a u}\, df_a \tag{5.10}$$

where $H(f_r, f_a) = \int_{\frac{-u_a}{2}}^{\frac{u_a}{2}} e^{j\pi \frac{2v^2u^2}{\lambda r}} \cdot e^{-j2\pi f_a u}\, du.$

5.3 Simulation

Using 36-point targets, a simulation has been implemented to examine the performance of the algorithm. The parameters used in the simulation are given in Table 5.1. The heights of the four targets are adjusted to be 5 m and the others are set at 0 m. The positional data from the real-world trial is used to generate the trajectory deviations shown in Figure 5.3(a).

In Figure 5.3(b), the range compressed data is shown. At first, positional data based MoCo is implemented as described in the previous section. The assumed positional data error in the

Table 5.1: Simulation Parameters

Operating Frequency	77 GHz
Bandwidth	1 GHz
Azimuth Beamwidth	14°
The Scene Size	$40\ m\ \times\ 36\ m$
Velocity	5 m/s
Altitude	20 m
Number of targets	36
PRF	2 kHz
Sweep Time	20 µs

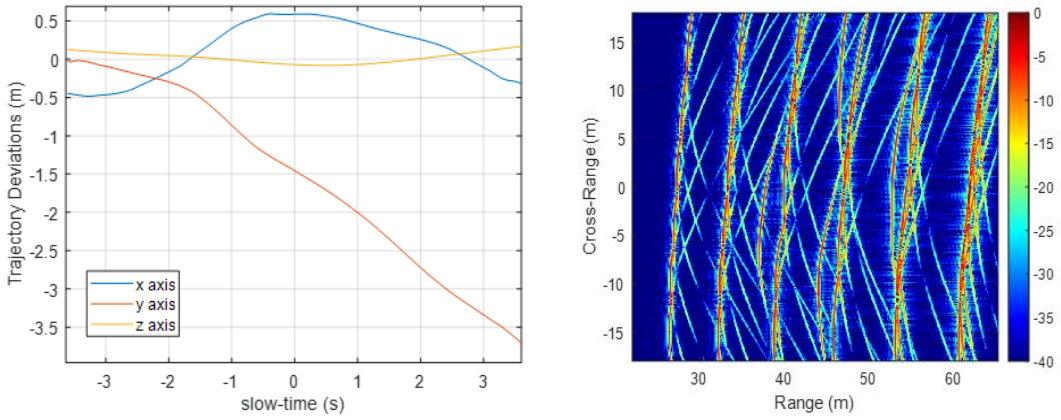

(a) (b)

Figure 5.3 (a) The given motion error. (b) Range compressed data.

simulation is demonstrated in Figure 5.4(a). The calculated phase error using equation (4.20) is shown in Figure 5.4(b). After range walk error correction and phase error compensation, the prominent targets must be selected from within the coarse image. Here, although all the targets have the same quality, only the four targets which have a 5 m height are chosen to show the impact of the targets' height on the autofocus process. A coarse image is generated with a 20 cm azimuth resolution as shown in Figure 5.4(c). Selected targets are shown in the yellow

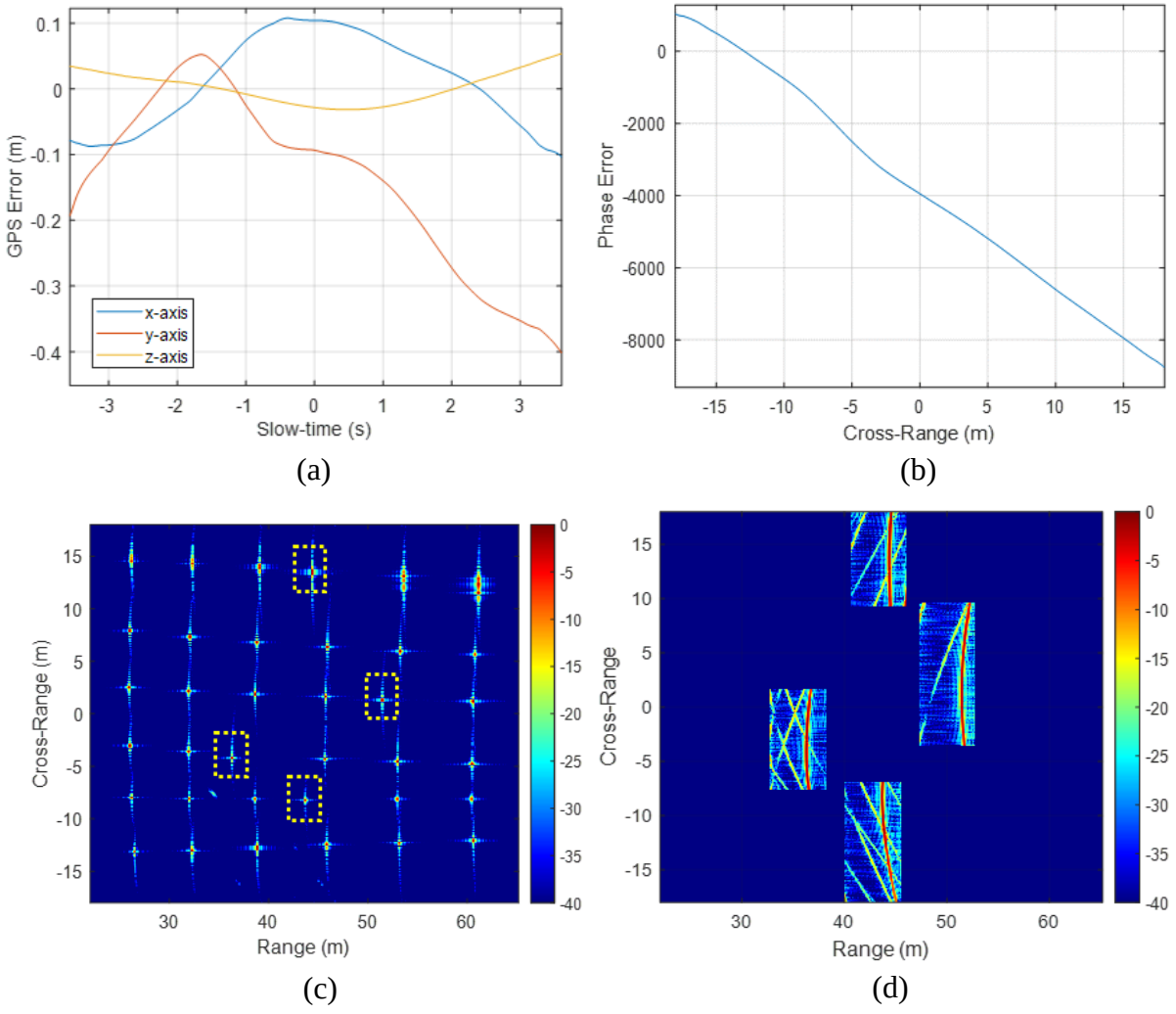

Figure 5.4 (a) GPS/INS error. (b) The phase error calculated using GPS/INS data. (c) The coarse image after GPS/INS based MoCo. (d) The data after multiplication with the window matrix, w_e.

rectangles. Using the location of the selected targets and the footprint of the beam, the window matrix, w_e, is created as described in the previous section. The range compressed data becomes as illustrated in Figure 5.4(d) after the windowing operation.

The space-invariant phase error estimation is made using this data set. For the LQMD autofocus, the data is divided into 18 half-overlapped azimuth blocks. Then, the steps described in Section III are repeated. The estimated result is subsequently shown in Figure 5.5(a). Using (5.6), range-walk is corrected, and the phase error is compensated based on the estimation result.

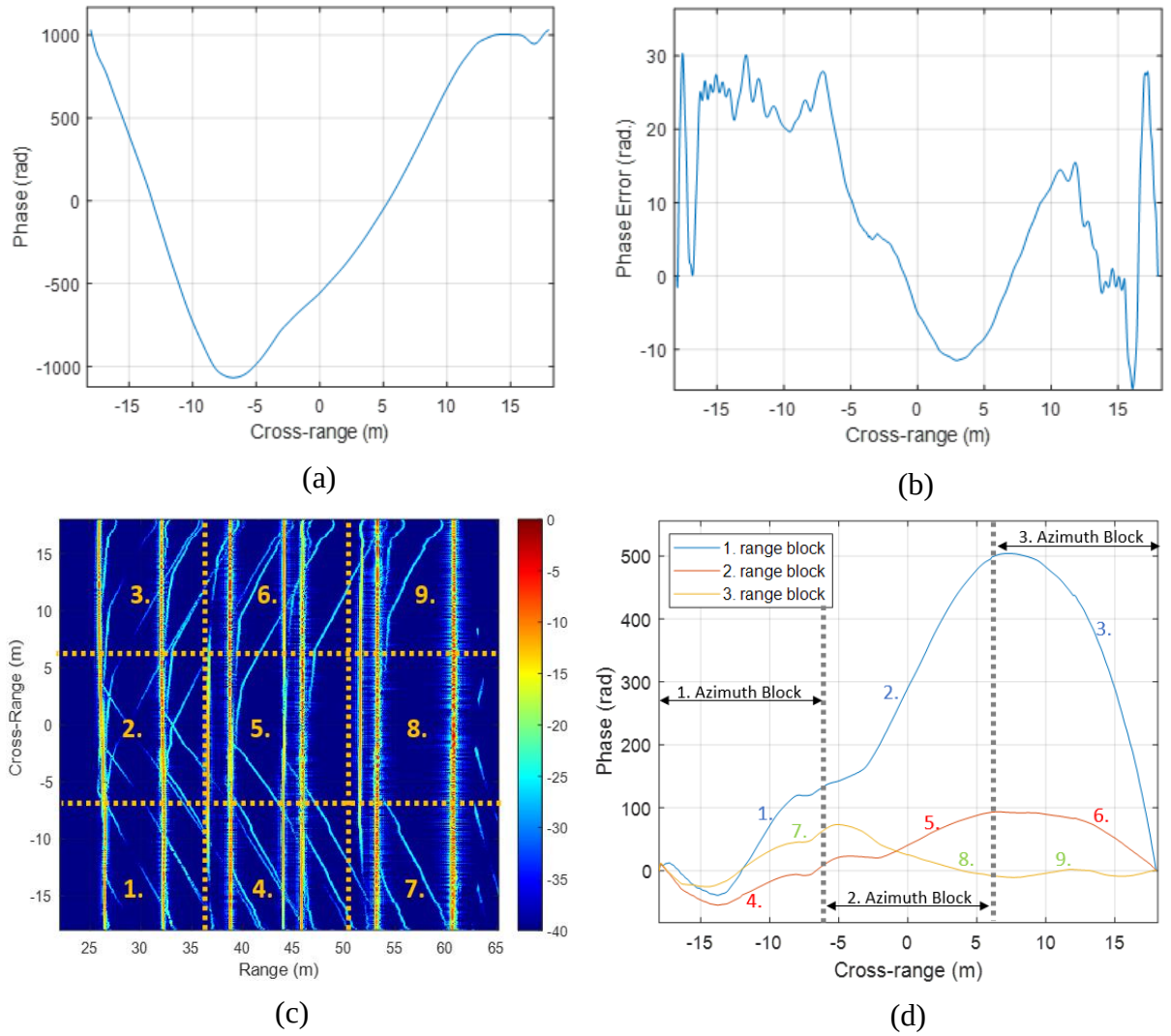

Figure 5.5 (a) LQMD phase error estimation. (b) PGA phase error estimation. (c) The azimuth/range blocks. (d) Estimated phase errors in each block.

The residual space-invariant phase error is estimated by PGA and as illustrated in Figure 5.5(b). In the PGA step, the data is not divided into azimuth blocks because the PRF is chosen to be high enough to avoid aliasing. After compensating the residual range-walk and phase errors, the RCMC step is completed. At this point, the obtained image is shown in Figure 5.6. After RCMC, the scene is divided into three azimuth and three range blocks as shown in Figure 5.5(c). As seen, nine local scenes are created. At first, PGA is applied to each local scene. Then, by implementing LQMD to each range block, the phase corrected data is obtained without discontinuities in the cross-range direction. The estimated phase errors from 9 local scenes by

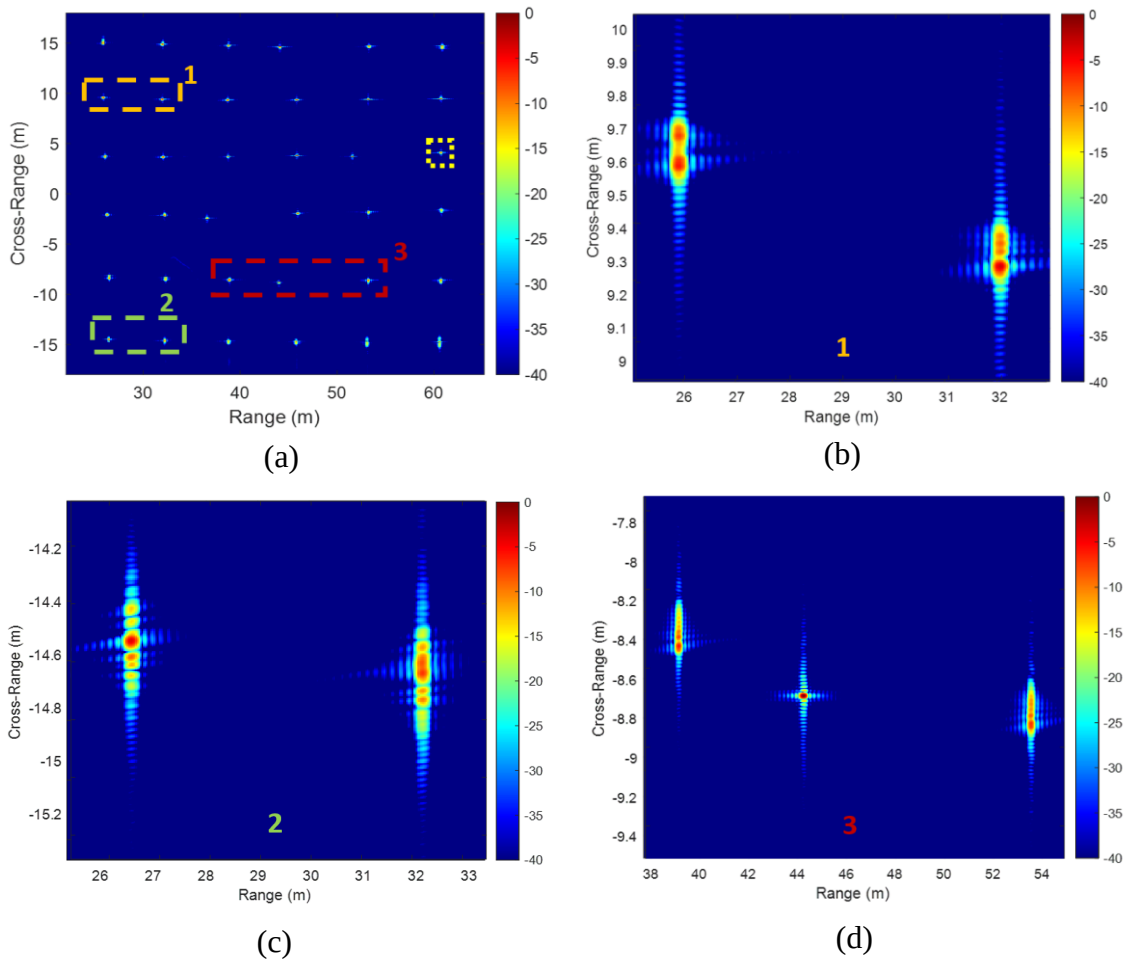

Figure 5.6 (a) The obtained image after RCMC step. (b) The first local scene shown in orange rectangle in (a). (c) The second local scene shown in green rectangle in (a). (d) The third local scene shown in red rectangle in (a).

PGA are shown in Figure 5.5(d) after removing discontinuities in the cross-range direction by LQMD.

The result obtained after azimuth compression is shown in Figure 5.7. This result is compared with the image obtained after the RCMC step (Figure 5.6). Most of the targets in the image shown in Figure 5.6 is not focused especially well. However, after azimuth/range-block based phase error compensation, most of the remaining residual errors are eliminated, and a 2 cm resolution is achieved (Figure 5.7). As an example, one of the target's cross-range profiles

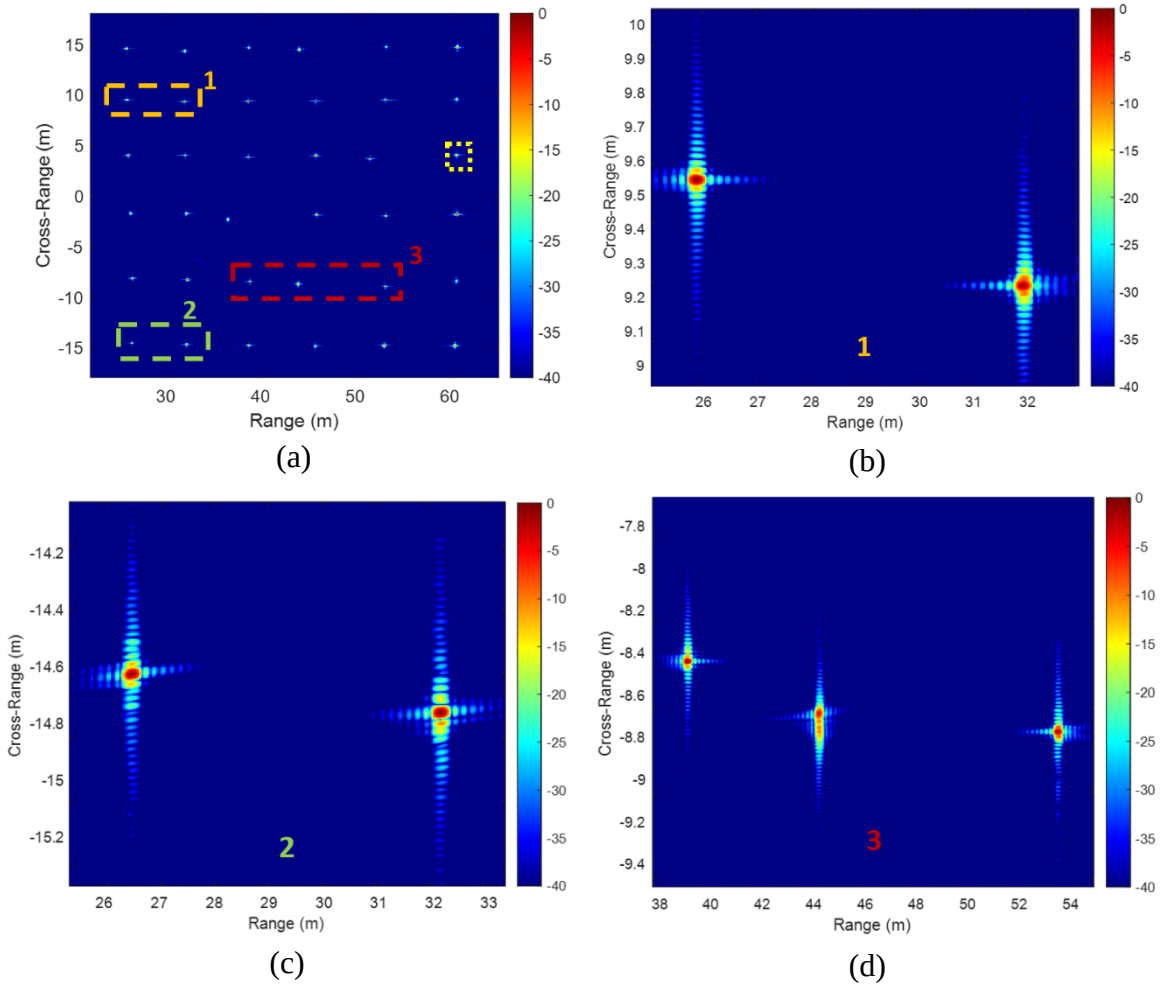

Figure 5.7 (a) The final image. (b) The first local scene shown in orange rectangle in (a). (c) The second local scene shown in green rectangle in (a). (d) The third local scene shown in red rectangle in (a).

is shown at different processing stages in Figure 5.8. Also, when the three targets in the red rectangle are examined, it is seen that whereas the target at the mid-point is focused, the others are unfocused in Figure 5.6(d). The main reason for this is the height difference amongst the targets. The first and the third targets have a height of 0 m and the second target has a height of 5 m. The phase error was estimated using the second target, so no focusing problem is observed related to this target. However, the others do have significant phase errors.

After phase compensation within the local scenes, some focusing problems still exist in the area shown by the red rectangle in Figure 5.7 due to the height difference between targets. However, here, the second target is unfocused whereas others are focused. This is because the number of targets having 0 m height is more in the local scenes, so they contribute more to the phase error estimation. The only way to correctly focus all three targets at the same time is to create separate local scenes for each target. Nevertheless, reducing the range block size is not always useful for real-world implementation. As a result, the target's height plays an important role in phase error estimation and compensation. Even low target height differences cause focusing problems. Therefore, compensating phase errors globally is highly difficult without

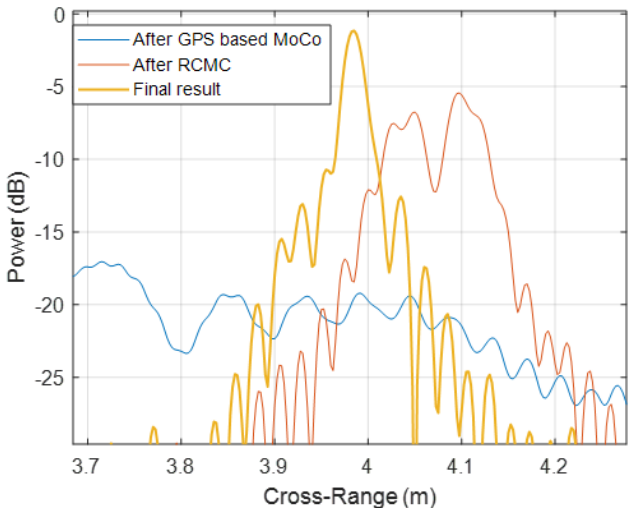

Figure 5.8 Cross-range profile of the target in the yellow rectangle in Figure 5.6 and 5.7.

knowing or estimating targets' heights. Our aim here is to produce correctly focused SAR images by compensating phase errors as much as possible within local scenes which have less target height variation without considering height-dependent errors.

5.4 Experimental Results

A SAR system was formed by using 24 and 77 GHz radars mounted on a DJI S900 drone together with an A3 flight controller, and a Raspberry-Pi microcontroller as detailed in Chapter 4. The overall cost of the system is roughly £15K. The radar is controlled by a laptop remotely via the Raspberry-Pi. The Pi also stores the radar raw data and the GPS/IMU data. The max data transfer speed between the radar and the Raspberry-Pi is approximately 300 Mbps. The IMU refresh rate is 40 Hz and the GPS update rate is 10 Hz. The resulting positional accuracy is between 0.5 m and 1 m. The drone-borne SAR system is shown in Figure 5.9 whereas the radar parameters of the system are given in Table 5.2.

Figure 5.9 Drone-borne SAR system.

Table 5.2: Radar Parameters of the System

Parameters	24 GHz	77 GHz
Bandwidth	0.5 GHz	0.5 – 1 GHz
Azimuth Beamwidth	12.6°	13.2°
Elevation Beamwidth	76.5°	51°
Tx/Rx Antenna gains	13.2 dBi	16 dBi
Transmit Power	8 dBm	10 dBm
Transmit and Receive Channels	2-Tx, 8-Rx	4-Tx, 8-Rx
Noise Figure	~10 dB	~12 dB
System Losses	~3 dB	~ 3 dB
Weight	0.41 kg	0.41 kg
Look Angle	60°	60°

In this section 2 different experimental results are shown. The first one is the experiment carried out by employing the 77 GHz radar with the 1 GHz bandwidth. In this scenario, less than 2 cm resolution is achieved. In the second experiment, the 24 GHz radar with a 500 MHz bandwidth is used, and a 6 cm resolution is obtained.

5.4.1 Experiment with 77 GHz radar

In this scenario, the scene size is 67 m in azimuth and 43 m in the down-range direction. Experiments were carried out at Deenethorpe Airfield in the United Kingdom setting the bandwidth of the radar to 1 GHz, giving a nominal range resolution of 15 cm. The experimentation site is shown in Figure 5.10(a). The photo was taken from a camera on the drone during flight. The drone was flown at an altitude of 20 m at a speed of 5 m/s.The image before any MoCo is displayed in Figure 5.10(b). As can be observed, the signal-to-noise ratio (SNR) is rather low, and the image is poorly focused. The smoothed GPS record is shown in Figure 5.11(a). Only the GPS record is used because using IMU/INS data does not improve the result significantly. The calculated phase error using (4.20) is illustrated in Figure 5.11(b) where the linear phase error has been compensated. After the GPS based MoCo and Doppler centroid

(a)

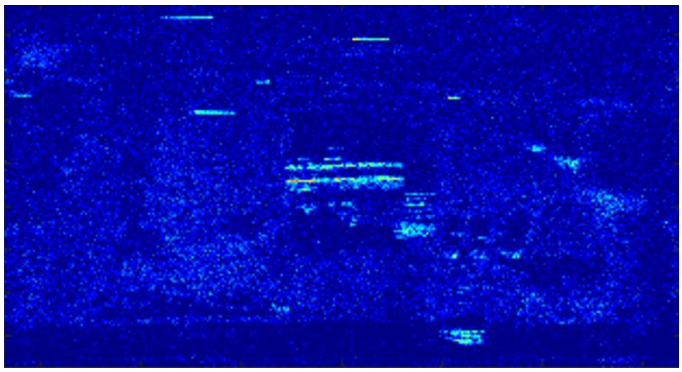

(b)

Figure 5.10 (a) A picture from the experimentation site. (b) The image without MoCo.

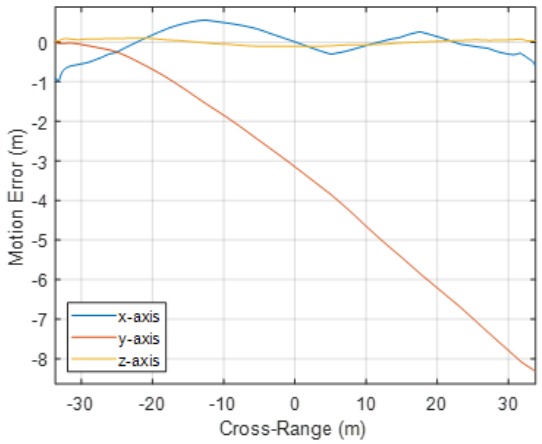

(a)

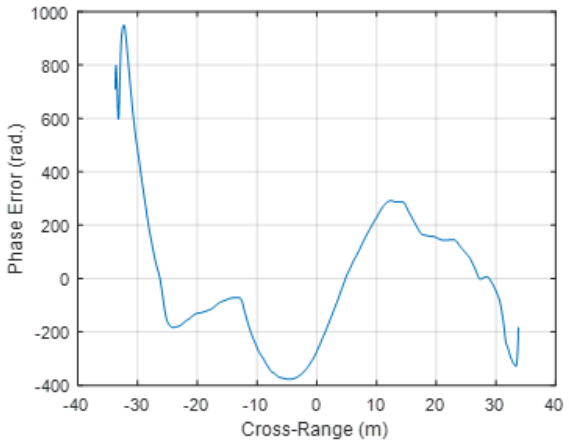

(b)

Figure 5.11 (a) GPS measured deviation from the ideal sensor track. (b)The phase error according to GPS without the linear term.

steps (shown in Figures. 5.1 and 5.2) the range compressed data shown in Figure 5.12(a) is obtained. Further, a Kaiser weighting is applied in the range dimension to reduce sidelobes. The resulting image can be seen in Figure 5.13(a). In this image, 14 prominent targets shown in orange circles are selected. According to the location of the selected targets and the beam footprint size, the window matrix, w_e is created as described in Section 5.2. This windowed range compressed data is shown in Figure 5.12(b) after multiplication by w_e. In this figure, the selected targets' range histories can be seen. The space-invariant phase error estimation is done using this data. In the LQMD step, 60 half-overlapped azimuth blocks are created, and steps described in Chapter 3 are implemented. The range walk and phase errors are corrected using equation (5.6). After four iterations, the phase error is estimated as that shown in Figure 5.14(a).

After LQMD, PGA is implemented to compensate residual higher order errors. The PRF is chosen to be 2 kHz. As seen from equation (3.20), PGA cannot be implemented directly. By considering the windowed data, three half-overlapped sub-apertures are created so that aliasing is avoided. After de chirping the data, PGA steps are applied as per Section 3.1.4.

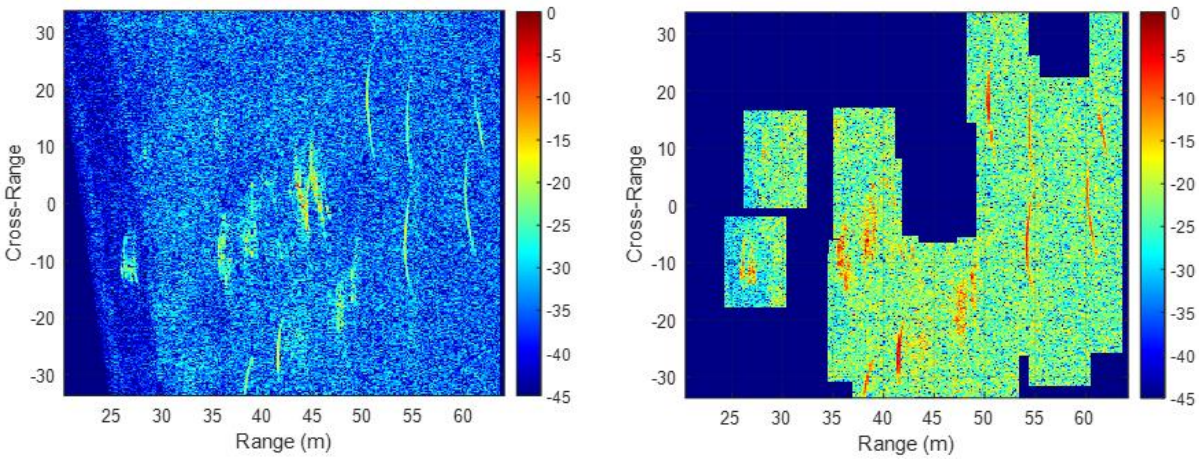

(a) (b)

Figure 5.12 (a) The range compressed data after GPS based MoCo. (b) The data after multiplication with the window matrix, w_e.

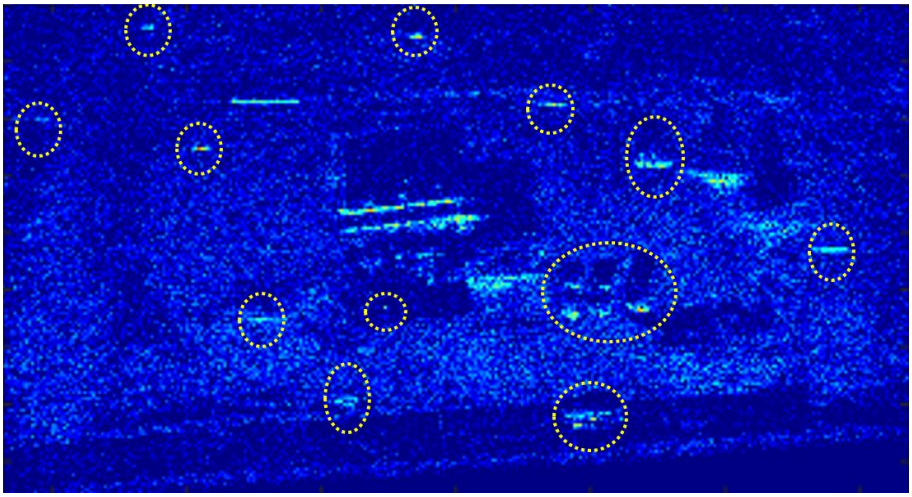

(a)

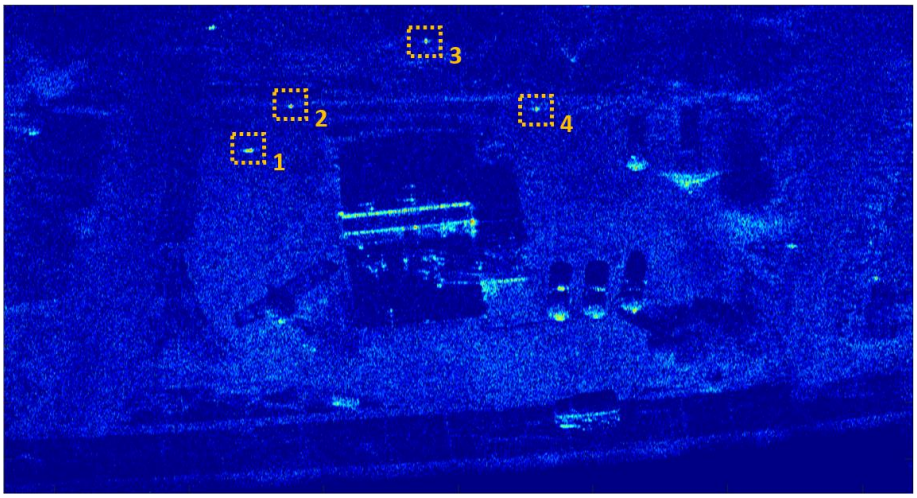

(b)

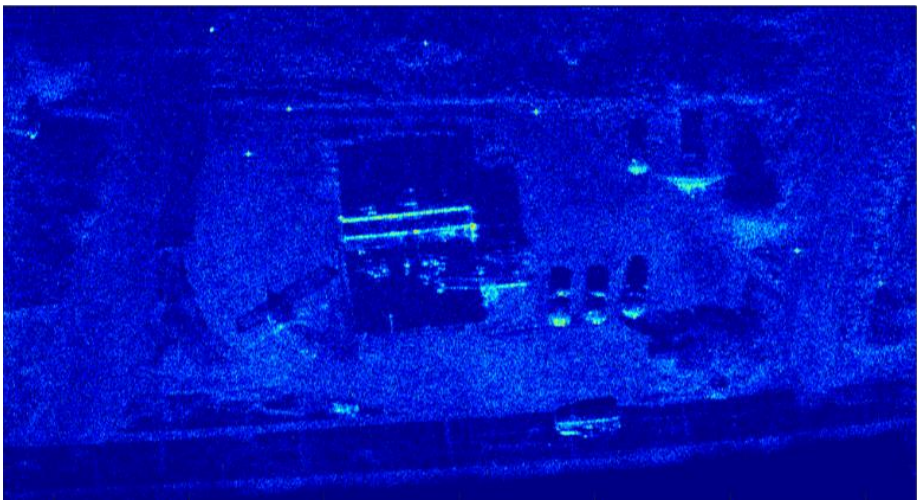

(c)

Figure 5.13 (a) The image with MoCo using GPS data. (b) The image after the RCMC step. (c) The final image after azimuth and range blocks based MoCo.

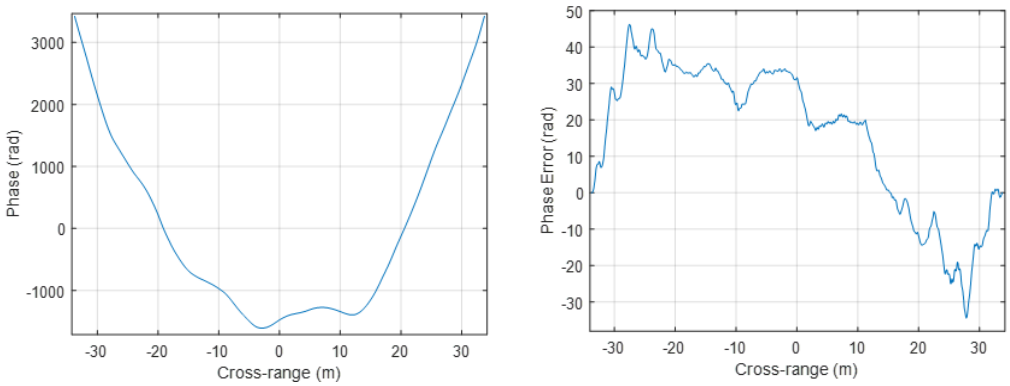

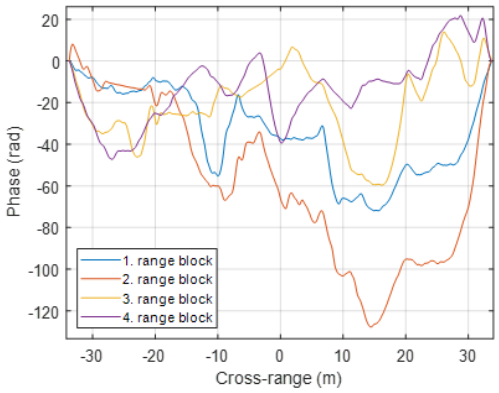

(c)

Figure 5.14 (a) LQMD phase error estimation. (b) PGA phase error estimation. (c) Estimated phase errors in each azimuth and range blocks by PGA after reducing discontinuities in the cross-range direction by LQMD.

The estimation result is shown in Figure 5.14(b). Again, the range-walk and phase errors are corrected as in (5.7). As can be seen, LQMD estimates high magnitude but low frequency phase errors, whereas PGA estimates low magnitude but high frequency phase errors. In this way LQMD and PGA complement each other well. Figure 5.13(b) shows the formed image after space-invariant error compensation and the RCMC step. Here, the image structures and individual objects start to become much better defined, along with shadows that they cast. However, this image is still not in perfect focus at all pixels. In order to compensate remaining phase errors, the image is divided into 5 azimuth and 4 range blocks. As a result, 20 local scenes are generated, and PGA is implemented on each one. Following this step, LQMD is

implemented to each range block to decrease discontinuities between azimuth blocks. Here, local images are translated onto a logarithmic scale and hence the dynamic range is narrowed to improve the phase error estimation (as explained in Section 5.2.2). After reducing discontinuities in the cross-range direction by LQMD, the estimated phase error from each local scene by PGA is illustrated in Figure 5.14(c). After phase error compensation, the image shown in Figure 5.13(c) is formed by azimuth compression. Resolutions of 1.7 cm cross-range and 16 cm down-range are obtained verified through measurement of the response from point targets. When Figure 5.13(b) and Figure 5.13(c) are compared with each other, it seems that there is no significant difference between them, at first glance. However, if the corner reflector shown in the 1st rectangle in Figure 5.13(b) is compared with that of Figure 5.13(c) the difference can be seen clearly. This comparison is demonstrated in both Figure 5.15 and Figure 5.16(a). In addition, the cross-range profiles of the other two corner reflectors in the 2nd and 3rd rectangles are shown in Figure 5.16(b) and 5.16(c), respectively. As seen, azimuth and range blocking based autofocus improves the overall image quality. The other corner reflector in the 4th rectangle is well focused in both images (Figure 5.16(d)). There is only a linear shift between them.

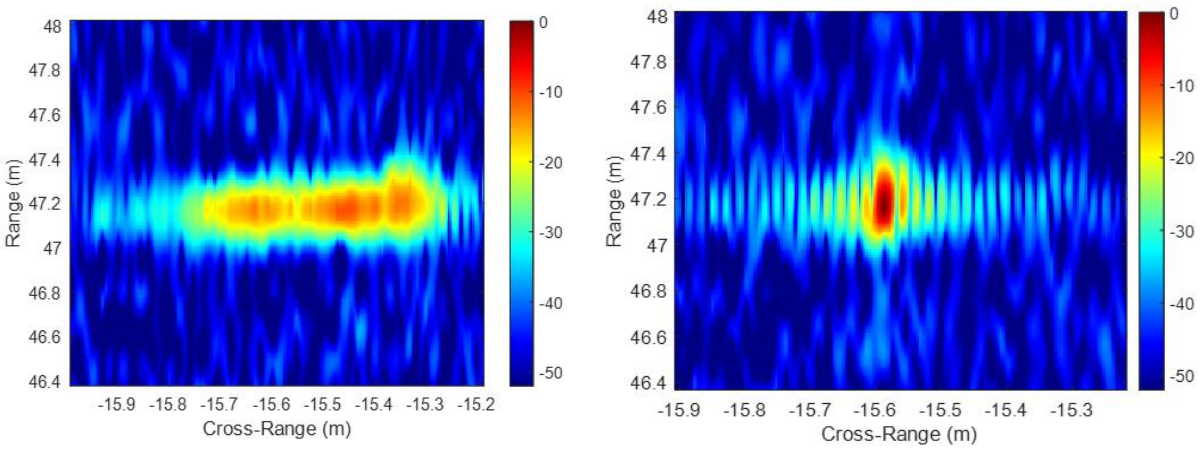

(a) (b)

Figure 5.15 (a) The corner reflector shown in the 1st rectangle in Figure 5.13 (b). (b) The same corner reflector in the final image (Figure 5.13 (c)).

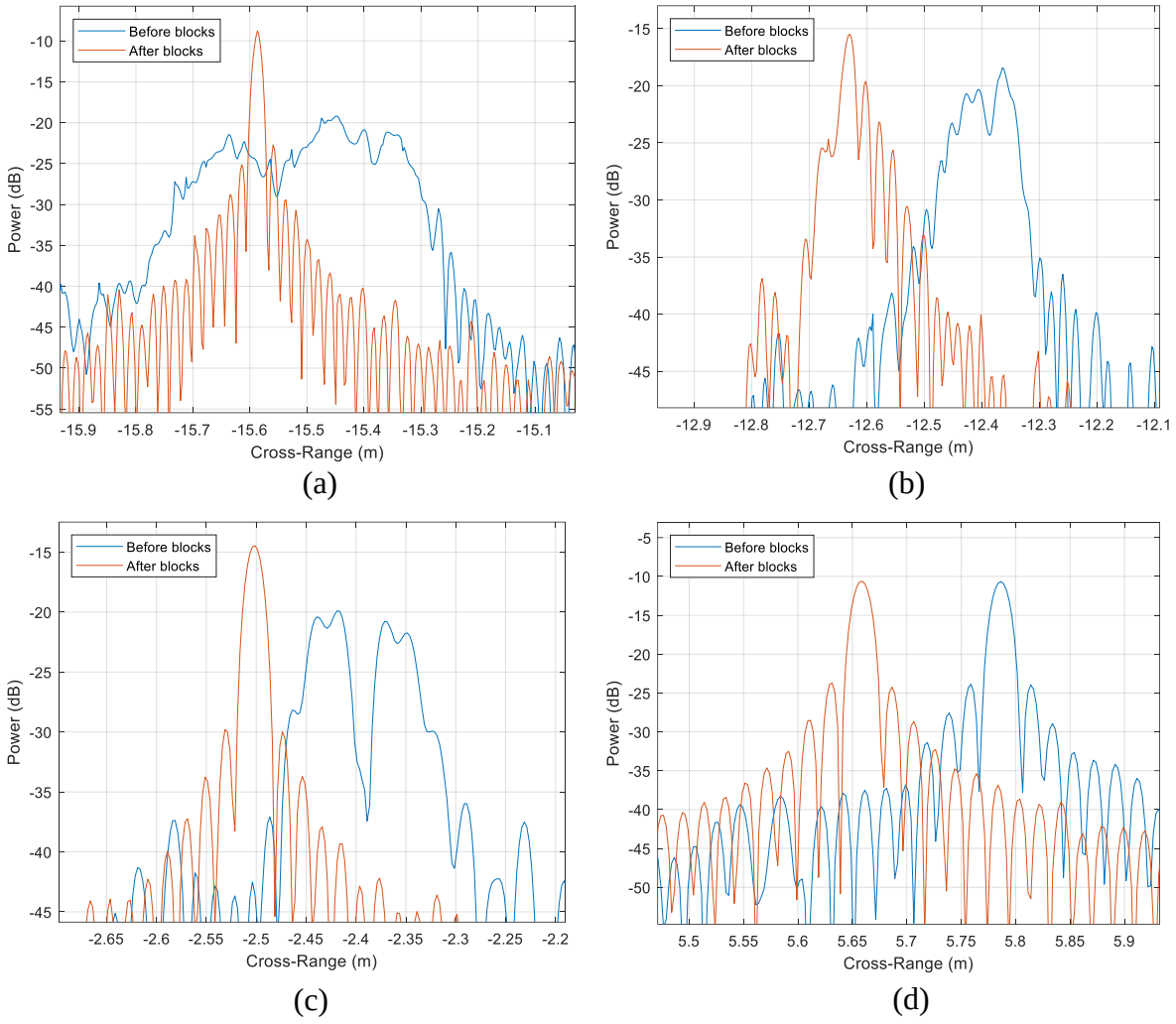

Figure 5.16 Comparison of the corner reflectors in the dashed rectangles shown in Figure 5.13(b) with Fig 5.13 (c). (a). The 1st reflector. (b) The 2nd reflector. (c) The 3rd reflector. d) The 4th reflector.

In Figure 5.13, it can be seen that there is a very good correspondence between the optical image and the SAR images. The cars, motorbike, roads and cracks on the roads can be easily observed in the SAR image. Due to low reflections from the aircraft, it is a little indistinct, but the radar shadow of the aircraft is obvious.

5.4.2 Experiment with the 24 GHz radar

This experiment was carried out at the University of Birmingham campus in the United Kingdom. A photograph of the experiment site is shown in Figure 5.17. A bandwidth of 500 MHz was used with the 24 GHz radar. The same drone was flown at an altitude of 20 m at a speed of 5 m/s. The scene size is around 50 m in azimuth and 110 m in the range direction.

As a first step, the measured motion deviation from the nominal trajectory by the GPS is smoothed as shown in Figure 5.18(a). The calculated phase error is illustrated in Figure 5.18(b).

Figure 5.17 A picture from the experiment site.

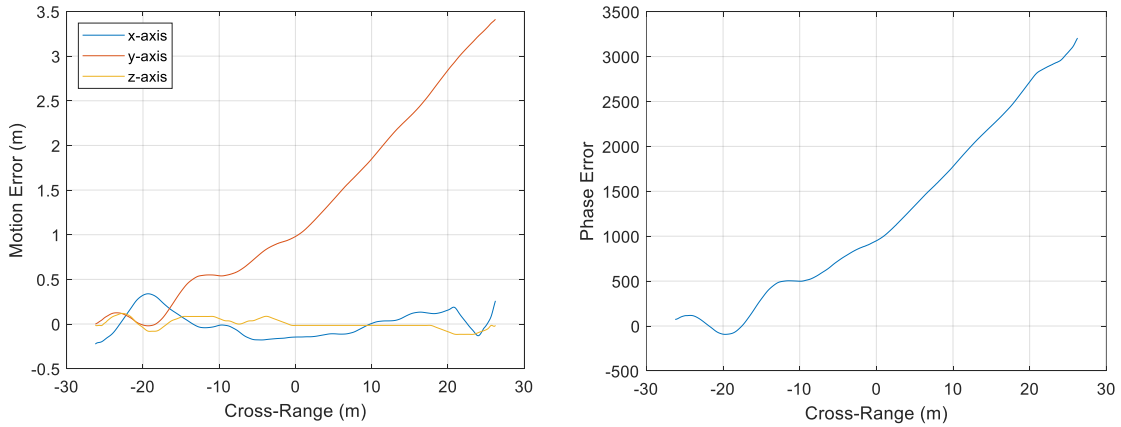

(a) (b)

Figure 5.18 (a) Motion error from GPS. (b)The phase error according to GPS.

By using this motion error, majority of range walk is corrected before the phase error compensation is applied, using the method described in Section 3.1.2.

In the second step, LQMD and PGA are implemented, respectively. In this scenario, window matrix chooses the half of the image (left part) which has more prominent, point-like, targets such as lamp-posts, pipes, or corner-type reflectors, to increase the space-invariant phase error estimation accuracy. The phase error estimation results are shown in Figure 5.19(a) and

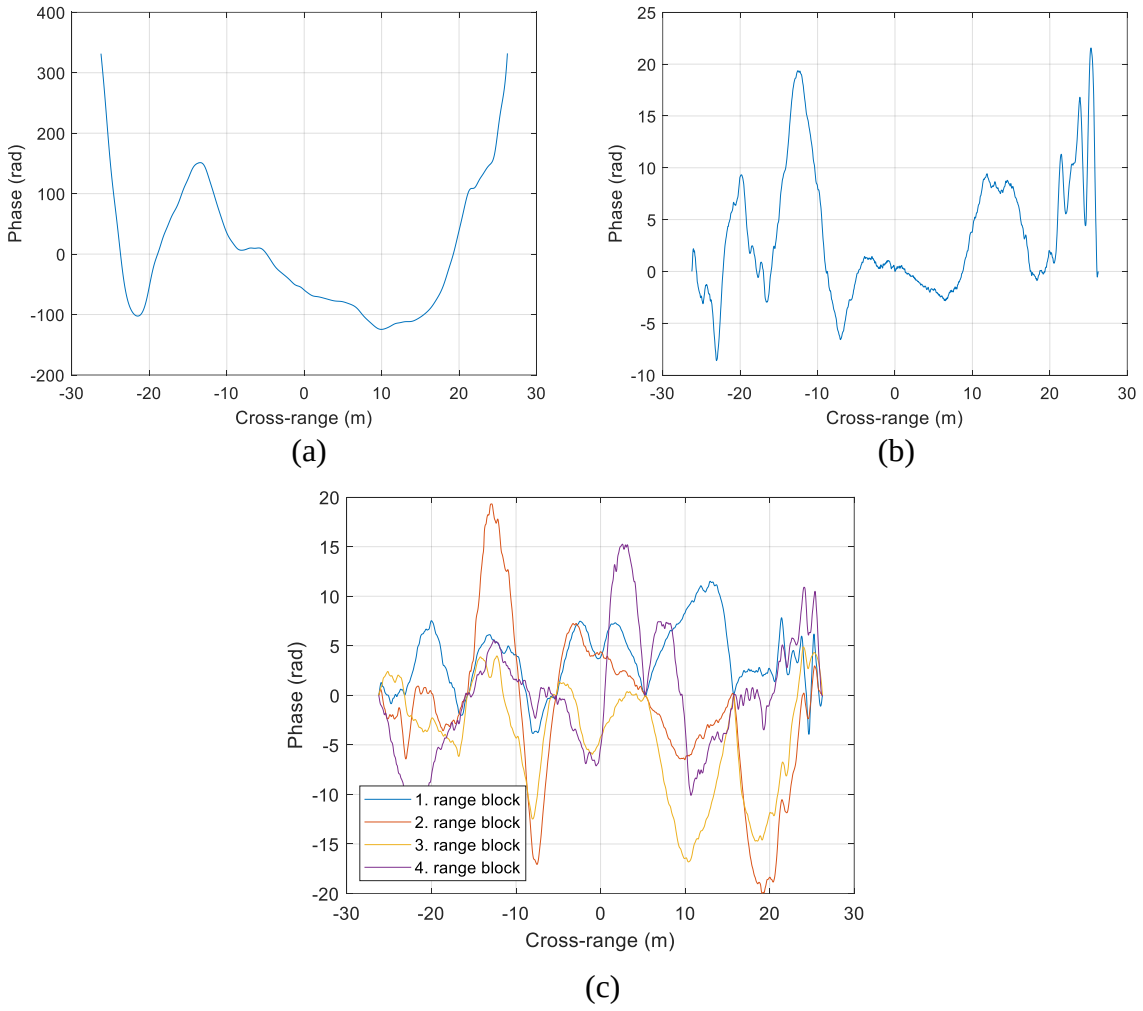

Figure 5.19 (a) LQMD phase error estimation. (b) PGA phase error estimation. (c) Estimated phase errors in each azimuth and range blocks.

(b). As can be seen, it is validated again that LQMD estimates high magnitude but low-frequency phase errors whereas PGA estimates low magnitude but high-frequency phase errors. After the RCMC step, the image is divided into 6 azimuth and 4 range blocks. As a result, 24 local scenes are generated, and PGA is implemented to each.

The estimated phase errors are shown in Figure 5.19(c). After phase error compensation for each local scene, an image is formed by azimuth compression. Also, a Kaiser window is used in both the range and azimuth dimensions.

The obtained results, after each step, are shown in Figure 5.20. As can be seen, image quality is improved with each step. In Figure 5.20(a) the image without MoCo is shown. The signal-to-noise ratio (SNR) is very low, and the image is severely defocused. Also, it is shifted in azimuth due to the non-zero Doppler centroid. The image after GPS based MoCo is demonstrated in Figure 5.20(b). The SNR increases and a coarse image is obtained. In Figure 5.20(c), the image after LMD and PGA based MoCo is shown. Here, the image structures and objects start to become apparent. However, it still suffers from defocusing. The final image, obtained after the blocking stage, is illustrated in Figure 5.20(d). Resolutions of 6 cm azimuth and 32 cm down-range are obtained. The responses of the two corner reflectors, the yellow dashed rectangle in Figure 5.20(d), are shown in Figure 5.21.

There is a very good agreement between the optical and the SAR images. The pipes, lamp-posts, fence, gate, buildings, and cars can be easily observed in the image. Also, a truck can be seen at the top (centre) of the image. Additionally, it is seen that the image quality difference among the local scenes (due to azimuth/range blocks) is low and acceptable.

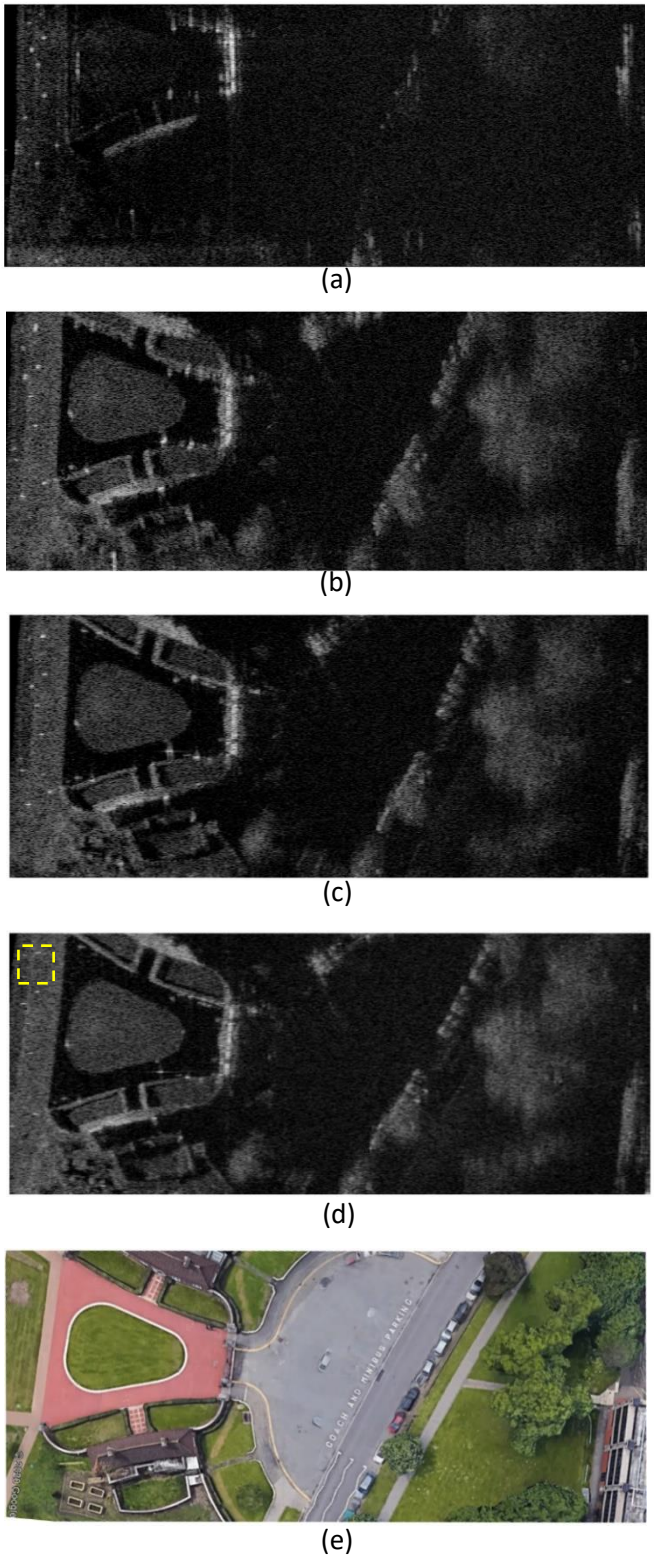

Figure 5.20 The 24 GHz results. (a) The image without MoCo. (b) The image with MoCo using only GPS data. (c) The image after LQMD+PGA autofocus. (d) The image after azimuth and range blocks phase compensation. (e) Google Earth image of the experiment site.

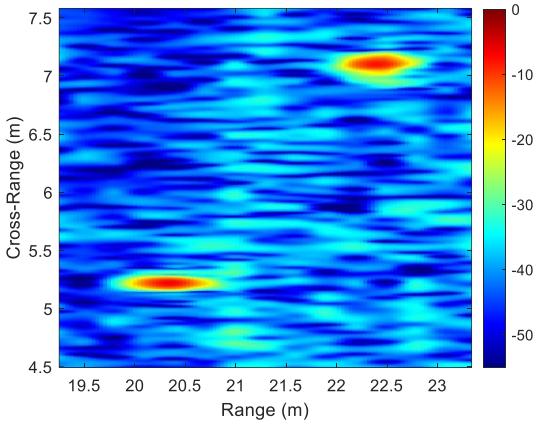

(a)

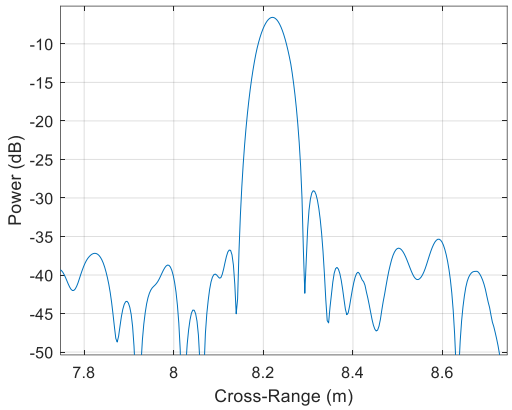

(b)

Figure 5.21 (a) Corner reflectors shown in the yellow rectangle in Figure 5.20 (d). (b) Azimuth profile of the below reflector shown in (a).

It is worth noting that an additional LQMD is not applied to each range-block before azimuth compression in this scenario. That is because the spatial resolution is lower, and discontinuities do not have a significant impact on the image quality.

Another image shown in Figure 5.22(b) is formed by using the same parameters. Then, it is co-registered with the image shown in Figure 5.20(d) by using the intensity-based registration algorithm which will be explained in Chapter 6. As shown, larger areas can be imaged by combining formed drone-borne SAR images.

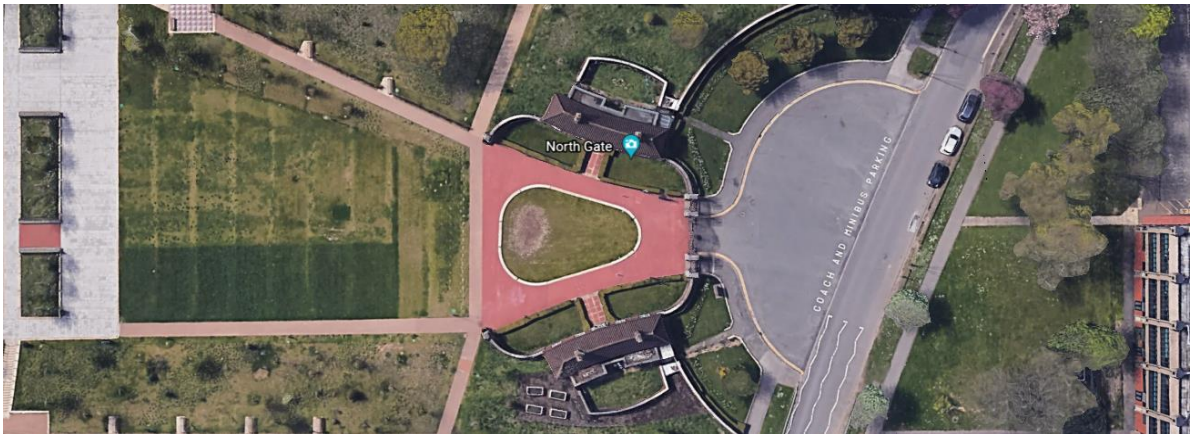

(a)

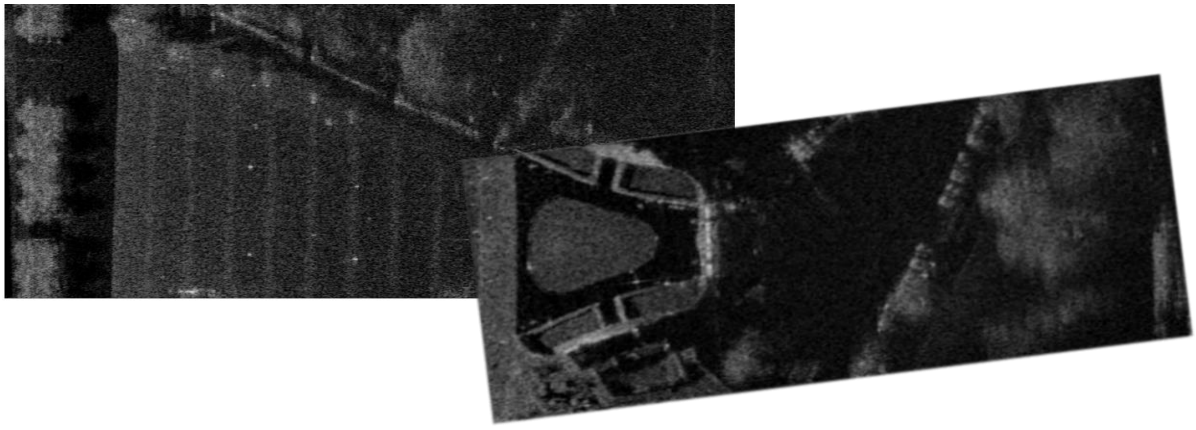

(b)

Figure 5.22 (a) Imaged area. (b) Co-registered drone-borne SAR images.

5.5 Summary

In this chapter, we have shown, for the first time, that a cross-range resolution of less than 2 cm can be achieved using a low-cost high-frequency vehicular radar mounted onboard a low-cost commercially available drone at short but highly useful ranges. An algorithm suitable for production of high-resolution imaging at 24 and 77 GHz has been developed. The performance of the algorithm has been validated through both simulation and experiments. Although this particular MoCo strategy does not compensate the phase errors perfectly over all of the imaged area, the results show practical usability at short ranges for which many applications may be envisaged. It is also noting that the presented examples result from multiple experiments conducted at different locations. In each case similar results have been obtained. On the other hand, wrong strong target selection and high target height variation in the scene can degrade the performance of the algorithm.

5.6 References

[1] M. Soumekh, Synthetic aperture radar signal processing : with MATLAB algorithms / Mehrdad Soumekh. New York ; Chichester: Wiley, 1999.

[2] Cumming I.G., Wong F.H. (2005), Digital processing of Synthetic Aperture Radar data, Artech House.

[3] M. García Fernández *et al*., "Synthetic Aperture Radar Imaging System for Landmine Detection Using a Ground Penetrating Radar on Board a Unmanned Aerial Vehicle," in *IEEE Access*, vol. 6, pp. 45100-45112, 2018, doi: 10.1109/ACCESS.2018.2863572.

[4] M. Garcia-Fernandez, Y. Alvarez-Lopez, B. Gonzalez-Valdes, Y. Rodriguez-Vaqueiro, A. Arboleya-Arboleya and F. L. Heras, "Recent advances in high-resolution Ground Penetrating Radar on board an Unmanned Aerial Vehicle," 2019 13th European Conference on Antennas and Propagation (EuCAP), Krakow, Poland, 2019, pp. 1-5.

[5] E. Schreiber, A. Heinzel, M. Peichl, M. Engel and W. Wiesbeck, "Advanced Buried Object Detection by Multichannel, UAV/Drone Carried Synthetic Aperture Radar," 2019 13th European Conference on Antennas and Propagation (EuCAP), Krakow, Poland, 2019, pp. 1-5.

[6] M. Schartel, R. Bähnemann, R. Burr, W. Mayer and C. Waldschmidt, "Position Acquisition for a Multicopter-Based Synthetic Aperture Radar," 2019 20th International Radar Symposium (IRS), Ulm, Germany, 2019, pp. 1-7, doi: 10.23919/IRS.2019.8768172.

[7] Y. A. Su, W. Liu, H. Feng and B. P. Ng, "Study of multi-rotor UAV SAR processing," 2017 IEEE Radar Conference (RadarConf), Seattle, WA, 2017, pp. 0226-0232, doi: 10.1109/RADAR.2017.7944202.

[8] M. Ding, C. Ding, L. Tang, X. Wang, J. Qu and R. Wu, "A W-Band 3-D Integrated Mini-SAR System With High Imaging Resolution on UAV Platform," in IEEE Access, vol. 8, pp. 113601-113609, 2020, doi: 10.1109/ACCESS.2020.3003273.

[9] M. Lort, A. Aguasca, C. López-Martínez and T. M. Marín, "Initial Evaluation of SAR Capabilities in UAV Multicopter Platforms," in IEEE Journal of Selected Topics in Applied Earth Observations and Remote Sensing, vol. 11, no. 1, pp. 127-140, Jan. 2018, doi: 10.1109/JSTARS.2017.2752418.

[10] Hu, Xianyang et al. “Imaging for Small UAV-Borne FMCW SAR.” Sensors (Basel, Switzerland) vol. 19,1 87. 27 Dec. 2018, doi:10.3390/s19010087.

[11] S. Zhou, L. Yang, L. Zhao and G. Bi, "Quasi-Polar-Based FFBP Algorithm for Miniature UAV SAR Imaging Without Navigational Data," in IEEE Transactions on Geoscience and Remote Sensing, vol. 55, no. 12, pp. 7053-7065, Dec. 2017, doi: 10.1109/TGRS.2017.2739133.

[12] X. Mao, D. Li, L. Ding, and D. Zhu, “Signal processing for multi-rotors UAV SAR,” in Proceedings of IET International Radar Conference, Nanjing, China, Oct. 2018.

[13] Z. Xu and D. Zhu, “High-resolution miniature UAV SAR imaging based on GPU Architecture,” J. Phys. Conf. Ser., vol. 1074, no. 1, p. 012122, Sep. 2018.

[14] O. O. Bezvesilniy, I. M. Gorovyi and D. M. Vavriv, "Estimation of phase errors in SAR data by Local-Quadratic map-drift autofocus," 2012 13th International Radar Symposium, Warsaw, 2012, pp. 376-381, doi: 10.1109/IRS.2012.6233350.

[15] Bezvesilniy, O., Gorovyi, I., & Vavriv, D. (2016). Autofocusing SAR images via local estimates of flight trajectory. *International Journal of Microwave and Wireless Technologies, 8*(6), 881-889. doi:10.1017/S1759078716000180.

[16] Moreira, A., Mittermayer, J., and Scheiber, R.: 'Extended chirp scaling algorithm for air- and spaceborne SAR data processing in stripmap and ScanSAR imaging modes', IEEE Trans. Geosci. Remote Sens., 1996, 34, (5), pp. 1123–1136, doi: 10.1109/36.536528.

[17] I. M. Gorovyi, O. O. Bezvesilniy and D. M. Vavriv, "A novel trajectory restoration algorithm for high-resolution SAR imaging," 2014 15th International Radar Symposium (IRS), Gdansk, 2014, pp. 1-4, doi: 10.1109/IRS.2014.6869242.

[18] D. E. Wahl, P. H. Eichel, D. C. Ghiglia and C. V. Jakowatz, "Phase gradient autofocus - a robust tool for high resolution SAR phase correction," in IEEE Transactions on Aerospace and Electronic Systems, vol. 30, no. 3, pp. 827-835, July 1994, doi: 10.1109/7.303752.

[19] D. G. Thompson, J. S. Bates, D. V. Arnold and D. G. Long, "Extending the phase gradient autofocus algorithm for low-altitude stripmap mode SAR," IEEE 1999 International Geoscience and Remote Sensing Symposium. IGARSS'99 (Cat. No.99CH36293), Hamburg, Germany, 1999, pp. 564-566 vol.1, doi: 10.1109/IGARSS.1999.773566.

[20] L. Zhang, J. Sheng, M. Xing, Z. Qiao, T. Xiong and Z. Bao, "Wavenumber-Domain Autofocusing for Highly Squinted UAV SAR Imagery," in *IEEE Sensors Journal*, vol. 12, no. 5, pp. 1574-1588, May 2012, doi: 10.1109/JSEN.2011.2175216.

[21] A. Bekar, M. Antoniou and C. J. Baker, "High-Resolution Drone-Borne SAR using Off-the-Shelf High-Frequency Radars," 2021 IEEE Radar Conference (RadarConf21), Atlanta, GA, USA, 2021, pp. 1-6, doi: 10.1109/RadarConf2147009.2021.9455342.

[22] A. Bekar, M. Antoniou and C. J. Baker, "Low-Cost, High-Resolution, Drone-Borne SAR Imaging," in IEEE Transactions on Geoscience and Remote Sensing, vol. 60, pp. 1-11, 2022, Art no. 5208811, doi: 10.1109/TGRS.2021.3085235.

Chapter 6

Change Detection for High-Frequency High-Resolution Drone-Borne SAR

6.1 Introduction

In the previous chapter, high-frequency drone-borne SAR imaging was investigated. It was shown that cross-range resolution less than 2 cm can be achievable by using multi-stage data-driven autofocus techniques. Having the capability to obtain high-resolution imaging, a natural next step is to investigate how such imagery can be exploited through advanced SAR imaging modes. In this chapter, the feasibility of the high-frequency high-resolution drone-borne SAR system is examined for SAR change detection mode.

As an important SAR mode, incoherent change detection (ICD) and coherent change detection (CCD) relies on the comparison of repeat-pass, temporally separated SAR images [1]. Spaceborne and airborne SAR change detection have been thoroughly developed and widely used by the SAR community [1]-[7]. However, this is not yet well documented for drone-borne SAR. In [8], the first drone-borne repeat-pass interferogram was obtained using a 10-GHz radar. It was reported that the quality of the interferometric map is not sufficient due to motion errors.

In later research, lower operating frequencies were used. For example, the feasibility of repeat-pass L-band SAR interferometry and SAR tomography was presented in [9]. In [10], crop growth deficit maps with a 1 m spatial resolution and 5 cm accuracy were generated by using a drone-borne SAR system operating in the P, L, and C-bands. However, only the L-band was used to generate deficit maps. The same SAR system with [10] was used in [11] to predict the sugarcane harvesting date and productivity. Data was collected in 7 survey flights over 6 months. In [12], differential SAR interferometry capability of the L-band drone-borne SAR system was investigated. Corner reflector displacements were detected with a better than 1 cm accuracy. As seen, some repeat-pass interferometry works have been done on low frequency systems and up to X-band. However, higher frequency systems and drone-borne change detection have been less explored. Higher frequencies and shorter ranges allow for finer spatial resolutions. Also, higher sensitivity to subtle changes in the scene is achieved when higher frequencies are employed.

Fundamentally, the main challenge in change detection is ensuring a high correlation between the “before/after” images. Due to the short-range, high-frequency and high-resolution, the drone's motion deviation from the nominal trajectory results in both space-variant and space invariant errors. These errors are unique for each drone pass, which makes two-pass imaging geometries mismatched. Even if two focused images are formed, high co-registration errors and spatially invariant/variant phase errors exist in the resulting change map.

In this chapter, both ICD and CCD capability of the high-frequency and high-resolution drone-borne SAR system operating at short ranges is investigated. At first, based on the derived SAR change detection characteristics, the system’s operating parameters are determined e.g., altitude, range to the scene center, and look angle. Also, the impact of phase errors on the CCD map is evaluated. Then, the algorithms for coherent and incoherent change detection are

presented. Finally, the ability of the SAR system to detect changes by implementing the proposed algorithm is explored experimentally.

The remainder of this chapter is organized as follows. Section 6.2 explains SAR change detection characteristics and phase error impact on change detection whereas Section 6.3 explains the change detection algorithm. The experimental results are presented in Section 6.4. Finally, in Section 6.5, a summary is included.

6.2 Drone-Borne SAR System Characteristics for Change Detection

Change detection is a well-known technique. Both incoherent and coherent change detection methods have some limitations, and some requirements should be met to generate quality change maps. For example, baseline errors should not be so high otherwise high geometric mismatches and decorrelation occur between image pair. Hence, optimal SAR system operating parameters such as altitude, range to the scene center, and look angle should be derived. In this chapter, incoherent and coherent change methods are presented, and the SAR system is examined based on CCD decorrelation sources to evaluate the system's limitations and abilities.

Change detection is a repeat-pass, repeat-geometry SAR method. The change can be detected by incoherent and coherent methods. Incoherent methods are more sensitive to large-scale changes, such as the displacement of a sizeable object whereas coherent methods can detect subtle changes, such as tyre marks and footprints.

6.2.1 Incoherent Change Detection - ICD

In ICD, temporally separated SAR images are compared in terms of mean backscatter power. Conventionally, averaging of multiple resolution cells' intensities is taken to obtain the mean backscatter power. The change map can be generated by considering the difference between the intensities,

$$CD_N = \sum_{k=1}^{N} |f_k|^2 - \sum_{k=1}^{N} |g_k|^2 \tag{6.1}$$

where N is the number of resolution cell samples, f and g are the first and the second complex images obtained from two passes.

However, this method is not befitting to detect changes in SAR imagery because the result changes depending on the intensity levels of the images [13]. As an alternative approach, ratio method which is independent of intensity variance and only depends on the relative change can be used. Conventionally, the change is expressed in decibels, and estimated as shown below [13], [14].

$$CD_N = 10\ log\left(\frac{\sum_{k=1}^{N}|f_k|^2}{\sum_{k=1}^{N}|g_k|^2}\right) \tag{6.2}$$

6.2.2 Coherent Change Detection - CCD

In CCD, change detection relies on the comparison of repeat-pass, temporally separated SAR images at the phase level and the subsequent extraction of an image coherence map. The classical coherence estimator is given as follows [1]:

$$CD_C = \frac{|\sum_{k=1}^{N} f_k g_k^*|}{\sqrt{\sum_{k=1}^{N}|f_k|^2 \sum_{k=1}^{N}|g_k|^2}} \tag{6.3}$$

where the symbol $[\cdot]^*$ denotes the complex conjugate and the other parameters are the same as in (6.2).

However, the coherence can be affected by several decorrelation sources most of which are not associated with an actual scene change. Those are summarized in the expression below are [15]:

$$|\rho_t| = |\rho_{temp}| \cdot |\rho_{thermal}| \cdot |\rho_{spatial}| \cdot |\rho_{proc}| \tag{6.4}$$

where ρ_t is the total correlation, ρ_{temp} is the temporal decorrelation, $\rho_{thermal}$ is the thermal decorrelation, $\rho_{spatial}$ is the spatial decorrelation, and ρ_{proc} is processing decorrelation quantifying the decorrelation arising from the algorithms used in image formation and co-registration.

According to (6.4), the total correlation would be 1 when there is no thermal noise, temporal change, spatial error, and processing error. In this case, we may assume the two images are identical. If temporal changes are to be measured via (6.4) all de-correlation sources other than the temporal one should be negligible.

Temporal decorrelation results from scatterer changes, and it is introduced by the following equation [15].

$$\rho_{temp} = \exp\left(-\frac{8\pi^2}{\lambda^2}\left(\sigma_y^2 sin^2(\theta) + \sigma_z^2 cos^2(\theta)\right)\right. \tag{6.5}$$

where σ_y is the horizontal displacement, σ_z is the vertical displacement and θ is the look angle.

Thermal decorrelation can be expressed as a function of SNR [15]. The level of the noise is determined by the radar receiver chain.

$$\rho_{thermal} = \sqrt{\left(\frac{1}{1+SNR_1^{-1}}\right)\cdot\left(\frac{1}{1+SNR_2^{-1}}\right)} \tag{6.6}$$

The spatial decorrelation arises when two-pass imaging geometries are not identical. If this decorrelation is expressed as a function of the baseline and the look angle, the following equation can be written [15].

$$\rho_{spatial} = 1 - \frac{2\cos(\theta)\,|\delta\theta| d_r}{\lambda} \tag{6.7}$$

where $\delta\theta$ is the look angle difference, d_r is the range resolution and λ is the wavelength.

This equation assumes two baselines which are identical with only a constant bias offset between them. As a special case, the total baseline decorrelation is reached in correspondence with the critical baseline, B_{nc} [15]:

$$|B_{nc}| = \left|\frac{\lambda R_0 \tan(\theta)}{2d_r}\right| \tag{6.8}$$

where R_0 is the radar to target distance.

6.2.3 Drone-Borne SAR System Evaluation in terms of Change Detection

The drone-borne SAR systems built at the University of Birmingham is explained in Chapter 3. Here, DJI M300 drone shown in Figure 6.1 is employed with an onboard off-the-

Figure 6.1 Drone-borne SAR system.

shelf INRAS Radarbook operating at 24 GHz. The radar parameters are given in Table 6.1 as a reminder, including the spatial resolution which is an important parameter.

The capabilities and limitations of CCD using high-frequency drone-borne SAR are evaluated next, based on (6.5) -(6.8) and Table 6.1. Figure 6.2 shows the temporal decorrelation (6.5) observed by the system in Table 6.1, for different horizontal and vertical displacements. This, in turn, specifies CCD sensitivity limits. As indicated, the SAR system has a mm-level sensitivity. For example, at a 60° look angle, a horizontal displacement of 1.5 mm results in a correlation of 40%. Higher look angles are more sensitive to horizontal changes whereas low look angles have a better sensitivity to vertical changes as (6.5) also suggests.

Table 6.1: Radar Parameters of the System

Parameters	**24 GHz**
Bandwidth	500 MHz
Azimuth Beamwidth	12.6°
Elevation Beamwidth	76.5°
Tx/Rx Antenna gains	13.2 dBi
Transmit Power	8 dBm
Transmit and Receive Channels	2-Tx, 8-Rx
Noise Figure	~10 dB
System Losses	~3 dB
Weight	0.41 kg
Range resolution	0.3 m
Maximum azimuth resolution	0.03m

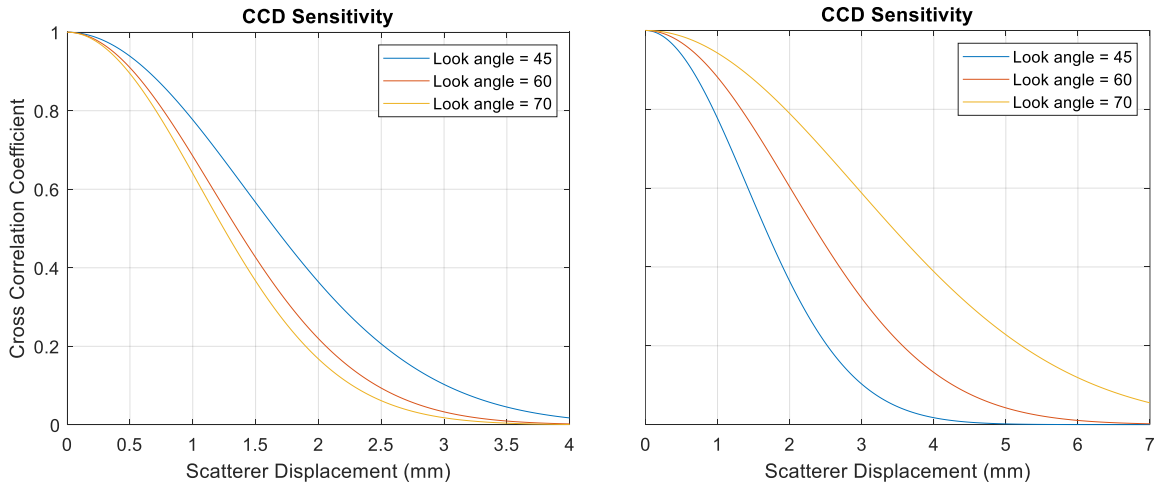

(a) (b)

Figure 6.2 CCD sensitivity. (a) Displacement is on the horizontal plane. (b) Displacement is on the vertical direction.

Thermal decorrelation is related to SNR as given in (6.6). The previous work shows that the image SNR for the considered radar system parameters is around 30 dB. This makes the thermal decorrelation negligible for our application.

In Figure 6.3, the critical baseline which is orthogonal to the line-of-sight (LOS) of the radar is plotted against the look angle for different target range values (6.8). For example, when the range to the target is 60 m, we have a 1 m critical baseline value at a 40° look angle, and 2.7 m baseline value at a 65° look angle. Apparently, higher look angles increase the critical baseline value. Similarly, higher range values make the critical baseline greater. However, it is important to note that the maximum transmit power of the radar is low (8 dBm), so a bigger range value may cause reduction in SAR image sensitivity. Also, it increases the required aperture length to achieve the desired azimuth resolution, hence the opportunity for motion error can be higher in the aperture. Therefore, choosing an acceptable R_0 is significant for this application. From experimentation experience, the baseline which is orthogonal to the LOS of the radar is less than 1.5 m in most cases. This value corresponds to a 3.3 m critical horizontal

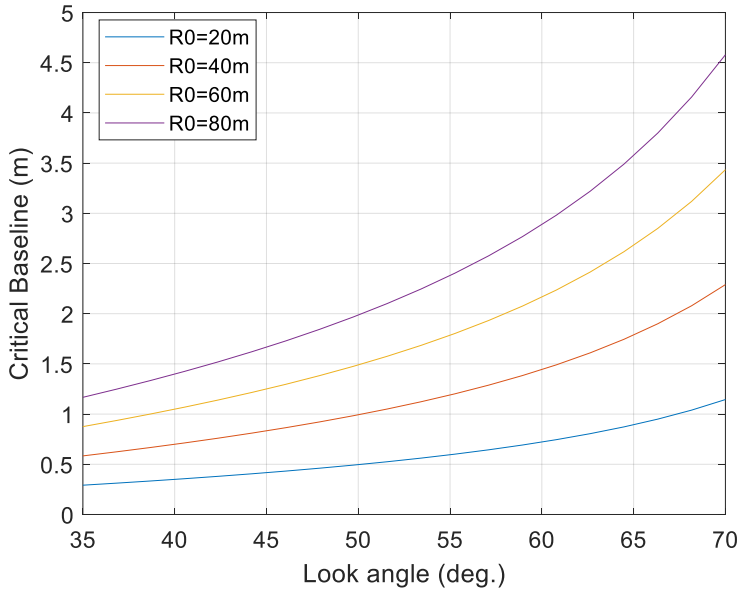

Figure 6.3 Critical baseline which is orthogonal to LOS of the radar as a function of the look angle for different R_0.

baseline and a 1.9 m critical vertical baseline. When we examine Figure 6.3, it is seen that higher than 40 m range with an around 60 degrees look angle can fulfil the requirements such as critical baseline, azimuth resolution, minimum motion error in the aperture and image sensitivity. Also, the vicinity of 60 degrees look angle gives us a moderate sensitivity to horizontal and vertical changes as illustrated in Figure 6.2.

6.2.4 Simulation for Spatial Decorrelation

Baseline errors result in spatial decorrelation. Drones as a SAR platform, operating at close range and prone to motion deviations, can exaggerate this effect. Equation (6.8) considers only constant baseline offset, but in a realistic scenario, the relative difference between the trajectories has constant, linear and non-linear components. To provide an analytical derivation with a closed-form solution to describe this problem is difficult, however it is possible to provide an example allowing numerical calculations to illustrate its effect. In this section, a CDD simulation is done by using an example pair of a drone's real, recorded positional data to

illustrate the actual impact of the motion errors on the CCD result. These data were acquired from a drone attempting to repeat the same trajectory twice, with a temporal separation of less than 20 mins, under good weather conditions (temperature was 25 ℃, and average wind speed was around 2.5 m/s).

In the simulation, all decorrelation sources other than spatial are ignored. A hypothetical SAR system with the parameters shown in Table 6.1 is considered. The range to the target area center was approximately 44 m, whereas the look angle to the center point of the image was adjusted to 63 degrees in order to fulfill the specifications given in Section 6.2.2. The scene dimensions were assumed as 10 m by 20 m, with the scene comprising uniformly distributed uncorrelated scatterers. Also, multiple scattering centers are located randomly within a resolution cell. The scene size was kept relatively small to minimize space-variant phase errors within each individual image. In Figure 6.4(a), the recorded positional data within one radar beam are shown for two flights. The constant baseline error is 5 cm along the z-axis whereas it is 3 cm along the y-axis. These values are much smaller than the critical baseline values when the range is higher than 40 m, and the look angle is around 60 degrees as shown in Figure 6.3. Hence, constant errors along the horizontal and vertical axes do not cause significant decorrelation on the CCD map for this scenario. Nonetheless, linear, and non-linear errors may still degrade the CCD map.

In the simulation, the phase of each pixel for both primary and repeat-pass images is calculated based on the given positional data in Figure 6.4(a). Then, the non-linear phase errors shown in Figure 6.4(b) and (c) were artificially compensated for to mimic a perfect autofocus routine. Calculating cross-correlation coefficients using (6.3) and a sliding window of 4×6 pixels, the result shown in Figure 6.5(a) and (b) is obtained. If there were no residual errors, the phase would be uniform, and the change map would show no change (all white).

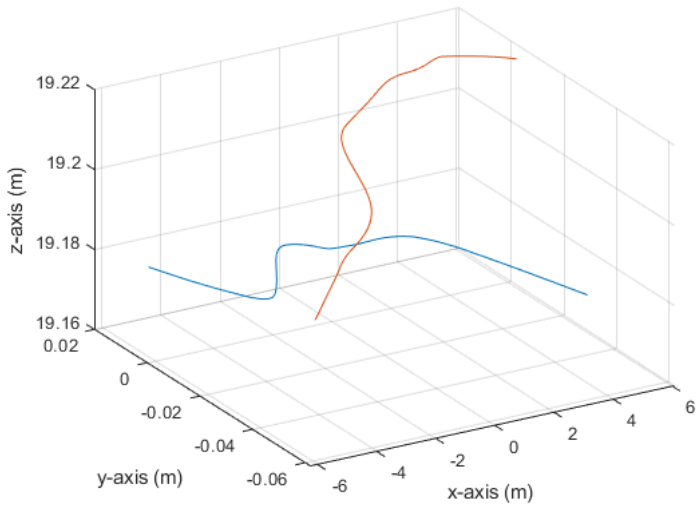

(a)

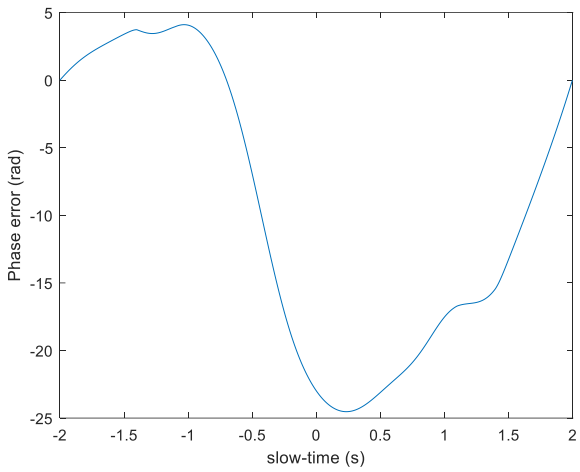

(b)

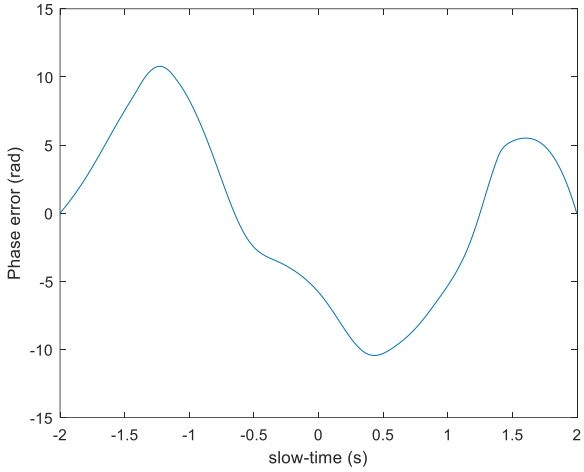

(c)

Figure 6.4 (a) Two-pass positional record. Blue - 1st track, and Red - 2nd track. (b) 1st flight non-linear phase error. (c) 2nd flight non-linear phase error.

Nevertheless, the residual phase error is non-linear and the resulting CCD map exhibits loss of coherency that is spatially variant across the target area, even for the limited scene size of this example, and with almost total loss of coherency in some parts (Figure 6.5(b)). These errors result from constant, linear, and space-variant non-linear phase errors. They should be removed from the CDD map to detect subtle changes repeatedly and robustly. In the next section, an algorithm is proposed to address this problem.

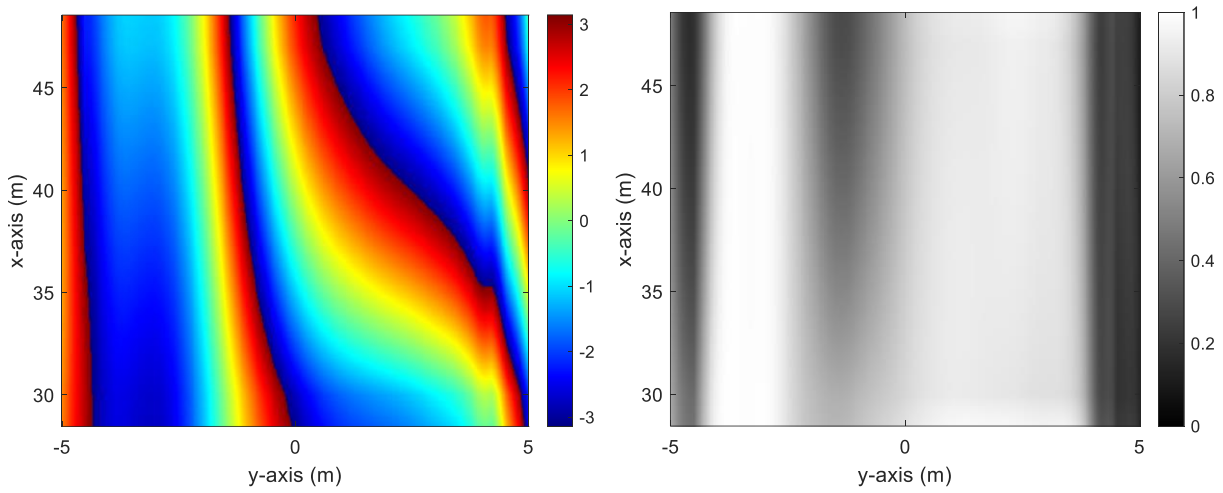

(a) (b)

Figure 6.5 (a) CCD phase. (b) CCD magnitude.

6.3 Change Detection Algorithm

The algorithm includes three main modules as shown in Figure 6.6. In the first one, two-pass radar raw data are processed to form high-resolution focused images. In drone-borne SAR, high deviations from the nominal trajectory that result in range walk errors and spatially variant/invariant phase errors are common, making the use of motion compensation techniques necessary as explained in the previous chapters. Here, LQMD and PGA based motion

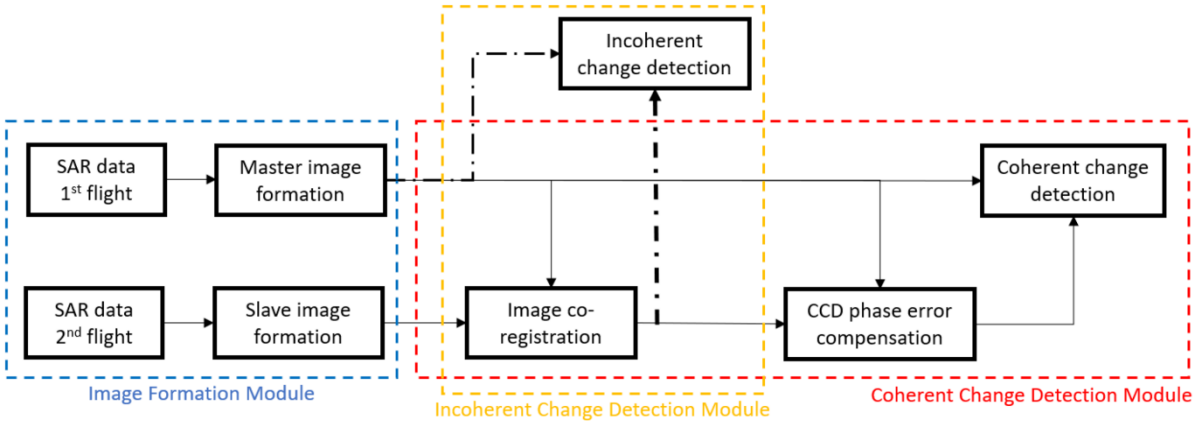

Figure 6.6 Change detection algorithm.

compensation approach presented in Chapter 5 is used and is briefly mentioned here for the sake completeness. The algorithm flow chart is shown in Figure 6.7. In short, after positional data-based MoCo, the Doppler centroid is adjusted to zero, and strong targets are selected in order to perform autofocus. Then, the space invariant errors are estimated by LQMD and PGA, respectively. After this step, RCMC is done, and N local scenes are created by dividing the image into azimuth and range blocks. Overlapped or non-overlapped local scenes can be created. Then, PGA is implemented to each block to minimize space-variant errors. The SAR data that contains each block can be expressed as:

$$s(f_r, u) = \left[s_{LS_1},\ s_{LS_2}, \cdots, s_{LS_N}\right] \tag{6.9}$$

where $s(f_r, u)$ is the range compressed SAR data, f_r represents range frequency, u is slow-time, and $s_{LS_n}$is the nth ($\mathrm{n} = 1, 2, \cdots, N$) phase error corrected local scene.

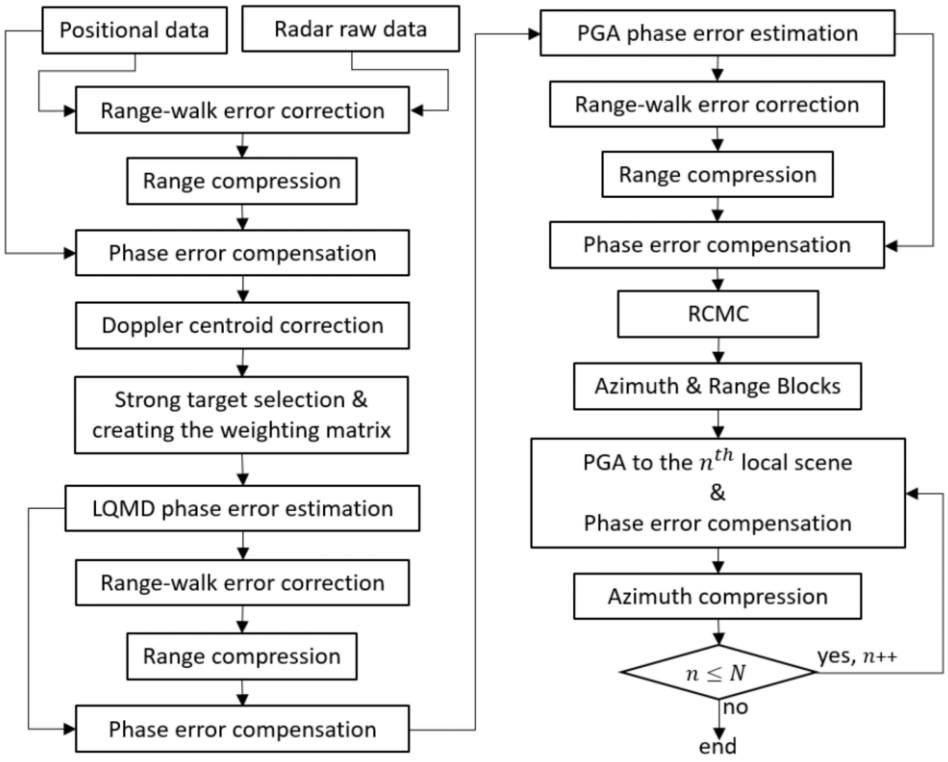

Figure 6.7 Image formation algorithm.

In this study, azimuth compression is done for each local scene separately. That is because the proposed CCD algorithm uses local scenes to reduce both geometrical errors and spatially variant phase errors After the azimuth compression, the local image, $S_{LS_n}(x, y)$, is formed on xy-plane after converting the slant range into ground range.

The image formation process is identical for both primary ("master") and repeat-pass ("slave") radar data. As a next step, the formed master and slave local images, $S_{MLS_n}(x, y)$ and $S_{SLS_n}(x, y)$, are sent to the change detection modules.

As it can be seen in Figure 6.6, the ICD module includes 2 main blocks as image co-registration and incoherent change detection whereas the CCD module includes 3 main blocks as image co-registration, CCD phase error compensation and CCD map generation. Next, each block will be explained in detail to provide a better understanding of the change detection process.

6.3.1 ICD Module

The ICD module uses two intensity images to form a change map. At first, master and slave images are co-registered and then, their backscatter powers are compared by (6.2). As a result, the change map of a local scene is generated. By repeating these steps for other local images, the full ICD map can be formed. The detailed flow-chart of the ICD module is given in Figure 6.8. In the resulting change map, the low-intensity area indicates targets that arrive at the scene whereas the high-intensity area indicates targets that leave the scene.

The first step for an ICD map generation is the image co-registration. In this stage, the slave image is aligned with the master image by geometrically modifying it. There are intensity-

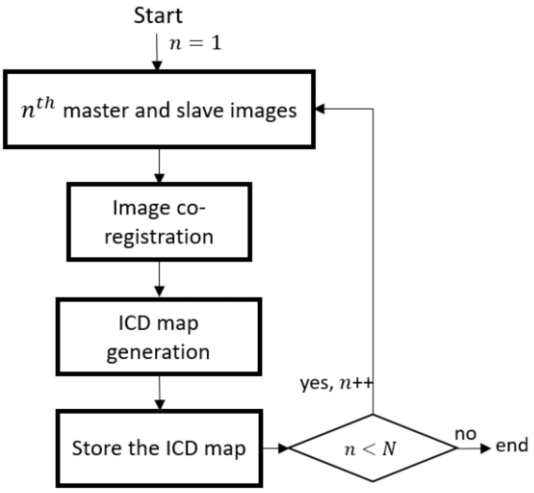

Figure 6.8 ICD module block diagram.

based and feature-based registration methods [16]. In this work, we use the intensity-based image registration approach as an initial attempt.

This approach seeks the maximum similarity of intensity patterns between the images by modifying the geometrical transformation matrix iteratively. As a similarity metric, mutual information (MI) is employed [17]-[19]. The main steps of the algorithm are shown in Figure 6.9. At first, the similarity of the interpolated slave image and the master image is calculated based on mutual information. Then, an image transformation matrix is formed by using an evolutionary optimizer as detailed in [20]. The transformation matrix includes variables for

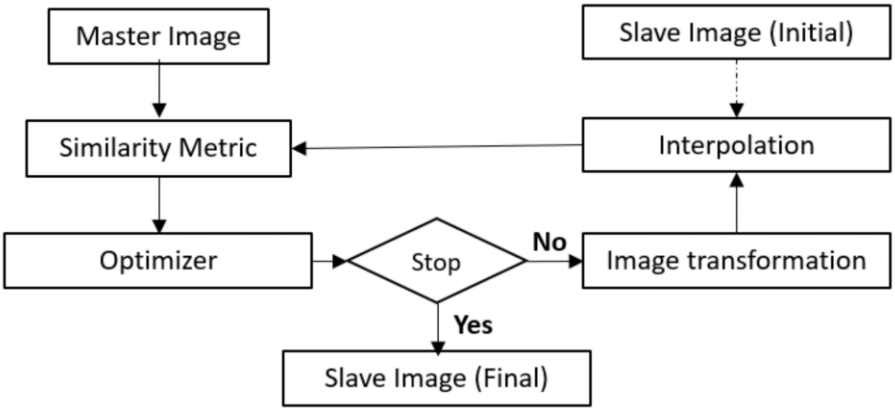

Figure 6.9 Intensity-based image co-registration.

different types of distortions such as translation, rotation, scale, and shear. The similarity value is maximized by modifying the transformation matrix iteratively. The process is ended, and the registered slave image is generated when the algorithm reaches the maximum number of iterations or the aimed similarity value. In this way, the geometrically aligned slave image, $\tilde{S}_{SLS_n}(x, y)$, is obtained.

After completing the image co-registration, the local ICD map is generated by employing the ratio method, and the change is shown in logarithmic unit as given in (6.2). At this stage, the formed ICD map is stored in a matrix, and by repeating these steps for all local scenes, the full map is formed as shown in Figure 6.8.

6.3.2 CCD Module

The CCD module uses the master and the slave complex local image data as its inputs. CCD relies on the comparison of these two local SAR images at the phase level. However, images should be co-registered and the phase errors between them should be compensated. The detailed flow-chart of the CCD module is given in Figure 6.10.

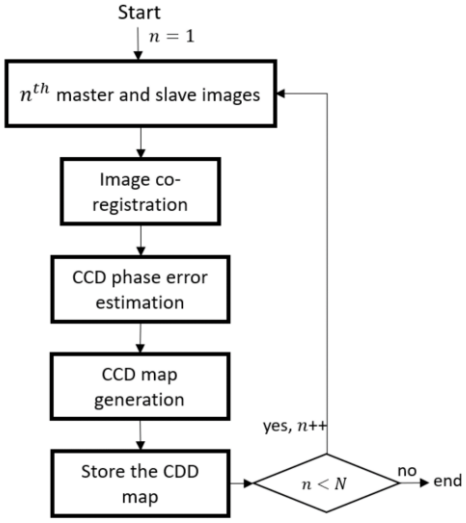

Figure 6.10 CCD module block diagram.

6.3.2.1 Image Co-Registration

At this stage, two complex SAR images taken from the image processing module are co-registered. The registration method and implementation are very similar to the presented approach in Section 6.3.1. The only difference is that the phase values of both master and slave images are preserved in the image co-registration stage. At first, the image transformation matrix is created by using the master and slave intensity images as described in 6.3.1 and shown in Figure 6.9. Then, the obtained image transformation matrix is applied to the complex slave image. In this way, the two images are co-registered by preserving the phase values.

6.3.2.2 CCD Phase Error Compensation

In CCD, the radar platform should follow the same path in each flight. In other words, the baseline between the passes should be zero. When motion deviations from the nominal trajectory exist, the phase difference of the SAR images may contain phase errors. Although most of the motion errors are compensated in the image formation stage, the residual errors may still degrade the change map. In most cases, the master image, $S_{MLS_n}(x,y)$ and the co-registered slave image, $\tilde{S}_{SLS_n}(x,y)$, contain residual constant, linear, and non-linear phase errors due to imperfect MoCo. As shown in Section 6.2.2, these errors cause time-varying baseline errors and loss of coherency that is spatially variant across the target area.

If the CCD phase error at point (x,y) is $\emptyset_{err}(x,y)$, the CCD map whose phase errors are compensated is given as follows based on (6.3).

$$\Lambda_{CCD}(x,y) = \left| \frac{\sum_{g=1}^{G} S_{MLS_n}(g)\tilde{S}_{SLS_n}(g)^{*}\, exp\left(-j\emptyset_{err}(g)\right)}{\sqrt{\sum_{g=1}^{G}\left|S_{MLS_n}(g)\right|^2 \sum_{g=1}^{G}\left|\tilde{S}_{SLS_n}(g)\right|^2}} \right| \tag{6.10}$$

where Λ_{CCD} is the change map, G is the total number of resolution cells and g represents the

pixel located at point (x, y), with values from 1 to G.

$\emptyset_{err}$ is unknown and should be estimated. To aid in its estimation, $\emptyset_{err}$ can be expressed as a polynomial of some order. Conducting a dedicated study for drone-based systems is a complex problem, so as a first step we rely on existing literature. Specifically, this work uses the model in [21]. This was originally developed to remove phase distortions due to flat-Earth and topographic effects in space-borne SAR interferometry. As will be shown in Section 6.4, the model given with equation (6.11) can be used to form acceptable CCD maps although some residual phase errors remain in the data.

$$\emptyset_{err}(x, y) = w_0 + w_1 x + w_2 y + w_3 xy + w_4 x^2 + w_5 y^2 \tag{6.11}$$

where w_i $(i = 0, 1, \cdots, 5)$ are the coefficients to be determined.

The coefficients may be obtained by implementing least-squares as in [22]. However, the method needs pixel selection outside of the deformation area. In drone-borne SAR case, the spatial decorrelation is generally high, and pixel selection outside of the deformation area may be difficult.

In this work, we employ a Genetic Algorithm (GA) based optimization technique [23] to estimate the coefficients of the CCD phase error function (6.11). This technique does not require any particular pixel selection and is able to compensate for phase errors globally within the change map. The main steps of GA to find the coefficients are demonstrated in Figure 6.11. In the first step, initial parameters are determined such as the number of individuals in the initial population, number of maximum generation (P), number of cross-over, mutation rate of each gene, desired average coherency (μ), and possible solution range of each phase error coefficient. Based on initial parameters, the first population is generated, and fitness value of each

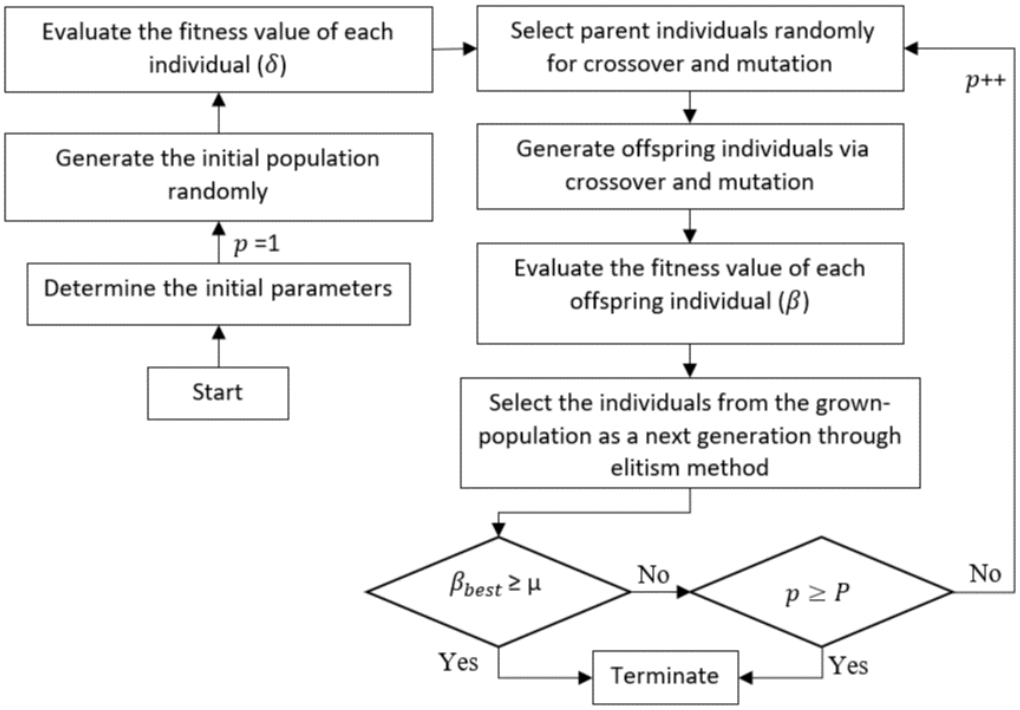

Figure 6.11 Genetic Algorithm.

individual, which is average value of equation (6.10) – (β), is evaluated. Then, some of individuals are selected for crossover and mutation, and offspring – new individuals are generated. As a next step, β value of each new individual is evaluated. With regard to selection part, as many individuals as in the initial population are selected from the existing population, and few of them must have the best coherency and other individuals can be chosen randomly – this method is known as elitism [24]. In the final step, if the best individual (β_{best}) is equal or bigger than μ or the generation number (p) reaches to P, the algorithm is terminated, otherwise the algorithm repeats itself from the parent selection part by increasing the generation number.

The local CCD map is generated by employing the conventional sample complex cross correlation method (6.3). After obtaining the error function, $\emptyset_{err}(x, y)$, the change map is formed by using (6.10). Then, the formed map is stored in a matrix. By repeating these steps for all local scenes, the full map is formed as shown in Figure 6.10.

6.4 Experimental Verification and Performance Assessment

Experiments were carried out at the University of Birmingham Metchley Lane sports pitches to verify the algorithms in Section 6.3 and to experimentally assess their performance. The ground was covered by 2.5 cm long grass. A number of corner reflectors were spread throughout the target area for georeferencing purposes and to assess algorithm outcomes with or without scene changes. 40 m-long SAR apertures were generated by flying the drone at an altitude of roughly 20 m with approximately 3 m/s velocity. In total, 32 flights were collected for different scenarios on the same day. The radar parameters are given in Table 6.1, and the experiment site can be seen in Figure 6.12.

In this experimental campaign, 3 different scenarios extracted from 5 different flights are considered to show the capability of the SAR system and validate the proposed algorithm. The first scenario is human footprint detection whereas the second includes a standing person and a car track with turns. The last scenario examines a car tyre mark detection in the presence of higher phase errors and geometric distortions in the formed image pair. Finally, the phase error impact on the change detection results is discussed.

6.4.1 Scenario-1

In this scenario, the first drone-borne SAR data were collected before making any changes in the scene. The second SAR data were collected after a person walks on the grass at normal speed. The human track can be seen in Figure 6.12(a) whereas the walking person's photo is shown in Figure 6.12(b). The total azimuth length the radar data were collected was 40 m whereas the scene size along the ground-range direction is 32 m.

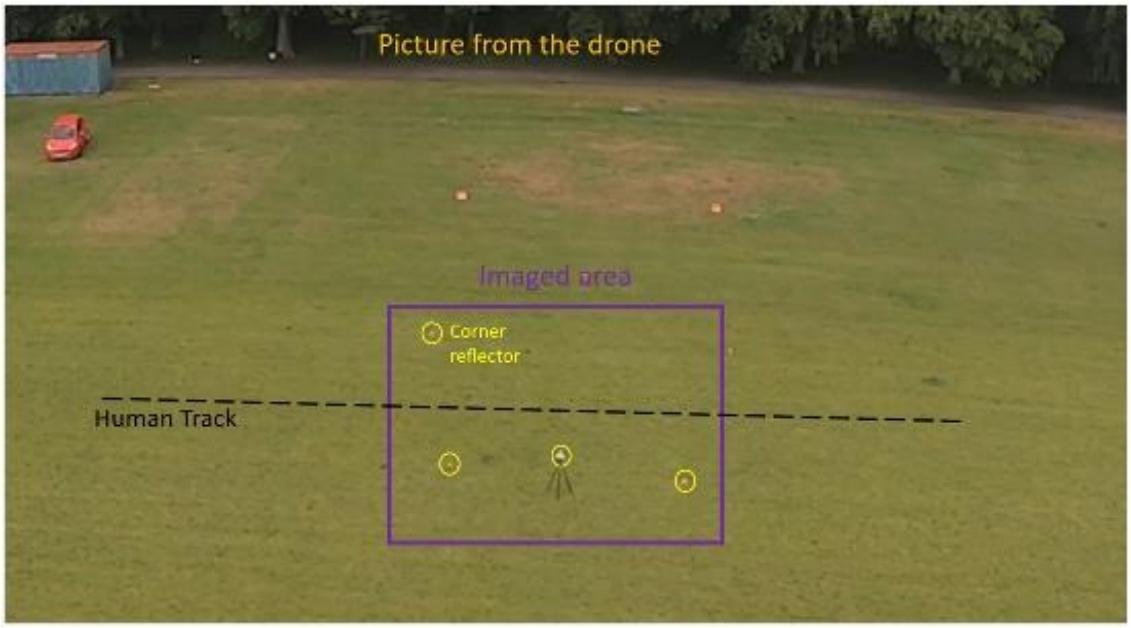

(a)

(b)

Figure 6.12 1st scenario (a) The scene, (b) Walking person after the 1st flight.

The processing begins with the positional data based MoCo as shown in Section 6.3. The recorded positional data of the two tracks are shown in Figure 6.13. The constant horizontal baseline was around 0.7 m whereas the constant vertical baseline was 0.06 m according to the recorded positional data. As described in Section 6.3, Doppler is centered to the zero Doppler before the space invariant MoCo is implemented, which is based on LQMD and PGA. However, we do not need to specifically select strong targets as in Chapter 5 because there are several corner reflectors in the scene. After space invariant MoCo, RCMC is done, and the images are divided into 4 azimuth and 2 range blocks. Then, another PGA is implemented to each sub-image. In this way, space-variant errors are minimized in the sub-images. Also, in this case, the azimuth length is equal to one antenna beam which is approximately 10 m along the azimuth direction. Here, we focus on only one sub-image shown in the purple rectangle in Figure 6.12(a). Figure 6.14(a) and (b) show the summed phase errors of the space-invariant and space-variant estimations for the interested sub-image. The master and the slave images are

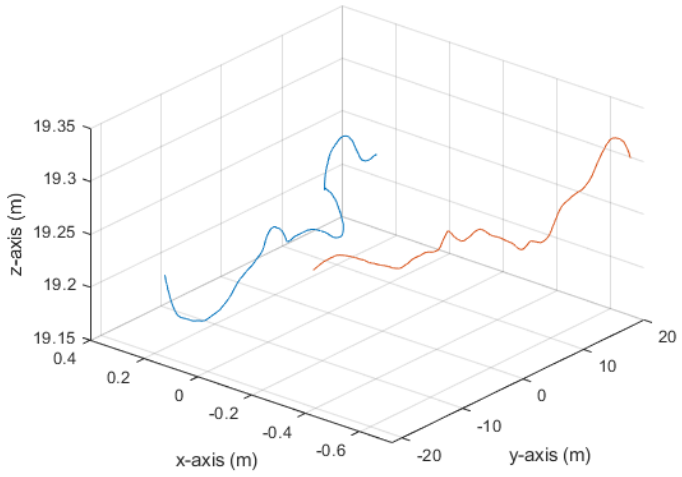

Figure 6.13 Positional data of the two tracks – 1st track is in blue, and 2nd track is in red.

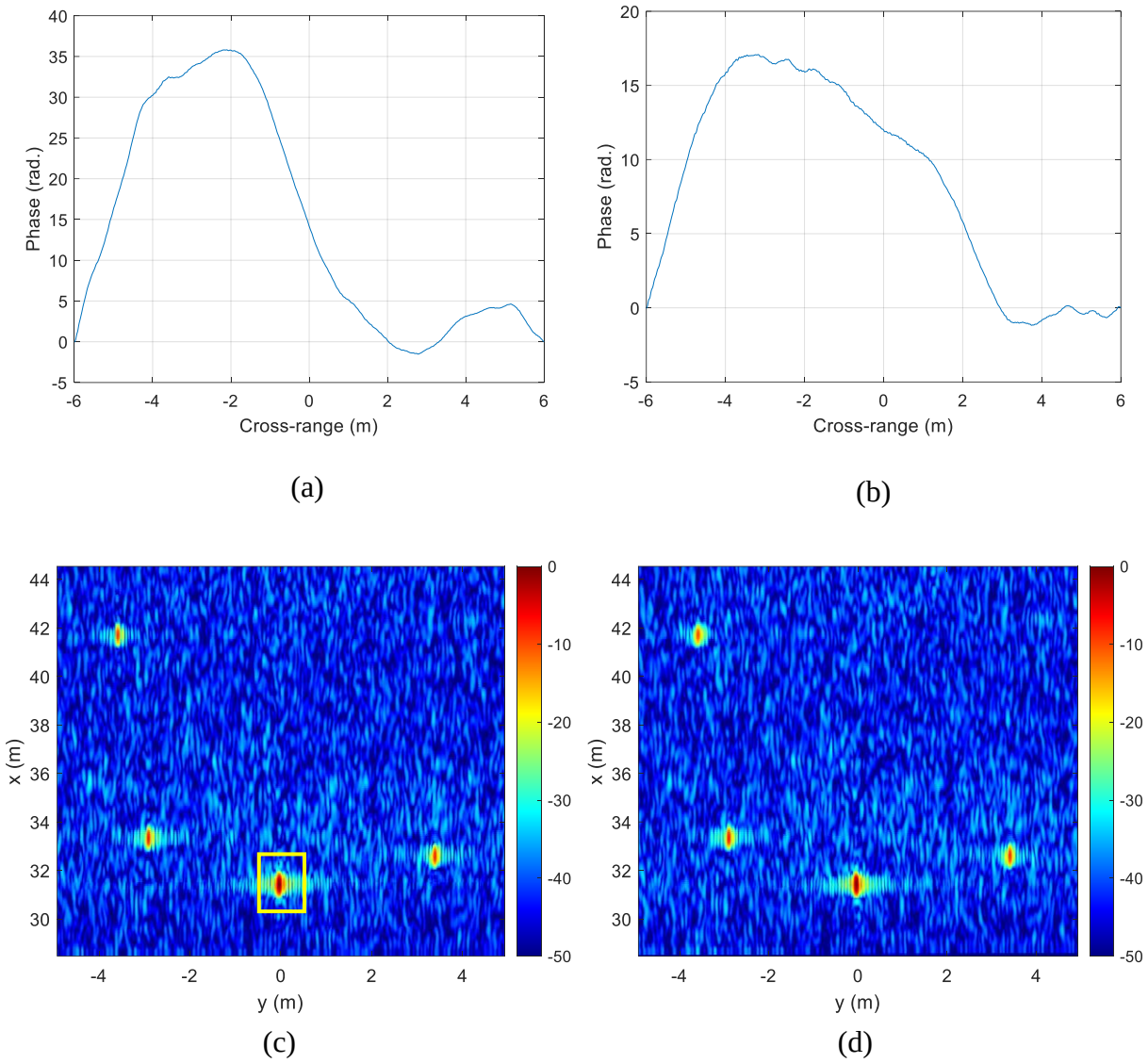

Figure 6.14 (a) Total estimated phase error for the master image, (b) Total estimated phase error for the slave image, (c) Formed master image, (d) Co-registered slave image, where the x-axis represents the ground range, and the y-axis represents the cross-range.

formed with a 6 cm azimuth and 40 cm ground-range resolution. Range and cross-range profile of the target shown in the yellow rectangle in Figure 6.14(c) are shown in Figure 6.15(a) and (b), respectively. The next step is to co-register the master and the slave images for both CCD and ICD maps. The master image and the co-registered slave image can be seen in Figure 6.14(c) and (d), respectively.

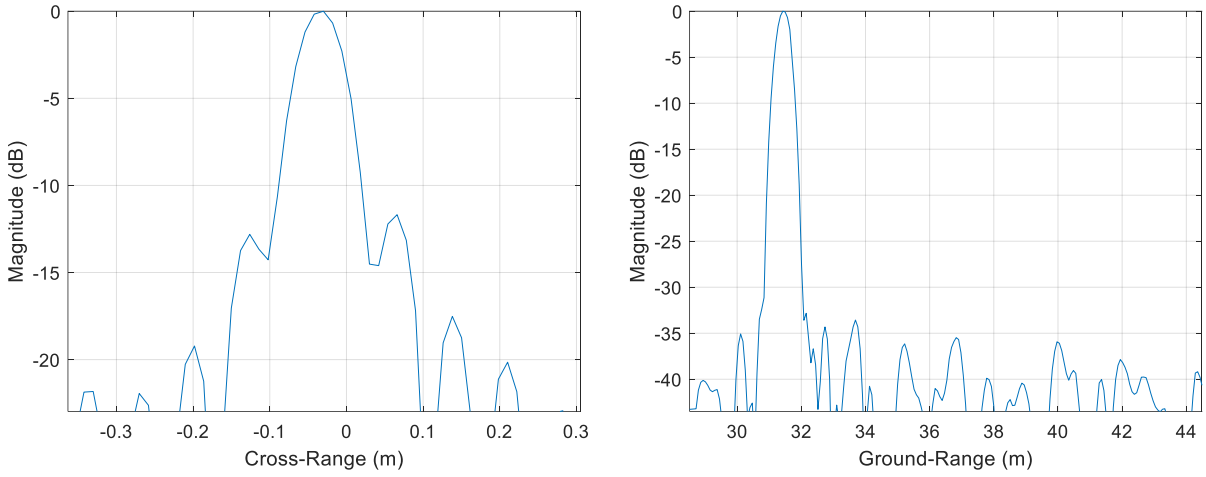

(a) (b)

Figure 6.15 Cross-section of the corner-reflector shown in the yellow rectangle in Figure 6.14(c), (a) Cross-range profile, (b) Ground-range profile.

At this point, if the cross-correlation coefficients are calculated by using a 2×8 sliding window, Figure 6.16(a) and (b) are obtained. The CCD phase has errors and resulting in the CCD map having a 0.6 average coherency, prior to the GA-based optimization. Also, the left part of the change map is degraded significantly. In GA, the number of crossovers is selected empirically as 25 whereas the mutation rate of each gene is 0.005. Also, the desired average coherency is decided as 0.95. The possible solution range of each phase error coefficient was empirically chosen as ±20 for w_1 and w_2, ±1 for w_3, and ±0.5 for w_4 and w_5. w_0 has no impact on the CDD map, so it was ignored. Also, as shown in Figure 6.17, 30 generations that each include 50 individuals were created by using the elitism method. The average value of each generation is shown in blue whereas the best individual in each generation is shown in red color. As a result, a 0.81 average coherency is achieved (Figure 6.16(c) and (d)). In this way, the human footprint is visible as shown in Figure 6.16(d) with a correlation coefficient of 0.65 (average). In this figure, the decorrelation on the right and left side of the corner reflectors are due to the high sidelobes of the reflectors seen in Figure 6.14(c) and (d).

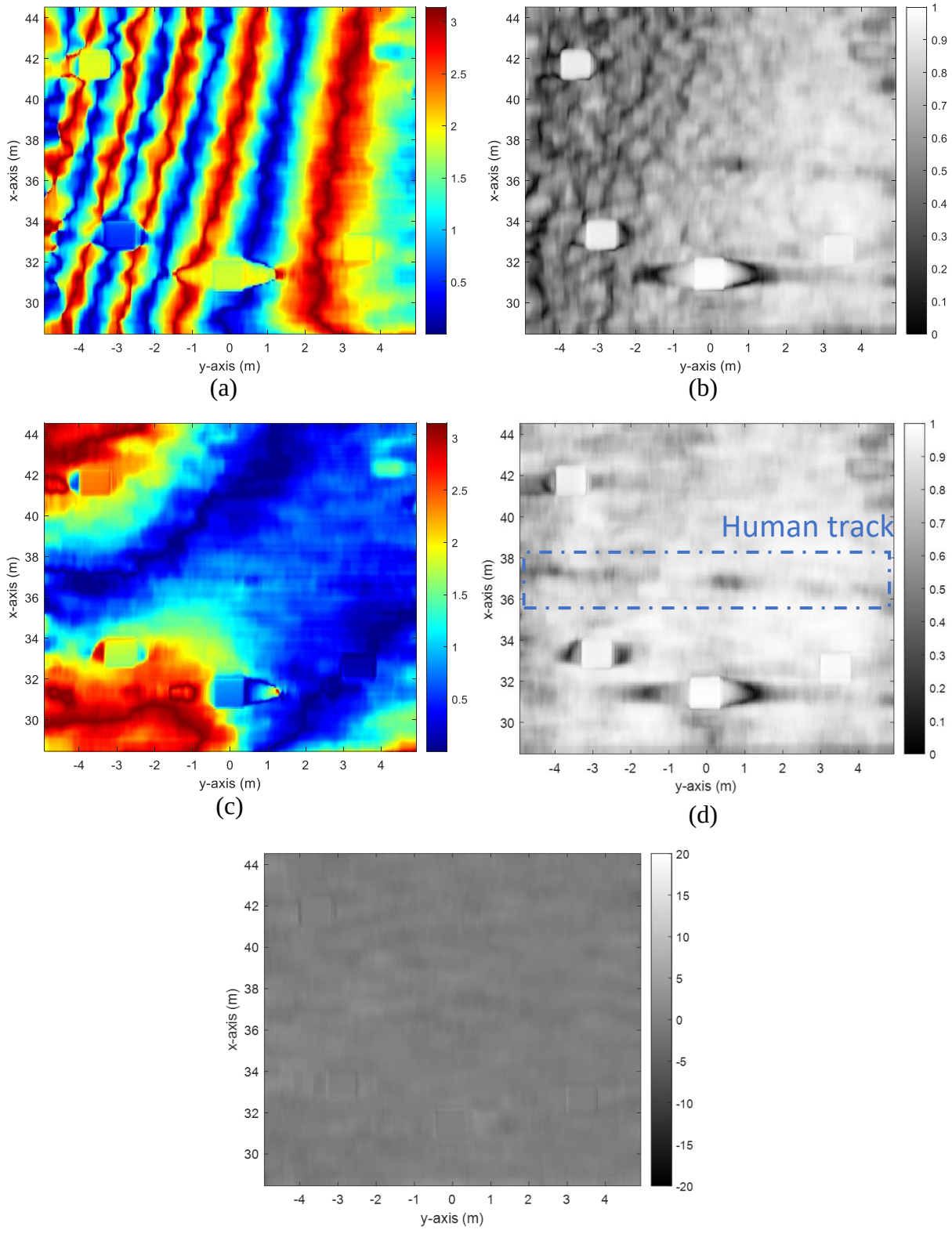

Figure 6.16 (a) CCD phase before GA-based optimization, (b) CCD map before GA-based optimization, (c) CCD phase after GA-based optimization, (d) CCD map after GA-based optimization, (e) ICD map, where the x-axis represents the ground range, and the y-axis represents the cross-range.

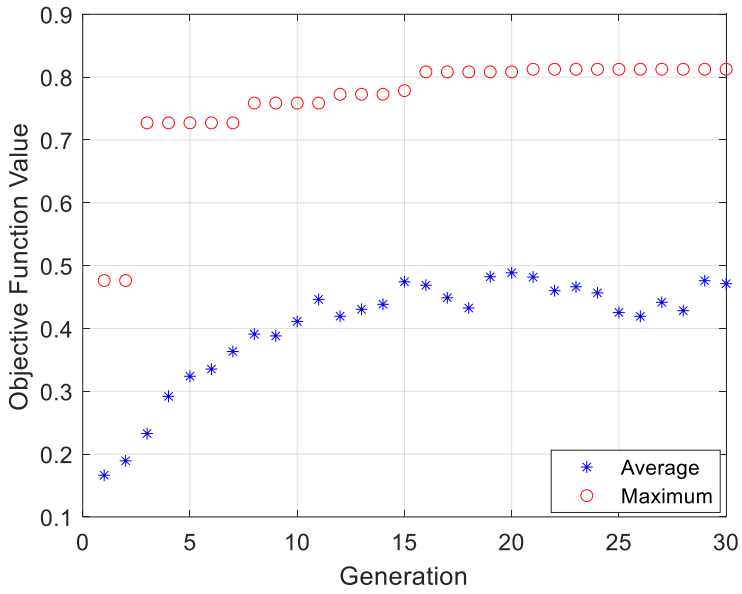

Figure 6.17 Created generations and the best solutions by GA.

After image co-registration, if the master and slave images are passed to the incoherent change detection (6.2), the change map shown in Figure 6.16(e) is obtained. As expected, a uniform response of around 0 dB is produced, and no change is visible. That is because ICD is more sensitive to large-scale changes.

6.4.2 Scenario-2

In this part, a larger scene (15×27 m) was considered (Figure 6.18(a)). After presenting how to form a local change map in detail, an example of generating a bigger CCD map is illustrated. In the scenario, a person stands on grass as seen in Figure 6.18(b) during the first flight. Prior to the second pass, the person is removed from the scene, and the track shown in Figure 6.18(a) is followed by the car. A picture of the car can be seen in Figure 6.18(c).

First, a local scene with a size of 10 by 16 m is chosen, and the MoCo strategy presented in Section 6.3 is implemented. The selected local scene is the same as the first scenario. After

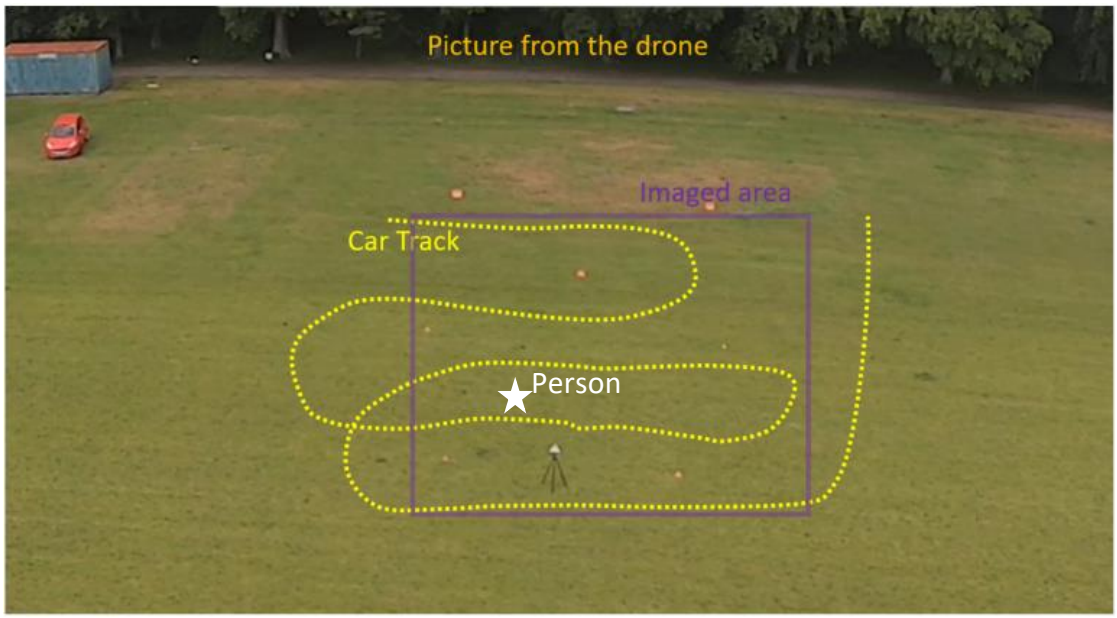

(a)

(b)

(c)

Figure 6.18 2nd scenario (a) The scene, (b) Standing person during the first flight, (c) Moving car before the 2nd flight.

forming the master and slave images with a 6 cm azimuth and 40 cm ground-range resolution, co-registration is done as described in Section 6.3. The formed and co-registered images are shown in Figure 6.19(a) and (b). The standing person and their shadow are obvious in the first figure.

By comparing the images using the incoherent change method, the map shown in Figure

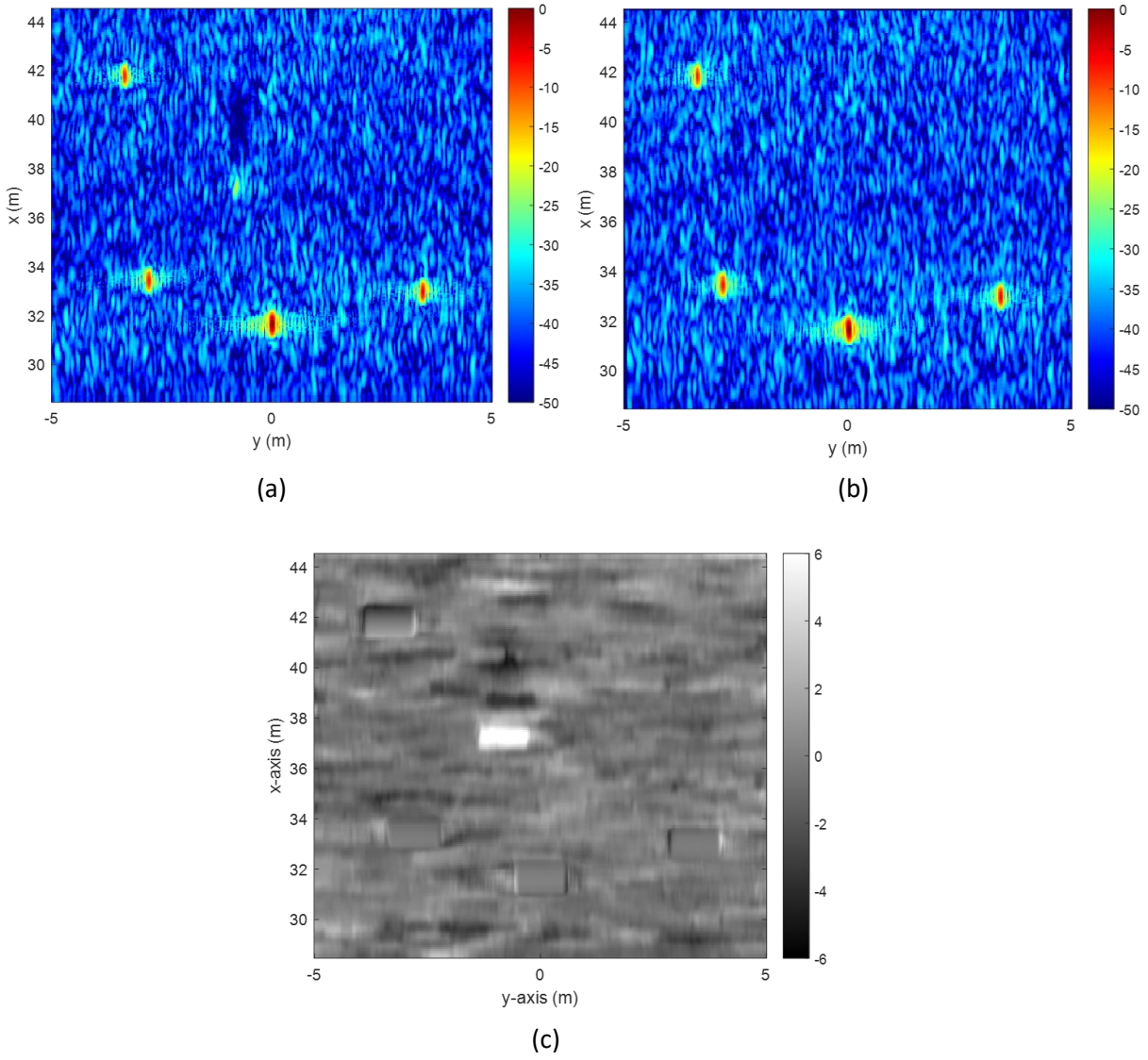

Figure 6.19 (a) Formed master image. (b) Co-registered slave image. (c) ICD result.

6.19(c) is obtained. As mentioned before, a low-intensity area indicates targets that arrive at the scene whereas a high-intensity area indicates targets that leave the scene. In the scenario, the person is removed from the scene. Hence, the person has a high intensity (almost 6 dB). However, the person's shadow has low intensity (almost -6 dB). That is because the shadow area shown in Figure 6.19(a) is occupied by clutters in the second image (Figure 6.19(b)).

After image co-registration, the CCD result is shown in Figure 6.20(a) and (b). As can be

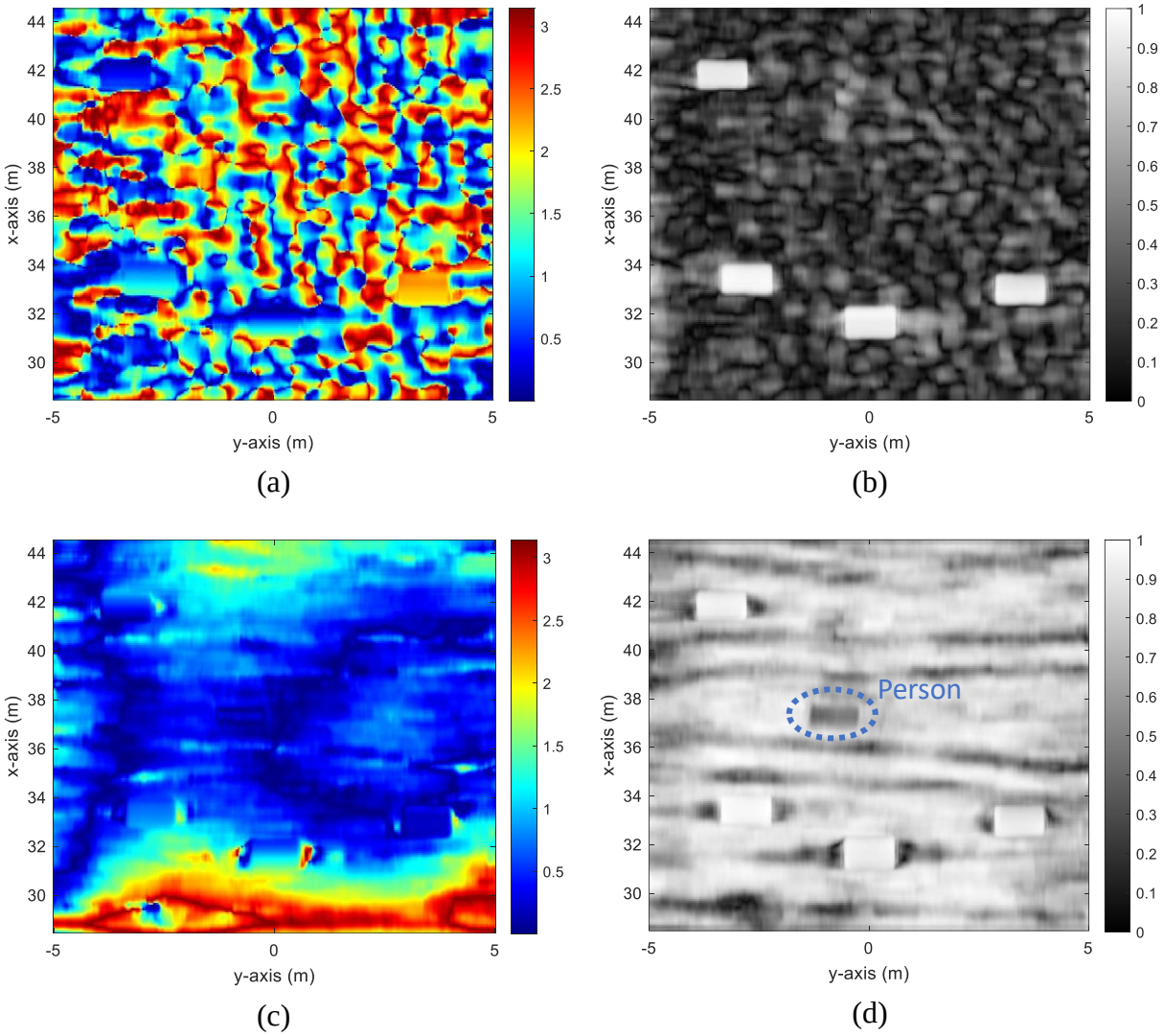

Figure 6.20 (a) CCD phase before GA-based optimization, (b) CCD map before GA-based optimization, (c) CCD phase after GA-based optimization, (d) CCD map after GA-based optimization, where the x-axis represents the ground range, and the y-axis represents the cross-range.

seen, the map is distorted completely, and no change is visible due to phase errors. In order to compensate for these errors, the GA-based optimization method is applied by using the same initial parameters as the first scenario except for the maximum iteration number, *P*. Here, P is selected as 60 to see how much difference occurs compared to 30 iterations. The improvement achieved by GA can be seen in Figure 6.21. The initial coherency is around 0.5. After creating

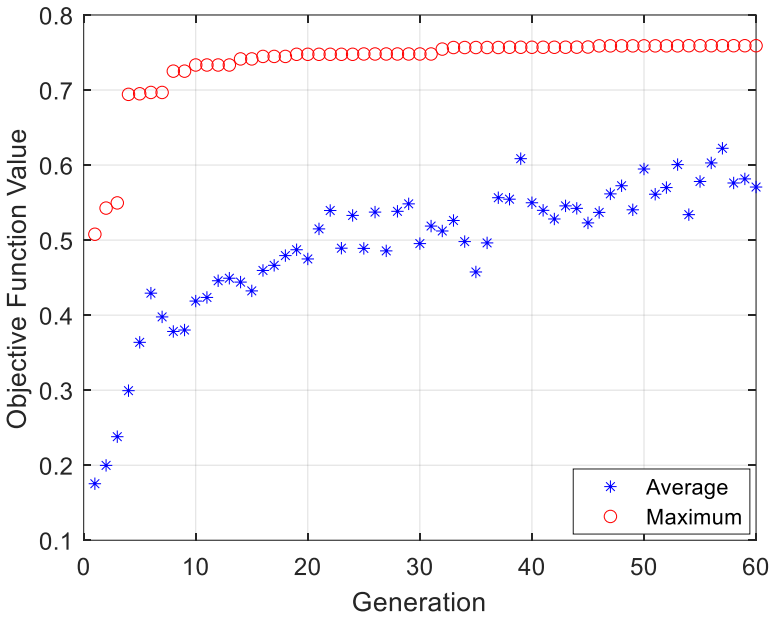

Figure 6.21 Created generations and the best solutions by GA.

30 generations, a 0.74 average coherency is obtained whereas, at the end of 60 generations, a 0.76 average coherency is achieved. The result is shown in Figure 6.20(c) and (d). Most of the phase errors are removed and as a result, the car tyre marks and the person who left the scene prior to the second flight are visible.

Moreover, subtle changes in a bigger scene can be detected as described in Section 6.3. The formed local change map shown in Figure 6.20(d) is stored. Then, another sub-scene is selected, and the local change map for it is formed by applying the same change detection processing steps. After registering the formed local maps, bigger change maps can be generated. In order to ease the registration accuracy, overlapped local scenes are selected. In this example, 4 sub-images that are half-overlapped along the azimuth direction and 30% overlapped along the ground-range direction are used. The sub-scenes are shown with dashed rectangles in different colors in Figure 6.22. Also, the obtained result can be seen in this figure. Apparently, besides aligning all the sub-scenes correctly, the algorithm achieved to detect the car track

including its turns.

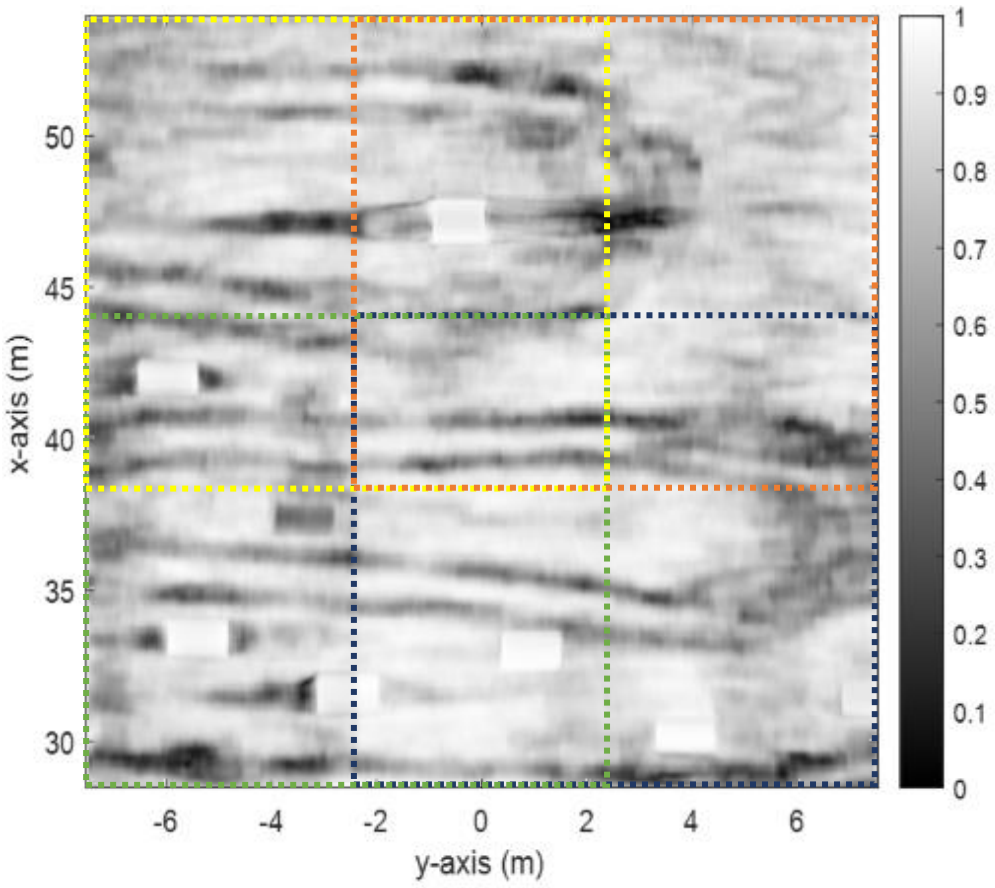

Figure 6.22 The final change map after combination of the 4 sub-images where the x-axis represents the ground range, and the y-axis represents the cross range.

6.4.3 Scenario-3

In this scenario, the drone-borne SAR data is collected before and after the car passes through the imaged area as shown in Figure 6.23(a) and (b). After following the same steps in the previous scenarios, the CCD map shown in Figure 6.24(d) is obtained. Although the car tyre mark is obvious, there is a decorrelated region between the 3rd and 5th meters along the azimuth direction. When we compare Figure 6.24 (a)-(b) with Figure 6.14 (a)-(b), it is apparent the phase error difference between the master and slave images is higher in this scenario. Due

to the high phase error difference, the quality of the change map is reduced. The reason for this is that as the phase error difference increases, geometric errors between the images increase, and accordingly the performance of the co-registration algorithm used decreases. In this scenario, the phase error difference function has a more than 50 radians peak value and 15 radians standard deviation as shown in Figure 6.24(c).

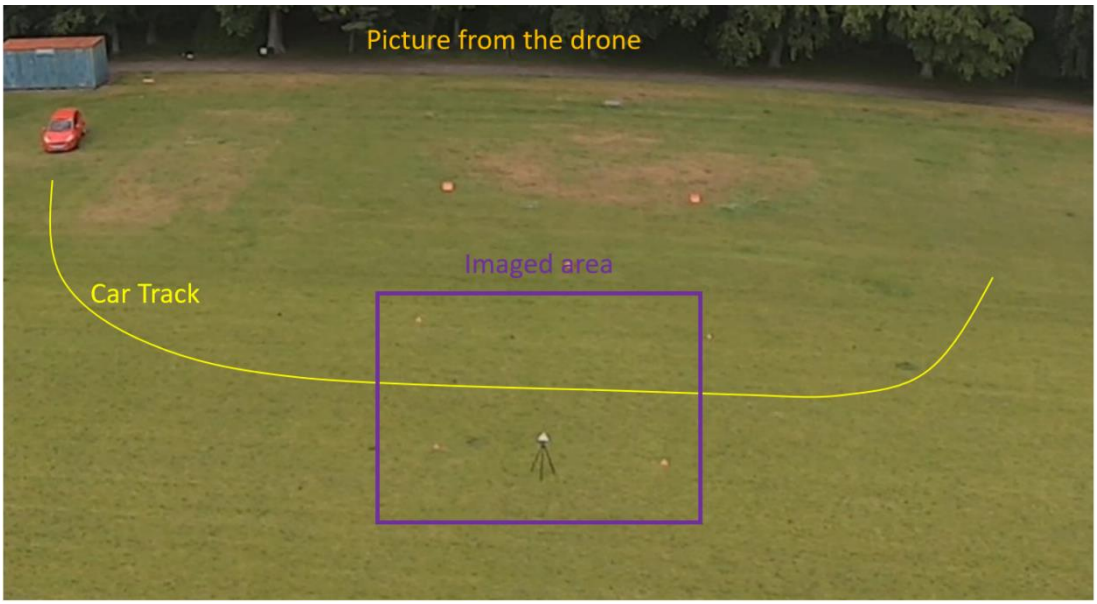

(a)

(b)

Figure 6.23 1st scenario (a) The scene, (b) Walking person after the 1st flight.

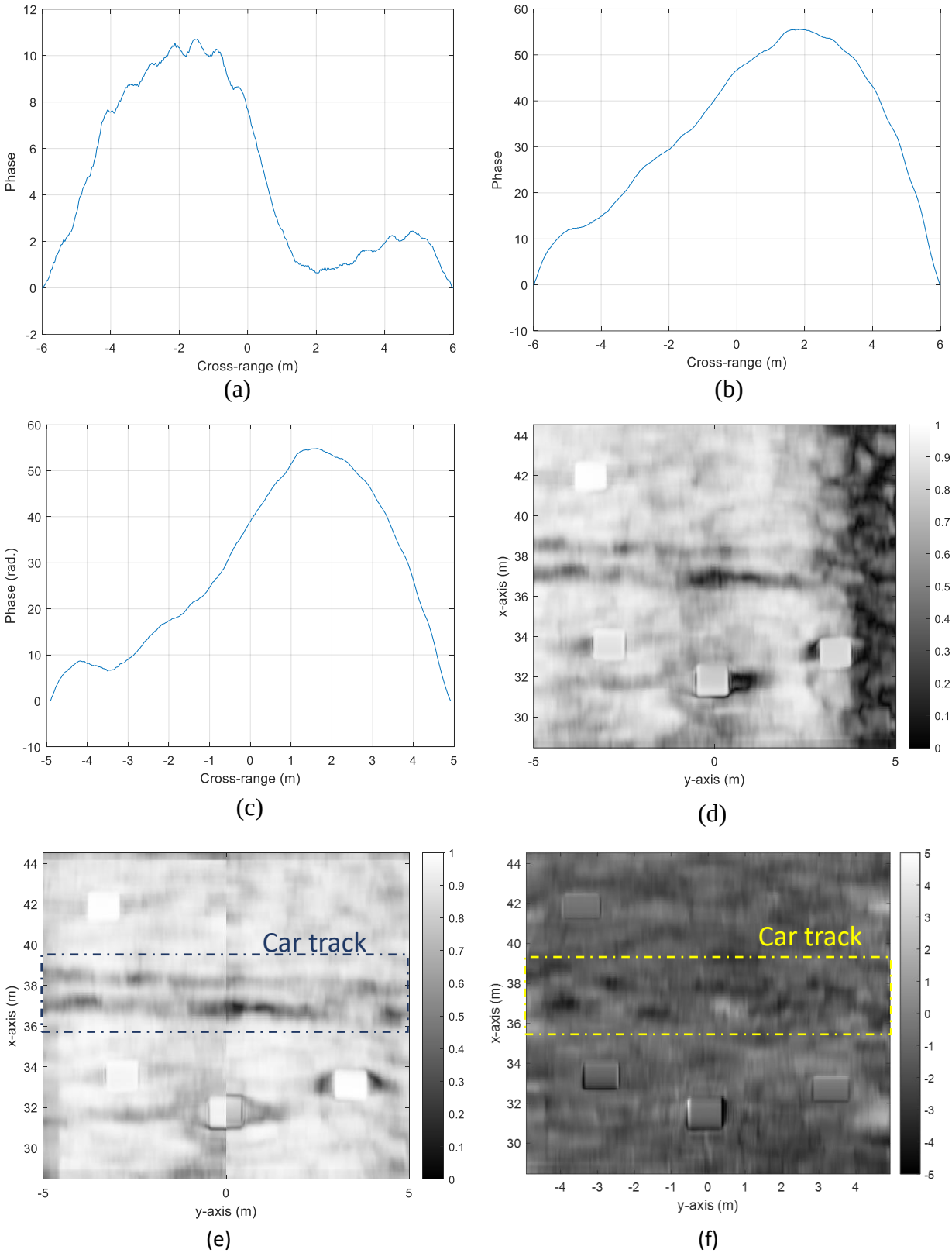

Figure 6.24 (a) Total estimated phase error for the master image. (b) Total estimated phase error for the slave image. (c) The phase error difference between the master and slave image error estimations. (d) CCD map after GA-based optimization. (e) CCD map after division and GA-based optimization. (f) ICD map

In order to solve this problem, the co-registration of the images should be improved. The simplest way is dividing the master and slave images into smaller images. In this example, the images are divided into 2 pieces along the azimuth direction. Then, co-registration and GA based optimization are repeated for each sub-image pair. Finally, the obtained change maps are combined, and the result shown in Figure 6.24(e) is obtained. The average coherency is found as 0.91. In the formed change map, the car track can be easily observed.

Regarding the ICD map, the low geometrical errors does not cause significant degradation in the incoherent change map. After co-registering the master and slave images, the obtained change map is shown in Figure 6.24(f). The car tyre mark is not obvious but some black marks along the car track can be seen.

6.5 Summary

In this chapter, it is shown, for the first time, that a high-frequency, high-resolution drone-borne SAR system operating at short ranges is capable of detecting both subtle changes such as the human footprint or car tyre marks, and sizeable object displacement such as human replacements. After evaluating change detection parameters, decorrelation sources and limitations of the SAR system, a change detection algorithm is proposed. The performance of the algorithm is validated through a number of experiments that includes different scenarios. The results show that the drone-borne SAR system has the ability to detect changes in the scene by achieving high correlation between the primary and the repeat-pass images. However, the performance of the algorithm highly depends on the selection of the local scene size and co-registration quality.

6.6 References

[1] C. V. Jakowatz, Jr., D. E. Wahl, P. H. Eichel, D. C. Ghiglia, and P. A. Thompson, Spotlight-mode Synthetic Aperture Radar: A Signal Processing Approach. Boston, MA, USA: Kluwer, 1996.

[2] D. G. Corr and A. Rodrigues, “Coherent change detection of vehicle movements,” in Proc. Sens. Manag. Environ. IEEE Int. Geosci. Remote Sensing. Symp. (IGARSS), Jul. 1998, pp. 2451–2453.

[3] M. L. Williams and M. Preiss, “Physics-based predictions for coherent change detection using X-band synthetic aperture radar,” EURASIP J. Adv. Signal Process., vol. 2005, no. 20, pp. 3243–3258, Dec. 2005.

[4] M. Preiss, D. A. Gray and N. J. S. Stacy, "Detecting scene changes using synthetic aperture Radar interferometry," in IEEE Transactions on Geoscience and Remote Sensing, vol. 44, no. 8, pp. 2041-2054, Aug. 2006, doi: 10.1109/TGRS.2006.872910.

[5] M. Cha, R. D. Phillips, P. J. Wolfe, and C. D. Richmond, “Two-stage change detection for synthetic aperture radar,” IEEE Trans. Geosci.Remote Sens., vol. 53, no. 12, pp. 6547–6560, Dec. 2015.

[6] D. E. Wahl, D. A. Yocky, C. V. Jakowatz and K. M. Simonson, "A New Maximum-Likelihood Change Estimator for Two-Pass SAR Coherent Change Detection," in IEEE Transactions on Geoscience and Remote Sensing, vol. 54, no. 4, pp. 2460-2469, April 2016, doi: 10.1109/TGRS.2015.2502219.

[7] M. Wang, G. Huang, J. Zhang, F. Hua and L. Lu, "A Weighted Coherence Estimator for SAR Coherent Change Detection," in IEEE Transactions on Geoscience and Remote Sensing, vol. 60, pp. 1-12, 2022, Art no. 5228912, doi: 10.1109/TGRS.2022.3180044.

[8] M. Lort, A. Aguasca, C. López-Martínez and T. M. Marín, "Initial Evaluation of SAR Capabilities in UAV Multicopter Platforms," in IEEE Journal of Selected Topics in Applied Earth Observations and Remote Sensing, vol. 11, no. 1, pp. 127-140, Jan. 2018, doi: 10.1109/JSTARS.2017.2752418.

[9] O. Frey and C. L. Werner, "UAV-borne repeat-pass SAR interferometry and SAR tomography with a compact L-band SAR system," EUSAR 2021; 13th European Conference on Synthetic Aperture Radar2021, pp. 1-4.

[10] G. Oré *et al.*, "Crop Growth Monitoring with Drone-Borne DInSAR," *Remote Sensing*, vol. 12, no. 4, p. 615, Feb. 2020, doi: 10.3390/rs12040615

[11] G. Oré et al., "Predicting Sugarcane Harvest Date and Productivity with a Drone-Borne Tri-Band SAR," Remote Sensing, vol. 14, no. 7, p. 1734, Apr. 2022, doi: 10.3390/rs14071734.

[12] D. Luebeck *et al.*, "Drone-borne Differential SAR Interferometry," *Remote Sensing*, vol. 12, no. 5, p. 778, Feb. 2020, doi: 10.3390/rs12050778.

[13] E. J. M. Rignot and J. J. van Zyl, "Change detection techniques for ERS-1 SAR data," in *IEEE Transactions on Geoscience and Remote Sensing*, vol. 31, no. 4, pp. 896-906, July 1993, doi: 10.1109/36.239913.

[14] Preiss, M. and N. Stacy, "Coherent Change Detection: Theoretical Description and Experimental Results," Intelligence, Surveillance and Reconnaissance Division, Defense Science and Technology Organisation, DSTO–TR–1851.

[15] H. A. Zebker and J. Villasenor, "Decorrelation in interferometric radar echoes," in IEEE Transactions on Geoscience and Remote Sensing, vol. 30, no. 5, pp. 950-959, Sept. 1992, doi: 10.1109/36.175330.

[16] B. Zitova and J. Flusser, “Image registration methods: A survey,” Image Vis. Comput., vol. 21, no. 11, pp. 977–1000, Oct. 2003.

[17] D. Loeckx, P. Slagmolen, F. Maes, D. Vandermeulen, and P. Suetens, “Nonrigid image registration using conditional mutual information,” IEEE Trans. Med. Imaging, vol. 29, no. 1, pp. 19–29, Jan. 2010.

[18] D. Lee, M. Hofmann, F. Steinke, Y. Altun, N. Cahill, and B. Scholkopf, “Learning similarity measure for multi-modal 3D image registration,” in Proc. IEEE CVPR, Jun. 2009, pp. 186–193.

[19] D. Mattes, D.R. Haynor, H. Vesselle, T. Lewellen, and W. Eubank. "Non-rigid multimodality image registration." (Proceedings paper).Medical Imaging 2001: Image Processing. SPIE Publications, 3 July 2001. pp. 1609–1620.

[20] Styner, M., C. Brechbuehler, G. Székely, and G. Gerig. "Parametric estimate of intensity inhomogeneities applied to MRI." IEEE Transactions on Medical Imaging. Vol. 19, Number 3, 2000, pp. 153-165.

[21] H. -S. Jung, J. -S. Won and S. -W. Kim, "An Improvement of the Performance of Multiple-Aperture SAR Interferometry (MAI)," in IEEE Transactions on Geoscience

and Remote Sensing, vol. 47, no. 8, pp. 2859-2869, Aug. 2009, doi: 10.1109/TGRS.2009.2016554.

[22] B. Xu, Z. -w. Li, Q. -j. Wang, M. Jiang, J. -j. Zhu and X. -l. Ding, "A Refined Strategy for Removing Composite Errors of SAR Interferogram," in IEEE Geoscience and Remote Sensing Letters, vol. 11, no. 1, pp. 143-147, Jan. 2014, doi: 10.1109/LGRS.2013.2250903.

[23] Holland, John H. Adaptation in natural and artificial systems: an introductory analysis with applications to biology, control, and artificial intelligence. MIT press, 1992.

[24] De Jong, Kenneth Alan, *An analysis of the behavior of a class of genetic adaptive systems*. University of Michigan, 1975.

Chapter 7

Conclusions and Future Work

7.1 Summary and Outcomes

This thesis has conducted fundamental and systematic research on forming high-frequency high-resolution drone-borne SAR imagery of a target area and detecting changes in it with a mm-level sensitivity. Fundamentally, the research has included theoretical analyses, validation using simulations, and experimental performance assessments in real conditions with a drone-borne SAR demonstrator (operating at 24 and 77 GHz) built and tested by myself. A part of our research in this field has presented to specialist audiences, and it has won an award at the top radar conference.

After introducing fundamentals of SAR imaging and motion compensation techniques, Chapter 4 presented the first part of this work that includes building a technology demonstrator and evaluating its characteristics and limitations based on SAR sensitivity, drone motion errors, and data collection. It was found that the built SAR systems are better suited to short-range applications of up to a few hundred meters in range. It was also shown that short range high-

frequency operation leads significant space-variant errors that limit the imaging capability of the system.

After evaluating motion errors and their effects on image formation, an algorithm suitable for production of high-resolution imaging at 24 and 77 GHz has been developed. The performance of the algorithm has been tested through both simulation and experiments. As a result, it has been proved that a cross-range resolution of less than 2 cm can be achieved using a low-cost high-frequency vehicular radar mounted onboard a low-cost commercially available drone at short but highly useful ranges. Although the motion compensation strategy does not compensate the phase errors globally within the imaged area, the results show practical usability at short ranges for which many applications may be envisaged. Also, it was noted that wrong strong target selection and high target height variation in the scene can degrade the performance of the algorithm.

Based on the proposed image formation algorithm that can provide precision SAR focusing, change detection capability of the drone-borne SAR system has been investigated. After evaluating basic change detection parameters, decorrelation sources and limitations of the SAR system, the ICD algorithm for detection of sizeable object displacement and CCD algorithm for subtle change detection by maximizing the coherence between repeat-pass images have been presented. The performance of the algorithms has been validated through a number of experiments that includes different scenarios. It has been shown, for the first time, that a high-frequency, high-resolution drone-borne SAR system operating at short ranges is able to detect both subtle changes such as the human footprint and car tyre marks, and sizeable object displacement such as human replacements. However, it was seen that the performance of the algorithm highly depends on the selection of the local scene size and co-registration quality.

7.2 Future Work

The presented study in this work makes possible to form high-frequency high-resolution drone-borne SAR imagery and change-maps with a mm-level displacement sensitivity. On the other hand, there is always potential for further improvement.

Future research on the proposed image formation algorithm could be making the selection of strong targets automatic and including height-dependent target focusing using digital elevation models to aid imaging quality and robustness.

Regarding the change detection algorithms, the next goal could be making the local scene size determination automatic based on image quality factors, improving the image co-registration performance by employing non-global and non-linear transformation models, and including an adaptive polynomial order model to remove residual CCD phase errors.

In addition to these improvements, tomographic SAR mode could be investigated as well. This mode allows the formation of volumetric high-resolution drone-borne SAR images by using spatially separated multiple apertures (these could be linear, circular or any kind of trajectory). In this way, the drone-borne SAR system can gain the capability of precisely measuring the distances and dimensions of an object. The method needs many drone flights that each will have unique motion errors, so motion error compensation and image co-registration will be more challenging in this mode. Also, collecting fully sampled 3D SAR data may not be possible in some scenarios due to limitations on the drone's positional accuracy. This may lead to aliasing artifacts and ambiguities in the volumetric image induced by the sparsity in the 3D SAR data. Hence, some gap-filling strategies based on autoregressive techniques may be needed.